Crystallization and Melting Studies of Poly(ε-caprolactone) and Poly(ethylene oxide) using Flash™ Differential Scanning Calorimetry and Preparation and Characterization of Poly(δ-valerolactone) Fractions

By

Matthew Vincent

Dissertation submitted to the faculty of the Virginia Polytechnic Institute and State University in partial fulfillment of the requirements for the degree of

Doctor of Philosophy

in

Chemistry

Hervé Marand, Committee Chair

Alan R. Esker

Louis A. Madsen

Robert B. Moore

May 9, 2019

Blacksburg, VA

Keywords: Polymer, Crystallization, Melting, Kinetics, Fast Differential Scanning Calorimetry, Poly(ε-caprolactone), Poly(ethylene oxide), Poly(δ-valerolactone), Fold Surface Free Energy, Gibbs-Thomson, Hoffman-Weeks, Equilibrium Melting Temperature

Crystallization and Melting Studies of Poly(ε-caprolactone) and Poly(ethylene oxide) using Flash™ Differential Scanning Calorimetry and Preparation and Characterization of Poly(δ-valerolactone) Fractions

Matthew Vincent

ABSTRACT

The isothermal crystallization and melting temperatures of poly(ε-caprolactone) were correlated using fast differential scanning calorimetry. The melting kinetics was found to be independent of isothermal crystallization temperature and time. The conventional Hoffman-Weeks method could not be used to determine the equilibrium melting temperature because the observed melting temperatures were greater than the crystallization temperatures by a constant, so the Gibbs-Thomson method was used instead, yielding an equilibrium melting temperature of 103.4 ± 2.3°C. A modification was proposed to the non-linear Hoffman-Weeks equation that included a non-linear undercooling dependence for the kinetic fold surface free energy upon crystallization and permitted accurate modeling of the observed melting behavior.

The isothermal crystallization rates of four narrow molecular weight poly(ethylene oxide) fractions were characterized using fast differential scanning calorimetry for crystallization temperatures spanning 100°C range with the lower limit approaching the glass transition. A transition from homogeneous to heterogeneous primary nucleation was observed at −5°C. The kinetic analysis suggested that the crystal growth geometry depends strongly on temperature, where rod-like structures begin to appear near the glass transition temperature, highly branched

solid sheaves grow throughout the homogeneous primary nucleation temperature range, and spherulites grow in the heterogenous primary nucleation range.

Poly(δ-valerolactone) was synthesized using microwave-assisted techniques. Narrow molecular weight fractions were obtained using successive precipitation fractionation. Preliminary isothermal crystallization studies suggest that conventional thermal analysis methods are not adequate to measure the melting temperatures accurately due to reorganization during heating.

Crystallization and Melting Studies of Poly(ε-caprolactone) and Poly(ethylene oxide) using Flash™ Differential Scanning Calorimetry and Preparation and Characterization of Poly(δ-valerolactone) Fractions

Matthew Vincent

GENERAL AUDIENCE ABSTRACT

Plastics may be classified into two general categories: those which form ordered domains upon solidification, i.e. undergo crystallization, and those which remain disordered upon solidification, i.e. form glasses. This work is focused on studying the crystallization and melting processes in two linear polymers, poly(ε-caprolactone) and poly(ethylene oxide), using new experimental technology. In the case of poly(ε-caprolactone), the experimental data could not be rationalized by existing theories, and we have proposed modifications to these theories that explained the results. In the case of poly(ethylene oxide), the application of new experimental technology resulted in previously unreported data that indicated novel behavior at very low crystallization temperatures. In the last portion of this work, poly(δ-valerolactone) was made using a novel approach. Conventional experimental approaches to measuring the crystallization and melting behavior were shown to be inadequate.

To my wife, Kiaya, and my sons, Montgomery and Sebastian

Ut prosim

Acknowledgements

There are several people who I would like to thank for their contributions to my graduate studies and life in general:

- Prof. Hervé Marand for being my graduate advisor and showing me the wonderful world of polymer crystallization
- Dr. Hadi Mohammadi for the years of comradery and inquisition during our time together in the Marand group
- The Department of Chemistry for financial support throughout my graduate studies.
- Prof. Alan Esker, Prof. Louis Madsen, and Prof. Robert Moore for serving on my committee
- Dr. Bruce Orler for being a mentor and fellow polymer science nerd
- Tony Williams and TA Instruments for temporarily loaning the Marand group a TA Q2000 conventional differential scanning calorimeter
- Dr. Priya Hewavitharanage for teaching me the wonders of chemical research, believing in me, and encouraging me to apply to Virginia Tech
- My friends at Virginia Tech who have come to be like family and made my time in Blacksburg so very special. In particular, Alex Hawes, Chrissy DuChane, Chad Bernier, and Celia Amick
- My parents, Holly and Jim Vincent, for their continued love and support over the years
- My wife, Kiaya Vincent, for being my best friend and companion through all of life's journeys. Her unfaltering love, support, and encouragement made this work possible. I cannot imagine my life without her

Table of Contents

List of Figures

List of Tables

List of Schemes

CHAPTER 1

General Introduction

1.1 DISSERTATION SCOPE

This dissertation is largely focused on understanding polymer crystallization at large undercoolings. To that end, fast differential scanning calorimetry (FDSC) was employed to study the crystallization and melting behavior of poly(ε-caprolactone) and the crystallization kinetics of poly(ethylene oxide). The final portion of this dissertation is focused on the preparation of a model material, poly(δ-valerolactone), for use in studies of polymer crystallization. All of the work considered herein was part of my graduate research, which was conducted without significant contributions from others.

Chapter 2 is a literature review that presents fundamentals of semi-crystalline morphology in addition to the thermodynamics and kinetics of polymer crystallization. Methods for determining polymer equilibrium melting temperature are also considered.

Chapters 3 focuses on correlating the melting and crystallization temperatures of poly(ε-caprolactone) measured using fast differential scanning calorimetry. The effects of isothermal crystallization temperature and time on the melting kinetics were investigated. When heated fast enough to suppress the effects of reorganization or stabilization, poly(ε-caprolactone) displays melting temperatures that are parallel to the line $T_{\mathrm{m}}' = T_{\mathrm{x}}$. This behavior persists over the entire range of measurable isothermal crystallization temperatures, and it prevents determining the equilibrium melting temperature using either the linear or non-linear Hoffman-Weeks methods.[1] We determined the equilibrium melting temperature using the Gibbs-Thomson method,[2] then used these results to validate a proposed modification to the non-linear Hoffman-Weeks method, which incorporates a kinetic fold

surface free energy upon crystallization that depends non-linearly on undercooling. This work will be submitted to the *Journal of Polymer Science: Polymer Physics* in two parts.

Chapter 4 presents the isothermal crystallization kinetics of poly(ethylene oxide) with different molar masses studied using fast differential scanning calorimetry over a ca. 100°C temperature range. There are currently no reports in the literature detailing the crystallization behavior of poly(ethylene oxide) with fast differential scanning calorimetry. The peak crystallization times exhibited two distinct lobes with a cusp at −5°C, which was attributed to a change from homogeneous to heterogeneous primary nucleation at low and high crystallization temperature, respectively. The crystallization kinetics were analyzed according to the Avrami model.[3, 4] The Avrami exponent took on values larger than 4 at high undercoolings, which is indicative of a highly branched, solid sheaf morphology.[5, 6] This work will be submitted to *Polymer*.

Chapter 5 details the preparation of poly(δ-valerolactone) using microwave-assisted synthesis and subsequent fractionation by successive precipitation fraction to obtain narrow molecular weight samples. Basic thermal characterization of fractionated samples is presented. This work will be submitted to the *Journal of Applied Polymer Science*.

Chapter 6 reviews the general conclusions from the preceding chapters and provides suggestions for future work.

1.2 REFERENCES

1. Marand, H.; Xu, J.; Srinivas, S., Determination of the Equilibrium Melting Temperature of Polymer Crystals: Linear and Nonlinear Hoffman-Weeks Extrapolations. *Macromolecules* **1998,** *31* (23), 8219-8229.

2. Hoffman, J. D.; Davis, G. T.; Lauritzen, J. I., Jr., The Rate of Crystallization of Linear Polymers with Chain Folding. In *Treatise on Solid State Chemistry, Vol. 3: Crystalline and Noncrystalline Solids*, Hannay, N. B., Ed. Plenum Press: New York, 1976.

3. Avrami, M., Kinetics of phase change. II. Transformation-time relations for random distribution of nuclei. *J. Chem. Phys.* **1940,** *8*, 212-24.

4. Wunderlich, B., CHAPTER VI - The Growth of Crystals. In *Macromolecular Physics*, Wunderlich, B., Ed. Academic Press: 1976; pp 115-347.

5. Booth, A.; Hay, J. N., An extension of polymer crystallisation kinetics to a branching mechanism for spherulitic growth. *British Polymer Journal* **1972,** *4* (1), 9-17.

6. Morgan, L. B., Crystallization phenomena in polymers-The course of the crystallization. *Phil. Trans. R. Soc. Lond. A* **1954,** *247* (921), 13-22.

CHAPTER 2

Literature Review

2.1 OVERVIEW

This literature review will examine the fundamentals of semi-crystalline polymer morphology in addition to the thermodynamics and kinetics of polymer crystallization. Detailed theoretical background and derivations are provided at the beginning of each chapter, and the current review is meant to serve as a primer on fundamental topics. The thermodynamics of polymer crystallization will be considered in the framework of the Gibbs-Thomson theory. The kinetics of polymer crystallization will be reviewed for the cases of the Lauritzen-Hoffman secondary nucleation theory, the Lauritzen-Passaglia stem length fluctuation theory, and the Avrami theory. Different methods for determining the equilibrium melting temperature of polymers will be discussed, including the Gibbs-Thomson method, linear Hoffman-Weeks method, non-linear Hoffman-Weeks method, and fitting of spherulite growth rate data.

2.2 SEMI-CRYSTALLINE POLYMER MORPHOLOGY: LAMELLAR AND SPHERULITIC STRUCTURES

Unlike small molecules, which have great mobility in the bulk melt or solution states, macromolecules cannot crystallize completely due to the restriction in mobility arising from their chain-like structure and the non-crystalline fold surfaces of lamellae.[1] Crystallinity and crystal orientation affect a material's properties.[2-4] Thus, a thorough understanding of semi-crystalline morphology and the development thereof are required in order to tailor material properties for specific applications.

In early models of semi-crystalline polymers, their morphology was viewed as "fringed micelles", in which crystalline domains coexisted with disordered, amorphous regions (Figure 2.1a).[1, 5, 6] Ordered, discrete particles suspended and connected through a disordered continuum helped to explain their

mechanical properties and wide angle x-ray diffraction patterns,[5] but did not help explain the periodicity observed with small angle x-ray scattering[7] or the spherical symmetry of the semi-crystalline morphology often observed for quiescently crystallized polymers by polarized optical microscopy.[8, 9] Even though Storks[10] put forth the idea of chain folded crystals in 1938, it was not until Keller[11] observed the first single crystals of polyethylene in 1957 that strong empirical evidence from electron diffraction experiments confirmed that polymer chains are oriented approximately perpendicular to the crystal surface, indicating chain folding at the basal planes of the crystal. Following primary nucleation, lamellar growth is accompanied by branching and splaying to maximize crystallinity, which leads to spherulitic morphology at typical crystallization temperatures accessible by conventional experimental methods. The lamellae organize radially in spherulites with chain folding tangential to the spherical surface.[1, 9, 12] Depictions of a chain-folded lamella and of spherulitic organization are shown below in Fig. 2.1c and 2.1d, respectively.

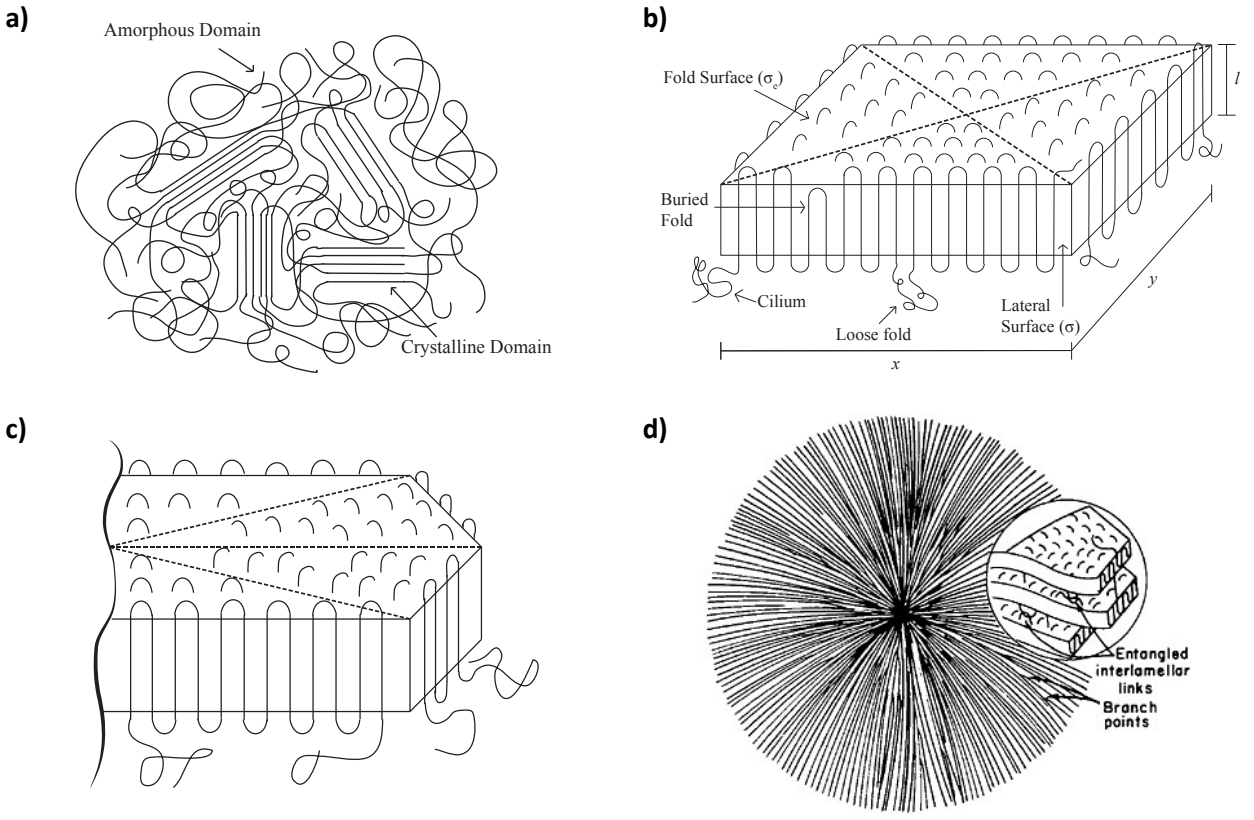

Figure 2.1: Idealized representations of a) fringed micelle, b) single crystal, c) lamellar, and d) spherulitic morphologies.[13]

Polymer spherulites are birefringent, meaning they exhibit two different refractive indices in different directions, resulting from the anisotropy of chain-folded lamellae.[1, 12] Birefringence allows their visualization using polarized optical microscopy. In contrast, amorphous domains are approximately isotropic and can be described by a single refractive index. The growth of semi-crystalline spherulites can be visualized against the amorphous background by placing orthogonally oriented polarizers before and after the sample. The observations of a linear spherulite growth process under isothermal conditions and the systematic increase of lamellar thickness with crystallization temperature formed the foundation for the development of all models of polymer crystallization from the melt.[13-16]

2.3 THERMODYNAMICS OF POLYMER CRYSATLLIZATION

If a two-phase model is assumed, i.e. melt and crystal, then the crystallization process can be considered classically from the change in Gibbs free energy as a function of temperature. Evocation of an infinitely large crystal with an equilibrium number of defects is necessary to establish a reference crystalline state. However, actual polymer crystals are quite thin, on the order of 10 nm, and have widths and lengths on the order of micrometers.[1, 12] At the equilibrium melting temperature, T_{m}, the infinite crystal is in equilibrium with the melt.[17-20] Surface energy contributions destabilize crystals of finite dimensions, thereby depressing their melting temperature, T_{m}', below the equilibrium melting temperature.[14, 17-20] The topic of equilibrium melting temperature determination will be examined in a subsequent section.

Experimental evidence indicates that T_{m}' increases with increasing lamellar thickness. A concise thermodynamic explanation for this phenomenon is summarized by the Gibbs-Thomson equation for thin lamellar crystals:

$$T_{\mathrm{m}}' = T_{\mathrm{m}}\left(1 - \frac{2\sigma_{\mathrm{em}}}{\Delta H_{\mathrm{f}}^{o} l_{\mathrm{x}}}\right) \tag{2.1}$$

where σ_{em} is the equilibrium fold surface free energy upon melting, $\Delta H_{\mathrm{f}}^{\mathrm{o}}$ is the heat of fusion of an infinite crystal at the equilibrium melting temperature, and l_{x} is the lamellar thickness. The minimum lamellar thickness, l_{min}, that is thermodynamically stable at a given crystallization temperature, T_{x}, can be found by rearranging Eqn. (2.1)

$$l_{\mathrm{min}} = \frac{2\sigma_{\mathrm{em}} T_{\mathrm{m}}}{(T_{\mathrm{m}} - T_{\mathrm{x}})\Delta H_{\mathrm{f}}^{\mathrm{o}}} = \frac{2\sigma_{\mathrm{em}}}{\Delta G_{\mathrm{f}}^{\mathrm{o}}} \tag{2.2}$$

where the substitution in the second equality assumes that the heat capacities of the crystalline and amorphous phases are independent of temperature and their difference is equal to 0.

2.4 KINETICS OF POLYMER CRYSTALLIZATION

Although polymer crystallization is a thermodynamically driven process, the ordering process is kinetically controlled, so the fastest growing crystals are those we observe. It is assumed that the thermodynamic driving force for crystallization is proportional to the change in free energy upon forming a lamellar crystal with lateral dimensions x and y and thickness l_{x} according to

$$\Delta G_{\mathrm{c}} = 2xy\sigma_{\mathrm{em}}\left(1 - \frac{l_{\mathrm{x}}}{l_{\mathrm{min}}}\right) \tag{2.3}$$

As the lamellar thickness increases, the change in free energy upon crystallization becomes more negative, and crystallization becomes more thermodynamically favorable[1, 17, 18] In direct contrast, physical intuition suggests that the secondary nucleation rate should decrease with increasing lamellar thickness, making crystallization less kinetically favorable. The Lauritzen-Hoffman (LH) secondary nucleation theory was proposed in 1960 to explain polymer crystallization by describing the interplay between the thermodynamic driving force and kinetic control for a "melt-to-crystal" phase transition,[14, 20, 21] and the Lauritzen-Passaglia (LP) stem length fluctuation theory was proposed in 1967 in an effort to generalize the LH theory to lamellae with rough fold surfaces.[22] The Avrami theory of isothermal phase conversion was originally proposed to describe the bulk kinetics of phase changes in metallic compounds in terms of

volume conversion.[23-25] It contrast to the LH and LP theories, the Avrami theory describes the bulk kinetics of crystallization, and it does not assume a molecular mechanism for the phase change.

2.4.1 Lauritzen-Hoffman secondary nucleation theory

The Lauritzen-Hoffman theory assumes flexible, monodisperse chains, so it is only rigorously applicable to narrow molecular weight fractions. It assumes that the macroscopic spherulite growth rate is equal to the atomic scale lamellar growth rate. The physics and mathematics are simplified by assuming that only crystalline stems with uniform length deposit on the crystal growth front. Polarized optical microscopy measurements indicated that isothermal crystal growth rates are independent of crystallization time and depend exponentially on the undercooling ($\Delta T = T_{\mathrm{m}} - T_{\mathrm{x}}$). Additionally, the observation of facetted single crystals formed in dilute solution suggested that the crystal growth process is controlled by secondary surface nucleation.[13, 14, 21] The LH theory does not consider the process of primary nucleation whereby the critical nucleus that initiates phase change forms. Instead, it only describes crystal growth via secondary nucleation. Figure 2.2 shows a pictorial representation of polymer crystal growth via secondary surface nucleation and substrate completion with chain folding.

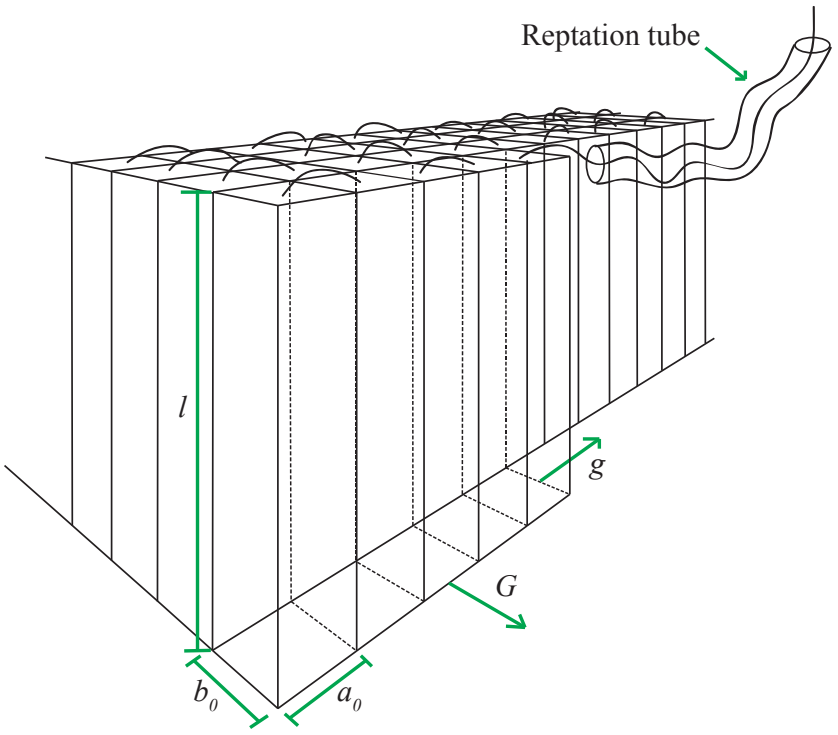

Figure 2.2: Idealized representation of polymer crystallization according to the LH theory. The following characteristic values are shown: the lamellar thickness (l), the stem width (a_0), the stem depth (b_0), the spherulite growth rate (G), and the substrate completion rate (g).

The rate constants for the deposition and detachment of crystallographically aligned chain segments take the form of Arrhenius relationships. The rate-determining step in the secondary nucleation process is the attachment of the first crystalline stem. Consider a stem of length l, width a_0, and depth b_0, then the rate constant for the deposition of the first stem is

$$A_0 = \beta \exp\left(-\frac{2b_0 l\sigma}{kT_x}\right) \tag{2.4}$$

where β is a constant associated with the transport of chain segments across the melt-crystal interface, σ is the lateral surface free energy, and the term $2b_0 l\sigma$ accounts for the work required to make two new lateral melt-crystal interfaces on the growth front. The rate constant for the detachment of the first stem is given by

$$B_1 = B = \beta \exp\left(-\frac{a_0 b_0 l \Delta G_\mathrm{f}}{k T_\mathrm{x}}\right) \tag{2.5}$$

where $a_0 b_0 l \Delta G_\mathrm{f}$ is the free energy change required to remove a stem of volume $a_0 b_0 l$. The LH treatment assumes that removing subsequent stems has identical rate constants to B_1. The deposition of all subsequent stems after the first stem to form a fold has a rate constant

$$A = \beta \exp\left(-\frac{2 a_0 b_0 \sigma_\mathrm{ec}}{k T_\mathrm{x}}\right) \tag{2.6}$$

where $2 a_0 b_0 \sigma_\mathrm{ec}$ is the work required to make a new fold spanning two crystalline stems. Note that no new lateral melt-crystal interfaces are made by depositing subsequent stems from the melt. Figure 2.3 pictorially represents the stem deposition process and the decrease in free energy upon subsequent stem addition onto the growth face to form a stable crystal under the condition of adjacent re-entry folding.

a)

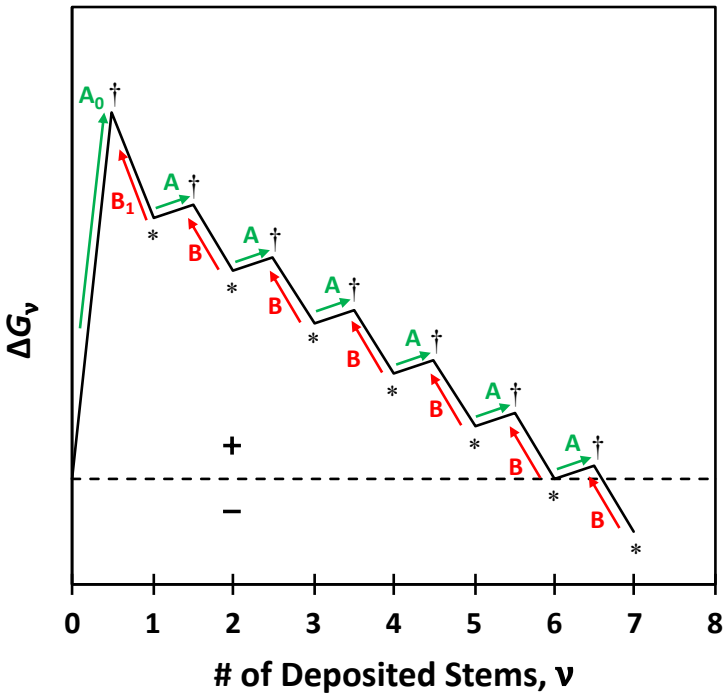

b)

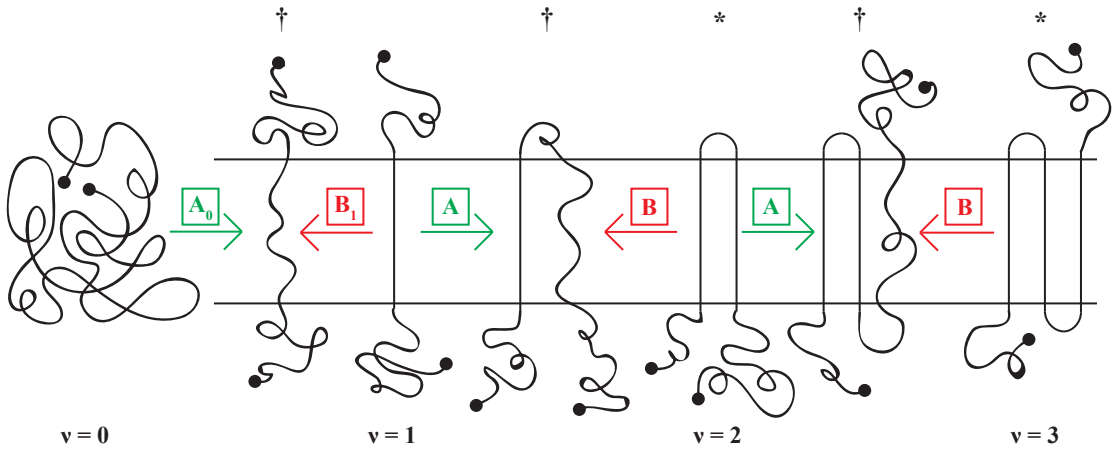

Figure 2.3: a) Generic plot of ΔG_ν vs. ν, the number of deposited crystalline stems. b) Cartoon of stem attachment and subsequent crystallographic registration. † indicates the activated complex and * indicates the formation of a ν-stem secondary nucleus.

The flux equation equations for the attachment and detachment of stems can be written and solved under steady-state conditions to obtain the flux as a function of crystalline stem length

$$S(l) = N_0 A_0 \left(1 - \frac{B}{A}\right) \tag{2.7}$$

The total flux is found by integrating the steady-state flux from the minimum lamellar thickness to infinite lamellar thickness

$$S_{\mathrm{T}} = \frac{1}{l_{\mathrm{u}}} \int_{l_{\min}}^{\infty} S(l)\, dl = \frac{1}{l_{\mathrm{u}}} \int_{\frac{2\sigma_{\mathrm{em}}}{\Delta G_{\mathrm{f}}^{\mathrm{o}}}}^{\infty} S(l)\, dl \tag{2.8}$$

where l_{u} is the monomer unit length. The average initial lamellar thickness prior to isothermal lamellar thickening is defined as

$$l_{\mathrm{g}}^{*} = \frac{1}{l_{\mathrm{u}}} \int_{\frac{2\sigma_{\mathrm{em}}}{\Delta G_{\mathrm{f}}^{\mathrm{o}}}}^{\infty} lS(l)\, dl \Bigg/ \frac{1}{l_{\mathrm{u}}} \int_{\frac{2\sigma_{\mathrm{em}}}{\Delta G_{\mathrm{f}}^{\mathrm{o}}}}^{\infty} S(l)\, dl \tag{2.9a}$$

$$l_{\mathrm{g}}^{*} = l_{\min} + \delta l = \frac{2\sigma_{\mathrm{ec}} T_{\mathrm{m}}}{\Delta H_{\mathrm{f}}^{\mathrm{o}} \Delta T} + \delta l \tag{2.9b}$$

where $l_{\min}$ was taken from Eqn. (2.2) and δl is expressed as

$$\delta l = \frac{kT_{\mathrm{x}}}{2b_0\sigma} \left(\frac{\Delta G_{\mathrm{f}}^{\mathrm{o}} + \frac{4\sigma}{a_0}}{\Delta G_{\mathrm{f}}^{\mathrm{o}} + \frac{2\sigma}{a_0}} \right) \tag{2.10}$$

δl is a small increment in lamellar thickness necessary to impart thermodynamic stability at a given crystallization temperature. The value is typically approximated by $\delta l \approx kT_{\mathrm{x}}/b_0\sigma$ at small to moderate undercoolings.

One of the most important features of the LH theory is the prediction of the spherulite growth rate according to

$$G = G_0 \exp\left(-\frac{Q_{\mathrm{D}}^{*}}{RT_{\mathrm{x}}} \right) \exp\left(-\frac{K_{\mathrm{g}}}{T_{\mathrm{x}} \Delta T} \right) \tag{2.11}$$

Here, the growth rate front factor (G_0) is a constant that is inversely proportional to chain length, R is the gas constant, Q_{D}^{*} is the activation energy for center of mass diffusion, and K_{g} is the regime-dependent secondary nucleation rate constant. The expression for K_{g} is given by

$$K_{\mathrm{g}} = \frac{j b_0 \sigma \sigma_{\mathrm{ec}} T_{\mathrm{m}}}{\Delta H_{\mathrm{f}}^{\mathrm{o}} k} \tag{2.12}$$

where j = 4 for regime I and III crystallization, j = 2 for regime II crystallization, and k is Boltzmann's constant. Kinetic data is typically analyzed by linearizing Eqn. (2.11) to yield

$$\ln G + \frac{Q_{\mathrm{D}}^*}{R T_{\mathrm{x}}} = \ln G_0 - \frac{K_{\mathrm{g}}}{T_{\mathrm{x}} \Delta T} \tag{2.13}$$

Lauritzen-Hoffman plots are made by plotting $\ln G + \frac{Q_{\mathrm{D}}^*}{R T_{\mathrm{x}}}$ versus $\frac{1}{T_{\mathrm{x}} \Delta T}$ to yield the growth rate front factor from the y-intercept and the secondary nucleation rate constant from the slope. Figure 2.4a shows a generic Lauritzen-Hoffman plot. Regime transition temperatures correspond to discontinuities in the first derivative of the growth rate with respect to temperature. The crystallization regimes are controlled by competition between surface nucleation and substrate completion, and a cartoon comparing the three regimes is shown in Fig. 2.4b. Regime I crystallization takes places at low undercoolings and is characterized by a low surface nucleation rate compared to the substrate completion rate. On the other extreme, regime III crystallization takes places at large undercoolings and is characterized by prolific multiple surface nucleation events such that surface nucleation is much faster than substrate completion. Regime II crystallization occurs at intermediate undercoolings where surface nucleation and substrate completion occur on similar time scales such that neither process dominates the kinetics.

a)

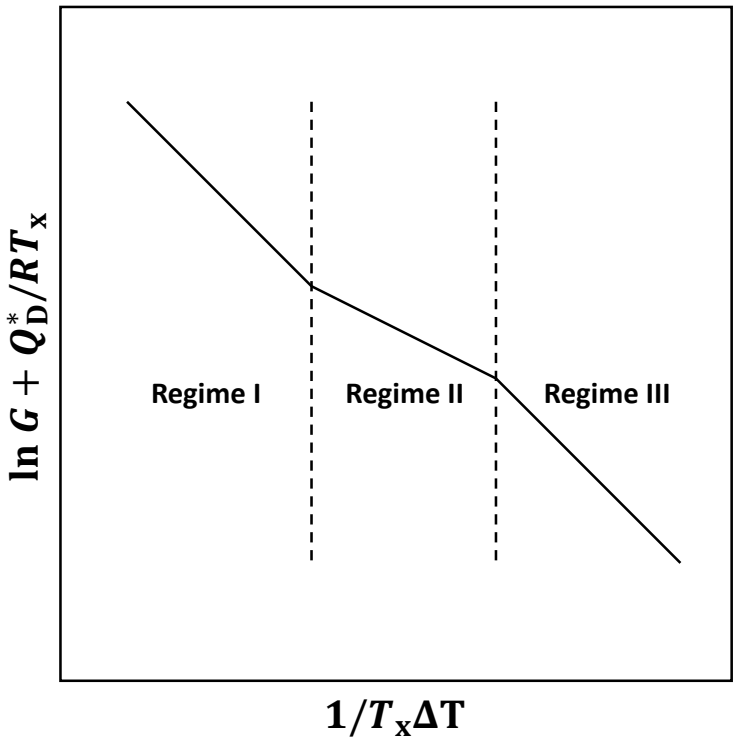

b)

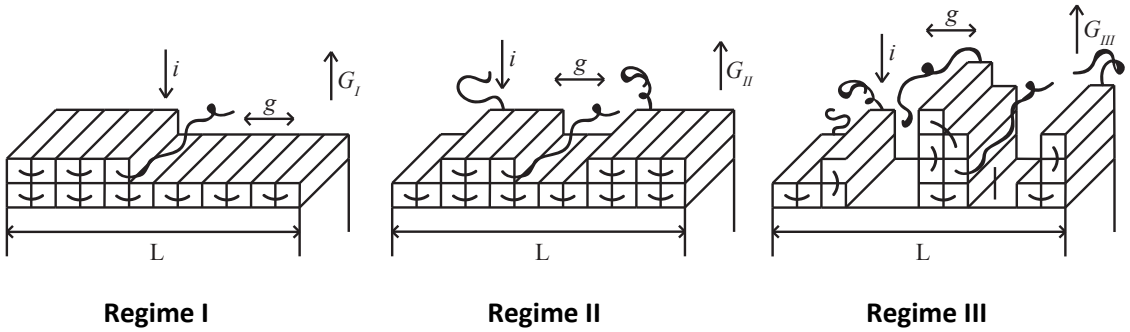

Figure 2.4: a) Schematic representation of an LH plot used to analyze the temperature dependence of spherulite growth rates and b) cartoon depicting crystal growth in regimes I, II, and III.

2.4.2 Lauritzen-Passaglia stem length fluctuation theory

The Lauritzen-Passaglia (LP) stem length fluctuation theory of polymer crystal growth is an extension of the LH theory that utilizes the mathematical formalism of the Lauritzen-DiMarzio-Passaglia (LDP) kinetic theory of multicomponent chain growth.[22, 26] The LP theory assumes that crystallization occurs through the deposition of stems with varying lengths, depicted in Figure 2.5, where each stem length has unique forward and reverse rate constants for crystallization. As a result, the lamellar fold

surfaces that form during crystallization are rough due to varying amounts of protruding crystalline stems. The amount of surface roughness depends on the undercooling of crystallization, which leads to a kinetic fold surface free energy upon crystallization that varies non-linearly with undercooling. Numerical simulations of linear polyethylene crystallization by Lauritzen and Passaglia[22] resulted in a divergence of the average lamellar thickness at an undercooling of $\Delta T = \sigma T_{\mathrm{m}}/a_0 \Delta H_{\mathrm{f}}^{\mathrm{o}}$. The authors also determined that the total flux approached zero at this temperature. Despite limitations of the LP theory, it provides a physical basis for understanding both crystallization with stem length fluctuations and the origin of undercooling-dependent kinetic fold surface free energy upon crystallization.

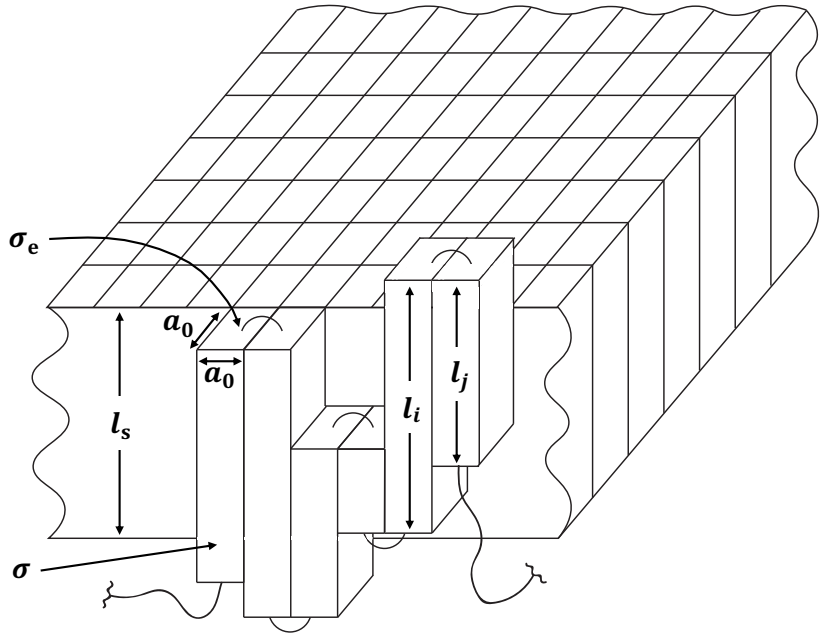

Figure 2.5: Idealized representation of polymer crystallization with stem length fluctuations. The following characteristic values are shown: the substrate thickness (l_{s}), a stem with length i (l_i), a stem with length j (l_j), the width and depth of the stem (a_0), the lateral surface free energy (σ), and the fold surface free energy (σ_{e}).

2.4.3 Strobl's three-stage model

A three-stage model of polymer crystallization has been proposed and studied by Strobl.[16, 27, 28] According to Strobl, crystallization obeys the Ostwald's stage rule whereby a metastable mesophase forms

from the melt then undergoes core crystallization and reordering into the thermodynamically stable crystalline state. The process is illustrated in Figure 2.6. The initially formed structures are referred to as native crystals (c_n) and the final structures following complete stabilization and merging are referred to as stable crystals (c_s).

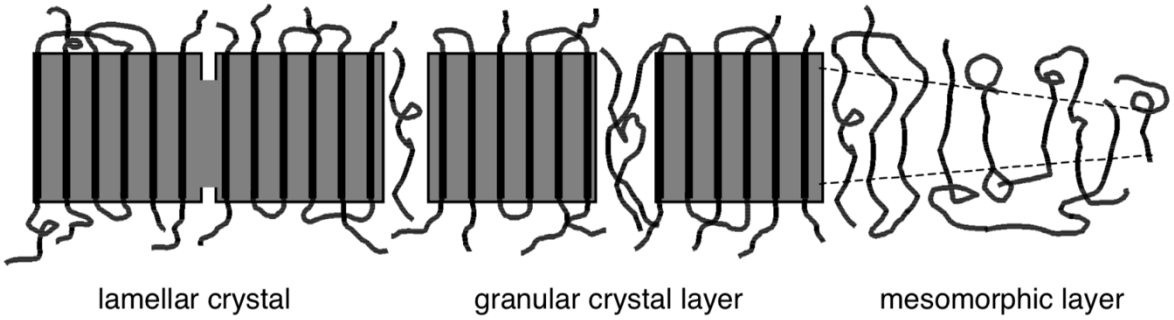

Figure 2.6: Depiction of mesophase-mediated crystallization.[28]

Strobl's three-stage model requires three equilibrium transition temperatures: amorphous-to-mesophase (T_{am}^{∞}), amorphous-to-crystal (T_{ac}^{∞} or T_f), and mesophase-to-crystal (T_{mc}^{∞} or T_c^{∞}). Figure 2.7 shows the phase diagram for the three-stage crystallization mechanism. The equilibrium amorphous-to-mesophase transition temperature is determined by extrapolation of the spherulite growth rate data to zero growth rate, so this value is often referred to as the zero-growth temperature (T_{zg}). The melting temperature is related to the inverse lamellar thickness at the time of melting, l_m, by

$$T_m' = T_{ac}^{\infty} - \frac{2\sigma_{ec}^{ac} T_{ac}^{\infty}}{\Delta H_f^o l_m} \tag{2.14}$$

where σ_{ec}^{ac} is the equilibrium fold surface free energy upon crystallization between the amorphous and crystalline phases. The equilibrium amorphous-to-crystal transition temperature is determined by extrapolation of the observed melting temperatures as a function of inverse lamellar thickness to 0 (Eqn. (2.14)), and is equivalent to the equilibrium melting temperature determined via the Gibbs-

Thomson method. The line formed by this data is referred to as the melting line. Similarly, the crystallization temperature is related to the inverse lamellar thickness at the time of crystallization, l_x, by

$$T_x = T_{mc}^{\infty} - \frac{2\sigma_{ec}^{mc} T_{mc}^{\infty}}{\Delta H_f^o l_x} \tag{2.15}$$

where σ_{ec}^{mc} is the equilibrium fold surface free energy upon crystallization between the mesomorphic and crystalline phases. The determination of the equilibrium mesophase-to-crystal transition temperature follows a similar protocol by extrapolating the crystallization temperature as a function of inverse lamellar thickness to 0 (Eqn. (2.15)), and the line formed by this data is referred to as the crystallization line. Notice that this equilibrium transition temperature is a virtual value because it lies above the equilibrium melting temperature, above which no crystalline structures can exist. If this temperature does not lie above the equilibrium melting temperature, then the thermodynamic scheme of the three-stage method cannot work. The recrystallization line is also shown in Fig. 2.7. It is determined by correlating the temperature of recrystallization with inverse lamellar thickness measured during slow heating experiments.

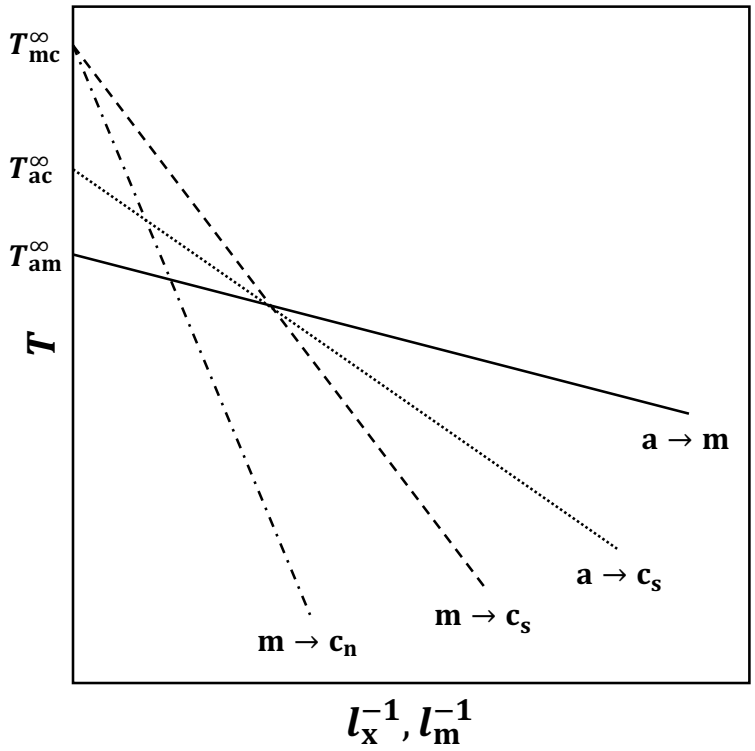

Figure 2.7: Illustration of the phase diagram for Strobl's three-stage model. The lines represent the amorphous-to-mesophase transition (_____), the amorphous-to-stable-crystal transition (.....) (Gibbs-Thomson melting line), the mesophase-to-stable-crystal transition (_ _ _ _ .) (recrystallization line), and the mesophase-to-native-crystal transition (_ . _ . _) (crystallization line).

2.4.4 Avrami model

The Avrami equation was originally formulated to describe the observation of sigmoidal volume transformation curves for phase transitions in metals.[23-25, 29] Since then, it has found widespread applications in various scientific disciplines, perhaps most notably describing phase transformation kinetics in polymers. The time-dependent crystallinity, $X_c(t)$, is defined as

$$X_c(t) = X_c^{\infty}[1 - \exp(-kt^n)] \tag{2.16}$$

where X_c^{∞} is the maximum crystallinity developed in the long-time limit, k is the Avrami crystallization rate constant, and n is the Avrami exponent. The value of the Avrami exponent is related to the primary nucleation mechanism, thermal or athermal, and the crystal growth geometry, one-, two-, or three-dimensional. The Avrami equation models the bulk crystallization rate, so the rate constant is proportional

to the primary nucleation and crystal growth rates.[24, 30] The reader is referred to Chapter 5 for a detailed description of the assumptions and theoretical background of the Avrami model.

Isothermal conversion data is typically collected with differential scanning calorimetry, and the kinetics are analyzed by rearranging Eqn. (2.16) to obtain

$$\ln\left[-\ln\left(1-\frac{X_{\mathrm{c}}(t)}{X_{\mathrm{c}}^{\infty}}\right)\right] = \ln k + n \ln t \tag{2.17}$$

Linear regression on the transformed data yields the Avrami crystallization rate constant, k, from the y-intercept and the Avrami exponent, n, as the slope. A theoretical conversion curve and a plot according to Eqn. (2.17) are shown in Figure 2.8. Note that experimental data typically displays non-linearity in a plot like Fig. 2.8b for high degrees of crystallinity due to the occurrence of secondary processes at long crystallization times.

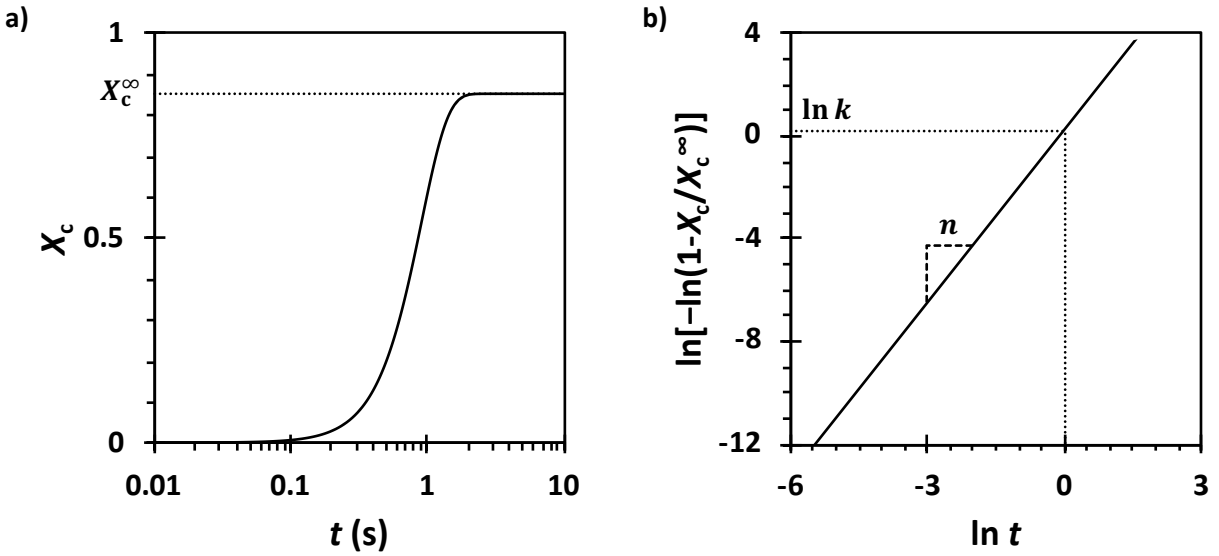

Figure 2.8: Theoretical plots of a) the degree of crystallinity, X_{c}, as a function of time and b) $\ln\left[-\ln\left(1-\frac{X_{\mathrm{c}}}{X_{\mathrm{c}}^{\infty}}\right)\right]$ versus $\ln t$ (Eqn. (2.17)).

2.5 POLYMER EQUILIBRIUM MELTING TEMPERATURE DETERMINATION

The equilibrium melting temperature is the reference temperature for thermodynamic and kinetic theories of polymer crystallization. Therefore, an accurate estimate of this value is paramount for physically-meaningful kinetic analyses of polymer crystallization. When analyzing spherulite growth rate data, incorrect values of the equilibrium melting temperature can lead to false kinetic regime transitions, incorrect estimations of the chain length dependence of spherulite growth rates, and inaccurate values of the secondary nucleation rate constant, the growth rate front factor, and the fold surface free energy upon crystallization.

2.5.1 Gibbs-Thomson method

According to Eqn. (2.1), a plot of the observed melting temperature as a function of the inverse lamellar thickness should be linear. A generic Gibbs-Thomson plot is shown in Figure 2.9. Linear extrapolation to infinite lamellar thickness (l_x^{-1} = 0) yields the equilibrium melting temperature as the y-intercept of Eqn. (2.1).[13] The equilibrium fold surface free energy upon melting is also obtained from the slope of the plot if the theoretical heat of fusion is known. Lamellar thicknesses are typically measured using small-angle x-ray scattering or longitudinal acoustic mode Raman spectroscopy. Melting temperatures are typically measured using differential scanning calorimetry, but they can be measured *in situ* while measuring lamellar thickness with the aforementioned methods. An in-depth discussion of experimental considerations concerning the Gibbs-Thomson analysis is provided in Chapter 3.

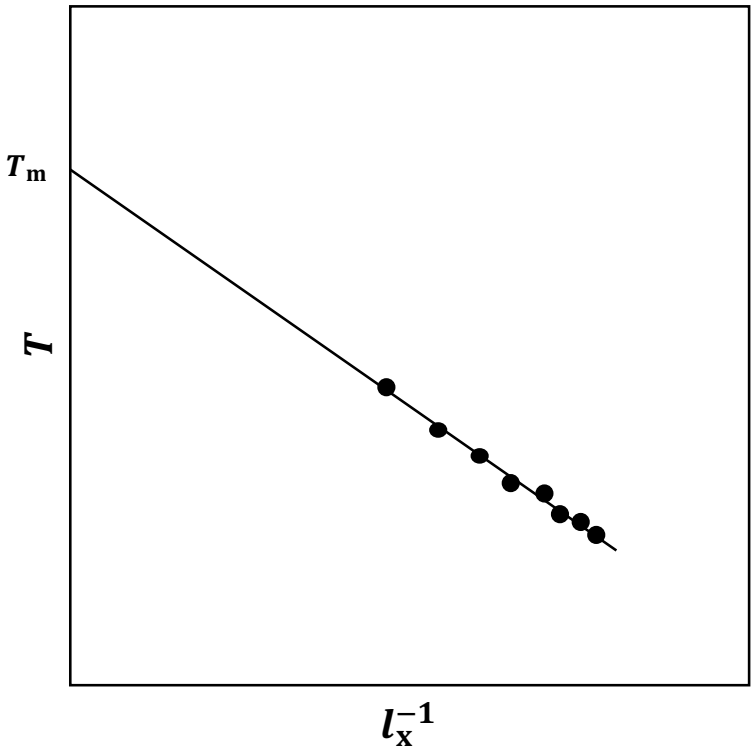

Figure 2.9: Generic plot of observed melting temperature, T_m', as a function of inverse lamellar thickness, l_x. The line represents the linear fit and extrapolation according to Eqn. (2.1).

2.5.2 Hoffman-Weeks method

The Hoffman-Weeks method was originally developed to determine the equilibrium melting temperature by correlating the melting temperature to the crystallization temperature according to the equation[13, 31]

$$T_m' = T_m \left\{ 1 - \left[\frac{1}{\gamma(t_x, T_x)} \right] \left(\frac{T_m - T_x}{T_m} \right) \left(\frac{\sigma_{em}}{\sigma_{ec}} \right) \left[\frac{1}{1 + \frac{\delta l \Delta H_f^o}{2\sigma_{ec}} \left(\frac{T_m - T_x}{T_m} \right)} \right] \right\} \tag{2.18}$$

where $\gamma(t_x, T_x)$ is the time- and temperature-dependent isothermal lamellar thickening coefficient. The linear Hoffman-Weeks equation is obtained by assuming that the isothermal lamellar thickening coefficient is constant, the fold surface free energy upon crystallization is constant and equal to the equilibrium fold surface free energy upon melting, and the product containing δl is much smaller than 1. The resulting equation takes the form

$$T_{\mathrm{m}}' = T_{\mathrm{m}}\left(1 - \frac{1}{\gamma}\right) + \left(\frac{1}{\gamma}\right)T_{\mathrm{x}} \tag{2.19}$$

Linear extrapolation of the melting temperatures as a function of crystallization temperature to the point of intersection with the line $T_{\mathrm{m}}' = T_{\mathrm{x}}$ yields the equilibrium melting temperature, and an approximation of the isothermal lamellar thickening coefficient is obtained from the slope.[13]

Experimental data and theoretical predictions from primary nucleation theory[32-34] and secondary nucleation theory[22, 35-37] suggest that the fold surface free energy upon crystallization should depend on undercooling. By assuming the kinetic fold surface free energy upon crystallization depends linearly on undercooling ($\sigma_{\mathrm{ec}}^{\mathrm{k}} = \sigma_{\mathrm{ec}}^{\mathrm{o}}(1 + y\Delta T)$), the generalized non-linear Hoffman-Weeks equation takes the form[31]

$$T_{\mathrm{m}}' = T_{\mathrm{m}}\left\{1 - \left[\frac{1}{\gamma(t_{\mathrm{x}}, T_{\mathrm{x}})}\right]\left(\frac{T_{\mathrm{m}} - T_{\mathrm{x}}}{T_{\mathrm{m}}}\right)\left(\frac{\sigma_{\mathrm{em}}}{\sigma_{\mathrm{ec}}^{\mathrm{o}}}\right)\left[\frac{1}{1 + \frac{C_2\Delta H_{\mathrm{f}}^{\mathrm{o}}}{2\sigma_{\mathrm{ec}}}\left(\frac{T_{\mathrm{m}} - T_{\mathrm{x}}}{T_{\mathrm{m}}}\right)}\right]\right\} \tag{2.20}$$

Notice the appearance of $\sigma_{\mathrm{ec}}^{\mathrm{o}}$, the equilibrium fold surface free energy upon crystallization, and C_2, which is defined as

$$C_2 = \left(\frac{2\sigma_{\mathrm{ec}}^{\mathrm{o}} y T_{\mathrm{m}}}{\Delta H_{\mathrm{f}}^{\mathrm{o}}} + \delta l\right) \tag{2.21}$$

The constant y accounts for stem length fluctuations during crystallization and makes the magnitude of C_2 considerably larger than δl. As a result, the term containing C_2 in Eqn. (2.20) should not be neglected. The non-linear Hoffman-Weeks equation can be rearranged to obtain the MX equation such that

$$M = \gamma(t_{\mathrm{x}}, T_{\mathrm{x}})\left(\frac{\sigma_{\mathrm{ec}}^{\mathrm{o}}}{\sigma_{\mathrm{em}}}\right)(X + a) \tag{2.22}$$

where $M = \frac{T_{\mathrm{m}}}{T_{\mathrm{m}} - T_{\mathrm{m}}'}$, $X = \frac{T_{\mathrm{m}}}{T_{\mathrm{m}} - T_{\mathrm{x}}}$, and $a = \frac{C_2\Delta H_{\mathrm{f}}^{\mathrm{o}}}{2\sigma_{\mathrm{ec}}^{\mathrm{o}}}$.[31] Two assumptions are necessary to determine the equilibrium melting temperature using Eqn. (2.22): 1) the isothermal lamellar thickening coefficient is equal to one by utilizing the first measurable melting temperature at each isothermal crystallization temperature and 2) the equilibrium fold surface free energies upon crystallization and melting are equal.

Under these two assumptions, the linear plot of M versus X will have a slope equal to one for the correct choice of the equilibrium melting temperature, and the value of C_2 can be determined from the y-intercept (a). Figure 2.10 shows an idealized plot of the melting temperature versus the crystallization temperature illustrating both linear (Eqn. (2.19)) and non-linear extrapolations (Eqn. (2.20)). The non-linear extrapolation includes the contribution from C_2, so it will always yield a higher equilibrium melting temperature compared to the linear extrapolation.

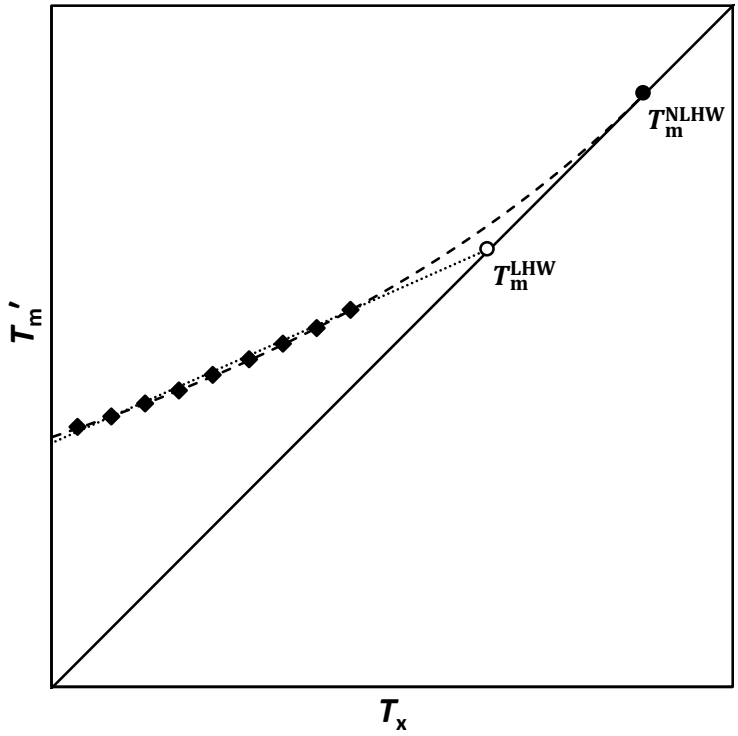

Figure 2.10: Theoretical plot of the melting temperature, T_m', as a function of the crystallization temperature, T_x. The lines represent $T_m' = T_x$ (———) the linear Hoffman-Weeks equation (Eqn. (2.19), ...), and the non-linear Hoffman-Weeks equation (Eqn. (2.20), _ _ _ _ .).

The reader is referred to Chapter 3 for detailed derivations of the linear and non-linear Hoffman-Weeks equations. Additionally, Chapter 3 deals with generalizing the non-linear Hoffman-Weeks model to include kinetic fold surface free energies upon crystallization that are non-linear functions of undercooling.

2.5.3 Spherulite growth rate analysis

There are three approaches to determining the equilibrium melting temperature from spherulite growth rate data. First, linear regression is performed according to Eqn. (2.13) using different choices of T_m, and the equilibrium melting temperature is determined as the value which minimizes the variance of the fit.[38-42] This approach also yields the growth rate front factor and the secondary nucleation rate constant. Second, the growth rate front factor and the secondary nucleation rate constant are determined via linear regression, then the variance of Eqn. (2.11) is minimized for different choices of the equilibrium melting temperature.[41] Third, non-linear regression is performed on experimental data according to Eqn. (2.11) using the equilibrium melting temperature, growth rate front factor, and secondary nucleation rate constant as fitting parameters.[41, 43]

An alternative approach is determining the zero-growth temperature from spherulite growth rate data. The premise is simple: the temperature at which the spherulitic growth rate equals zero must correspond to $\Delta T = 0$, so $T_{zg} = T_m$. This method was developed and popularized by Strobl where it was employed in the context of the three-phase model to determine $T_{zg} = T_{am}^{\infty}$, but it is valid for two-stage models as well.[44-46] The growth rate equation (Eqn. (2.11)) is differentiated with respect to the crystallization temperature to yield

$$\left(-\frac{d\ln(G/G_0)}{d\,T_x}+\frac{Q_D^*}{RT_x^2}\right)^{-\frac{1}{2}} = K_g'^{-\frac{1}{2}}\left(T_{zg}-T_x\right) \tag{2.23}$$

where $K_g' = \frac{K_g}{T_x}$. Assuming that K_g' is constant, a plot of $\left(-\frac{d\ln(G/G_0)}{d\,T_x}+\frac{Q_D^*}{RT_x^2}\right)^{-\frac{1}{2}}$ against the crystallization temperature will yield the secondary nucleation rate constant from the slope and the zero-growth temperature as the y-intercept. A generic plot illustrating the zero-growth temperature determination according to Eqn. (2.23) is shown in Figure 2.11.

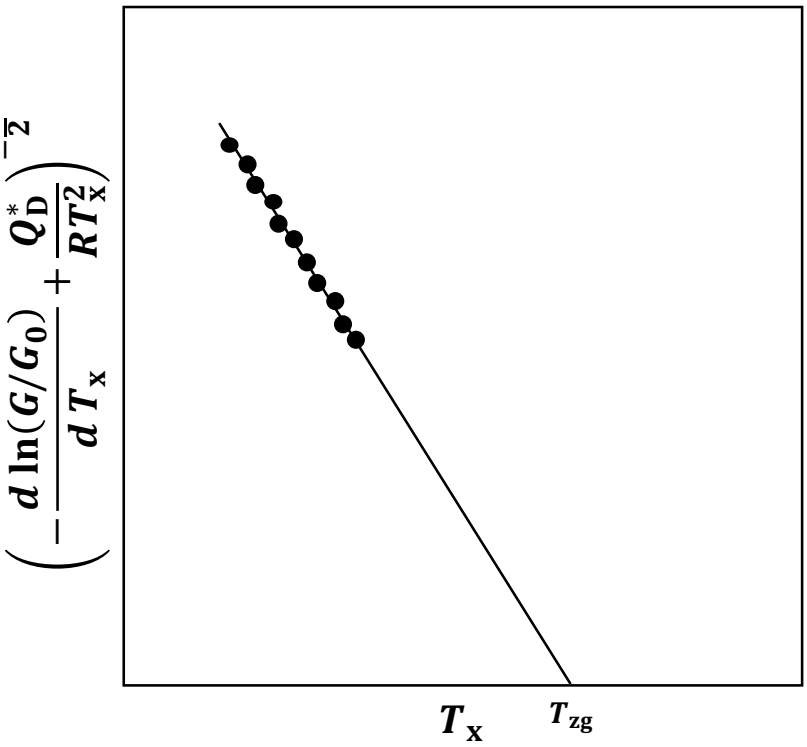

Figure 2.11: Generic plot of $\left(-\frac{d\ln(G/G_0)}{d\,T_x}+\frac{Q_D^*}{RT_x^2}\right)^{-\frac{1}{2}}$ against the crystallization temperature, T_x. The line represents the linear fit and extrapolation according to Eqn. (2.23).

Caution must be advised when fitting the growth rate equation or determining the zero-growth rate temperature because the results will be heavily influenced by the choice of the spherulite growth rate model. Recent studies from our group have suggested the undercooling dependence of the kinetic fold surface free energy upon crystallization must be accounted for when modeling the spherulite growth rate.[36] However, this quantity is assumed constant in classical secondary nucleation theories, and there are no reports of either growth rate fitting or zero-growth temperature determination that account for the undercooling dependence of the kinetic fold surface free energy upon crystallization. Any model errors could result in significant errors in the zero-growth temperature depending on the magnitude and range of undercoolings that are studied.

2.6 REFERENCES

1. Bassett, D. C., *Principles of Polymer Morphology*. Cambridge University Press: 1981.

2. Starkweather, H. W., Jr.; Jordan, T. F.; Dunnington, G. B., Mechanical properties of certain oriented crystalline polymers. *Polym. Eng. Sci.* **1974,** *14* (10), 678-81.

3. Dong, X.; McDowell, D. L.; Kalidindi, S. R.; Jacob, K. I., Dependence of mechanical properties on crystal orientation of semi-crystalline polyethylene structures. *Polymer* **2014,** *55* (16), 4248-4257.

4. Monami, A.; Langer, B.; Sadilek, J.; Kucera, J.; Grellmann, W., Fracture Mechanics Properties of Polymorphic Polypropylene. *Procedia Mater. Sci.* **2014,** *3*, 276-281.

5. MacGillavry, C. H., Anisotropy in the so-called amorphous part of polyvinyl alcohol. *Recl. Trav. Chim. Pays-Bas Belg.* **1950,** *69*, 509-14.

6. Bayerl, V.; Roos, K., Micellar structure of cellulose. *Kunstseide* **1930,** *12*, 424-6.

7. Fankuchen, I.; Mark, H., X-ray studies of chain polymers. *J. Appl. Phys.* **1944,** *15*, 364-70.

8. Keller, A., Morphology of crystallizing polymers. *Nature (London, U. K.)* **1952,** *169*, 913-14.

9. Keller, A., Spherulitic structure of crystalline polymers. I. Investigations with the polarizing microscope. *J. Polym. Sci.* **1955,** *17*, 291-308.

10. Storks, K. H., Electron-diffraction examination of some linear high polymers. *J. Am. Chem. Soc.* **1938,** *60*, 1753-61.

11. Keller, A., Single crystals in polymers: evidence of a folded-chain configuration. *Philos. Mag. (1798-1977)* **1957,** *2*, 1171-5.

12. Keller, A., Morphology of crystalline polymers. *Makromol. Chem.* **1959,** *34*, 1-28.

13. Hoffman, J. D.; Davis, G. T.; Lauritzen, J. I., Jr., The Rate of Crystallization of Linear Polymers with Chain Folding. In *Treatise on Solid State Chemistry, Vol. 3: Crystalline and Noncrystalline Solids*, Hannay, N. B., Ed. Plenum Press: New York, 1976.

14. Lauritzen, J. I., Jr.; Hoffman, J. D., Theory of formation of polymer crystals with folded chains in dilute solution. *J. Res. Natl. Bur. Stand., Sect. A* **1960,** *64A* (No. 1), 73-102.

15. Sadler, D. M., Roughness of growth faces of polymer crystals: evidence from morphology and implications for growth mechanisms and types of folding. *Polymer* **1983,** *24* (11), 1401-9.

16. Strobl, G., From the melt via mesomorphic and granular crystalline layers to lamellar crystallites: A major route followed in polymer crystallization? *Eur. Phys. J. E* **2000,** *3* (2), 165-183.

17. Hoffman, J. D.; Davis, G. T.; Lauritzen, J. I., Jr., The Rate of Crystallization of Linear Polymers with Chain Folding. In *Treatise on Solid State Chemistry, Vol. 3: Crystalline and Noncrystalline Solids*, Hannay, N. B., Ed. Plenum Press: New York, 1976.

18. Armitstead, K.; Goldbeck-Wood, G.; Keller, A., Polymer crystallization theories. In *Macromolecules: Synthesis, Order and Advanced Properties*, Springer Berlin Heidelberg: 1992; Vol. 100/1, pp 219-312.

19. Tammann, G., A method for determining the relationship between the melting point of a crystal lamella and its thickness. *Z. Anorg. Allg. Chem.* **1920,** *110*, 166-8.

20. Hoffman, J. D.; Miller, R. L., Kinetic of crystallization from the melt and chain folding in polyethylene fractions revisited: theory and experiment. *Polymer* **1997,** *38* (13), 3151-3212.

21. Hoffman, J. D.; Lauritzen, J. I., Jr., Crystallization of bulk polymers with chain folding: theory of growth of lamellar spherulites. *J. Res. Natl. Bur. Stand., Sect. A* **1961,** *65A*, 297-336.

22. Lauritzen, J. I.; Passaglia, E., Kinetics of crystallization in multicomponent systems: II. Chain-folded polymer crystals. *J. Res. Natl. Bur. Stand* **1967,** *71*, 261-275.

23. Avrami, M., Kinetics of phase change. I. General theory. *J. Chem. Phys.* **1939,** *7*, 1103-12.

24. Avrami, M., Kinetics of phase change. II. Transformation-time relations for random distribution of nuclei. *J. Chem. Phys.* **1940,** *8*, 212-24.

25. Avrami, M., Granulation, phase change and microstructure. Kinetics of phase change. III. *J. Chem. Phys.* **1941,** *9*, 177-84.

26. Lauritzen Jr, J. I.; DiMarzio, E. A.; Passaglia, E., Kinetics of growth of multicomponent chains. *The Journal of Chemical Physics* **1966,** *45* (12), 4444-4454.

27. Strobl, G., A thermodynamic multiphase scheme treating polymer crystallization and melting. *Eur. Phys. J. E* **2005,** *18* (3), 295-309.

28. Strobl, G., Crystallization and melting of bulk polymers: New observations, conclusions and a thermodynamic scheme. *Prog. Polym. Sci.* **2006,** *31* (4), 398-442.

29. William, J.; Mehl, R., Reaction kinetics in processes of nucleation and growth. *Trans. Metall. Soc. AIME* **1939,** *135*, 416-442.

30. Wunderlich, B., CHAPTER VI - The Growth of Crystals. In *Macromolecular Physics*, Wunderlich, B., Ed. Academic Press: 1976; pp 115-347.

31. Marand, H.; Xu, J.; Srinivas, S., Determination of the Equilibrium Melting Temperature of Polymer Crystals: Linear and Nonlinear Hoffman-Weeks Extrapolations. *Macromolecules* **1998,** *31* (23), 8219-8229.

32. Spaepen, F., Homogeneous nucleation and the temperature dependence of the crystal-melt interfacial tension. In *Solid State Physics*, Elsevier: 1994; Vol. 47, pp 1-32.

33. Turnbull, D., Kinetics of solidification of supercooled liquid mercury droplets. *The Journal of chemical physics* **1952,** *20* (3), 411-424.

34. Turnbull, D.; Cormia, R. L., Kinetics of crystal nucleation in some normal alkane liquids. *The Journal of Chemical Physics* **1961,** *34* (3), 820-831.

35. Hoffman, J. D.; Lauritzen, J. I.; Passaglia, E.; Ross, G. S.; Frolen, s. L. J.; Weeks, J. J., Kinetics of polymer crystallization from solution and the melt. *Kolloid-Zeitschrift und Zeitschrift für Polymere* **1969,** *231* (1-2), 564-592.

36. Mohammadi, H. On the Melting and Crystallization of Linear Polyethylene, Poly(ethylene oxide), and Metallocene Linear Low-Density Polyethylene. Ph.D. Thesis, Virginia Polytechnic Institute and State University, Blacksburg, VA, 2018.

37. Vincent, M. Crystallization and Melting Studies of Poly(ε-caprolactone) and Poly(ethylene oxide) using Flash™ Differential Scanning Calorimetry and Characterization of Poly(δ-valerolactone) Fractions. Virginia Polytechnic Institute and State University, Blacksburg, VA, 2019.

38. Arnold, L. Crystallization and Melting Behavior of (ε-caprolactone)-based Homopolymer and Triblock Copolymer. Ph.D Thesis, Virginia Polytechnic Institute & State University, Blacksburg, VA, 1995.

39. Huang, J.; Marand, H., Kinetics of Spherulitic Growth of Poly(pivalolactone) in Blends with Poly(vinylidene fluoride-co-tetrafluoroethylene): Effect of Specific Interactions on the Thermodynamic and Kinetic Secondary Nucleation Parameters. *Macromolecules* **1997,** *30* (4), 1069-1073.

40. Huang, J.; Prasad, A.; Marand, H., Study of the temperature dependence of isothermal spherulitic growth rate data for poly(pivalolactone) in blends with poly(vinylidene fluoride): a link between coherent secondary nucleation theory and mixing thermodynamics. *Polymer* **1994,** *35* (9), 1896-908.

41. Sheth, S. Self-Consistency of the Lauritzen-Hoffman and Strobl Models of Polymer Crystallization Evaluated for Poly(Epsilon-Caprolactone) Fractions and Effect of Composition on the Phenomenon of Concurrent Crystallization in Polyethylene Blends. Ph.D Thesis, Virginia Polytechnic Institute and State University, Blacksburg, VA, 2013.

42. Xu, J. Virginia Polytechnic Institute and State University, 1999.

43. Iler, H. D. A Study of the Crystallization Kinetics of Isotactic Polystyrene. Doctor of Philosophy, Vriginia Polytechnic Institute and State University, Blacksburg, VA, 1995.

44. Cho, T. Y.; Stille, W.; Strobl, G., Zero growth temperature and growth kinetics of crystallizing poly(ε-caprolactone). *Colloid Polym. Sci.* **2007,** *285* (8), 931-934.

45. Cho, T. Y.; Stille, W.; Strobl, G., Zero growth temperature of crystallizing polyethylene. *Macromolecules* **2007,** *40* (7), 2596-2599.

46. Strobl, G.; Cho, T. Y., Growth kinetics of polymer crystals in bulk. *Eur. Phys. J. E* **2007,** *23* (1), 55-65.

CHAPTER 3

Correlation of the Isothermal Crystallization and Melting Temperatures of Poly(ε-caprolactone) Measured Using Fast Differential Scanning Calorimetry with Application to the Non-linear Hoffman-Weeks Method for Determination of the Equilibrium Melting Temperature

3.1 INTRODUCTION

Conventional differential scanning calorimetry (CDSC) has become the most commonly employed technique for measuring the thermal properties of materials, such as heat capacity and melting temperature, since its first publication in 1964.[1, 2] Considering for instance modern instrumentation manufactured by TA Instruments, linear heating rates, β, ranging from 0.1 to 180 K.min^{-1} and linear cooling rates, $-\beta$, as high as 30 K.min^{-1} can be achieved with an intracooler unit. Higher linear cooling rates can be attained depending on the temperature range, by employing a liquid nitrogen cooling system, and by substituting helium as the purge gas. Fast differential scanning calorimetry (FDSC) utilizing chip-based MEMS furnaces has developed within the past twenty years. The Mettler-Toledo Flash™ DSC 1 is one of two commercially available FDSCs, and it offers linear heating rates in the range of 1 to 10^4 K.s^{-1} and linear cooling rates as high as 2×10^3 K.s^{-1} when using samples that are thin enough, ca. 1 μm, and of low enough mass, ca. tens of nanograms.[3-5] There are a number of non-commercial chip-based FDSCs reported in the literature that can heat and cool at higher rates than the Flash™ DSC 1.[3] The chip-based design and low sample masses give fast DSCs small time constants, which permit investigation of isothermal crystallization at short timescales. The combination of high cooling rates and the low instrumental time constants grants insight into crystallization over a broad range of temperatures, as low as the glass transition temperature in the case of poly(ε-caprolactone) (PCL), with temporal resolution of the entire development of crystallinity.[6-10]

The chain-folded lamellar structures resulting from crystallization are metastable, so they can reorganize and/or anneal not only during isothermal crystallization but also during heating. In particular, the relatively low heating rates typically employed in conventional DSC can lead to crystal reorganization during heating, meaning the measured melting temperatures or enthalpies of fusion may not accurately reflect the previous thermal treatment. In contrast, the high heating rates available with fast DSC allow the measurement of polymer melting free from the effects of annealing or reorganization.[3, 11-18] This, in combination with the large range of available crystallization temperatures and short response time, makes fast DSC an ideal technique for correlating the isothermal crystallization and melting temperatures in semi-crystalline polymers.

Several publications investigated the isothermal crystallization behavior of PCL using fast DSC,[6-10, 19] but all of them have presented data for samples with molecular weights less than 25 kg.mol^{-1} and focused on measuring and analyzing the enthalpies of fusion or crystallization. No attention was paid to the melting temperature dependence on crystallization temperature and time. Adamovsky and Schick[19] were the first to study PCL using FDSC, and they reported the crystallization half times covering a 120°C temperature interval. Note that this sample's molecular weight was not actually reported, and the CAS number corresponds to a discontinued product. Zhuravlev et al.[9] presented a detailed study of the crystallization and nucleation kinetics of PCL with M_n = 11.6 kg.mol^{-1} by simultaneously analyzing the enthalpies of cold crystallization and fusion over a 150°C crystallization temperature window. A change from heterogeneous nucleation to homogeneous nucleation was observed for crystallization at low temperatures. Wurm et al.[8] studied the crystallization and homogeneous nucleation kinetics for various molecular weights in the range M_n = 1.4 – 6.1 kg.mol^{-1}. Zhuravlev et al.[10] examined the effects of multiwalled carbon nanotubes with concentrations ranging from 0.2 to 5 wt% on the crystallization and nucleation kinetics of PCL with M_n = 6.7 kg.mol^{-1}. Wang et al.[7] compared the bulk crystallization rates for linear and cyclic PCL with M_n = 2.3 kg.mol^{-1}, and Li et al.[6] extended this work by comparing the

crystallization rates of linear and cyclic PCL with molecular weights in the range M_n = 2 – 22 kg.mol^{-1}. The only published measurement of PCL's melting temperature gave values corresponding to long-time crystallization for crystallization temperatures ranging from −88 to 57°C and were measured with only one heating rate, β = 10^3 K.s^{-1}.[9] The data can be characterized by melting temperatures, T_m', equal to crystallization temperatures, T_x, plus a constant value of 40°C ($T_m' = T_x + 40°C$) over the entire range of crystallization temperatures. In other words, the melting temperature as a function of crystallization temperature is parallel to the line $T_m' = T_x$. Similar behavior has been observed for poly(ether ether ketone) (PEEK),[13, 20, 21] poly(butylene terephthalate) (PBT),[11, 22] poly(butylene succinate) (PBS),[23] polyamide-6 (PA-6),[12] isotactic polypropylene (*i*-PP),[15] and poly(vinylidene fluoride) (PVDF).[24] Some attempt was made to explain this phenomenon using thermodynamic arguments by proposing that the number of chain segments deposited during secondary nucleation is approximately constant across a broad range of isothermal crystallization temperatures.[13, 23]

The equilibrium melting temperature, T_m, of a polymer is defined as the temperature at which an infinitely large crystal with an equilibrium number of defects is in equilibrium with the melt. This value is used as the reference point for all thermodynamic and kinetic models of polymer crystallization to define the undercooling, ΔT, which is the difference between the equilibrium melting temperature and the crystallization temperature, $\Delta T = T_m - T_x$. The equilibrium melting temperature of PCL has been investigated by many groups in the past.[25-53] It is an attractive model polymer for the study of the thermodynamics and kinetics of polymer crystallization due its commercial availability, relative ease of synthesizing narrow molecular weight fractions,[54] good thermal stability,[55-57] and low melting temperatures. A thermodynamic approach using the Gibbs-Thomson method has been used to determine PCL's equilibrium temperature,[25, 28, 43, 45, 48, 50, 51] and a kinetic approach extrapolating to the zero-growth temperature of spherulites has also been used.[25, 28, 33, 44, 50] Additionally, the linear Hoffman-Weeks method, which combines the Gibbs-Thomson thermodynamic approach with the Lauritzen-Hoffman

secondary nucleation kinetic model of crystal growth, has been utilized extensively.[25-27, 29, 30, 32, 34-42, 45, 53] There is one report of a non-linear Hoffman-Weeks determination,[36] but it was not executed in the conventional manner proposed by Marand et al.[58] Table 3.1 contains an exhaustive compilation of the equilibrium melting temperatures determined using the aforementioned approaches in addition to sample molecular weight, the fold surface free energy, and the product of lateral surface and fold surface free energies. The reported values of the equilibrium melting temperatures for similar molecular weight samples vary by as much as ca. 40°C. Obviously, no consensus has been reached on the relationship between equilibrium melting temperature and chain length for this polymer. Description of the different approaches to equilibrium melting temperature determination, including the Gibbs-Thomson, the linear Hoffman-Weeks, and the non-linear Hoffman-Weeks methods will be provided in the following theoretical background section.

Table 3.1: Comprehensive list of equilibrium melting temperatures, T_m, fold surface free energies, σ_e, and product of lateral and fold surface free energies available in the literature for PCL.

Reference	M_n (kg.mol^{-1})	M_w (kg.mol^{-1})	T_m (°C)	σ_e (mJ.m^{-2})[a]	$\sigma\sigma_e$ (mJ^2.m^{-4})[a]	Method
Arnold[25]	15.0	25.5	65 85 ± 4 84[f]	– 64 ± 6 –	669[f]	LHW GT Zero growth rate from POM
Chen et al.[26]	2.7 4.4 6.7 44.7 64.7	4.4 5.7 7.8 59.1 77.6	64.0 67.5 72.6 78.5 78.9	–	418–525[g]	LHW
Chen et al.[27,b]	–	20	64	–	–	LHW
Ciardelli et al.[29,b]	–	45	67	–	–	LHW
Córdova et al.[30]	7.00[cyclic] 7.34	7.28 7.49	81 80	–	–	LHW

Reference	M_n (kg.mol^{-1})	M_w (kg.mol^{-1})	T_m (°C)	σ_e (mJ.m^{-2})[a]	$\sigma\sigma_e$ (mJ^2.m^{-4})[a]	Method
Fan et al.[31,c]	2.73 4.46 6.53 7.39 10.6 13.2	2.95 4.77 6.86 8.35 12.0 14.8	70.2	156 116 95 80 80 80	–	T_m assumed based on data from Philips et al.[39, 40]
Goulet et al.[32,c]	43.6	48.0	73.9	106 ± 5[h]	648 ± 32[h]	LHW
Jonza et al.[34,b]	–	40	71	–	–	LHW
Nie et al.[35,b]	19.3	36.3	59.9	34.1	–	LHW
Núñez et al.[36,d,e]	1.9 4.5 13 40[i]	2.3 6.8 18 –	56[j] 69[j] 78[j] 83.6[j] 86.1[k] 85.4[l]	–	–	NLHW Variable
Ong et al.[37, 38,b]	13	25	66	27.0	174.7	LHW
Philips et al.[39, 40]	7 15 40	– – –	67.9 69.4 70.4	87.9 87.1 94.7	589.2 583.3 634.6	LHW
Pucciariello et al.[41,b]	–	14.9	67.2	–	–	LHW
Rohindra[42,b]	15	30.3	77.8	–	–	LHW
Sanandaji et al.[43]	0.45 (4-mer) 0.90 (8-mer) 1.80 (16-mer) 3.60 (32-mer) 7.20 (64-mer)	0.45 0.90 1.80 3.60 7.20	77, 84[m]	–	–	GT

Reference	M_n (kg.mol^{-1})	M_w (kg.mol^{-1})	T_m (°C)	σ_e (mJ.m^{-2})[a]	$\sigma\sigma_e$ (mJ^2.m^{-4})[a]	Method
Sheth[44]	21	32	80.6 ± 0.3[f]	95 ± 10	606 ± 61	Zero growth rate from POM
	36	49	87.0 ± 1.9[f]	138 ± 14	879 ± 88	
	13	14	75.9 ± 1.6[f]	65 ± 7	415 ± 42	
	25	28	81.1 ± 1.7[f]	91 ± 9	582 ± 58	
	40	47	89.2 ± 2.4[f]	151 ± 15	964 ± 96	
	55	70	90.1 ± 2.5[f]	166 ± 17	1060 ± 110	
Shin[45]	79[cyclic]	145	84.2 ± 0.3	–	–	LHW
	168	217	82.0 ± 0.2	–		
	168	217	97	67		GT
Siqueira[46,b]	42.5	65.0	79	–	887	LHW
Strobl[28, 33, 47-50]	42.5	65.0	77[28, 50,n]	–	–	Zero growth rate from POM GT
			70[33,n]	–		
			99[28, 48, 50,o]	74, 87[o]		
			135[28, 48, 50,p]	117[p]		
Su[51]	7.0[cyclic]	7.3	80	42.8	–	GT
	7.3	7.4	91.2	30.3		
Vion[52,b,c]	43.6	48.0	76.15	–	–	DSC on nascent sample
Xing[53,b]	42	60	61.3	–	–	LHW

[a]Note that the fold surface free energies determined using the Gibbs-Thomson method would correspond to σ_{em} values. All of the values determined using the linear Hoffman-Weeks method or zero growth rate determination from polarized optical microscopy measurements correspond to the constant fold surface free energy that is assumed in the classical LH theory. That is, these values are not equivalent to the equilibrium fold surface free energy upon crystallization, σ_e^o, from the non-linear Hoffman-Weeks analysis. Experimental details for the determination of T_m can be found in the given references. Data is for linear polymers unless otherwise indicated. [cyclic]data for cyclic polymers. [b]Additional data from blends available. [c]Additional data from copolymers is available. [d]Additional data for star polymers available. [e]Additional data for dendrimers available. [f]Average of different analytical methods on same data set. [g]Product of $\sigma\sigma_e$ found from classical LH growth rate analysis was found to vary (nonmonotonically) with T_x. [h]Values of $\sigma\sigma_e$ and σ_e calculated using classical LH growth rate analysis on a combined data set of homopolymer and copolymer spherulite growth rate data. [i]Data from Philips et al. that was reanalyzed. [j]Calculated using nonlinear extrapolation using NLHW equation, but not MX method. [k]Calculated using method of Hay.[59] [l]Calculated using method of Broadhurst.[60, 61] [m]Different endgroups yielded different T_m values for the GT analysis of extended chain crystal melting of varying length oligomers. [n]Strobl's multiphase thermodynamic scheme equates the zero-growth temperature, T_{zg}, to the equilibrium amorphous-to-mesophase transition

temperature, T_{mc}^{∞}. [o]Strobl's multiphase thermodynamic scheme equates the equilibrium melting temperature determined via the Gibbs-Thomson method to the equilibrium amorphous-to-crystal transition temperature, T_{ac}^{∞}, which is also denoted as T_{f}^{∞}. This model defines the amorphous-to-crystal fold surface free energy of stabilized crystals, σ_{ac_s}, and the amorphous-to-crystal fold surface free energy of nascent crystals, σ_{ac_n}, where the latter quantity is always larger than the former. [p]Strobl's multiphase thermodynamic scheme requires a virtual transition temperature that is the equilibrium mesophase-to-crystal transition temperature, T_{mc}^{∞}, which is also denoted as T_{c}^{∞}. There is a mesophase-to-crystal fold surface free energy, σ_{mc}, associated with this transition. These values are determined by linear extrapolation of $T_x(l_x^{-1})$, the crystallization line, to infinite lamellar thickness in a similar manner to a Gibbs-Thomson analysis.

We will first analyze the isothermal crystallization of PCL to determine the melting temperature dependence on crystallization temperature and time with the objective of obtaining the initial melting temperatures across a range of isothermal crystallization temperatures. In doing so, we will compare two different experimental approaches for measuring the melting temperature of isothermally crystallized PCL, both of which can potentially be applied to other polymers. We will utilize the initial melting temperatures as a function of crystallization temperature to determine the equilibrium melting temperature of PCL with the Gibbs-Thomson and the non-linear Hoffman-Weeks approaches. We will modify the non-linear Hoffman-Weeks method to propose a possible explanation for why any polymer can exhibit a constant difference between the observed melting temperature and the crystallization temperature.

3.2 THEORETICAL BACKGROUND

3.2.1 Polymer melting kinetics

The model for polymer melting kinetics[4, 62-64] assumes that the time-dependent reduction of crystallinity, ϕ, is a first-order process that is described by

$$\frac{d\phi}{d\Delta t} = -a(\Delta T_{melt})^{Y}\phi,\ y \geq 1 \tag{3.1}$$

where a and Y are constants and $\Delta T_{melt} = T - T_m(\beta = 0)$ is the superheating at any temperature T above the melting temperature when the heating rate equals 0 K.s^{-1}. The constant Y is related to the

kinetic barrier of melting, where Y = 1 corresponds to the maximum rate without a kinetic barrier and $Y \geq 1$ corresponds to rates affected by a kinetic barrier. The superheating can be defined in terms of the applied heating rate, β, and the time spent above the melting temperature prior to melting, Δt_{melt}, such that $\Delta T_{\mathrm{melt}} = \beta \Delta t_{\mathrm{melt}}$. The differential equation above can be rewritten in terms of Δt_{melt}, then solved by separating the variables and integrating to yield

$$\phi = \phi_0 \exp\left[-\left(\frac{\Delta t_{\mathrm{melt}}}{\tau_{\mathrm{c}}}\right)^{Y+1}\right] \tag{3.2}$$

where ϕ_0 is the distribution function of melting points and τ_{c} is the mean time of crystallite melting. The heating rate dependence of the mean time of crystallite melting is given by[4, 63, 64]

$$\tau_{\mathrm{c}} = (Y+1)^{\frac{1}{Y+1}} a^{-\frac{1}{Y+1}} \beta^{-\frac{Y}{Y+1}} \tag{3.3}$$

For melting in the absence of thermal lag effects, the increase in melting temperature can be expressed as

$$\Delta T'_{\mathrm{m}} = \beta \tau_{\mathrm{c}} = \left(\frac{Y+1}{a}\beta\right)^{\frac{1}{Y+1}} \tag{3.4}$$

where $\Delta T'_{\mathrm{m}} = T'_{\mathrm{m}}(\beta) - T'_{\mathrm{m}}(\beta = 0)$ is the apparent superheating given by the difference between the observed melting temperature at the applied heating rate and the melting temperature when the heating rate equals 0 K.s^{-1}. Note that the zero-heating-rate melting temperature is commonly referred to as the zero-entropy-production melting temperature, T_{ZEP}, in the literature. The following definitions are introduced to simplify Eqn. (3.4)

$$A = \left(\frac{Y+1}{a}\right)^{\frac{1}{Y+1}} \tag{3.5}$$

and

$$z = \frac{1}{Y+1} \leq 0.5 \tag{3.6}$$

to give the final form[4, 63, 64] that will be utilized in the present work

$$T'_{\mathrm{m}}(\beta) = T'_{\mathrm{m}}(\beta = 0) + A\beta^{z} \tag{3.7}$$

It should be noted that a rigorous treatment of melting at a constant heating rate should also include the linear contribution of thermal lag, $B\beta$, such that Eqn. (3.7) becomes[4, 62]

$$T'_{\mathrm{m}}(\beta) = T'_{\mathrm{m}}(\beta = 0) + A\beta^{z} + B\beta \tag{3.8}$$

However, the thermal lag effects in Eqn. (3.8) can be neglected by utilizing samples of sufficiently low mass and thickness. The samples used in the present study, to be described in Section 3.3.1, meet these criteria by having masses on the order of 10 ng and thickness of 1.1 µm. Toda and Konishi[4] have demonstrated that the effects of thermal lag can be neglected for samples with thicknesses less than 3 µm. These authors also demonstrated in the same publication that Eqn. (3.7) can still be utilized in place of Eqn. (3.8) when samples with thicknesses greater than 3 µm are analyzed, but an effective z is obtained that ranges from 0.5 to 1.

3.2.2 Average lamellar thickness predictions from the Lauritzen-Hoffman secondary nucleation model of polymer crystal growth

The following will reiterate the final conclusions of the classical LH model's initial lamellar thickness equation[65, 66] and outline the modifications to this equation if the temperature dependences of the fold surface and lateral surface free energies are taken into account. The initial lamellar thickness, l_{g}^{*}, in the classical LH model is given by

$$l_{\mathrm{g}}^{*} = \frac{2\sigma_{\mathrm{ec}}T_{\mathrm{m}}}{\Delta H_{\mathrm{f}}^{\mathrm{o}}\Delta T} + \delta l \tag{3.9}$$

where σ_{e} is fold surface free energy upon crystallization, T_{m} is the equilibrium melting temperature, $\Delta H_{\mathrm{f}}^{\mathrm{o}}$ is the theoretical heat of fusion at the equilibrium melting temperature, ΔT is the undercooling ($\Delta T = T_{\mathrm{m}} - T_{\mathrm{x}}$), and δl is a small increment in lamellar thickness that imparts thermodynamic stability at a given undercooling. In other words, δl makes the isothermal crystallization irreversible. The lamellar thickness increment, δl, is defined as

$$\delta l = \frac{kT_x}{2b_0\sigma}\left(\frac{\Delta G_c^o + \frac{4\sigma}{a_0}}{\Delta G_c^o + \frac{2\sigma}{a_0}}\right) \tag{3.10}$$

where k is Boltzmann's constant, b_0 is the crystalline stem width, ΔG_c^o is the change in Gibbs free energy upon crystallization, σ is the lateral surface free energy, and a_0 is the crystalline stem depth.[67] Note that Eqn. (3.9) assumes that the fold surface free energy is constant, and Eqn. (3.10) assumes that the lateral surface free energy free energy is constant. Furthermore, both Eqns. (3.9) and (3.10) assume that the difference between the heat capacities of the amorphous and crystalline phases is zero. In other words, the theoretical heat of fusion and theoretical entropy of fusion are assumed to be independent of temperature. The value of δl is typically assumed constant, but this assumption is only valid for small undercoolings since the quantity is directly proportional to the crystallization temperature and the free energy of crystallization varies with temperature.

Although the classical Lauritzen-Hoffman theory assumes that the lateral and fold surface free energies are independent of temperature, convincing arguments have been proposed to the contrary. Hoffman et al.[68] derived the temperature dependence of the lateral surface free energy by assuming that σ was related to the loss of configurational entropy upon alignment of a crystalline stem with the substrate. In this context, $\sigma(T_x)$ is defined as

$$\sigma(T_x) = T_x\left(\frac{\Delta H_f^o}{T_m}\right)\left(\frac{a_0}{2}\right)\left(\frac{l_b}{l_u}\right)\left(\frac{1}{C_\infty}\right) = \sigma^o\left(\frac{T_x}{T_m}\right) \tag{3.11}$$

where l_b is the length of a backbone bond, l_u is the projected bond length in the chain direction of the unit cell, and C_∞ is the characteristic ratio. Recall that δl includes contributions from σ, so the lamellar thickness increment will depend more strongly on temperature when the temperature dependence of the lateral surface free energy is considered. The temperature dependence of the fold surface free energy was derived by Lauritzen and Passaglia[69] (LP) in the context of their kinetic roughening theory. Here, crystalline stems with different lengths are assumed to deposit with unique forward and reverse rate

constants leading to a kinetically rough fold surface. The temperature dependence of the kinetic fold surface free energy upon crystallization, σ_{ec}^{k}, arises from varying amounts of exposed lateral surface of the crystalline stems.[69, 70] Assuming a linear dependence of σ_{ec}^{k} on undercooling, then

$$\sigma_{ec}^{k} = \sigma_{ec}^{o}(1 + y\Delta T) \tag{3.12}$$

where σ_{ec}^{o} is the equilibrium fold surface free energy upon crystallization and y is a small constant that accounts for kinetic roughening of the fold surface during stem deposition. It is important to note that Lauritzen and Passaglia[69] explicitly defined the kinetic fold surface free energy upon crystallization as a non-linear function of crystallization temperature (or undercooling). However, Hoffman et al.[70] showed that a linear approximation was sufficiently accurate to analyze experimental spherulite growth rate data of linear polyethylene (LPE) at small undercoolings, and this finding was supported by Mohammadi for the cases of LPE and poly(ethylene oxide) (PEO).[71] Despite this, there is no *a priori* reason or experimental precedent that would justify analyzing data collected at large undercoolings with the linear form of the kinetic fold surface free energy upon crystallization given by Eqn. (3.12).

The effect of the temperature-dependent kinetic fold surface free energy upon crystallization on the initial lamellar thickness predicted by LH theory can be realized by substituting σ_{ec}^{k}, (Eqn. (3.12)), into l_g^*, (Eqn. (3.9)), and rearranging to yield

$$l_g^* = \frac{2\sigma_{ec}^{k}T_m}{\Delta H_f^o \Delta T} + \delta l = \frac{2\sigma_{ec}^{o}T_m}{\Delta H_f^o \Delta T} + \left(\frac{2\sigma_{ec}^{o}yT_m}{\Delta H_f^o} + \delta l\right) \tag{3.13a}$$

$$l_g^* = \frac{C_1}{\Delta T} + C_2 \tag{3.13b}$$

where the constants in the first term are grouped together as C_1, and the terms in the parentheses, which are approximately independent of temperature for small undercoolings, are grouped together as C_2. The contribution from the kinetic roughening parameter, y, makes C_2 larger than δl and its effects should be considered in any analysis that uses the lamellar thickness as a variable.

Accounting for the temperature dependence of the lateral and fold surface free energies also changes the spherulite growth rate equation from the Lauritzen-Hoffman model. However, this is outside the scope of the current work, and the reader is referred elsewhere for an overview.[71]

3.2.3 Gibbs-Thomson method for determining a polymer equilibrium melting temperature

Basic assumptions for the derivation of the Gibbs-Thomson (GT) theory will be reviewed, the final functional will be reiterated, and some crucial details regarding the experimental approach to determining the equilibrium melting temperature of a polymer using the GT theory will be examined. Consider an infinitely large, chain-extended crystal containing an equilibrium number of defects. By definition, this crystal would melt at the equilibrium melting temperature, T_m. A finite crystal with thickness l_x and basal dimensions x and y would be in equilibrium with the melt at the observed melting temperature, T_m'. The change in Gibbs free energy for the fusion of this finite crystal can be expressed as

$$\Delta G_\mathrm{f}(T_\mathrm{m}') = xyl_\mathrm{x}\Delta G_\mathrm{f}^\mathrm{o}(T_\mathrm{m}') - 2(x+y)l_\mathrm{x}\sigma - 2xy\sigma_\mathrm{em} = 0 \tag{3.14}$$

Under the assumptions that the enthalpy and entropy of fusion are independent of temperature, that $x, y \gg l_\mathrm{x}$, and that $\sigma_\mathrm{em} \gg \sigma$, the well-known Gibbs-Thomson equation relates the melting temperature to the inverse lamellar thickness according to[65, 72]

$$T_\mathrm{m}' = T_\mathrm{m} - \frac{2\sigma_\mathrm{em}T_\mathrm{m}}{\Delta H_\mathrm{f}^\mathrm{o} l_\mathrm{x}} \tag{3.15}$$

where σ_em is the equilibrium fold surface free energy upon melting. Melting temperatures measured by differential scanning calorimetry can be plotted against inverse lamellar thickness measured by either small-angle X-ray scattering (SAXS) or longitudinal acoustic mode (LAM) Raman spectroscopy, and the equilibrium melting temperature is obtained by linear extrapolation to infinite lamellar thickness. In all reality, lamellae are limited to a finite thickness equal to the chain's contour length, but the difference between the melting temperature at this finite thickness and infinite thickness is negligible.

Some caution must be exercised when measuring both melting temperatures and lamellar thicknesses for use in a Gibbs-Thomson analysis. The melting temperature in semi-crystalline polymers is known to depend on both the crystallization temperature and crystallization time. The origin of this phenomenon has been attributed to isothermal lamellar thickening for crystal-mobile polymers, such as LPE,[73-77] *i*-PP,[78] and low molecular weight PEO.[79, 80] Lamellar thickening is a thermally-activated process, so it should occur faster the higher the temperature (below the crystal melting temperature). As a result, the thickening effects will be more pronounced in a conventional differential scanning calorimeter and hot stage where the melting temperature is typically measured using low heating rates (10–40 $K.min^{-1}$). While the increase in polymer melting temperature with crystallization time may result from lamellar thickening, it can also arise from increasing crystal perfection or lateral dimensions, or even increasing constraints at the crystal-liquid interface. The exact mechanism that causes melting temperature to increase with crystallization time is currently unclear for polymers that do not exhibit isothermal lamellar thickening, or crystal-fixed polymers, such as PCL,[81] poly(ethylene terephthalate) (PET),[82] PBT,[83] and PEEK.[84] Simultaneous time-resolved small-angle and wide-angle X-ray scattering data from Kohn and Strobl[85] suggests that there is a continuous increase in crystal ordering in PCL throughout the course of isothermal crystallization. Recent studies of PCL by Schulz et al.[81] and Kurz et al.[86] suggest that the structure of the amorphous phase, in particular the chain entanglements, may play a significant role in determining the lamellar thickness and crystallite dimensions. These studies also posit that the lack of intracrystalline dynamics in crystal-fixed polymers leads to the formation of marginally stable lamellae that continuously melt-recrystallize-remelt during sufficiently slow heating. The melting temperature is also known to depend on heating rate, sample mass, and sample thickness, all of which can be accounted for through experimental design and careful sample preparation. With these facts in mind, the following considerations are crucial for collecting reliable melting temperature and lamellar thickness data in order to conduct an accurate Gibbs-Thomson analysis: 1) careful sample preparation to minimize the effects of

thermal lag during heating, 2) measuring the melting temperature with heating rates that are high enough to suppress reorganization, annealing, increasing perfection, and/or thickening, 3) accounting for the effects of superheating and melting kinetics on the melting temperature, and 4) controlling the crystallization temperature and crystallization time to ensure that the lamellar thickness and melting temperature measurements correspond to nascent lamellae.

3.2.4 Hoffman-Weeks method for determining a polymer equilibrium melting temperature

Special focus will be placed on the linear Hoffman-Weeks equation (LHW), the non-linear Hoffman-Weeks (NLHW) equation, and the necessary experimental details required to use the NLHW method for equilibrium melting temperature determination of a polymer. It is important to note that the Hoffman-Weeks model assumes that lamellar thickening is the sole mechanism through which the melting temperature increases with crystallization time. The following background theory will be presented under this assumption, and the application of the non-linear Hoffman-Weeks method to polymers that do not exhibit thickening will be justified at the end of this subsection.

The Hoffman-Weeks approach assumes that the lamellar thickness at any time during crystallization is related to the initial lamellar thickness by

$$l_{\mathrm{x}} = \gamma(t_{\mathrm{x}}, T_{\mathrm{x}}) l_{\mathrm{g}}^{*} \tag{3.16}$$

where $\gamma(t_{\mathrm{x}}, T_{\mathrm{x}})$ is the isothermal lamellar thickening coefficient and t_{x} is the crystallization time. The temperature and time dependences have been verified experimentally by several groups for the case of HDPE.[74, 87-89] The original formulation of the Hoffman-Weeks equation assumes the initial lamellar thickness in Eqn. (3.16) takes the form of Eqn. (3.9), i.e. the fold surface free energy of crystallization is constant, and the Gibbs-Thomson equation (Eqn. (3.15)) accurately describes the relationship between the melting temperature and the lamellar thickness. Combining these equations and rearranging to obtain the melting temperature as a function of crystallization temperature yields

$$T_{\mathrm{m}}' = T_{\mathrm{m}}\left\{1 - \left[\frac{1}{\gamma(t_{\mathrm{x}}, T_{\mathrm{x}})}\right]\left(\frac{T_{\mathrm{m}} - T_{\mathrm{x}}}{T_{\mathrm{m}}}\right)\left(\frac{\sigma_{\mathrm{em}}}{\sigma_{\mathrm{ec}}}\right)\left[\frac{1}{1 + \frac{\delta l \Delta H_{\mathrm{f}}^{\mathrm{o}}}{2\sigma_{\mathrm{ec}}}\left(\frac{T_{\mathrm{m}} - T_{\mathrm{x}}}{T_{\mathrm{m}}}\right)}\right]\right\} \tag{3.17}$$

Hoffman and Weeks assumed that δl can be neglected at low undercoolings since it is typically less than 10 Å and relatively temperature independent near the equilibrium melting temperature. Furthermore, they assumed that σ_{ec} is equivalent to σ_{em} and that $\gamma(t_{\mathrm{x}}, T_{\mathrm{x}})$ is constant for all crystallization temperatures and times to obtain the linear Hoffman-Weeks (LHW) equation

$$T_{\mathrm{m}}' = T_{\mathrm{m}}\left(1 - \frac{1}{\gamma}\right) + \left(\frac{1}{\gamma}\right)T_{\mathrm{x}} \tag{3.18}$$

A plot of experimental melting temperature as a function of crystallization temperature can then be used to determine the equilibrium melting temperature by linear extrapolation to the point of intersection with the line $T_{\mathrm{m}}' = T_{\mathrm{x}}$. The thickening coefficient can also be obtained from the slope of this plot, but this value may not accurately reflect the true nature of the thickening process since its crystallization time and temperature dependencies were both ignored to obtain Eqn. (3.18).

The generalized non-linear Hoffman-Weeks (NLHW) equation is obtained by assuming that the fold surface free energy of crystallization depends on the undercooling such that the initial lamellar thickness in Eqn. (3.16) is instead given by Eqn. (3.13). Taking the same steps as above yields a new expression for the melting temperature

$$T_{\mathrm{m}}' = T_{\mathrm{m}}\left\{1 - \left[\frac{1}{\gamma(t_{\mathrm{x}}, T_{\mathrm{x}})}\right]\left(\frac{T_{\mathrm{m}} - T_{\mathrm{x}}}{T_{\mathrm{m}}}\right)\left(\frac{\sigma_{\mathrm{em}}}{\sigma_{\mathrm{ec}}^{\mathrm{o}}}\right)\left[\frac{1}{1 + \frac{C_2 \Delta H_{\mathrm{f}}^{\mathrm{o}}}{2\sigma_{\mathrm{ec}}^{\mathrm{o}}}\left(\frac{T_{\mathrm{m}} - T_{\mathrm{x}}}{T_{\mathrm{m}}}\right)}\right]\right\} \tag{3.19}$$

where C_2 is larger than δl, so its contribution to the observed melting temperature cannot be neglected. Eqn. (3.19) is rearranged to obtain the MX equation, a linear relationship between the reduced melting temperature, M, and the reduced crystallization temperature, X, given by

$$M = \gamma(t_{\mathrm{x}}, T_{\mathrm{x}})\left(\frac{\sigma_{\mathrm{ec}}^{\mathrm{o}}}{\sigma_{\mathrm{em}}}\right)(X + a) \tag{3.20}$$

where a contains the contribution from C_2. M, X, and a are defined as

$$M = \frac{T_\mathrm{m}}{T_\mathrm{m} - T'_\mathrm{m}} \tag{3.21}$$

$$X = \frac{T_\mathrm{m}}{T_\mathrm{m} - T_\mathrm{x}} \tag{3.22}$$

$$a = \frac{C_2 \Delta H_\mathrm{f}^\mathrm{o}}{2\sigma_\mathrm{ec}^\mathrm{o}} \tag{3.23}$$

Two assumptions must be made in order to use the MX equation to determine a polymer's equilibrium melting temperature. First, it is assumed that $\sigma_\mathrm{ec}^\mathrm{o}$ is equal to σ_em, i.e. $\left(\frac{\sigma_\mathrm{ec}^\mathrm{o}}{\sigma_\mathrm{em}}\right) = 1$. Physically, this assumes that the fold surface formed under equilibrium conditions is the same as the fold surface that melts under equilibrium conditions. In other words, the fold surface of crystals formed at the equilibrium melting temperature is the same as the fold surface of crystals that melt at the observed melting temperature. Second, it is assumed that $\gamma(t_\mathrm{x}, T_\mathrm{x}) = 1$, i.e. the crystalline lamellae have not thickened either during crystallization or during heating to observe melting. This assumption can be realized experimentally by 1) using only the initial melting temperatures that can be measured following isothermal crystallization and 2) carefully selecting the range of experimental crystallization temperatures such that there is a short plateau in the plot of melting temperature versus logarithm of crystallization time, indicating that there is neither isothermal lamellar thickening nor crystal perfection taking place at those crystallization temperatures and over a range of crystallization times. Taking these two assumptions into account, the MX equation reduces to $M = X + a$. A polymer's equilibrium melting temperature can then be determined simply by plotting M versus X and varying the equilibrium melting temperature until the slope of the linear plot is unity. The linear Hoffman-Weeks method will always underestimate the equilibrium melting temperature compared to the non-linear Hoffman-Weeks method because C_2 is

positive by definition, meaning that a plot of melting temperature as a function of crystallization exhibits positive curvature that is clearly observable as the equilibrium melting temperature is approached.

The non-linear Hoffman-Weeks method implicitly generalizes itself to systems, which do not exhibit lamellar thickening, i.e. PCL, because the experimental approach relies on the melting temperatures of initially formed lamellae. Utilizing the initial melting temperatures not only removes the effects of isothermal lamellar thickening on the melting temperature but also removes the effects of any other processes that may increase the melting temperature with increasing crystallization time. Accordingly, explicit knowledge concerning the origin of the time-dependence of the melting temperature is no longer required as long as the proper experimental precautions are taken.

3.3 EXPERIMENTAL

3.3.1 Materials and sample preparation

Poly(ε-caprolactone) (M_w = 36 kg.mol^{-1}, PDI = 1.38) was purchased from Sigma-Aldrich (St. Louis, MO, USA) and used without further purification. Films with a thickness of 340 µm were prepared using a Carver laboratory press operated at 110°C under a nitrogen atmosphere and used for the preliminary CDSC experiments. Two samples, referred to as PCL-1 and PCL-2 throughout this work, were used for the fast calorimetry study. The sample information is listed in Table 3.2. A film with 1.1 µm thickness was cut from a pellet using a Leica EM UC-6 cryoultramicrotome. It has been shown that 1 µm is the lower limit of film thickness for crystallization to proceed without confinement effects.[90-92] The film was cut down to the proper lateral dimensions using a scalpel and optical microscope, then it was placed onto the Flash™ DSC chip and positioned using an eyelash. The sample was heated from 0 to 100°C with β = 1 K.s^{-1}, held for 1 s, and cooled with β = 1 K.s^{-1}. This process was repeated three times for each heating rate β = 1, 2, and 5 K.s^{-1} to ensure good thermal contact between the sample and the sensor and to allow any residual stresses induced during microtoming and cutting to relax. Polarized optical micrographs were

collected at 23°C to measure the sample area, and the density of the pellets at 25°C was measured using a density gradient column with saturated brine and water. The density at 25°C was found to be $\rho_{25°C}$ = 1.164 g.cm^{-3}. The sample area, thickness, and density were used to determine the sample mass assuming a cylindrical geometry. There is an uncertainty of ca. 15% in the estimated mass using this approach.[4] The difference between densities at 23°C and 25°C is negligible compared to the errors arising from the uncalibrated heat flow of the FDSC and the film thickness as cut by the cryoultramicrotome.

Table 3.2: Sample characteristics.

Sample	m_{PCL} (ng)	m_{In} (ng)	ΔT_{cal} (°C)	L (μm)
PCL-1	5	41	−0.4	1.1
PCL-2	8	107	−3.1	1.1

3.3.2 Conventional different scanning calorimetry

A TA Instruments Q2000 DSC equipped with an RCS-90 intracooler was operated under a nitrogen purge of 50 mL.min^{-1} for preliminary investigations of the isothermal crystallization behavior of PCL. The heat flow was calibrated using a sapphire standard and the temperature was calibrated using an indium standard according to the recommended calibration protocols from TA Instruments. Aluminum Tzero hermetic sample pans were used. The thermal history was erased between experiments by heating to 100°C, followed with a 1 min isothermal hold. The thermograms were recorded by directly heating from the isothermal crystallization temperature with heating rates over the range β = 10 – 100 K.min^{-1}. For reasons we will justify in the following RESULTS AND DISCUSSION section, CDSC was not utilized to correlate the melting and crystallization temperatures.

3.3.3 Fast differential scanning calorimetry

A power-compensated Mettler-Toledo Flash™ DSC 1 operated under a nitrogen purge of 20 mL.min^{-1} and equipped with the UFS1 sensors (XENW11 23929, XENW11 23933) was used to investigate both the non-isothermal and isothermal crystallization behavior of PCL. The thermal history

was erased between experiments with heating rates $\beta \leq 10^3$ K.s^{-1} by heating to 110°C with a 0.5 s isothermal hold. The maximum temperature was increased by 5°C for every 10^3 K.s^{-1} in excess of $\beta = 10^3$ K.s^{-1} in order to capture the full melting event when superheating and peak broadening effects are present. For example, a maximum temperature of 130°C was chosen for $\beta = 5\times10^3$ K.s^{-1}. The non-isothermal crystallization behavior was studied over the range of cooling rates $-\beta = 10 - 10^3$ K.s^{-1} with a minimum temperature of −90°C.

Two different methods for measuring the melting temperatures following isothermal crystallization were compared. For both methods, the thermal history was erased as described above, then the sample was cooled to the crystallization temperature with $-\beta = 10^3$ K.s^{-1} and allowed to crystallize for some time. For the direct heating (DH) method, the thermograms were recorded by directly heating from the isothermal crystallization temperature with different heating rates. This approach necessitates a baseline interpolation and subtraction procedure in order to remove the effects of the instrumental response at high heating rates. The baseline was interpolated using a cubic Hermite polynomial, then subtracted from the raw data to obtain the final endotherm from which the peak melting temperatures were obtained. For the quench (Q) method, the sample was quenched to −90°C with $-\beta = 10^3$ K.s^{-1} following isothermal crystallization, held there for 0.5 s, then the thermograms were recorded by heating with different rates. This approach does not require a baseline subtraction procedure because there is sufficient time for the instrument to reach the programmed, constant heating rate prior to the endothermic events of interest. Note that the quench method has been the experimental approach utilized by others to analyze the isothermal crystallization and nucleation kinetics of PCL.[6-10] The two different methods are compared schematically in Figure 3.1. The time-dependent isothermal crystallization was investigated at T_x = 34.1 and 39.1°C with seventeen heating rates over the range $\beta = 10^2 - 10^4$ K.s^{-1} for PCL-1 and at eight isothermal crystallization temperatures from T_x = 31.4 to 51.4°C with seven heating rates over the range $\beta = 5\times10^2 - 10^4$ K.s^{-1} for PCL-2. These crystallization temperatures

will be referred to as the "high T_x." The time-dependent isothermal crystallization behavior of PCL-2 was also investigated at six crystallization temperatures from T_x = −94.1 to −23.6°C over the range β = 5×10^2 – 5×10^3 K.s^{-1}. These crystallization temperatures will be referred to as the "low T_x."

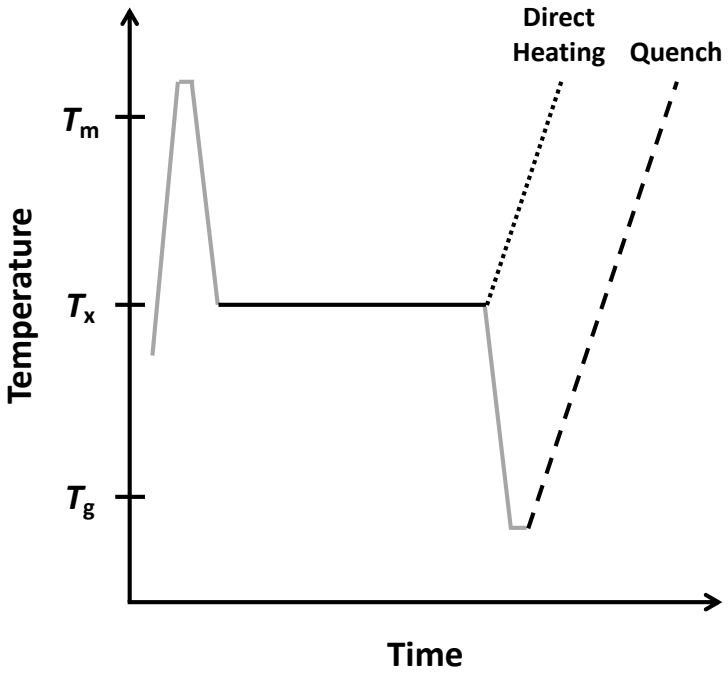

Figure 3.1: A schematic representation of the temperature time profiles for the direct heating (……) and quench (_ _ _ _ .) methods.

For the purpose of temperature calibration, a small piece of indium was cut with a scalpel under an optical microscope and placed on top of each PCL film using an eyelash after the completion of all crystallization experiments. The melting onset, T_m^{onset}, was recorded in triplicate for eighteen heating rates for PCL-1 and thirteen heating rates for PCL-2 over the range β = 50 – 10^4 K.s^{-1}. The melting onset data was non-linearly extrapolated to β = 0 K.s^{-1} using the equation:

$$T_m^{onset}(\beta) = T_m^{onset}(\beta = 0) + A\beta^{0.5} + B\beta \quad (3.24)$$

The same non-linear extrapolation procedure has been employed recently by Mohammadi et al.[71, 93] to calibrate the temperature scale of the Mettler-Toledo Flash™ DSC 1. A linear extrapolation procedure with heating rates $\beta \leq 10^3$ K.s^{-1} was also performed for temperature calibration when studying the

crystallization kinetics of PEO (see Chapter 5). The masses and thicknesses of these PEO samples were much greater than these characteristic of PCL samples utilized in the present study ($L \approx$ 2–5 μm, m = 150–300 ng). This prohibited collection of data at heating rates $\beta \geq 5\times10^3$ K.s^{-1} due to oscillations in the heat flow signal. The linear function of heating rate fit the data well, and any error that may have arisen from the linear extrapolation in place of a non-linear extrapolation was minimized by limiting the data to heating rates $\beta \leq 10^3$ K.s^{-1}. It should be noted that Eqn. (3.24) was originally proposed by Toda[62] to model the peak melting temperature, $T_{\mathrm{m}}^{\mathrm{peak}}$, as a function of heating rate, but it phenomenologically models the onset melting temperature as a function of heating rate very well. The difference between the extrapolated and literature values of the melting onset was used to determine the single-point calibration constant, ΔT_{cal}, and correct both the crystallization and the melting temperatures. The values of ΔT_{cal} for the two samples are listed in Table 3.2. As expected, both of the chips were within the ±5°C error limit for sensors following pre-calibration during manufacturing.[5]

Figure 3.2 shows the results of $T_{\mathrm{m}}^{\mathrm{onset}}$ vs. β for the indium samples used to calibrate the individual FDSC chips. Non-linear fits according to Eqn. (3.24) and linear fits are shown for each chip. The data in Fig. 3.2 is obviously non-linear in contrast to theoretical predictions,[62, 94] but there are previous reports of a non-linear onset melting temperature as a function of heating rate from Zhuravlev and Schick[95] for indium, Vanden Poel et al.[5] for indium, and from Toda and Konishi[4] for tin. Furthermore, Toda[62] observed similar non-linearity for tin melting measured with a heat flux CDSC in addition to results from Vanden Poel and Mathot[96] for indium melting measured with a PerkinElmer HyperDSC, a high-rate, power-compensated CDSC. Based on previous reports and the current data, the non-linearity appears to be exaggerated for very small masses of metals such that the onset melting temperature actually begins to decreases at sufficiently high heating rates. Sufficiently high is relative to the type of DSC employed, i.e. FDSC or CDSC. The data in Fig. 3.2a and in Fig. 3.2b correspond to masses m_{In} = 41 ng and 107 ng, respectively, where the low mass gives rise to a decrease in melting temperature for heating rates

$\beta \geq 3\times10^3$ K.s^{-1}. The greater extent of superheating demonstrated in Fig. 3.2b results from the larger mass of indium. A linear extrapolation of both data sets would yield a ΔT_{cal} that is 1°C lower for both chips. The present study aims to compare melting and crystallization temperature data between chips and with lamellar thickness data measured with SAXS, so the non-linear calibration method seems preferable because it more accurately captures the melting behavior over the entire range of heating rates. Additionally, any linear extrapolation would be highly dependent on the selected range of heating rates.

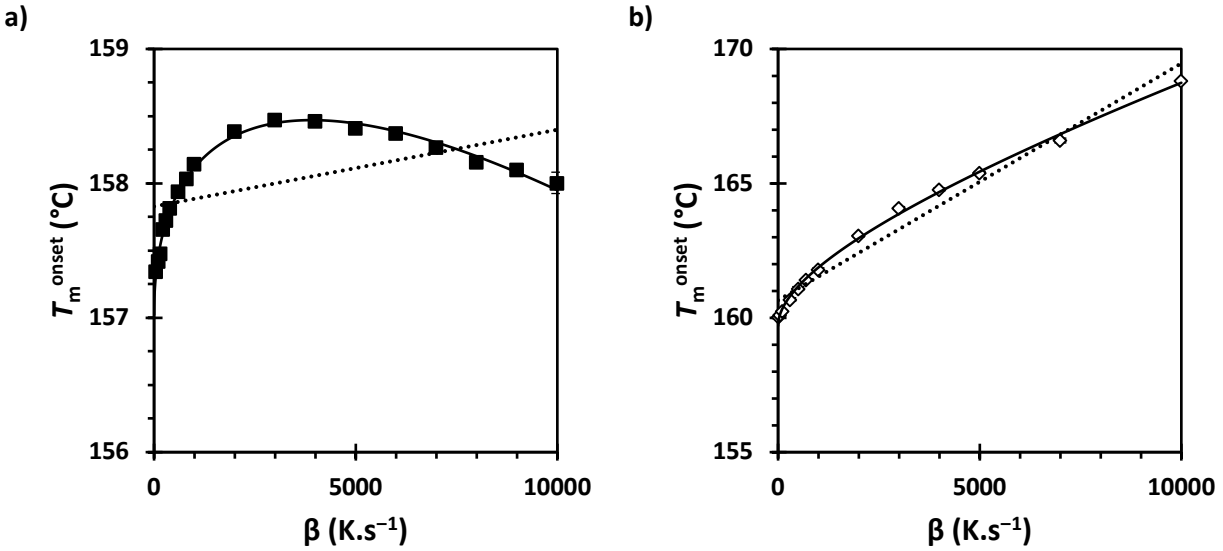

Figure 3.2: Plots of melting onset, $T_{\mathrm{m}}^{\mathrm{onset}}$, as a function of heating rate, β, with non-linear fits (_____) and linear fits (.....) for indium on top of a) PCL-1, b) PCL-2.

3.3.4 Small-angle X-ray scattering

Lamellar thickness data at different isothermal crystallization temperatures was taken from the dissertation of Sheth and is shown in Figure 3.3. Details of the sample preparation, experiments, data analysis, and results can be found elsewhere.[44] Sheth's data was fit with a quadratic polynomial, and lamellar thicknesses corresponding to the isothermal crystallization temperatures from our FDSC experiments were interpolated according to the fitted quadratic function. The two lowest temperature data points from our study were not included in the Gibbs-Thomson or Hoffman-Weeks analyses since

they fell outside the temperature range of the lamellar thickness data from small-angle X-ray scattering experiments.

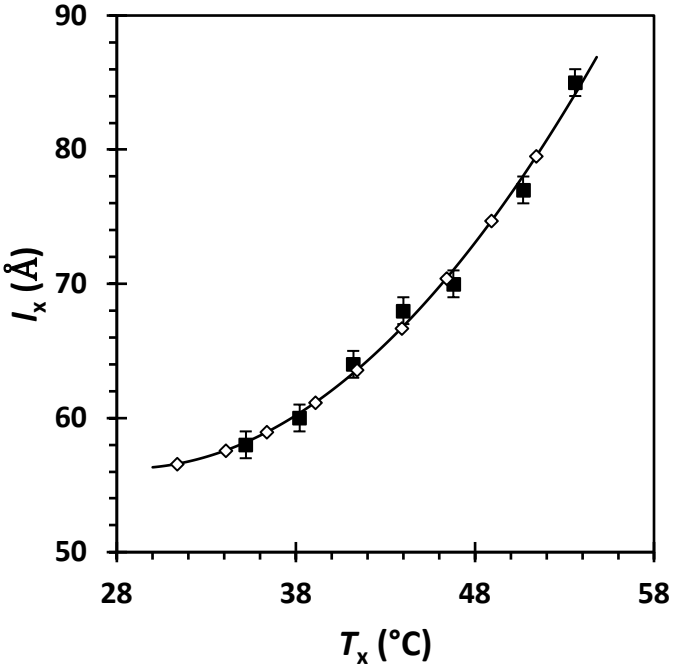

Figure 3.3: Lamellar thickness, l_x, as a function of crystallization temperature, T_x, for data from Sheth[44] (■) and interpolated lamellar thicknesses corresponding to the present isothermal crystallization studies conducted using FDSC (◇). The solid line represents the quadratic function that was used to interpolate the data points for this study.

3.4 RESULTS AND DISCUSSION

3.4.1 Non-isothermal crystallization

The peak crystallization temperature measured at constant linear cooling rate is shown in Figure 3.4. Crystallization is suppressed for $-\beta \geq 500$ K.s^{-1}, which agrees with previous reports from Zhuravlev et al.[9] and Adamovsky and Schick.[19] Not only does this grant access to the entire range of crystallization temperatures, but this result is also crucial for the applicability of the quench method that was tested to measure the melting temperature following isothermal crystallization. PCL is known to exhibit a bimodal function of crystallization half times.[6-10, 19] PBT,[97, 98] *i*-PP,[98-100] polyamide-11 (PA-11),[101] polyamide-12 (PA-12),[102] and isotactic polypropylene-co-polyethylene (*i*-PP-co-PE),[103] all of which exhibit

bimodal crystallization kinetics, also display two distinct non-isothermal crystallization processes depending on the cooling rate. In these cases, low cooling rates lead to the formation of a stable crystalline phase, high cooling rates lead to formation of a mesophase, and intermediate cooling rates lead to the formation of both. However, PCL only exhibits one distinguishable crystallization process during cooling. The exact meaning of this result is unknown at this time, and it does beg the question: why is only one non-isothermal process observed in PCL while other polymer exhibiting bimodal functions of crystallization half times exhibit two non-isothermal processes? The sub-ambient glass transition temperature of PCL prevents convenient analysis of the crystal structure and morphology at room temperature following a non-isothermal crystallization with varying cooling rates. *In situ* X-ray measurements of the crystalline structure and morphology would be required since crystallization at temperatures below ambient conditions leads to metastable structures that completely reorganize upon heating.

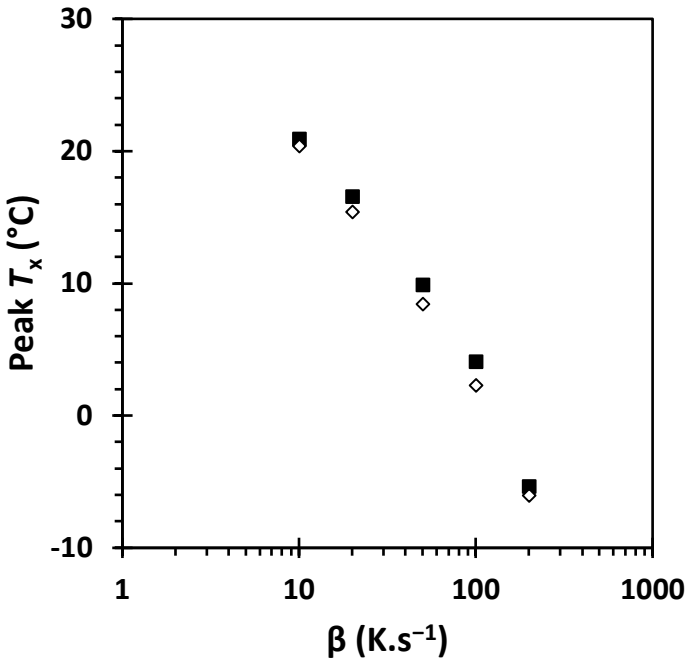

Figure 3.4: Peak crystallization temperature, T_x, as a function of cooling rate, $-\beta$, for PCL-1 (■) and PCL-2 (◇) measured using FDSC.

3.4.2 Isothermal crystallization

Thermograms collected with CDSC for isothermal crystallization at T_x = 45°C and t_x = 8 min are shown in Figure 3.5. This time corresponds to the initial development of crystallinity at 45°C when crystallization took place in the CDSC. At the lowest heating rate, 10 K.min^{-1}, the melting endotherm appears to have a small, high-temperature shoulder. This shoulder separates from the dominant peak and moves to higher temperatures as the heating rate increases, until the shoulder becomes indiscernible at β = 80 K.min^{-1}. The relative magnitude of the first peak to the high temperature shoulder increases as the heating rate increases. These features suggest the occurrence of melting-recrystallization-remelting during heating for heating with rates $\beta \leq$ 80 K.min^{-1}. Although this process can be suppressed with CDSC at high heating rates, the large range of lower heating rates available to the instrument provides erroneous information. We would like to note that longer crystallization times, corresponding to increased degrees of crystallinity, require even higher heating rates to eliminate the high-temperature shoulder. The present focus is to correlate isothermal crystallization and melting temperatures, so it is clear that FDSC is necessary to ensure that the true melting behavior is observed free from any annealing, stabilization, or melting-recrystallization-remelting effects that may occur during heating in a CDSC.

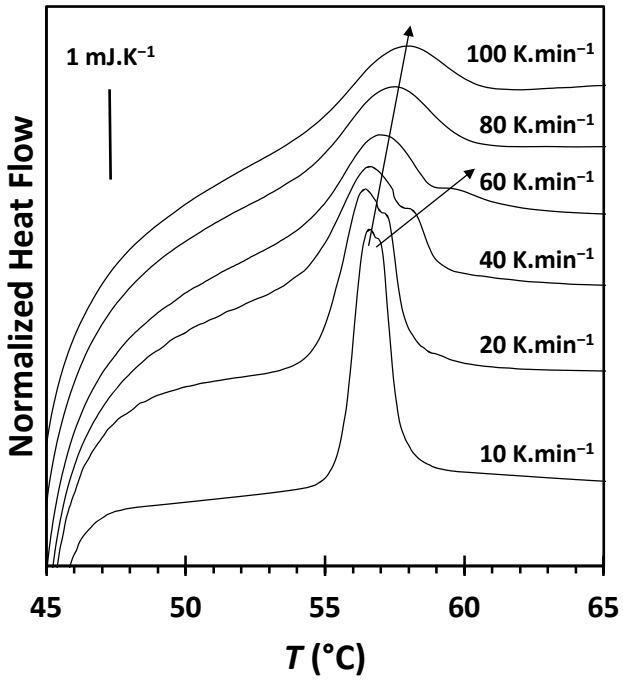

Figure 3.5: Melting thermograms measured with CDSC for β = 10, 20, 40, 60, 80, and 100 K.min^{-1} following isothermal crystallization at T_x = 45°C for t_x = 8 min. Note that endo is up.

The melting behavior following isothermal crystallization for varying crystallization times was studied with FDSC from T_x = 31.4 to 51.4°C ("high T_x") by the direct heating method. Examples of thermograms collected with this approach are shown in Figure 3.6 following isothermal crystallization at T_x = 41.4°C for crystallization times ranging from t_x = 16 to 360 s. The instrumental response begins to overlap with the endothermic peak for $\beta \geq 2\times10^3$ K.s^{-1}. The overlap is greater at short crystallization times where the melting temperatures are lower, and it increases with increasing heating rate until the endothermic peaks start to become obscured by the transient response (Fig. 3.6c,d). A baseline interpolation and subtraction procedure was used to remove this instrumental artifact. Examples of raw thermograms with interpolated baselines and final thermograms following baseline subtraction are shown in Fig. 3.7 for T_x = 41.4°C and t_x = 16 s (a,b) and 360 s (c,d). The baseline interpolation was performed with Mathematica to obtain the final thermograms and determine the melting temperatures at different crystallization temperatures, times, and heating rates. First, the first derivative of the heat

flow versus temperature was used to determine where the endothermic peak started and ended. Next, the data points corresponding to the peak were removed from the raw data set, and a baseline was interpolated in their place using a cubic Hermite polynomial. Then, the new baseline was subtracted from the original data set containing the peak data points to yield the baseline-corrected thermogram. Last, a first derivative smoothing filter was applied to the final data set to reduce the noise, and the peak melting temperature was determined as the root of the first derivative. The smoothing filter was necessary to measure the peak positions accurately for $\beta < 10^3$ K.s^{-1}, and it was used for all heating rates to maintain consistency throughout the analysis. There was no significant difference in melting temperatures determined with or without the first derivative smoothing filter for $\beta \geq 10^3$ K.s^{-1}. The direct heating method was not used to investigate crystallization from T_x = −94.1 to −23.6°C ("low T_x") due to immediate melting and reorganization upon heating from the isothermal crystallization temperature which prohibited a reliable baseline interpolation.

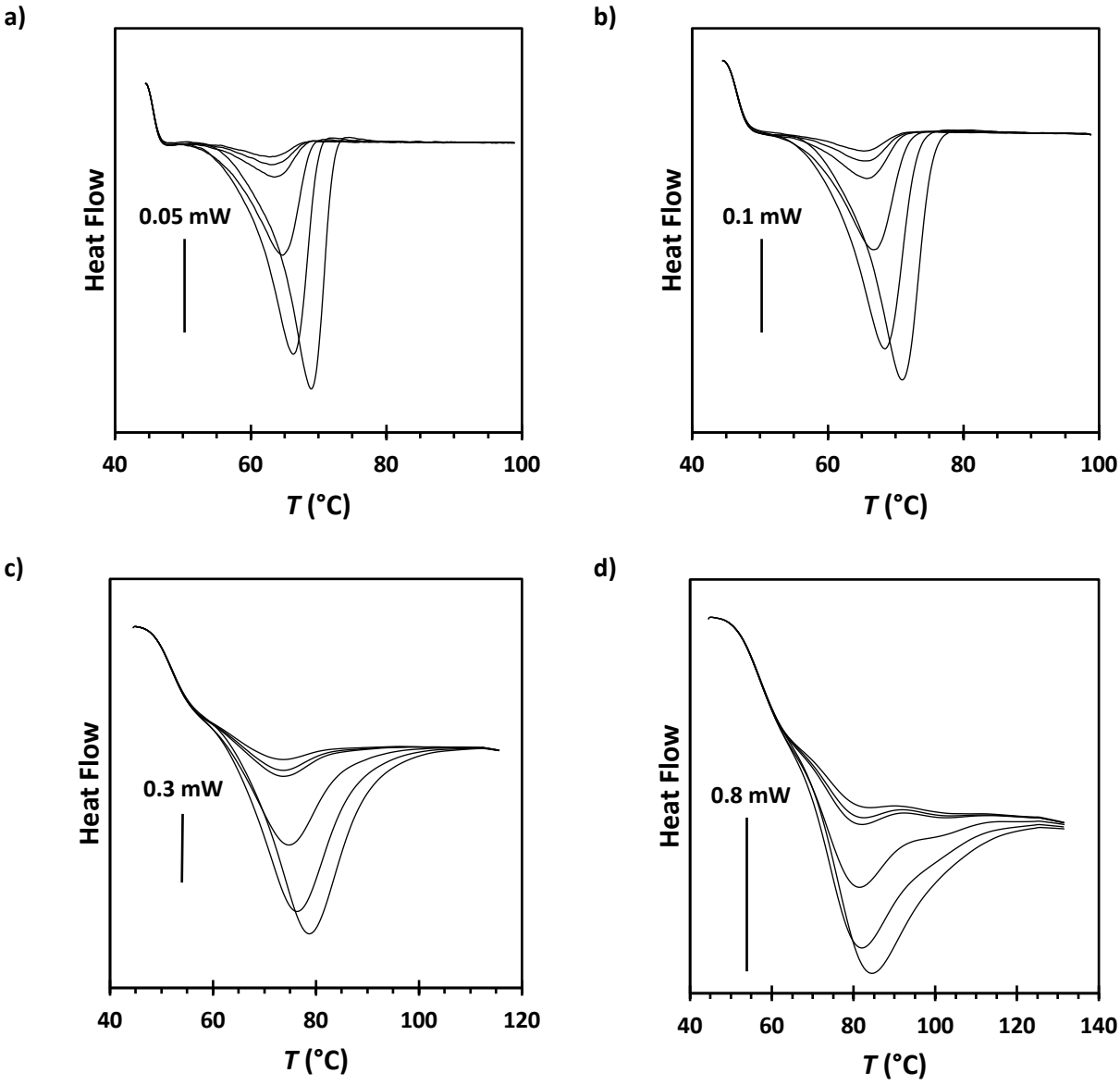

Figure 3.6: Thermograms measured with the direct heating method following isothermal crystallization of PCL-2 at T_x = 41.4°C and t_x = 16 to 360 s. The data was collected with heating rates of a) $\beta = 5\times10^2$ K.s^{-1}, b) $\beta = 10^3$ K.s^{-1}, c) $\beta = 5\times10^3$ K.s^{-1}, and d) $\beta = 10^4$ K.s^{-1}. Note that endo is down.

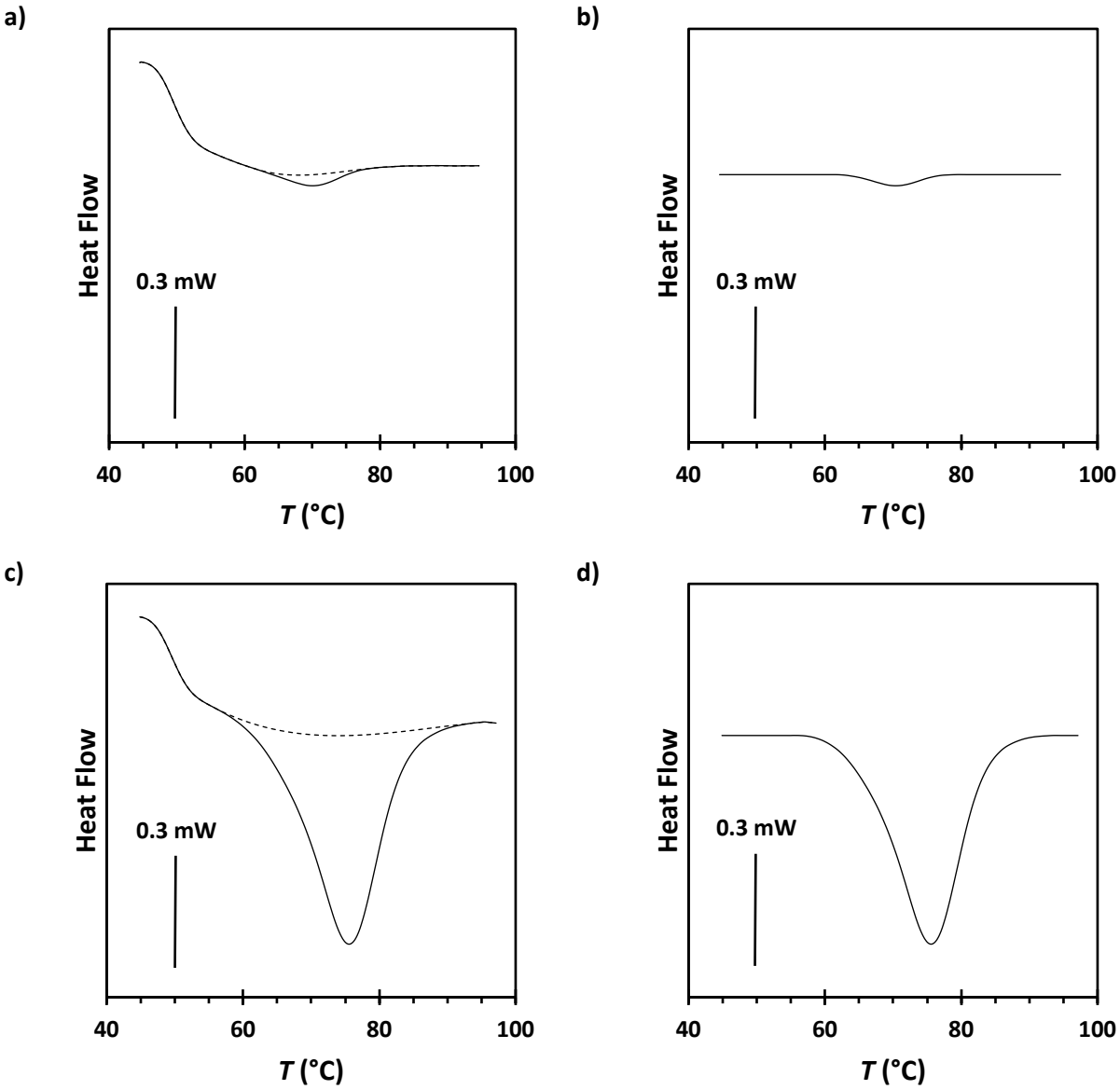

Figure 3.7: Thermograms measured with the direct heating method following isothermal crystallization of PCL-2 at T_x = 41.4°C for t_x = 16 s a) before and b) after baseline subtraction and for t_x = 360 s c) before and d) after baseline subtraction. Note that endo is down.

The quench method was used to investigate the melting behavior following isothermal crystallization for varying crystallization times at both high and low crystallization temperatures. Thermograms measured with the quench approach are shown in Figure 3.8 for the same crystallization conditions shown for the direct heating method in Fig. 3.6 (T_x = 41.4°C, t_x = 16 to 360 s), and Figure 3.9 shows data following isothermal crystallization at T_x = −63.5°C for t_x = 0.2 to 1800 s. The baseline

interpolation procedure is no longer required to analyze the data collected with the quench method because the instrument reaches steady state heating before melting. However, note that while cold crystallization occurs upon heating the vitrified sample following crystallization at high temperatures, melting followed by cold recrystallization takes place during heating after crystallization at low temperatures. The quench method was not used to study the melting characteristics following crystallization between T_x = −23.6 and 31.4°C due to a high degree of overlap between melting, cold crystallization, cold recrystallization, and remelting peaks that prohibited accurate measurement of the peak melting temperatures over a broad range of heating rates.

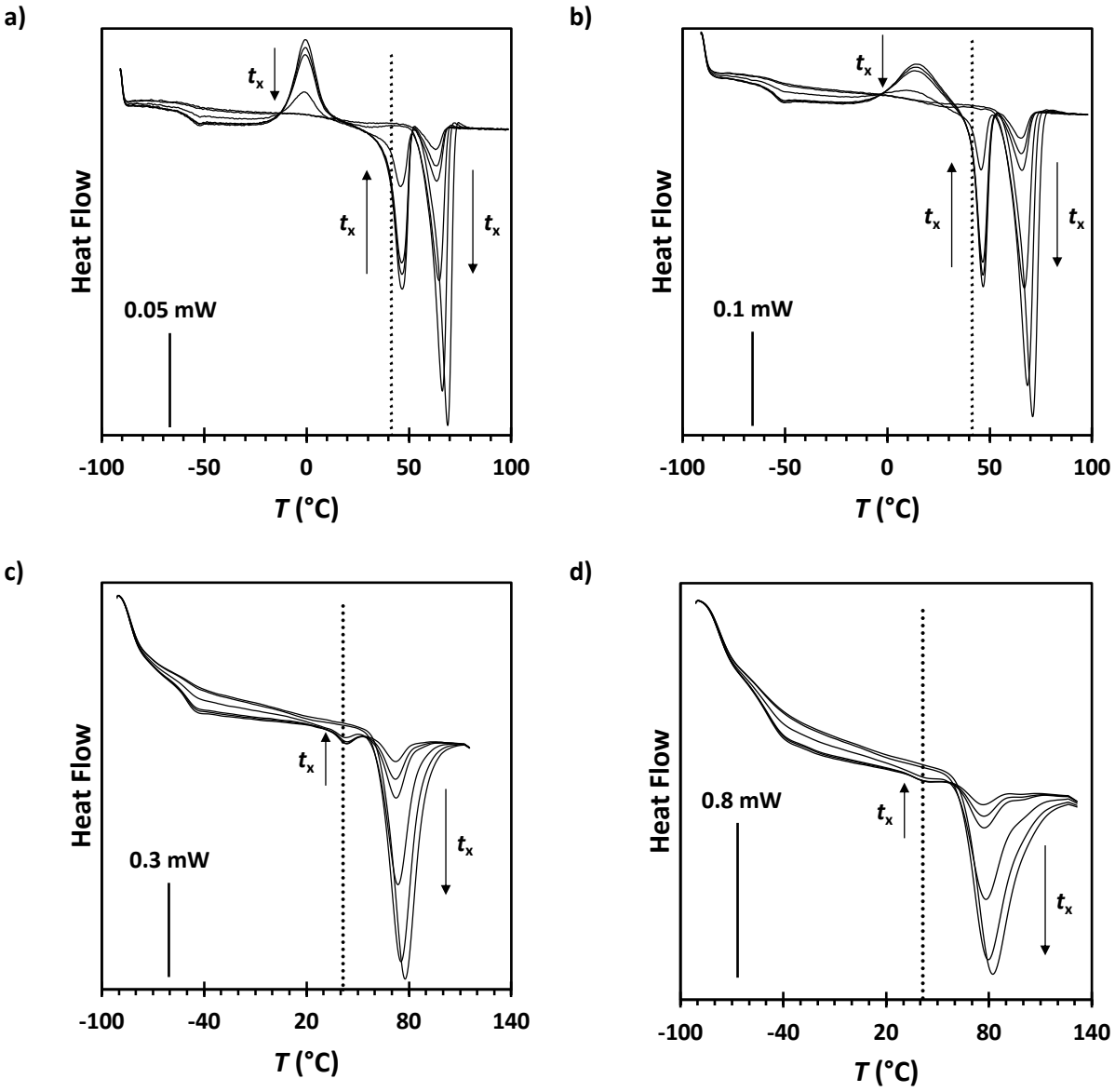

Figure 3.8: Thermograms measured with the quench method following isothermal crystallization of PCL-2 at T_x = 41.4°C vertical, dotted line) and t_x = 16 to 360 s. The data was collected with heating rates of a) $\beta = 5\times10^2$ K.s^{-1}, b) $\beta = 10^3$ K.s^{-1}, c) $\beta = 5\times10^3$ K.s^{-1}, and d) $\beta = 10^4$ K.s^{-1}. Note that endo is down.

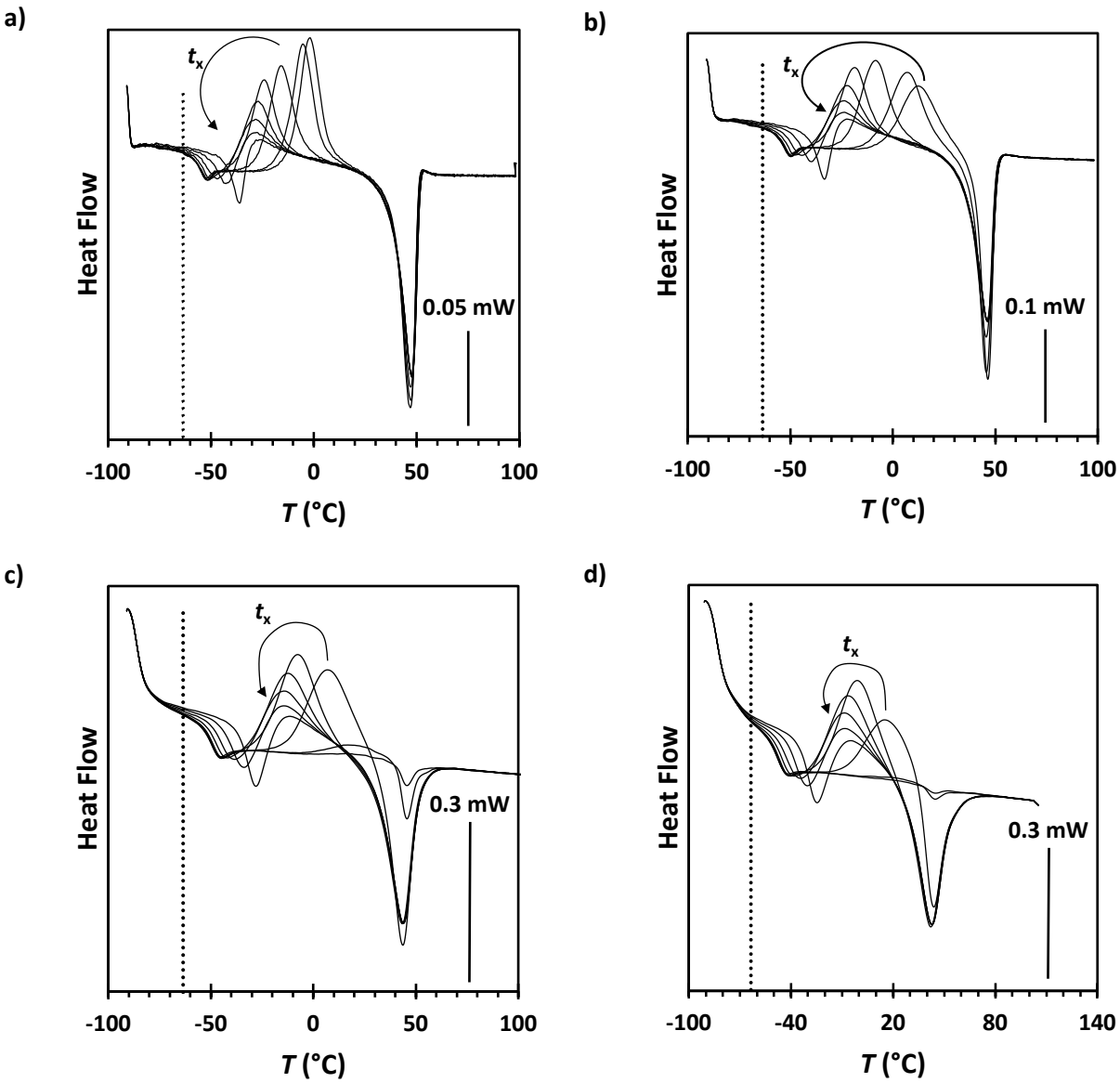

Figure 3.9: Thermograms measured with the quench method following isothermal crystallization of PCL-2 at T_x = −63.5°C (shown by the vertical, dotted line) and t_x = 0.2 to 1800 s. The data was collected with heating rates of a) $\beta = 5\times10^2$ K.s^{-1}, b) $\beta = 10^3$ K.s^{-1}, c) $\beta = 3\times10^3$ K.s^{-1}, and d) $\beta = 5\times10^3$ K.s^{-1}. Note that endo is down.

The amount of material available for cold crystallization depends on the extent of the preceding isothermal crystallization at high crystallization temperatures (Fig. 3.8). The amorphous phase is still quite mobile when the degree of crystallinity is low (i.e. short crystallization times) because there are few crystallites to inhibit long-range motion of chains, resulting in a larger degree of cold crystallization. Eventually a minimum degree of crystallinity is reached that inhibits cold crystallization due to

immobilization of the amorphous fraction. Restriction of the amorphous phase is also apparent from the increase in the glass transition temperature following longer isothermal crystallization times. The cold crystallization peak temperatures are independent of the previous thermal history for crystallization at high temperatures, but higher heating rates shift the cold crystallization exotherms to higher temperatures because there is less time for the process to occur during heating. No exotherm is visible for heating rates $\beta \geq 3\times10^3$ K.s^{-1}, but a melting endotherm corresponding to material formed by cold crystallization is still discernible (Fig. 3.8c,d). This indicates that some degree of cold crystallization still occurs even when heating at rates up to $\beta = 10^4$ K.s^{-1}.

The cold recrystallization peak temperatures following isothermal crystallization at low temperatures display a marked dependence on the prior thermal treatment and, to some extent, the heating rate (Fig. 3.9). Increasing isothermal crystallization time first leads to a decrease in the cold recrystallization peak temperatures followed by an after long isothermal crystallization times. This fundamental difference between the cold recrystallization and cold crystallization behaviors following isothermal crystallization at low vs. high temperatures can be attributed to the relative positions of the exothermic peak and the endothermic peak corresponding to melting of isothermally formed crystals. Isothermal crystallization at low temperatures results in melting at temperatures below which cold crystallization occurs, leaving behind semi-ordered chains, which act as nuclei for cold recrystallization. Increasing crystallization time leads to more residual order following melting, so cold recrystallization shifts to lower temperatures. Very long crystallization times give rise to crystals that melt at considerably higher temperatures, causing the eventual increase in cold recrystallization peak temperatures. In contrast, the cold crystallization peak temperature after isothermal crystallization at high temperatures does not shift with increasing crystallization time because the melting of isothermally formed crystals occurs at temperatures above cold crystallization. For low heating rates (Fig. 9a,b), the amount of material that undergoes cold recrystallization decreases slightly with increasing isothermal crystallization time

based on a small decrease in the melting temperature of material formed by cold recrystallization, but the effects are indiscernible for high heating rates (Fig. 3.9c,d). A large degree of cold recrystallization is apparent at heating rates up to $\beta = 5\times10^3$ K.s^{-1}, most likely due to the presence of semi-ordered material following melting of the isothermally formed crystallites.

In all cases, the material formed by cold crystallization and cold recrystallization exhibit identical melting temperatures that are independent of the previous thermal treatment. However, increasing the heating rate leads to slightly lower melting temperatures with a total variation of ca. 4°C for $\beta = 5\times10^2$ to 10^4 K.s^{-1}. The crystalline structures formed during heating from below the glass transition temperature are unstable, so higher heating rates suppress stabilization during heating and result in lower melting temperatures. In general, these observations agree with findings by Zhuravlev et al.[9] regarding the isothermal crystallization of PCL at low and high crystallization temperatures.

The melting temperatures measured by the two procedures were analyzed as a function of heating rate according to Eqn. (3.7). An illustrative data set from PCL-1 is shown in Figure 3.10 for crystallization at T_x = 34.1°C and 720 s. A systematic difference between the two experimental approaches is apparent upon visual inspection of the data in Fig. 3.10a,b whereby the melting temperatures obtained with the direct heating method are higher than those obtained with the quench approach. The difference is negligible for heating rates less than 10^3 K.s^{-1}, and the difference grows with increasing heating rate to ca. 2°C at the maximum heating rate of 10^4 K.s^{-1}. This trend is observed for all crystallization temperatures and times that were investigated. The data for PCL-2 shows a slightly larger difference in melting temperatures that approaches ca. 4°C at 10^4 K.s^{-1}. The overlap between the instrumental response and melting endotherms increases with increasing heating rate above 10^3 K.s^{-1}, so it is possible that the baseline interpolation does not fully capture the instrument's transient response. The variance of the fits according to Eqn. (3.7) is shown as a function of the melting kinetic exponent in Fig. 3.10c. The two curves are nearly superimposable by shifting the data along the ordinate.

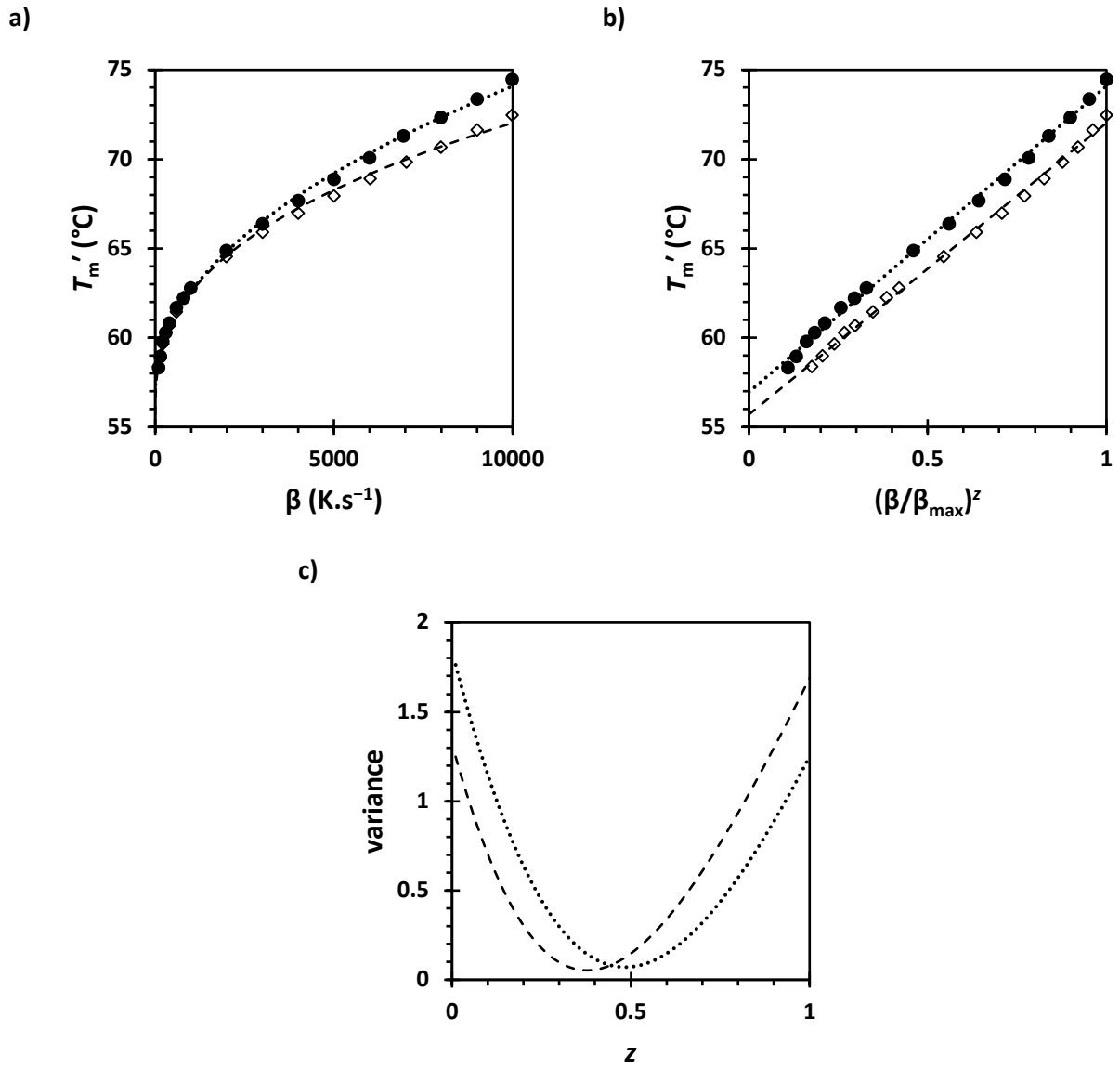

Figure 3.10: a) Relationship between the melting temperature, T'_m, and the heating rate, β, following isothermal crystallization at T_x = 34.1°C for t_x = 720 s for the direct heating (●) and quench (◇) procedures. The minimum variance fits are shown for the direct heating data with z = 0.48 (……) and the quench data with z = 0.38 (_ _ _ _ .). b) Linearized plots of the $T'_m(\beta)$ data using the respective minimum variance values of z. c) Relationship between variance and melting kinetic exponent, z for the direct heating data (……) and the quench data (_ _ _ _ .).

Figure 3.11 shows the melting kinetics exponent that minimized the variance of Eqn. (3.7) as a function of the base-10 logarithm of crystallization time for the two different experimental methods. Melting of low crystallinity samples results in higher scatter in the measured melting temperatures and consequently higher error in the melting kinetics exponent. Some crystallization times corresponding to

low crystallinity even show values higher than 0.5, the limit for melting without superheating, but this is not physically meaningful and can be attributed to random error. There does not appear to be a correlation between crystallization time and the melting kinetics exponent at any of the crystallization temperatures, but longer crystallization times do appear to yield more reliable estimates of the parameter. The quench method yields an average z = 0.38 ± 0.06 for the high crystallization temperatures and z = 0.38 ± 0.12 for the low crystallization temperatures, and the direct heating method yields an average z = 0.49 ± 0.12. The limit of z = 0.5 means that the melting rate coefficient depends linearly on superheating, and the non-linear dependence of the melting rate coefficient on superheating becomes stronger as z decreases (Eqns. (3.1) and (3.6)).[4, 62-64] The difference in the average melting kinetics exponents between the two methods may be attributed to the systematic difference in melting temperatures for heating rates greater than 10^3 K.s^{-1} (Fig. 3.10). Note that the experiments for PCL-1 (T_x = 34.1 and 39.1°C) were conducted with 17 heating rates while the experiments for PCL-2 (all other T_x) were conducted with 7 heating rates, so the error on the fitted parameters for the former sample is lower. Also, there is generally larger error on the direct heating data from PCL-2. The quench method appears to be more reliable given the higher precision of the measurements and results. Thus, we propose that a constant value of z = 0.38 should be used to analyze the melting kinetics of poly(ε-caprolactone) for all crystallization temperatures and times since this corresponds to the average value that minimized the variance of Eqn. (3.7) (Figs. 3.10 and 3.11a,b). Furthermore, the quench method should be used preferentially for this polymer since it results in more precise measurements and gives access to a larger range of isothermal crystallization temperatures. We will not consider the results for A because the large uncertainty in the average, minimum-variance values precludes definite conclusions.

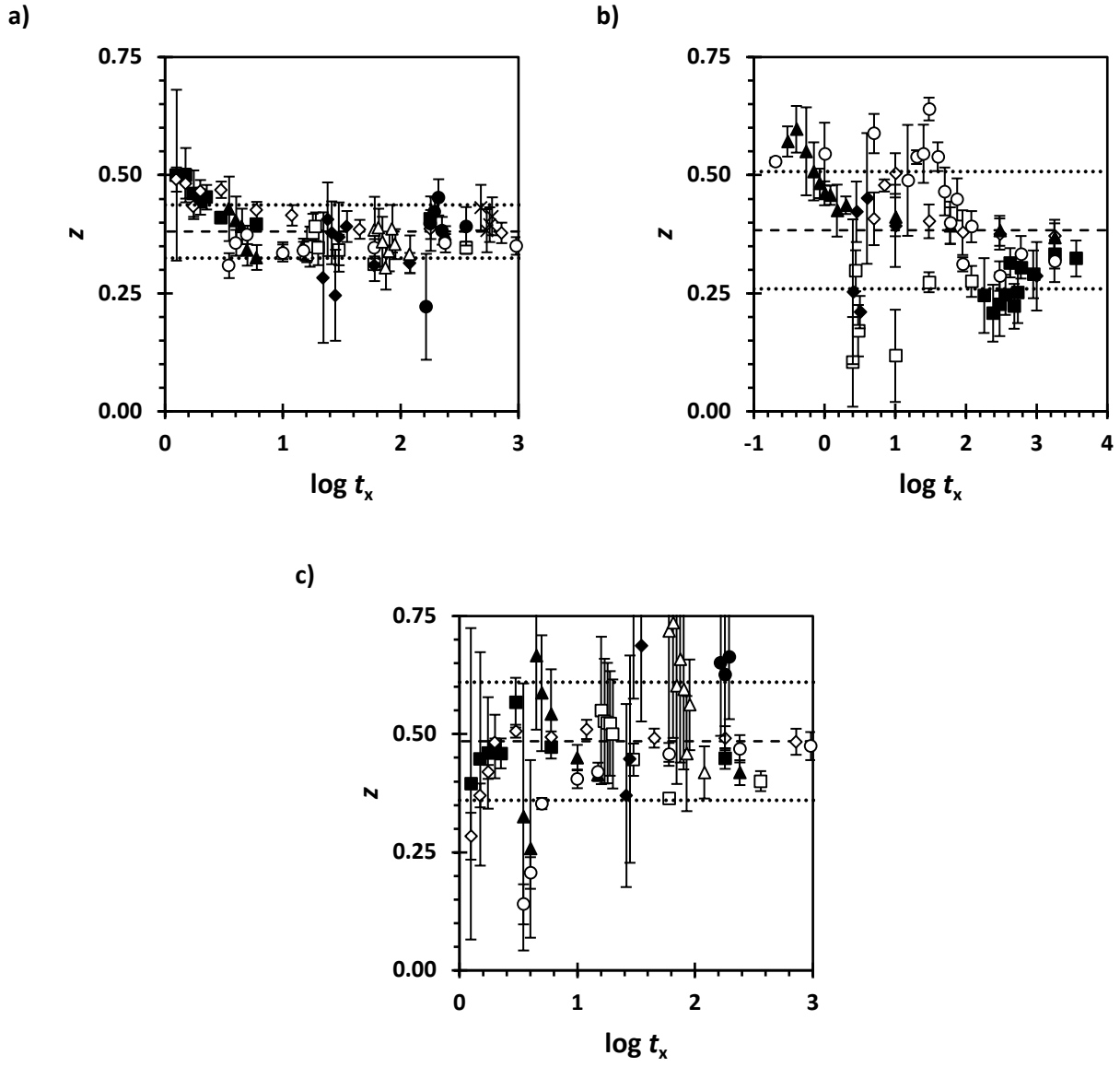

Figure 3.11: All three plots show the relationship between the melting kinetics exponent, z, that minimized the variance of Eqn. (3.7) and the base-10 logarithm of the crystallization time, $\log t_x$, and the average z and its standard deviation are represented by (_ _ _ _ .) and (.....), respectively. a) Data for the quench method at T_x = 31.4 (■), 34.1 (◇), 36.4 (▲), 39.1 (○), 41.4 (□), 43.9 (◆), 46.4 (△), 48.9 (●), and 51.4°C (╳). b) Data for the quench method at T_x = −94.1 (■), −83.8 (◇), −73.6 (▲), −63.5 (○), −43.5 (□), −23.6 (◆). c) Data for the direct heating method at T_x = 31.4 (■), 34.1 (◇), 36.4 (▲), 39.1 (○), 41.4 (□), 43.9 (◆), 46.4 (△), and 48.9°C (●).

There is mixed agreement between our results and those from the literature regarding the melting kinetics exponent and its dependence on isothermal crystallization conditions. Toda et al.[63] reported z = 0.14 for PCL measured by CDSC with heating rates ranging from 0.2 to 40 K.min^{-1}. Their

samples were annealed for very long times (ca. one week) just below the melting temperature, which may have resulted in a lower melting kinetics exponent due to thick, highly stabilized crystals. It is also possible that the relatively small range of low heating rates used in their study did not fully capture the non-linear dependence of the melting temperature on heating rate. There are contradictory reports regarding the possibility of an isothermal crystallization temperature dependence for the melting kinetics exponent. In the case of completely crystallized LPE, Toda et al.[17] reported that z ranged from ca. 0.25 to 0.5 for crystallization at high and low temperatures, respectively. A study on *i*-PP[15] also revealed an isothermal crystallization temperature dependence for the melting kinetics exponent ranging from 0.23 to 0.5 for crystallization at high and low temperatures, respectively. The case of *i*-PP is somewhat unique because *i*-PP is known to exhibit thermally controlled polymorphism,[99, 104] and the FDSC study of *i*-PP[15] cited herein attributed the observed temperature dependence of the melting kinetics exponent to melting of the α_1 and α_2 phases. A smaller, and opposite, temperature dependence was observed for PA-6[12] where the melting kinetics exponent ranged from 0.3 to 0.35 at low and high temperatures, respectively. The cause for the decreasing melting kinetics exponent with decreasing temperature was attributed to rapid lamellar thickening during crystallization, but PA-6 does not undergo lamellar thickening on a measurable time scale since it is a crystal-fixed polymer. In contrast, Furushima et al.[13] showed a constant melting kinetics exponent of 0.45 over a 80°C temperature range for the case of PEEK. Studies on poly(phenylene sulfide)[105] and PBT[11] indicated melting kinetics exponents of 0.3 and 0.5, respectively, but these findings were limited to single crystallization temperatures. The former study actually investigated crystallization and melting kinetics over a 100°C temperature range, but the results of the heating rate analysis were only detailed at a single temperature. It is generally accepted that the melting kinetics exponent depends on the sample mass and thickness, with a minimum value of z = 0.5 for thin, low mass samples (ca. 1 μm and <50 ng for FDSC) and a maximum value of z = 1 for thicker, higher mass samples.[4, 64] In the latter case,

the observed melting kinetics exponent is an apparent value that includes a contribution from the thermal lag. A similar trend is observed for CDSC data but with larger limits for sample mass and thickness.[62]

Despite the fact that the direct heating method yields higher melting temperature than the quench method, fixing the value of the melting kinetics exponent will yield zero heating melting temperatures within ca. 0.5°C. This conclusion is significant because it means that the two methods yield self-consistent results and either method could potentially be used to obtain reliable zero-heating-rate melting temperatures given *a priori* knowledge of the melting kinetics exponent. The results for determining the zero-heating-rate melting temperatures and A for both experimental methods with z = 0.38 and 0.49 are shown in Figure 3.12 for the same crystallization conditions appearing in Fig. 3.10 (T_x = 34.1°C, t_x = 1.25 to 720 s). Fixing the melting kinetics exponent reduces the standard deviation of the fitted values of the zero-heating-rate melting temperatures and A, so we assumed that the errors were equal to those obtained from the minimum variance fit from non-linear regression. The results for the two methods are indistinguishable within experimental uncertainty for a given melting kinetics exponent. Since A depends on the melting kinetics exponent (Eqn. (3.5)), fixing the value of the melting kinetics exponent also results in a constant value of A for all of the crystallization times that were investigated.

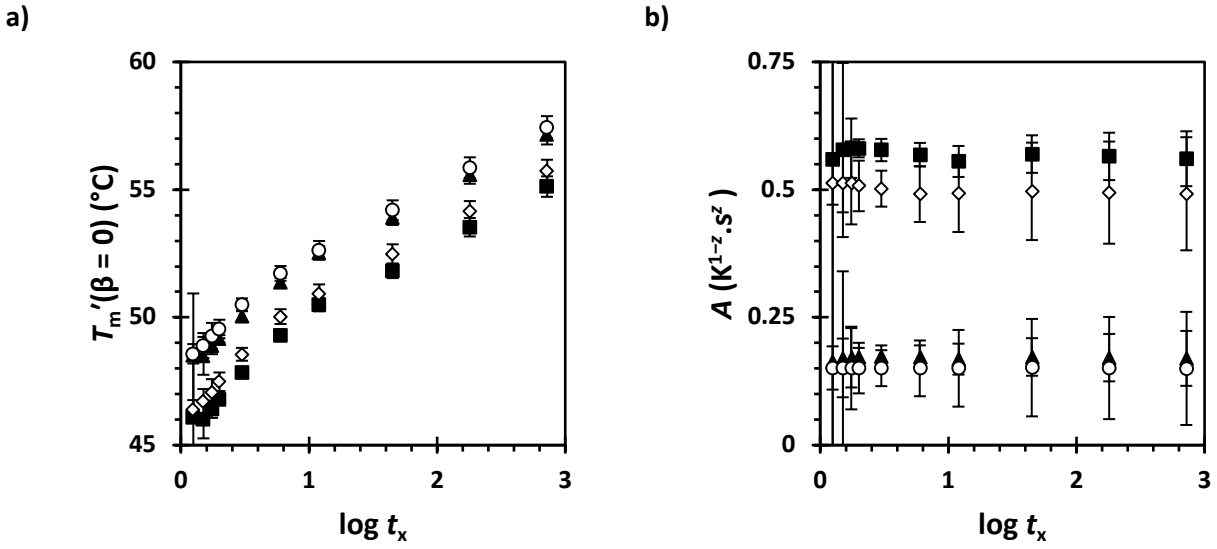

Figure 3.12: Relationship between a) the zero-heating-rate melting temperature, $T_{\mathrm{m}}'(\beta = 0)$, and the base-10 logarithm of the crystallization time, $\log t_{\mathrm{x}}$ following isothermal crystallization and b) A and the base-10 logarithm of the crystallization time, $\log t_{\mathrm{x}}$. at T_{x} = 34.1°C for t_{x} = 1.25 to 720 s. Data in both plots were collected with the: direct heating analyzed with z = 0.38 (■), quench analyzed with z = 0.38 (◇), direct heating analyzed with z = 0.49 (▲), and the quench analyzed with z = 0.49 (○). a) Error bars were determined according from the standard deviation of the non-linear regression according to Eqn. (3.7) without fixed z.

There is a short period of time following the first detectable melting endotherm where the melting temperatures stay constant, albeit with some degree of scatter. This behavior is illustrated in Figure 3.13 following isothermal crystallization at T_{x} = 39.1°C for 3.5 to 960 s. In this case, the melting temperature is relatively constant from t_{x} = 3.5 to 5 s. The magnitude of this time scale depends on the crystallization temperature such that higher crystallization temperatures correspond to longer time scales simply as a result of decreasing crystallization rate. The time window for relatively constant melting temperatures appears to be independent of the experimental method. The initial melting temperatures at each crystallization temperature and heating rate were taken as the average of the melting temperatures in the short period of time following the first detectable melting endotherm. The exact number of data points used in the average varied from two to four, depending on crystallization temperature and heating rate.

a)

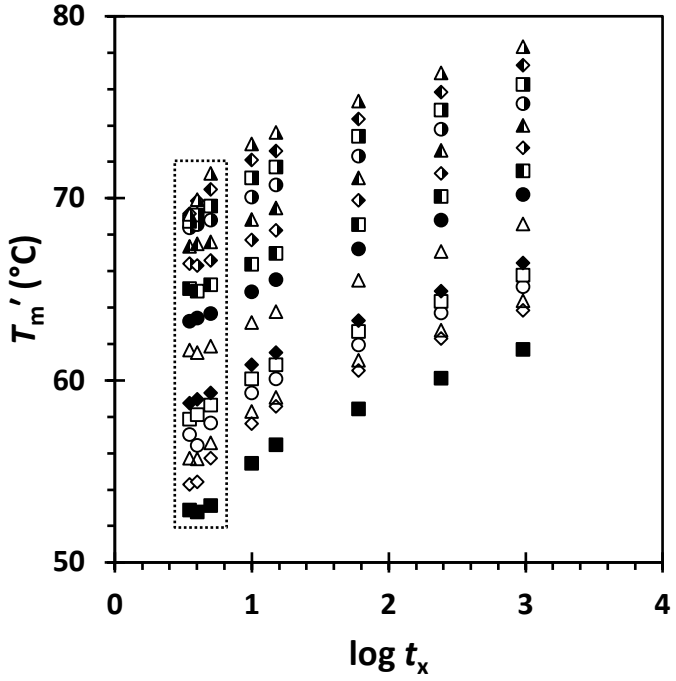

b)

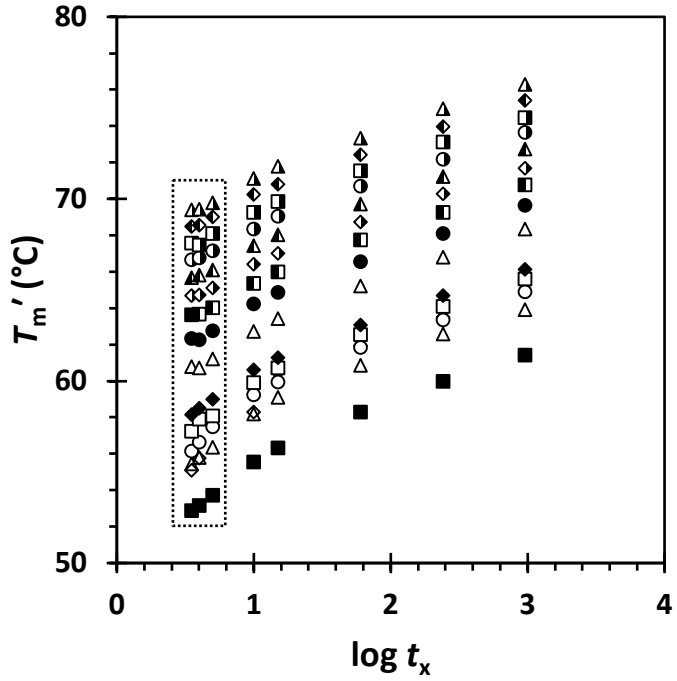

Figure 3.13: Relationship between the melting temperature, T_m', and the base-10 logarithm of crystallization time, $\log t_x$, following isothermal crystallization at T_x = 39.1°C from 3.5 to 960 s for a) the direct heating method and b) the quench method. Data markers in both plots represent β = 10^2 (■), 3×10^2 (◇), 4×10^2 (▲), 6×10^2 (○), 8×10^2 (□), 10^3 (◆), 2×10^3 (△), 3×10^3 (●), 4×10^3 (◧), 5×10^3 (◈), 6×10^3 (◭), 7×10^3 (◑), 8×10^3 (◨), 9×10^3 (◈), and 10^4 K.s^{-1} (◭). The dotted box in both plots represents the time window where the melting temperatures were averaged to obtain the initial melting temperatures.

The zero-heating-rate initial melting temperatures were determined by analyzing the initial melting temperatures as a function of heating rate according to Eqn. (3.7), as previously described. Figure 3.14 shows both the fixed heating rate and the zero-heating-rate initial melting temperatures as a function of crystallization temperature for the quench method. The initial melting temperature data was extrapolated to zero-heating-rate using melting kinetics exponents of z = 0.25, 0.38, and 0.50. The data corresponding to z = 0.38 is of special interest because this was the average value that minimized the variance of the quench data (Figs. 3.10 and 3.11a,b). Since the zero-heating-rate melting temperatures depend strongly on the melting kinetics exponent, the values of z = 0.25 and 0.50 are also considered as extreme limits of the melting kinetics exponent to estimate the range of possible results in the subsequent analyses. Below the glass transition temperature (T_g = −63°C), the initial melting temperatures are nearly invariant with respect to the crystallization temperature over a range spanning ca. 30°C. This behavior is true of initial melting temperatures at both fixed heating rate and zero-heating-rate. Above the glass transition temperature, the fixed heating rate initial melting temperatures as a function of crystallization temperature diverge from the line $T_m' = T_x$. The fixed heating rate initial melting temperatures are shifted above the crystallization temperatures by ca. 15 to 30°C for heating rates ranging from 5×10^2 to 5×10^3 K.s^{-1} in the low crystallization temperature range, and they are shifted above the crystallization temperatures by ca. 20 to 30°C for heating rates ranging from 5×10^2 to 10^4 K.s^{-1} in the high crystallization temperature range. The zero-heating-rate initial melting temperatures for all three values of the melting kinetics exponent are essentially parallel to the line $T_m' = T_x$ at low crystallization temperatures that are above the glass transition. With respect to the line $T_m' = T_x$, the data for z = 0.25 lie ca. 5°C below the line, the data for z = 0.38 lie approximately on the line, and the data for z = 0.50 lie ca. 5°C above the line. The results for the z = 0.25 data in this temperature range obviously do not have any physical meaning, and they indicate that the melting kinetics exponent cannot be equal to 0.25 in this crystallization temperature range. Furthermore, these results suggest that the melting kinetics exponent z = 0.25 is not appropriate

at high crystallization temperatures because the melting kinetics exponent appears to be independent of crystallization temperature (Fig. 3.11). At high crystallization temperatures, the zero-heating-rate initial melting temperatures for z = 0.38 and 0.50 are essentially parallel to the line $T_{\mathrm{m}}' = T_{\mathrm{x}}$, while the data for z = 0.25 shows signs of convergence with the line $T_{\mathrm{m}}' = T_{\mathrm{x}}$. The two horizontal lines, spanning ca. 4°C, in Fig. 3.14 indicate the lower and upper limits of the melting temperatures corresponding to material formed by cold crystallization and cold recrystallization.

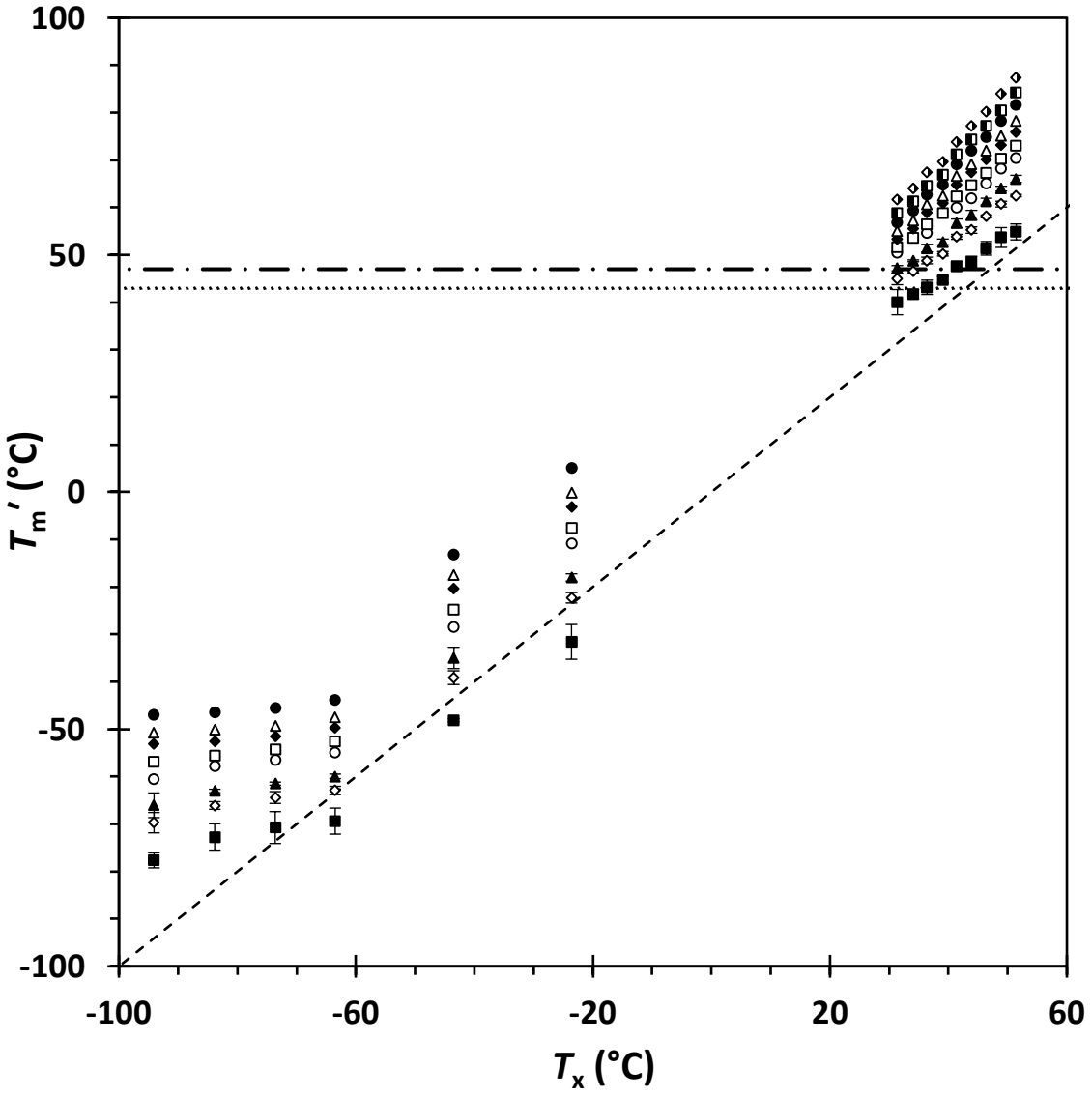

Figure 3.14: Relationship between the initial melting temperatures, T_m', and the crystallization temperature, T_x, for zero-heating-rate values with z = 0.25 (■), z = 0.38 (◇), and z = 0.50 (▲) in addition to fixed heating rate values with β = 5×10^2 (○), 10^3 (□), 2×10^3 (◆), 3×10^3 (△), 5×10^3 (●), 7×10^3 (◧), and 10^4 K.s^{-1} (◆). The lines represent $T_m' = T_x$ (_ _ _ _ .) and the lower (.....) and upper (__ . __ .) limits of the melting temperatures of material formed by cold crystallization and cold recrystallization.

Our data for crystallization in the high temperature range qualitatively agrees with results from Zhuravlev et al.[9] The authors showed that the melting temperature as a function of crystallization temperature was parallel to the line $T_m' = T_x$ and shifted upwards by 40°C for the entirety of the same range of crystallization temperatures investigated here. In contrast to the present study, their melting

data was measured at a single heating rate of 10^3 K.s^{-1} for annealed samples. The authors investigated crystallization times as long as 24 hr, but they did not report the crystallization times corresponding to the reported melting temperatures. The melting temperatures following isothermal crystallization at T_x = 39.1°C (Fig. 3.13) increase by ca. 10°C for increasing crystallization times from 3.5 to 960 s (0.06 to 16 min) when melted with β = 10^3 K.s^{-1}, and the melting temperature following crystallization for 960 s is shifted above the crystallization temperature by 17°C. A linear extrapolation of our melting temperature data measured with β = 10^3 K.s^{-1} in Fig. 3.13 to $\log 24$ hr yields T_m' = 72°C, which is 33°C greater than the crystallization temperature. A thorough discussion of the data in Fig. 3.14 and its implications for determining the equilibrium melting temperature of PCL with the Hoffman-Weeks method will follow in subsequent sections.

3.4.3 Gibbs-Thomson analysis to determine the equilibrium melting temperature

Only the high crystallization temperatures from the FDSC study that lie within the range of Sheth's lamellar thickness data[44] (Fig. 3.3) will be considered in the subsequent analysis ($T_x \geq$ 36.4°C). The melting temperature is plotted against the inverse lamellar thickness for zero-heating-rate initial melting temperatures obtained using z = 0.25, 0.38, and 0.50 (Eqn. (3.7)) in Figure 3.15, and the initial melting temperatures at fixed heating rates are plotted similarly in Figure 3.16. The equilibrium melting temperature and equilibrium fold surface free energy upon melting were determined for each data set according to the Gibbs-Thomson relation (Eqn. (3.15)). These results are summarized in Table 3.3. The equilibrium melting temperature determined with z = 0.38 (T_m^{GT} = 103.4 ± 2.3°C) is deemed the most reliable value since it corresponds to the average, minimum-variance melting kinetics exponent for the quench method. Toda et al.[17] reported the equilibrium melting temperature determination of LPE by correlating melting temperatures obtained via FDSC with lamellar thicknesses obtained via SAXS. They demonstrated good agreement between their value and accepted values from the literature. However, their analysis was conducted on completely crystallized samples of LPE, which are known to thicken during

crystallization from the melt. This approach should be more reliable in the case of PCL because it is a crystal-fixed polymer that does not undergo isothermal lamellar thickening.

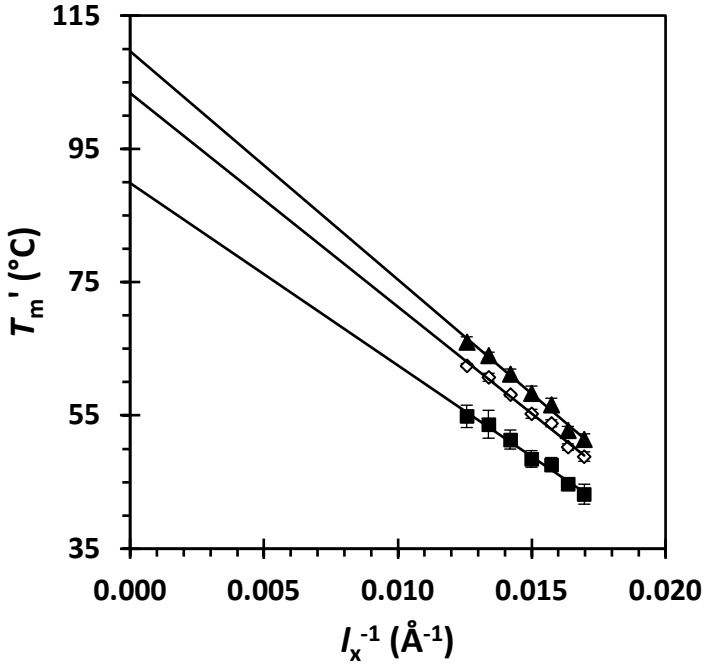

Figure 3.15: Relationship between the zero-heating-rate initial melting temperature, T_m', and inverse lamellar thickness, l_x^{-1}, for zero-heating-rate melting temperatures determined with z = 0.25 (■), z = 0.38 (◇), and z = 0.50 (▲). The lines are linear fits according to the Gibbs-Thomson equation (Eqn. (3.15)).

a)

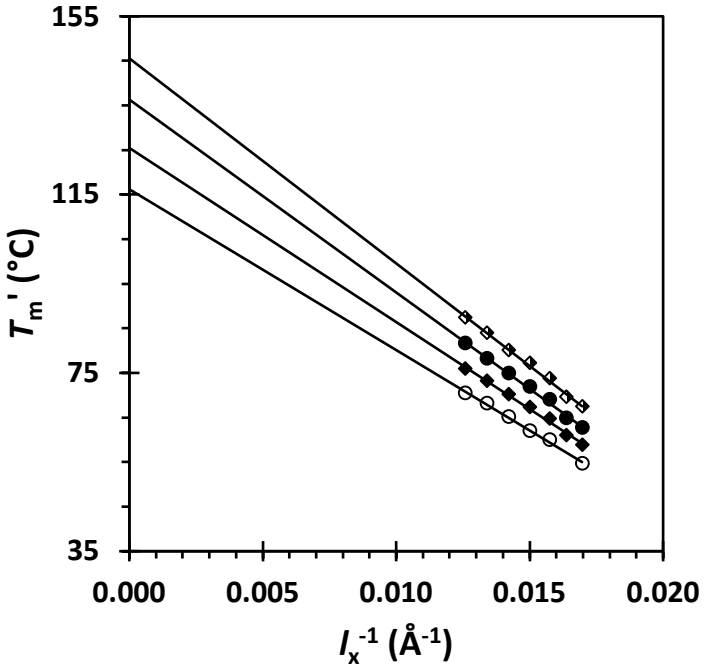

b)

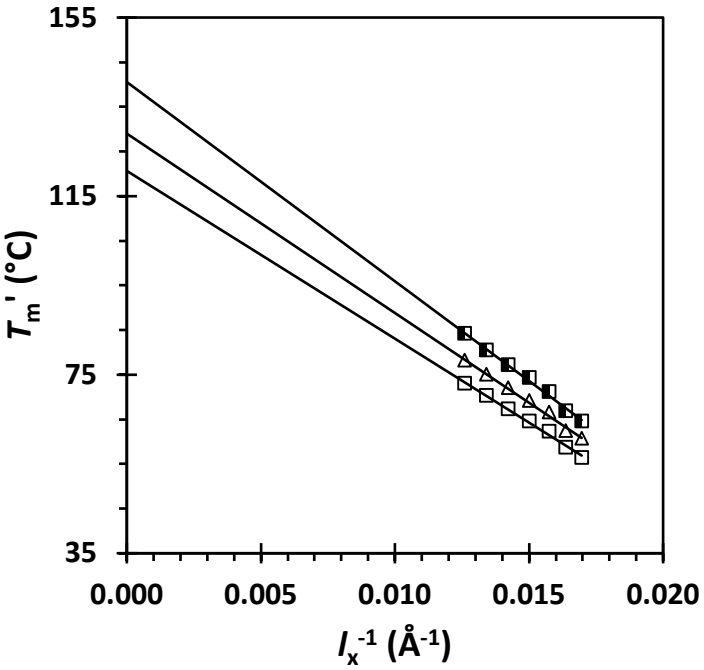

Figure 3.16: Relationship between the fixed heating rate initial melting temperature, T_m', and inverse lamellar thickness, l_x^{-1}, for melting temperatures measured with a) β = 5×10^2 (○), 2×10^3 (◆), 5×10^3 (●), and 10^4 K.s^{-1} (◈) and b) β = 10^3 (□), 3×10^3 (△), 7×10^3 K.s^{-1} (◧). The lines in both plots are linear fits according to the Gibbs-Thomson equation (Eqn. (3.15)).

Table 3.3: Values of the equilibrium melting temperature, T_m^{GT}, and equilibrium fold surface of free energy upon melting, σ_{em}, determined with the Gibbs-Thomson method using zero-heating-rate initial melting temperatures and fixed heating rate initial melting temperatures.

β (K.s^{-1})	T_m^{GT} (°C)[a]	σ_{em} (mJ.m^2)[a]	T_m (°C)[b]	σ_{em} (mJ.m^2)[b]
0, z = 0.25	89.9 ± 2.2	55.8 ± 3.1	89.0 ± 1.8	56.2 ± 1.1
0, z = 0.38	103.4 ± 2.3	63.0 ± 3.0	102.2 ± 0.7	62.2 ± 0.7
0, z = 0.50	109.6 ± 2.4	66.2 ± 3.2	108.3 ± 0.5	65.0 ± 0.6
5×10^2	116.2 ± 1.7	68.6 ± 2.3	–	–
10^3	120.6 ± 1.9	70.6 ± 2.4	–	–
2×10^3	125.5 ± 2.1	72.5 ± 2.7	–	–
3×10^3	129.0 ± 2.2	74.0 ± 2.7	–	–
5×10^3	136.3 ± 2.1	78.2 ± 2.6	–	–
7×10^3	140.6 ± 2.3	79.8 ± 2.8	–	–
10^4	145.6 ± 2.1	81.3 ± 2.5	–	–

[a]Values determined according to the Gibbs-Thomson method using Eqn. (3.15) (Figs. 3.15 and 3.16). [b]Fixed heating rate T_m^{GT} values were extrapolated to zero-heating-rate according to Eqn. (3.7) (Fig. 3.17).

The equilibrium melting temperatures and fold surface free energies upon melting are plotted as a function of heating rate in Figure 3.17. Analyzing the heating rate dependence of these values reveals the same non-linearity that is observed in the melting temperature data collected with FDSC (Fig. 3.10). Any non-linearity in the observed melting temperatures as a function of heating rate would be maintained upon linear extrapolation of the data according to Eqn. (3.15). The equilibrium melting temperature could instead be determined using the power law relationship in Eqn. (3.7) with the Gibbs-Thomson results for constant heating rate (Fig. 3.17a). Marand and Hoffman[106] employed a similar approach to determine the equilibrium melting temperature of α-phase poly(pivalolactone) with data collected via CDSC at high heating rates. However, the non-linear dependence of melting temperature on heating rate due to melting kinetics had not yet been proposed, so they performed a linear extrapolation from the highest heating rate data. The results for the two different approaches are summarized in Table 3.3. The values for the two different approaches are all within experimental error of each other for a given set of melting data with the exception of the equilibrium fold surface free energy upon melting for z = 0.50. Performing a heating rate analysis on the fixed heating rate Gibbs-Thomson equilibrium melting temperatures leads

to a minimum variance z = 0.46 ± 0.06 and $T_m(\beta = 0)$ = 106.5 ± 2.7°C. These values are within experimental error of the average z = 0.38 ± 0.06 obtained from the isothermal crystallization experiments conducted with the quench method and the equilibrium melting temperature obtained with z = 0.38 (Table 3.3). While the equilibrium fold surface free energies upon melting appear to exhibit a similar non-linear dependence on heating rate (Fig. 3.17c), no physical reason can be given to justify using Eqn. (3.7) to analyze the data. The equilibrium melting temperature of polymer crystals should be higher with increasing rates simply as a result of melting kinetics. However, the fold surfaces destabilize the crystalline lamellae, so a higher fold surface free energy means the lamellae are less stable and therefore should melt at a lower temperature. Despite this, the fold surface free energy increases with increasing heating rate while the melting temperatures are also increasing.

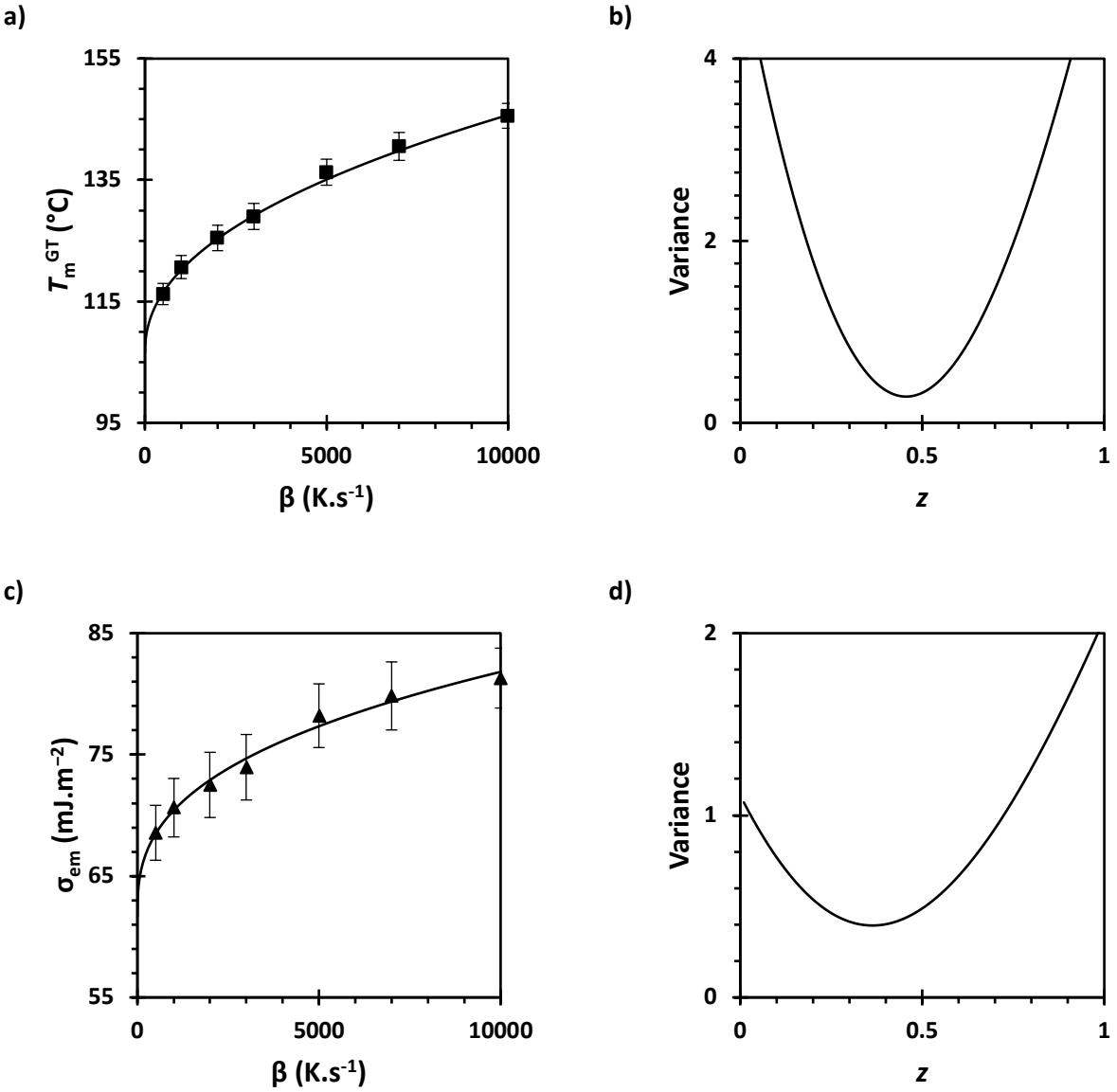

Figure 3.17: a) Relationship between the equilibrium melting temperature, $T_{\mathrm{m}}^{\mathrm{GT}}$, and the heating rate, β. The line represents the minimum variance fit with z = 0.46. b) Relationship between the variance and z for the non-linear least squares regression on $T_{\mathrm{m}}^{\mathrm{GT}}(\beta)$. c) Relationship between the equilibrium fold surface free energy upon melting, σ_{em}, and the heating rate, β. The line represents the minimum variance fit with z = 0.36. d) Relationship between the variance and z for the non-linear least squares regression on $\sigma_{\mathrm{em}}(\beta)$.

The equilibrium melting temperatures reported here depend strongly on the choice of melting kinetics exponent used to determine the initial zero-heating-rate melting temperatures. The $T_{\mathrm{m}}^{\mathrm{GT}}$ values range from 89.9 to 109.6°C for z values ranging from 0.25 to 0.50, respectively, and $T_{\mathrm{m}}^{\mathrm{GT}}$ = 103.4 ± 2.3°C determined with z = 0.38, is deemed the most reliable value (Table 3.3). A comprehensive list detailing

the published equilibrium melting temperatures of PCL is given in Table 3.1. The minimum value of T_m^{GT} = 89.9 ± 2.2°C, corresponding to z = 0.25, is within experimental error of the value reported by Sheth[44] for the same sample and for a fractionated sample with M_n = 40 kg.mol^{-1}, both determined by extrapolation to zero spherulite growth rate. Nuñez et al.[36] reported a value ca. 6°C lower for a polydisperse sample with M_n = 40 kg.mol^{-1} that was obtained using the non-linear Hoffman-Weeks analysis, but they assumed a value of C_2 and did not employ the MX method. Furthermore, this value is 7°C lower than the value reported by Strobl et al.[28, 48, 50] for a polydisperse sample with M_n = 42.5 kg.mol^{-1}, determined using the Gibbs-Thomson method. The equilibrium melting temperatures corresponding to z = 0.38 and 0.50 are greater than any previous reports. The closest literature value was published by Strobl,[50] but it is 4 and 10°C lower than the present results with z = 0.38 and 0.50, respectively.

The equilibrium fold surface free energies upon melting determined with the Gibbs-Thomson method (Eqn. (3.15)) are also affected by the choice of the melting kinetics exponent, with values ranging from σ_{em} = 55.8 to 66.2 mJ.m^{-2} for z values ranging from 0.25 to 0.50, respectively (Table 3.3). The equilibrium fold surface free energy upon melting determined with z = 0.38 is within error of those reported by Arnold[25] and Shin[45] for Gibbs-Thomson analyses and Sheth[44] for zero growth rate extrapolation. The value determined with z = 0.50 is within error of Strobl's results[50] using the Gibbs-Thomson method for melting of stabilized crystallites, but the equilibrium melting temperature determined with z = 0.50 is 10°C larger than the value determined by Strobl. Out of these four studies, only Strobl's sample was of comparable molecular weight to the sample from this study.

Although new results should always be considered in the context of previous reports, caution must be exercised when comparing the present results to any from the literature (Table 3.1). Extrapolation of the spherulite growth rate to the zero-growth temperature is influenced by the choice of the kinetic model. None of the equilibrium melting temperatures determined by zero growth rate extrapolation accounted for the undercooling dependence of the kinetic fold surface free energy upon

crystallization.[25, 28, 33, 50] This may not be necessary for crystallization at small undercoolings, but our data suggests that PCL crystallization is commonly analyzed at $\Delta T \approx 50$ to 70°C where the kinetic fold surface free energy upon crystallization would have a significant undercooling dependence. It is known that the linear Hoffman-Weeks analysis underestimates the equilibrium melting temperature since it neglects the temperature dependence of lamellar thickening and the contribution of C_2 to the initial lamellar thickness.[58] As such, the present results should indeed be higher than any previous linear Hoffman-Weeks analyses.[25-27, 29, 30, 32, 34-42, 45, 46, 53] Also, consider that no one has reported the equilibrium melting temperature of PCL using melting temperatures collected with FDSC. As we showed in the subsection on isothermal crystallization, PCL displays evidence of melting-recrystallization-remelting when analyzed using CDSC. All of the previous reports cited in Table 3.1 used CDSC with heating rates less than ca. 80 K.min^{-1}, the critical heating rate for suppression of recrystallization effects. Changes in lamellar structure and stability during heating would result in erroneous correlation of the melting and crystallization temperatures. As a result, the cited linear Hoffman-Weeks[25-27, 29, 30, 32, 34-42, 45, 46, 53] and Gibbs-Thomson[25, 28, 43, 45, 48, 50, 51] analyses may be invalid.

Given the issues described herein with the published Gibbs-Thomson analyses, it is useful to consider the outcome of correlating the melting temperatures measured via FDSC with inverse lamellar thicknesses reported by others. Figure 3.18 compares the lamellar thickness as a function of crystallization temperature from the present study[44] with other literature data.[25, 28, 45, 48, 50, 51] There is lamellar thickness data from several groups measured at the crystallization and melting temperatures, where the lamellae are always thicker at the melting temperature. This is simply an experimental artifact that arises from partial melting and recrystallization during slow heating to measure the melting temperature with CDSC, as we have already discussed. The lamellar thicknesses measured by our group[44] are ca. 10 to 60% smaller than those measured by other groups, depending on the isothermal crystallization temperature. The lamellar thicknesses from Sheth[44] were obtained by fitting the scattering profiles according to the

Hosemann-Bagchi model, while others utilized either an interface distribution function[33, 45, 50, 81] or the Bragg relation.[25, 51] Sheth also fit the scattering profiles with both a one-dimensional correlation function and an interface distribution function, but the lamellar thicknesses were ca. 10% smaller than those determined using the Hosemann-Bagchi model.[44] Crystal thickening should not affect the lamellar thickness results following isothermal crystallization because PCL is crystal-fixed[107] and does not undergo isothermal lamellar thickening.[81] Studies on moderate to high molecular weight LPE demonstrated that the average lamellar thickness is essentially independent of molecular weight while the distribution of lamellar thicknesses exhibited a complex dependence on molecular weight.[108, 109] These results suggested very different values for the most probable and average values of lamellar thickness. Simply put, there appears to be sizable, irreconcilable inconsistencies in the reported lamellar thicknesses of PCL.

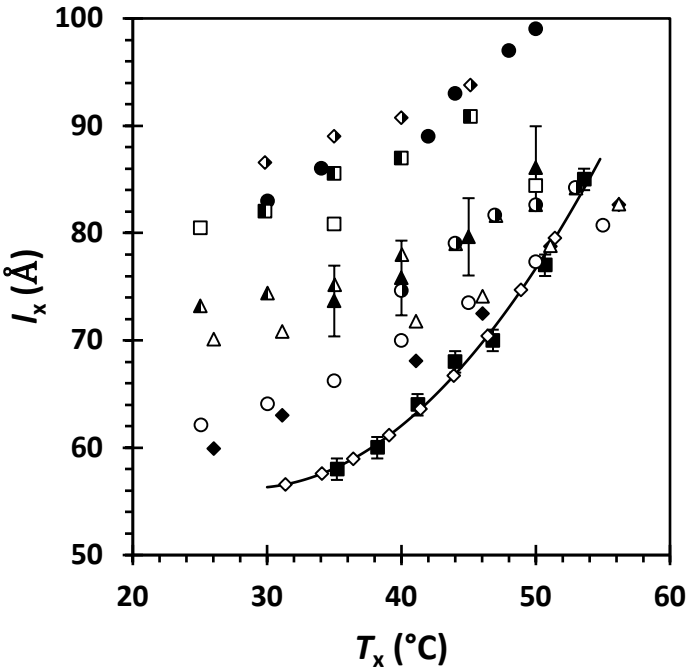

Figure 3.18: Relationship between the lamellar thickness, l_x, and the crystallization temperature, T_x, for PCL from this study and the literature. The markers correspond to data from Sheth[44] (■), interpolated values for FDSC crystallization temperatures in this study (◇, ————), Schulz et al.[81] $l_x(T_x)$ (▲), Schulz et al.[81] $T_x(l_x^{-1})$ (○), Schultz et al.[81] $T_m'(l_x^{-1})$ (□), Strobl et al.[28, 48, 50] $T_x(l_x^{-1})$ (◆), Strobl et al.[28, 48, 50] $T_m'(l_x^{-1})$ (△), Arnold[25] $l_x(T_x)$ (●), Shin et al.[45] $T_x(l_x^{-1})$ (◧), Shin et al.[45] $T_m'(l_x^{-1})$ (◈), Su et al.[51] $T_x(l_x^{-1})$ (◭), Su et al.[51] $T_m'(l_x^{-1})$ (◑). Sample characteristics can be found in Table 3.1. The solid line represents the quadratic function that was used to interpolate the data points for this study.

The lamellar thickness data from Schulz et al.,[81] Strobl et al.,[28, 48, 50] Arnold,[25] Shin et al.,[45] and Su et al.[51] (Fig. 3.18) were fit with quadratic polynomials. The lamellar thicknesses corresponding to the crystallization temperatures from our FDSC study were interpolated, similar to the approach used with Sheth's data (Fig. 3.2). Note that no lamellar thicknesses were extrapolated. Gibbs-Thomson plots are shown in Figure 3.19 with zero-heating-rate initial melting temperatures determined using z = 0.25 (Fig. 3.19a), 0.38 (Fig. 3.19b), and 0.50 (Fig. 3.19c). The equilibrium melting temperature and equilibrium fold surface free energy upon melting were determined for each data set according to the Gibbs-Thomson relation (Eqn. (3.15)), and these results are tabulated in Tables 3.4 and 3.5, respectively. The equilibrium melting temperatures obtained using lamellar thickness data from other groups are ca. 20 to 100% greater than the values obtained utilizing Sheth's data (Table 3.4). The corresponding equilibrium fold surface free energies upon melting are ca. 100 to 300% greater than our results (Table 3.5). The huge variation in results depending on the choice of lamellar thickness data is alarming, to say the least, and it calls into question the reliability of the data in the literature. The equilibrium melting temperature of PCL of any molar mass could not be larger than the limiting value obtained for LPE of infinite molar mass ($T_{\mathrm{m}}^{\mathrm{LPE}}$ = 141.3°C).[93] The C–O–C linkage in the backbone of polylactones results in higher configurational entropy compared to the C–C–C linkages in the backbone of LPE, which leads to a higher entropy of fusion and a lower melting temperature.[110] Examination of the equilibrium melting temperatures in Table 3.4 reveals that all results for z = 0.38, the most reliable melting kinetics exponent value, are greater than the limiting equilibrium melting temperature of LPE except for the value obtained from the data of Strobl and Cho.[50] However, this value is still unrealistically large and ca. 20°C greater than our result for the equilibrium melting temperature with z = 0.38 ($T_{\mathrm{m}}^{\mathrm{GT}}$ = 103.4 ± 2.3). Furthermore, the equilibrium melting temperature is known to increase with molecular weight,[111] but the results in Table 3.4 do not show any molecular weight dependence. Considering z = 0.38, the results from Su's data[51] yielded $T_{\mathrm{m}}^{\mathrm{GT}}$ = 184.4 ± 4.5°C (M_{n} = 7.3 kg.mol^{-1}) and Shin's data[45] yielded $T_{\mathrm{m}}^{\mathrm{GT}}$ = 155.1 ± 7.3°C (M_{n} = 168 kg.mol^{-1}).

a)

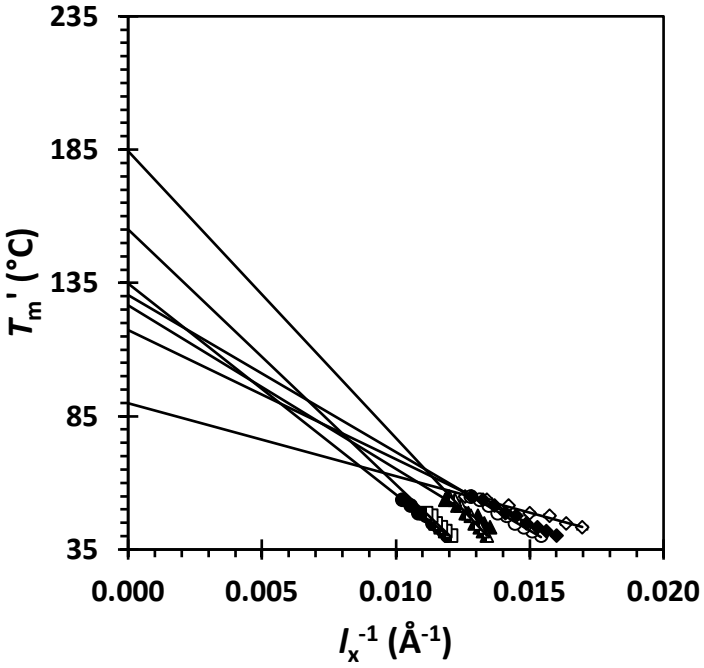
235
185
135
85
35
T_m' (°C)
0.000
0.005
0.010
0.015
0.020
I_x^{-1} (Å^{-1})

b)

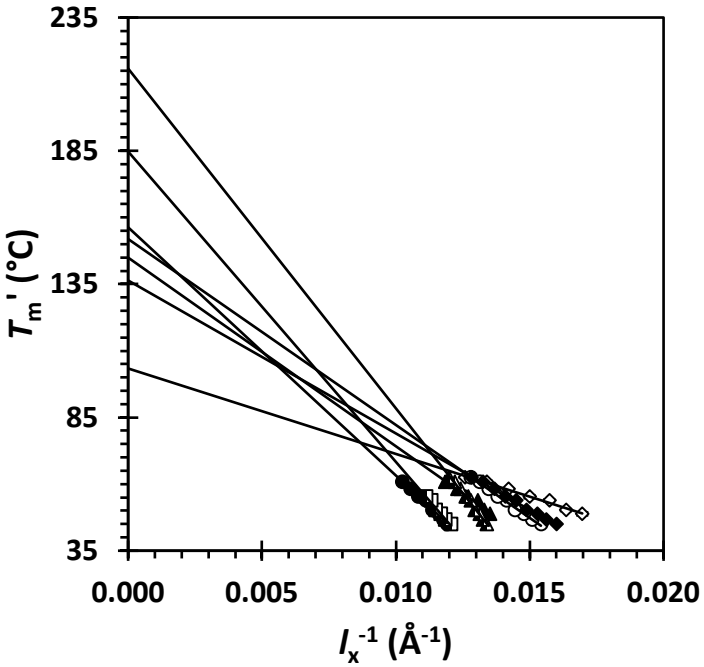
235
185
135
85
35
T_m' (°C)
0.000
0.005
0.010
0.015
0.020
I_x^{-1} (Å^{-1})

c)

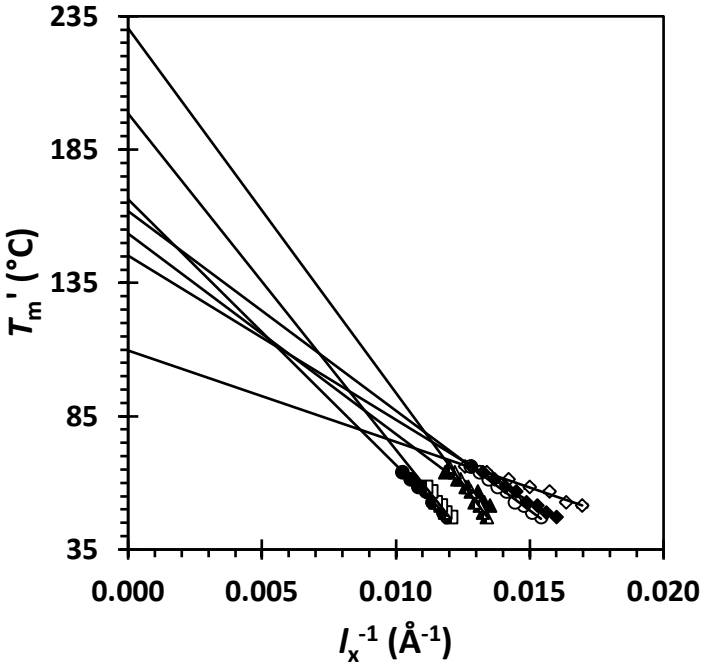

Figure 3.19: Relationship between the fixed heating rate initial melting temperature, T_{m}', and inverse lamellar thickness, l_{x}^{-1}, for a) z = 0.25, b) z = 0.38, and c) z = 0.50. The lamellar thickness data in all three plots was interpolated from the $l_{\mathrm{x}}^{-1}(T_{\mathrm{x}})$ data shown in Fig. 3.18, and the markers correspond to data from this study (◇), Schulz et al.[81] $l_{\mathrm{x}}(T_{\mathrm{x}})$ (▲), Schulz et al.[81] $T_{\mathrm{x}}(l_{\mathrm{x}}^{-1})$, Strobl et al.[28, 48, 50] $T_{\mathrm{x}}(l_{\mathrm{x}}^{-1})$ (◆), Arnold[25] $l_{\mathrm{x}}(T_{\mathrm{x}})$ (●), Shin et al.[45] $T_{\mathrm{x}}(l_{\mathrm{x}}^{-1})$ (◧), Su et al.[51] $T_{\mathrm{x}}(l_{\mathrm{x}}^{-1})$ (◭). Sample characteristics can be found in Table 3.1. The lines in all three plots are linear fits according to the Gibbs-Thomson equation (Eqn. (3.15)).

Table 3.4: Results for the equilibrium melting temperature, $T_{\mathrm{m}}^{\mathrm{GT}}$ determined using the Gibbs-Thomson method (Eqn. (3.15) and Fig. 3.19) with melting temperatures measured by FDSC and lamellar thicknesses from the literature (Fig. 3.18).

Source	M_{n} (kg.mol^{-1})	$T_{\mathrm{m}}^{\mathrm{GT}}(z = 0.25)$ (°C)	$T_{\mathrm{m}}^{\mathrm{GT}}(z = 0.38)$ (°C)	$T_{\mathrm{m}}^{\mathrm{GT}}(z = 0.50)$ (°C)
This study/Sheth[44] $l_{\mathrm{x}}(T_{\mathrm{x}})$	36	89.9 ± 2.2	103.4 ± 2.3	109.6 ± 2.4
Schulz et al.[81] $l_{\mathrm{x}}(T_{\mathrm{x}})$	65.8	126.6 ± 6.0	144.9 ± 7.1	153.5 ± 7.8
Schulz et al.[81] $T_{\mathrm{x}}(l_{\mathrm{x}}^{-1})$	65.8	130.4 ± 2.8	151.9 ± 2.9	161.9 ± 3.2
Strobl et al.[28, 48, 50] $T_{\mathrm{x}}(l_{\mathrm{x}}^{-1})$	42.5	117.3 ± 2.2	136.4 ± 2.2	145.2 ± 2.5
Arnold[25] $l_{\mathrm{x}}(T_{\mathrm{x}})$	15.0	134.8 ± 3.2	156.3 ± 3.9	166.3 ± 4.5
Shin et al.[45] $T_{\mathrm{x}}(l_{\mathrm{x}}^{-1})$	168	155.1 ± 7.3	184.7 ± 9.4	198.5 ± 11.0
Su et al.[51] $T_{\mathrm{x}}(l_{\mathrm{x}}^{-1})$	7.3	184.4 ± 4.5	215.9 ± 4.8	230.5 ± 5.3

Table 3.5: Results for the equilibrium fold surface free energy upon melting, σ_{em} determined using the Gibbs-Thomson method (Eqn. (3.15) and Fig. 3.19) with melting temperatures measured by FDSC and lamellar thicknesses from the literature (Fig. 3.18).

Source	M_n (kg.mol^{-1})	$\sigma_{em}(z = 0.25)$ (mJ.m^{-2})	$\sigma_{em}(z = 0.38)$ (mJ.m^{-2})	$\sigma_{em}(z = 0.50)$ (mJ.m^{-2})
This study/Sheth[44] $l_x(T_x)$	36	55.8 ± 3.1	63.0 ± 3.0	76.2 ± 3.2
Schulz et al.[81] $l_x(T_x)$	65.8	113.5 ± 8.9	125.2 ± 10.0	130.4 ± 10.4
Schulz et al.[81] $T_x(l_x^{-1})$	65.8	107.9 ± 3.7	121.4 ± 3.7	127.3 ± 4.0
Strobl et al.[28, 48, 50] $T_x(l_x^{-1})$	42.5	91.8 ± 2.9	103.7 ± 2.8	108.9 ± 3.1
Arnold[25] $l_x(T_x)$	15.0	143.6 ± 5.4	160.4 ± 6.2	167.7 ± 7.0
Shin et al.[45] $T_x(l_x^{-1})$	168	165.3 ± 11.2	188.1 ± 13.6	197.8 ± 15.7
Su et al.[51] $T_x(l_x^{-1})$	7.3	174.0 ± 6.0	192.8 ± 6.0	200.9 ± 6.5

3.4.4 Initial lamellar thickness as predicted by the Lauritzen-Hoffman theory

Figure 3.20 shows the initial lamellar thickness as a function of undercooling for the equilibrium melting temperatures corresponding to z = 0.25, 0.38, and 0.50. All plots can be fit with a linear function quite well. We have chosen not to conduct this analysis using the equilibrium melting temperatures obtained with the fixed heating rate data because they do not hold physical meaning here. The values of the equilibrium fold surface free energy upon crystallization and C_2 corresponding to the different equilibrium melting temperatures were determined according to Eqn. (3.13) and are shown in Table 3.6. Notice that the fold surface free energy here depends strongly on the value of the equilibrium melting temperature. The equilibrium fold surface free energy upon crystallization and C_2 corresponding to z = 0.25 (T_m^{GT} = 89.9°C) are both within experimental uncertainty of the values reported by Sheth[44] for a similar analysis of the same sample. This is also the only equilibrium fold surface free energy upon crystallization that overlaps the error bounds of the equilibrium fold surface free energy upon melting (Tables 3.3 and 3.5), and the only C_2 that is positive. The equilibrium fold surface free energies upon crystallization corresponding to z = 0.38 (T_m^{GT} = 103.4°C) and 0.50 (T_m^{GT} = 109.6°C) are 1.36 and 1.55 times bigger than the equilibrium fold surface free energies of melting, respectively. As a result, the key assumption that $\sigma_{em} = \sigma_{ec}^{o}$ from the non-linear Hoffman-Weeks analysis is not valid. We will consider the

consequences of this result in the next section. Both C_2 values corresponding to z = 0.38 and 0.50 are negative, which is clearly a non-physical result since C_2 must be positive by definition. Lamellar thinning to integral chain folding is the only instance where lamellar thinning would yield more thermodynamically stable crystals, which is not the case here because the chains are too long.[80] Since PCL is crystal-fixed,[107] it does not possess the molecular mechanism that permits chain-sliding diffusion for lamellar thickening and thinning.[81] Furthermore, C_2 is also the limiting lamellar thickness for crystallization at infinite undercooling, so the quantity cannot be negative.

Assuming $T_x = T_m^{GT}$, the values of y from Eqn. (3.13a) for all three choices of the equilibrium melting temperature were found to be negative (Table 3.6). The only reports of y in the literature are for LPE, where Hoffman et al.[70] reported y = 0.014 K^{-1}, Miller[112] found y = 0.026 K^{-1}, and Mohammadi et al.[93] determined y = 0.029 K^{-1}. The values reported herein are negative and one order of magnitude smaller. The non-linear Hoffman-Weeks and Lauritzen-Passaglia models relate y to the magnitude of stem length fluctuations during crystallization.[69, 70] Crystallization at larger undercoolings leads to a more disordered, i.e. rougher, fold surface due to kinetic trapping of crystalline stems with different lengths. Thus, y is positive by definition in order to account for increasing fold surface free energy with increasing undercooling. A negative y would imply that the fold surface becomes more ordered, or smoother, as the undercooling increases. We will show in the following subsections that these non-physical results can potentially be attributed to the assumption of a linear dependence on undercooling for the kinetic fold surface free energy upon crystallization. Additionally, we will see that LPE is a unique case because it crystallizes at much smaller undercoolings compared to PCL.

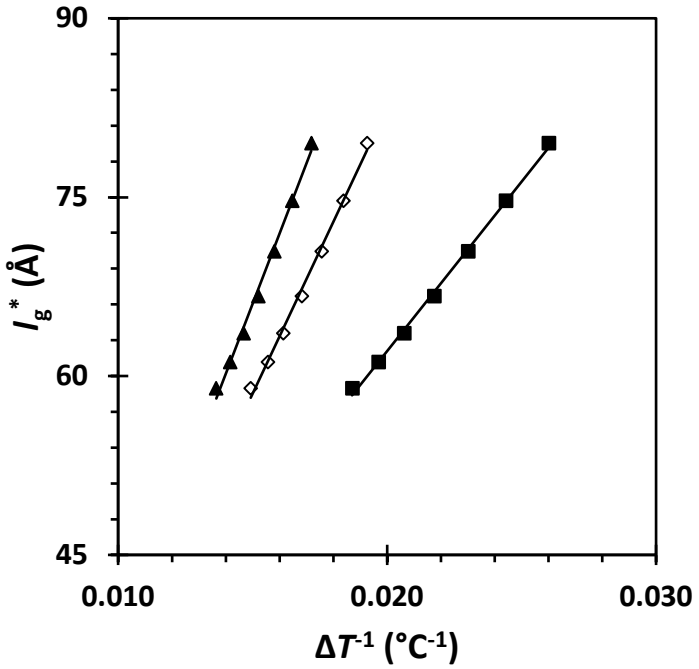

Figure 3.20: Relationship between the average lamellar thickness, l_g^*, and inverse undercooling, ΔT^{-1}, for T_m^{GT} = 89.9 (■), 103.4 (◇), and 109.6°C (▲) which correspond to zero-heating-rate melting temperature data for z = 0.25, 0.38, and 0.50, respectively. The lines are linear fits according to the Eqn. (3.13b).

Table 3.6: Values of the equilibrium fold surface free energy upon crystallization, σ_e^o, C_2, and y for the different zero-heating-rate equilibrium melting temperatures.

z	T_m^{GT} (°C)	σ_e^o (mJ.m^{-2})	C_2 (Å)	y (K^{-1})
0.25	89.9 ± 2.2	53.7 ± 2.1	10.1 ± 2.1	$-3.0\times10^{-3} \pm 8.6\times10^{-4}$
0.38	103.4 ± 2.3	85.6 ± 4.1	−5.8 ± 3.4	$-5.6\times10^{-3} \pm 8.2\times10^{-4}$
0.50	109.6 ± 2.4	102.6 ± 5.3	−13.1 ± 4.0	$-6.0\times10^{-3} \pm 7.9\times10^{-4}$

3.4.5 Non-linear Hoffman-Weeks analysis to determine the equilibrium melting temperature

For the purpose of accurate comparison, the subsequent analysis will only consider the same set of crystallization and melting temperatures that were utilized in the preceding Gibbs-Thomson analysis ($T_x \geq 36.4$°C).

A plot of initial melting temperature as a function of crystallization temperature is shown in Figure 3.21 for data with fixed heating rates and z = 0.25, 0.38, and 0.50. The nearly parallel behavior in a plot of melting temperature as a function of crystallization temperature has been observed for PCL,[9, 25] PEEK,[13,

[20, 21] PBT,[11, 22] PBS,[23] PA-6,[12] *i*-PP,[15] and PVDF.[24] The equilibrium melting temperatures and thickening coefficients determined from a linear Hoffman-Weeks (LHW) analysis are shown in Table 3.7. Linear regression on the different data sets yields slopes greater than one for all of the fixed heating rate data. Hence, linear extrapolation of these data sets would never intersect the line $T_{\mathrm{m}}' = T_{\mathrm{x}}$ at a melting temperature that is greater than the crystallization temperature. Additionally, all thickening coefficients would be less than one, implying that the lamellae actually thin. The possibility of isothermal lamellar thinning in PCL has already been addressed and ruled out in the previous subsection. The zero-heating-rate data sets with z = 0.38 and z = 0.50 yield slopes equal to 0.95 (γ = 1.05) and 1.01 (γ = 0.99), respectively. Although a linear Hoffman-Weeks extrapolation can be performed on the zero-heating-rate data with z = 0.38, the resulting equilibrium melting temperature of $T_{\mathrm{m}}^{\mathrm{LHW}}$ = 274.8°C is unreasonably high (Table 3.7). However, the resulting equilibrium melting temperature obtained for the zero-heating-rate data with z = 0.25 ($T_{\mathrm{m}}^{\mathrm{LHW}}$ = 71.4°C) lies within the ca. 25°C interval of results for other linear Hoffman-Weeks analyses from the literature (Table 3.1).[25-27, 29, 30, 32, 34-42, 45, 46, 53] As previously discussed, any analysis utilizing melting temperatures measured CDSC should be considered warily because of stabilization, annealing, or melting-recrystallization-remelting during heating with low rates. Additionally, the results of the linear Hoffman-Weeks analysis do not hold significant physical meaning because the method neglects the undercooling dependence of the kinetic fold surface free energy upon crystallization and assumes that stabilization of lamellae results solely from isothermal lamellar thickening. Since crystal-fixed polymers do not undergo lamellar thickening, the latter assumption would lead to melting at the crystallization temperature if the linear Hoffman-Weeks analysis was applicable. Obviously, this is not the case (Figs. 3.14 and 3.21).

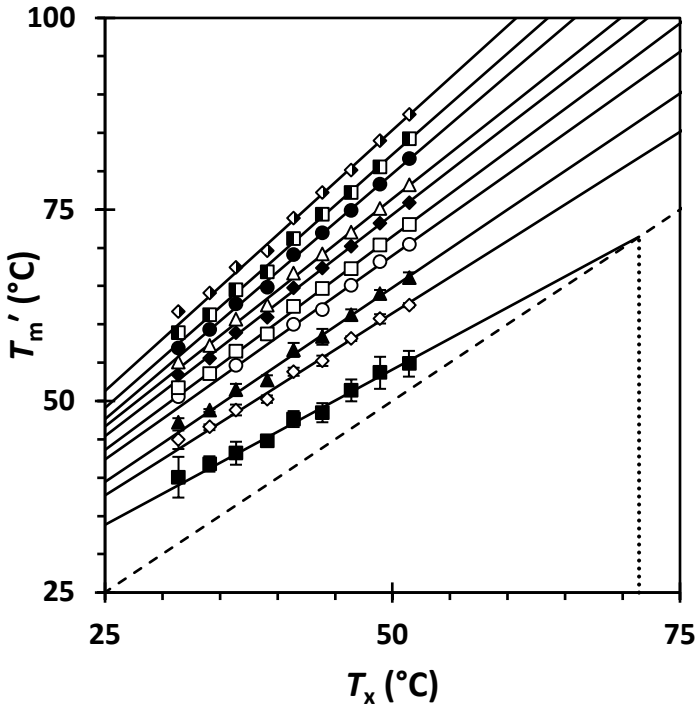

Figure 3.21: Relationship between the initial melting temperatures, T_m', and crystallization temperature, T_x, for zero-heating-rate values with z = 0.25 (■), z = 0.38 (◇), and z = 0.50 (▲) in addition to fixed heating rate values with β = 5×10^2 (○), 10^3 (□), 2×10^3 (◆), 3×10^3 (△), 5×10^3 (●), 7×10^3 (◧), and 10^4 K.s^{-1} (◆). The lines represent $T_m' = T_x$ (_ _ _ _ .) and linear fits to the data (———).

Table 3.7: Values of the equilibrium melting temperature, T_m^{LHW}, and the isothermal lamellar thickening coefficient, γ, determined with the linear Hoffman-Weeks method (Eqn. (3.18)) using zero-heating-rate initial melting temperatures. The zero heating initial melting temperatures with z = 0.50 and the fixed heating rate initial melting temperature could not be used for the linear Hoffman-Weeks analysis because linear extrapolation of these data sets diverged from the line $T_m' = T_x$.

β (K.s^{-1})	T_m^{LHW} (°C)	γ (dimensionless)
0, z = 0.25	71.4 ± 2.1	1.23 ± 0.06
0, z = 0.38	274.8 ± 3.6	1.05 ± 0.04
0, z = 0.50	–	–
5×10^2	–	–
10^3	–	–
2×10^3	–	–
3×10^3	–	–
5×10^3	–	–
7×10^3	–	–
10^4	–	–

Marand et al.[58] demonstrated that the non-linear Hoffman-Weeks equation is positively curved and the function $T'_{\mathrm{m}}(T_{\mathrm{x}})$ is tangent to the line $T'_{\mathrm{m}} = T_{\mathrm{x}}$ at the equilibrium melting temperature. Consequently, only the data set corresponding to z = 0.25 can be used in the non-linear Hoffman-Weeks analysis to obtain an equilibrium melting temperature of reasonable magnitude. This is also the only data set that satisfies the assumption that $\sigma_{\mathrm{em}} = \sigma_{\mathrm{e}}^{\mathrm{o}}$ (Tables 3.3 and 3.6). The conventional MX method was used to determine the equilibrium melting temperature and C_2 for the zero-heating-rate initial melting temperature data with z = 0.25. Figure 3.22 shows the slopes from plots of M vs. X (Eqn. (3.20)) for different choices of the equilibrium melting temperature in addition to a plot of M vs. X for $T_{\mathrm{m}}^{\mathrm{NLHW}}$ = 94.6°C which yields a slope of one. The melting temperatures are plotted as a function of crystallization temperature in Figure 3.23 according to the non-linear Hoffman-Weeks equation (Eqn. (3.19)). The values of the equilibrium melting temperature and C_2 determined using the non-linear Hoffman-Weeks analysis are summarized in Table 3.8.

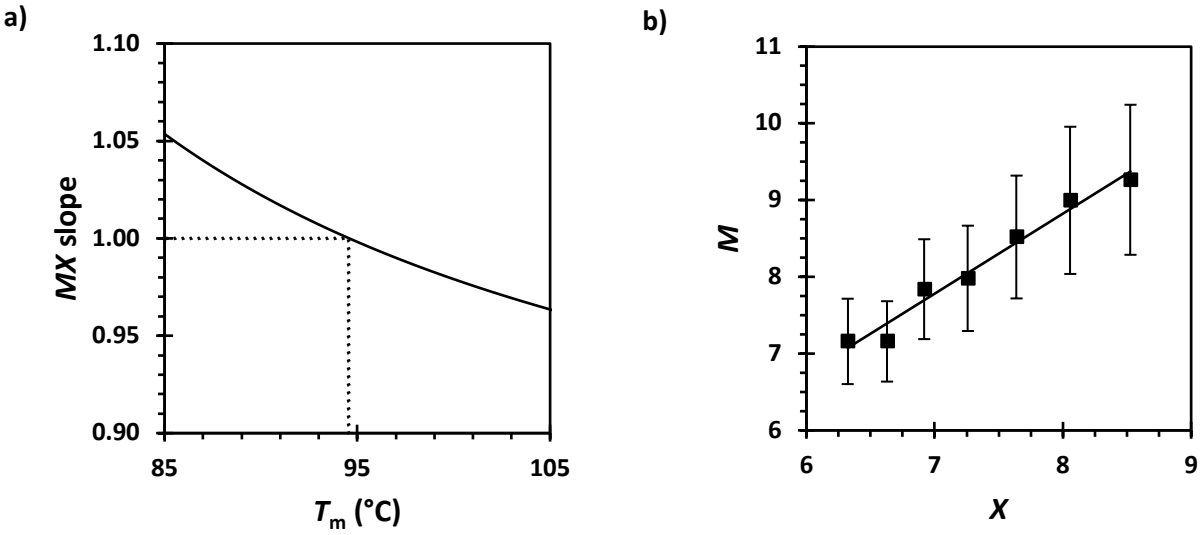

Figure 3.22: a) Relationship between the slope of the MX plot and the choice of equilibrium melting temperature, T_{m}, for zero-heating-rate initial melting temperatures determined with z = 0.25. The line represents the MX plot slope as a function of equilibrium melting temperature. b) Relationship between the reduced melting temperature, M, and the reduced crystallization temperature, X, for zero-heating-rate initial melting temperatures determined with z = 0.25. The line represents a linear fit according to the MX equation (Eqn. (3.20)) with the choice of equilibrium melting temperature that yields a slope equal to unity. The error bars are propagated from the extrapolated zero-heating-rates and the equilibrium melting temperature.

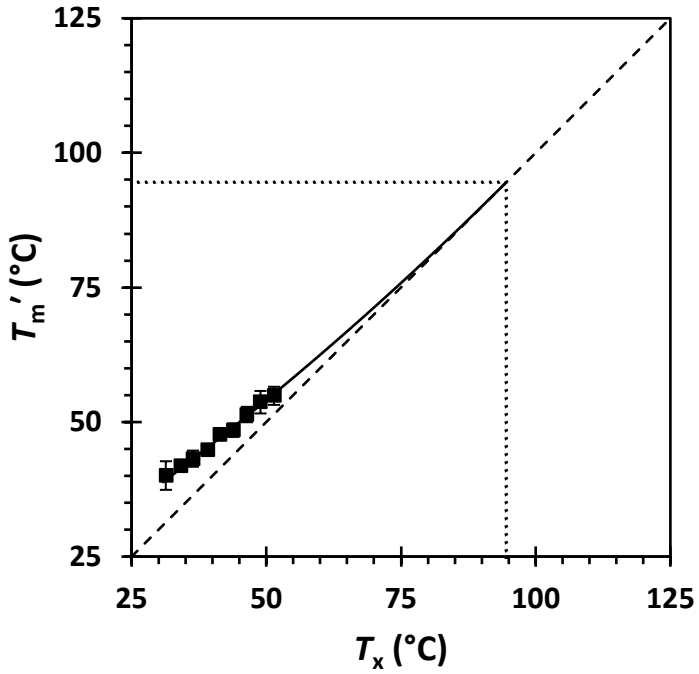

Figure 3.23: Relationship between the zero-heating-rate initial melting temperature, T_m', and crystallization temperature, T_x, for z = 0.25. The lines represent $T_m' = T_x$ (_ _ _ _ _) and $T_m'(T_x)$ (———) according to the non-linear Hoffman-Weeks equation (Eqn. (3.19)).

Table 3.8: Results for the non-linear Hoffman-Weeks analysis with the different zero-heating-rate melting temperature data sets.

z	T_m^{NLHW} (°C)	y (K^{-1})	a	C_2 (Å)
0.25[a]	94.6 ± 6.4	−4.3×10^{-3} ± 8.6×10^{-4}	0.82 ± 0.38	6.0 ± 2.7
0.38[a]	499.1	−4.0×10^{-3} ± 2.8×10^{-4}	0.045 ± 0.071	0.52 ± 0.83
0.38[b]	115.4 ± 4.1	−5.9×10^{-3} ± 8.2×10^{-4}	−0.89 ± 0.29	−7.6 ± 2.5
0.50[a]	–	–	–	–
0.50[b]	121.7 ± 3.7	−6.2×10^{-3} ± 7.9×10^{-4}	−1.60 ± 0.30	−14.3 ± 2.7

[a]Obtained using the MX method under the assumption that $\sigma_{em} = \sigma_{ec}^{o}$ (Figs. 3.22 and 3.23). [b]Obtained using the MX method under the assumption that $\sigma_{em} \neq \sigma_{ec}^{o}$ (Figs. 3.24 and 3.27).

The equilibrium melting temperature determined using the z = 0.25 data is similar to that reported by Nuñez et al.[36] for a similar molecular weight sample using a type of non-linear Hoffman-Weeks analysis (Table 3.1). This is most likely coincidental because the group measured the melting temperatures using CDSC following nearly complete isothermal crystallization as opposed to the initial melting

temperatures required by the non-linear Hoffman-Weeks analysis. However, they did use high enough heating rates to suppress reorganization during heating. Furthermore, they did not actually use the MX method, but assumed that γ = 1, $\frac{\sigma_e^o}{\sigma_{em}}$ = 1, and C_2 = 50 Å then fit the $T_m'(T_x)$ by varying the equilibrium melting temperature to minimize the variance. Notice that the value they assumed for C_2 is an order of magnitude larger than our results for z = 0.25, but it is comparable with values obtained for LPE.[93] The equilibrium melting temperature and C_2 determined using the z = 0.25 data are also within experimental error of the equilibrium melting temperature determined from the Gibbs-Thomson method (Fig. 3.18 and Table 3.3) and C_2 determined from the plot of lamellar thickness vs. inverse undercooling (Fig. 3.20 and Table 3.6). This indication of self-consistency is reassuring for the applicability of the non-linear Hoffman-Weeks method as an accurate method for determining a polymer's equilibrium melting temperature. Despite this, the heating rate analysis of the FDSC data suggests that z = 0.38 the correct melting kinetics exponent. Furthermore, the y value for the z = 0.25 data is still negative even though the values of a and C_2 are positive. This non-physical result calls into question any demonstration of self-consistency and indicates that the conventional formulation of the non-linear Hoffman-Weeks model may not be suited to analyze this data. As expected, the equilibrium melting temperature obtained with the z = 0.38 data is unrealistically large. The analysis cannot be conducted on the data with z = 0.50 because it diverges from the line $T_m'(T_x)$. The non-linear Hoffman-Weeks equation (Eqn. (3.19)) is not applicable to model the melting behavior of the z = 0.38 or 0.50 data sets due to the necessity of positive curvature in the function $T_m'(T_x)$.[58]

Let us consider now the effects of relaxing the assumption that $\sigma_{em} = \sigma_{ec}^o$, which is integral to the MX method, and instead utilize the values of σ_{em} and σ_{ec}^o found in Tables 3.3 and 3.6, respectively. Doing so changes the root behavior and curvature of the non-linear Hoffman-Weeks equation (Eqn. (3.19)), and it permits the determination of the equilibrium melting temperatures for the data with z = 0.38 and 0.50 using the non-linear Hoffman-Weeks method. The approach for determining the equilibrium melting

temperature using the MX method is the similar, but the equilibrium melting temperature is varied until the slope of the M vs. X plot (Eqn. (3.20)) is equal to $\frac{\sigma_{ec}^{o}}{\sigma_{em}}$ instead of unity. Figure 3.24 shows the slopes from plots of M vs. X for different choices of the equilibrium melting temperature in addition to plots of M vs. X for $T_m^{NLHW}(z = 0.38)$ = 115.4°C and $T_m^{NLHW}(z = 0.50)$ = 121.7°C, which yield slopes of $\frac{\sigma_{ec}^{o}}{\sigma_{em}}$. The results for this modification to the non-linear Hoffman-Weeks analysis are summarized in Table 3.8. The equilibrium melting temperatures are close, but not within experimental error, of those determine by the Gibbs-Thomson method (Table 3.3), and the same is true for the values of C_2 determined by analyzing the average lamellar thickness as a function of inverse undercooling (Table 3.6). The values of C_2 obtained via the non-linear Hoffman-Weeks analysis are still negative, which is a physically meaningless result. Figure 3.25 compares the predicted functions of $T_m'(T_x)$ for the data with z = 0.25, 0.38, and 0.50 over the full range of crystallization studied with FDSC. Interestingly, the non-linear Hoffman-Weeks equation has negative curvature for negative values of C_2, and there are two roots for the case of $\frac{\sigma_{ec}^{o}}{\sigma_{em}} > 1$, where the upper root corresponds to the equilibrium melting temperature and the lower root has no known physical meaning at this time. The lower roots are $T_{x,root}$ = −45.4 and −16.1°C for z = 0.38 (Fig. 3.25b) and 0.50 (Fig. 3.25c), respectively. The negative values of C_2 for the z = 0.38 and 0.50 data sets are a consequence of the model since negative curvature is required for the data to extrapolate to a physically reasonable equilibrium melting temperature. While the conventional approach cannot account for the melting behavior at the low crystallization temperatures, relaxing the assumption that $\sigma_e^o = \sigma_{em}$ does not correct the problem. Appendix A considers how the sign of C_2 and the ratio of the equilibrium fold surface free energies affects the curvature of the melting temperature as a function of crystallization temperature and the points of intersection with the line $T_m' = T_x$.

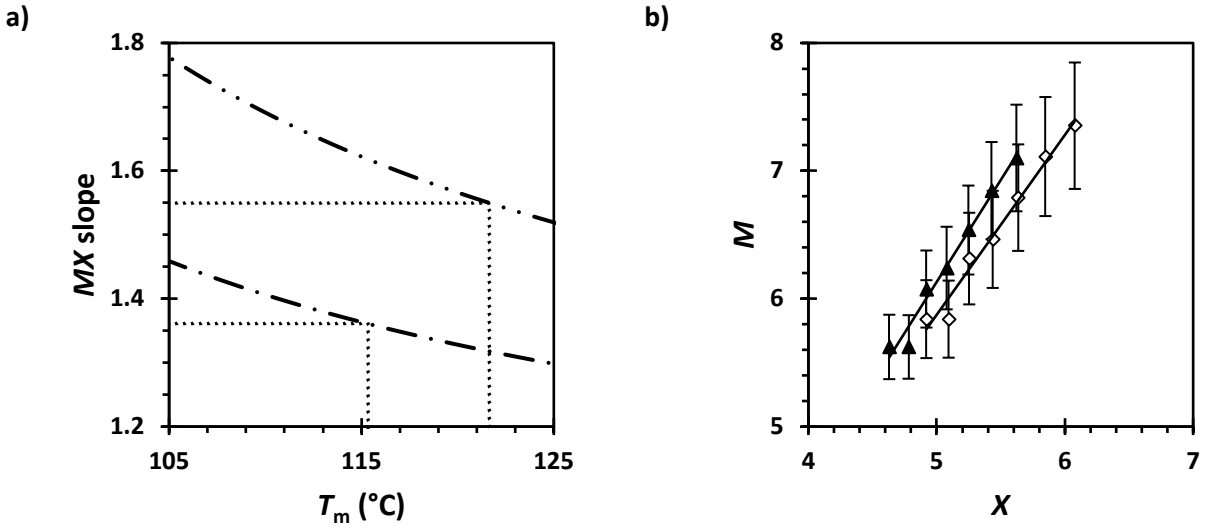

Figure 3.24: a) Relationship between the slope of the MX plot and the choice of equilibrium melting temperature, T_{m}, for zero-heating-rate initial melting temperatures determined with z = 0.38 (⎯ . ⎯ .) and 0.50 (⎯ . . ⎯). b) Relationship between the reduced melting temperature, M, and the reduced crystallization temperature, X, for zero-heating-rate initial melting temperatures determined with z = 0.38 (◇) and 0.50 (▲). The lines in b) represent linear fits according to the MX equation (Eqn. (3.20)) with the choice of equilibrium melting temperature that yields a slope equal to $\frac{\sigma_{\mathrm{e}}^{\mathrm{o}}}{\sigma_{\mathrm{em}}}$. The error bars are propagated from the extrapolated zero-heating-rate and equilibrium melting temperatures.

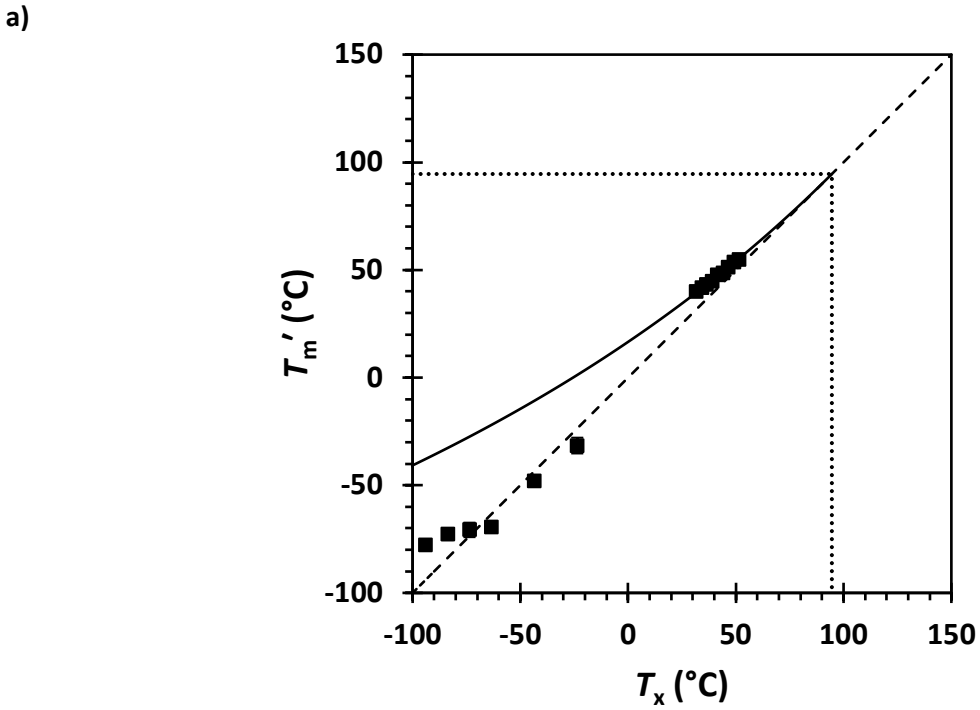

b)

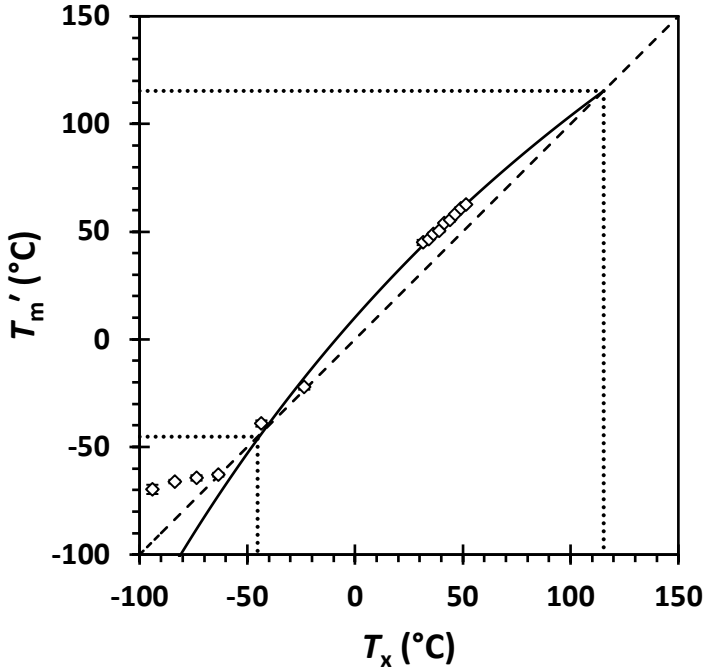

c)

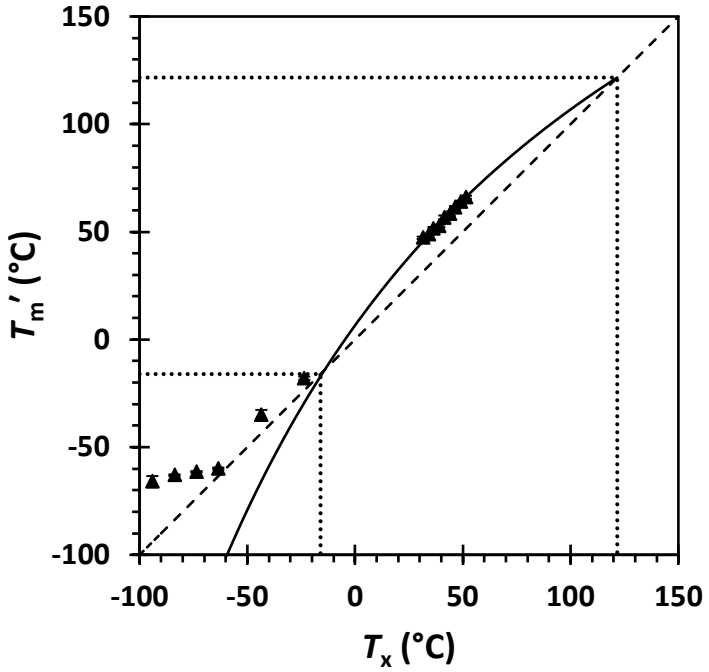

Figure 3.25: Relationship between the zero-heating-rate initial melting temperature, T_m', and crystallization temperature, T_x, for a) z = 0.25, b) z = 0.38, and c) z = 0.50. The lines in all three plots represent $T_m' = T_x$ (_ _ _ _ _) and $T_m'(T_x)$ (_____) according to the non-linear Hoffman-Weeks equation (Eqn. (3.19)).

3.4.6 Modified non-linear Hoffman-Weeks analysis to model the melting behavior using zero-heating-rate melting temperatures determined with z = 0.38 and z = 0.50

The original formulation of the Lauritzen-Passaglia kinetic roughening theory[69] defined the kinetic fold surface free energy as a non-linear function of undercooling. The successful analysis of LPE spherulite growth rate data employing a linear approximation to the kinetic fold surface free energy upon crystallization[70] influenced Marand et al.[58] to adopt the same approximation for the non-linear Hoffman-Weeks analysis. As a result, the non-linear Hoffman-Weeks model should only be valid for low to moderate undercoolings. While this may be true for LPE, the Gibbs-Thomson results from subsection 3.4.3 (Table 3.3) imply that PCL crystallizes at large undercoolings, ΔT > 50°C. Additionally, the non-physical, negative values of C_2 that were obtained using the assumption of a linear dependence on undercoolings for the kinetic fold surface free energy upon crystallization (Tables 3.6 and 3.8) suggest that the non-linear Hoffman-Weeks model in its original form is ill-suited for determining the equilibrium melting temperature of PCL and modeling the melting temperature as a function of crystallization temperature. As such, we will consider a modification of the non-linear Hoffman-Weeks equation that incorporates a kinetic fold surface free energy upon crystallization that is a non-linear function of undercooling. We will employ a series expansion in the kinetic fold surface free energy upon crystallization to capture the non-linearity at large undercoolings. This method is essentially a perturbation theory approach to the problem. Similar cases of series expansions to describe physical processes more accurately under conditions far from equilibrium can be found across a broad range of chemical and physical disciplines. A critical implication of this analysis is that it preserves the assumption $\sigma_{\mathrm{em}} = \sigma_{\mathrm{ec}}^{\mathrm{o}}$. While the validity of this assumption has been debated in the past,[70] it is supported by self-consistency between the Gibbs-Thomson, non-linear Hoffman-Weeks, and Lauritzen-Hoffman spherulite growth rate analyses for LPE and PEO.[70, 71]

The following will detail the necessary equations for the non-linear Hoffman-Weeks analysis assuming the kinetic fold surface free energy is a quadratic function of undercooling. The equations for a cubic function of undercooling are provided in Appendix A. The points of intersection between the temperature as a function of undercooling and the line $T_{\mathrm{m}}'(T_{\mathrm{x}})$ will also be considered. Assuming that the kinetic fold surface free energy upon crystallization is a quadratic function of undercooling, we write

$$\sigma_{\mathrm{ec}}^{\mathrm{k}} = \sigma_{\mathrm{ec}}^{\mathrm{o}}(1 + y\Delta T + p\Delta T^2) \tag{3.25}$$

where y and p are constants. Substituting Eqn. (3.25) into the expression for initial lamellar thickness, Eqn. (3.9), yields

$$l_{\mathrm{g}}^{*} = \frac{2\sigma_{\mathrm{ec}}^{\mathrm{o}} T_{\mathrm{m}}}{\Delta H_{\mathrm{f}}^{\mathrm{o}} \Delta T} + \left(\frac{2\sigma_{\mathrm{ec}}^{\mathrm{o}} y T_{\mathrm{m}}}{\Delta H_{\mathrm{f}}^{\mathrm{o}}} + \frac{2\sigma_{\mathrm{ec}}^{\mathrm{o}} p \Delta T T_{\mathrm{m}}}{\Delta H_{\mathrm{f}}^{\mathrm{o}}} + \delta l \right) \tag{3.26a}$$

$$l_{\mathrm{g}}^{*} = \frac{C_1}{\Delta T} + C_2(\Delta T) \tag{3.26b}$$

where C_1 has the same definition as in section 3.2 (theoretical background) and $C_2(\Delta T)$ combines the three terms contained within parentheses on the right-hand side of Eqn. (3.26a). Combining the expressions for lamellar thickness, Eqn. (3.26b), with the Gibbs-Thomson equation, Eqn. (3.15), and rearranging yields the modified non-linear Hoffman-Weeks equation

$$T_{\mathrm{m}}' = T_{\mathrm{m}} \left\{ 1 - \left(\frac{1}{\gamma}\right) \left(\frac{T_{\mathrm{m}} - T_{\mathrm{x}}}{T_{\mathrm{m}}}\right) \left(\frac{\sigma_{\mathrm{em}}}{\sigma_{\mathrm{ec}}^{\mathrm{o}}}\right) \left[\frac{1}{1 + \frac{C_2(\Delta T)\Delta H_{\mathrm{f}}^{\mathrm{o}}}{2\sigma_{\mathrm{ec}}^{\mathrm{o}}} \left(\frac{T_{\mathrm{m}} - T_{\mathrm{x}}}{T_{\mathrm{m}}}\right)} \right] \right\} \tag{3.27}$$

Rearranging Eqn. (3.27) yields the modified MX equation

$$\frac{T_{\mathrm{m}}}{T_{\mathrm{m}} - T_{\mathrm{m}}'} = \gamma \left(\frac{\sigma_{\mathrm{ec}}^{\mathrm{o}}}{\sigma_{\mathrm{em}}}\right) \left[\frac{T_{\mathrm{m}}}{T_{\mathrm{m}} - T_{\mathrm{x}}} + pT_{\mathrm{m}}^2 \left(\frac{T_{\mathrm{m}} - T_{\mathrm{x}}}{T_{\mathrm{m}}}\right) + \frac{\Delta H_{\mathrm{f}}^{\mathrm{o}}}{2\sigma_{\mathrm{e}}^{\mathrm{o}}} \left(\frac{2\sigma_{\mathrm{ec}}^{\mathrm{o}} y T_{\mathrm{m}}}{\Delta H_{\mathrm{f}}^{\mathrm{o}}} + \delta l \right) \right] \tag{3.28a}$$

$$M = \gamma \left(\frac{\sigma_{\mathrm{ec}}^{\mathrm{o}}}{\sigma_{\mathrm{em}}}\right) \left[X + \frac{b}{X} + a \right] \tag{3.28b}$$

where $b = pT_{\mathrm{m}}^2$ and $a = \frac{C_2 \Delta H_{\mathrm{f}}^{\mathrm{o}}}{2\sigma_{\mathrm{ec}}^{\mathrm{o}}}$.

When a linear approximation to the kinetic fold surface free energy upon crystallization is assumed, the conventional MX equation (Eqn. (3.20)) only has one unknown, the equilibrium melting temperature. The unknown equilibrium melting temperature is determined via the MX method by constraining the slope obtained from linear regression to a value of 1, which also yields a and C_2. However, the modified MX equation (Eqn. (3.28b)) is now a non-linear function of X, so the conventional MX method cannot be applied to determine the equilibrium melting temperature. As a result, a non-linear regression must be performed on Eqn. (3.28b) to obtain estimates of the equilibrium melting temperature, b, and a, but the variance minimization is extremely sensitive to the initial conditions. Hence, this approach is unreliable without *a priori* knowledge of at least one of these three values, preferably the equilibrium melting temperature. We will assume that good estimates of the equilibrium melting temperature and equilibrium fold surface free energy upon melting can be obtained using the Gibbs-Thomson analysis (Table 3.3) and that the equality $\sigma_{\mathrm{em}} = \sigma_{\mathrm{ec}}^{\mathrm{o}}$ holds, then fit the experimental data to Eqn. (3.28b) to determine a and b. In doing so we will demonstrate that the melting behavior observed for PCL and other polymers[11-13, 15, 20-24] can be explained by accounting for the temperature dependence of the kinetic fold surface free energy. The resulting function for the kinetic fold surface free energy upon crystallization can also be used to check the self-consistency of the Lauritzen-Hoffman secondary nucleation theory of polymer crystal growth, as others have done for the case of LPE,[70, 71] but this is outside the scope of the current work.

The results for the modified non-linear Hoffman-Weeks analysis using the zero-heating-rate melting temperature data corresponding to z = 0.38 and 0.50 are shown in Figure 3.26 with kinetic fold surface free energies that are quadratic and cubic functions of undercooling. The modified approach fits the experimental well. Additionally, the curvature of the function $T_{\mathrm{m}}'(T_{\mathrm{x}})$ is positive at crystallization temperatures approaching the equilibrium melting temperature, which is predicted by the conventional non-linear Hoffman-Weeks model[58] for crystallization at low to moderate undercoolings. Positive

curvature has been observed in previous reports of the initial melting temperature (i.e. non-thickened lamellae) as a function of crystallization temperature for LPE,[93, 113] PEO,[71] and *i*-PP.[114, 115] The predicted melting temperatures quickly show unrealistic deviations below the lowest crystallization temperature (T_x = 36.4°C), as shown in Fig. 3.26. For instance, the second-order approximation for the z = 0.38 data crosses the line $T_m' = T_x$ at T_x = −1.7°C, and the third-order approximation swings to questionably large melting temperatures (Fig. 3.26a). The second-order approximation for the z = 0.50 data crosses the line $T_m' = T_x$ at T_x = 16.3°C (Fig. 3.26b), and the third-order approximation behaves similarly to that for the z = 0.38 data. These results are not surprising since extrapolating polynomials without constraining data is known to be unreliable. As such, there is no physical meaning to the results without data at lower temperatures to constrain the model.

a)

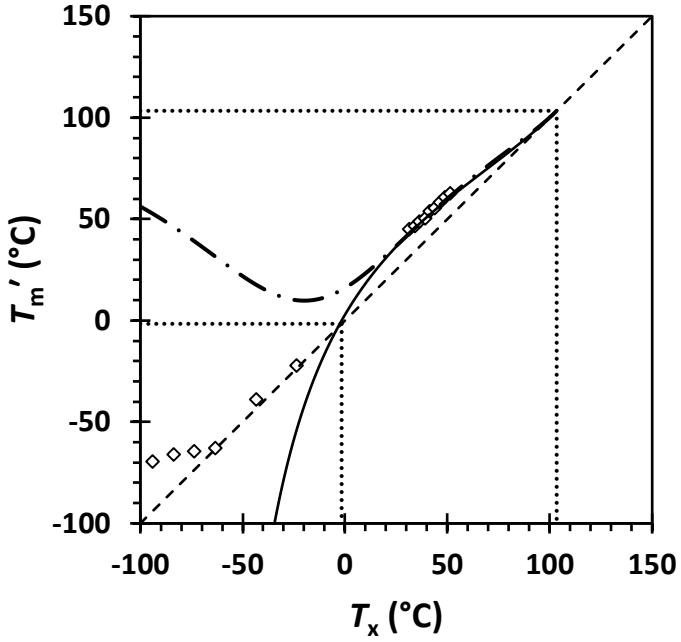

b)

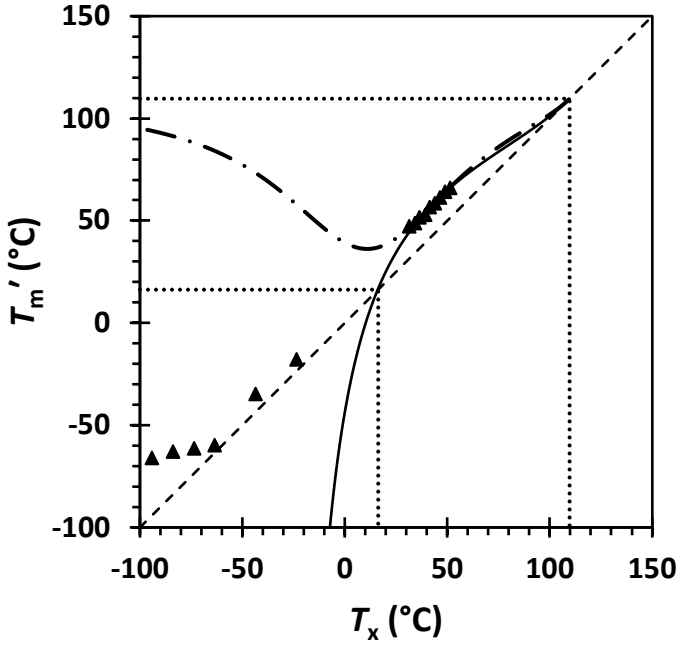

Figure 3.26: Relationship between the zero-heating-rate initial melting temperature, T_m', and crystallization temperature, T_x, for a) z = 0.38 and b) z = 0.50. The lines in both plots represent $T_m' = T_x$ (_ _ _ _ .), $T_m'(T_x)$ (———) with a quadratic $\sigma_{ec}^{k}(\Delta T)$ (Eqn. (3.27)), and $T_m'(T_x)$ (— . — .) with a cubic $\sigma_{ec}^{k}(\Delta T)$ (Eqn. (3A.19)). Only data for $T_x \geq$ 36.4°C were used to model $T_m'(T_x)$.

Table 3.9 contains the fitted coefficients for the kinetic fold surface free energy polynomials. The signs of the coefficients alternate, and the magnitude of the coefficients decreases with increasing order. This behavior is expected to result from perturbation theory solutions, where each additional term provides a further correction. The value of y remains positive for the second- and third-order kinetic fold surface free energies upon crystallization, but the physical interpretation of y as a measure of stem length fluctuations has less meaning upon the incorporation of higher order terms. The fitted parameters from the modified MX equation (Eqns. (3.28b) and (3A.20b)) and the kinetic fold surface free energy upon crystallization (Eqns. (3.25) and (3A.17)) increase by a factor of ca. 2 to 4 and their errors increase by ca. one order of magnitude when increasing from a second-order to third-order approximation. The increase in the magnitudes of the coefficients and their errors could simply result from increasing the number of fitting parameters in the non-linear least squares regression. Of special interest are the values of C_2. The values for the second-order approximation are similar to those for LPE[93] (C_2^{LPE} = 57 Å) and *i*-PP[114] ($C_2^{i\text{-PP}}$ = 52 Å), but the results for the third-order approximations are ca. 50 and 120% larger for the z = 0.38 and 0.50 data, respectively. Physically, C_2 can only be the limiting lamellar thickness at infinite undercooling when the kinetic fold surface free energy upon crystallization is a linear function of undercooling because this yields a linear relationship between the lamellar thickness and inverse undercooling. Hence, the large magnitudes of C_2 are not troublesome since its physical meaning is lost by expanding the kinetic fold surface free energy upon crystallization to polynomial functions of undercooling.

Table 3.9: Results for the modified non-linear Hoffman-Weeks analysis on the data for $T_x \geq 36.4$°C incorporating quadratic and cubic undercooling dependences for the kinetic fold surface free energy of crystallization.

$\boldsymbol{M = \gamma\left(\frac{\sigma_{ec}^{o}}{\sigma_{em}}\right)\left[X + \frac{b}{X} + a\right], \sigma_{ec}^{k}(\Delta T) = \sigma_{ec}^{o}(1 + y\Delta T + p\Delta T^{2})}$		
$\boldsymbol{z}$	0.38[a]	0.50[b]
$\boldsymbol{a}$	4.66 ± 0.38	5.81 ± 0.42
$\boldsymbol{C_2}$ **(Å)**	39.7 ± 3.3	52.0 ± 3.7
$\boldsymbol{y}$ **(K^{-1})**	$6.6\times10^{-3} \pm 1.2\times10^{-3}$	$9.7\times10^{-3} \pm 1.3\times10^{-3}$
$\boldsymbol{b}$	−19.4 ± 2.4	−23.8 ± 2.4
$\boldsymbol{p}$ **(K^{-2})**	$-1.4\times10^{-4} \pm 1.7\times10^{-5}$	$-1.6\times10^{-4} \pm 1.6\times10^{-5}$
$\boldsymbol{M = \gamma\left(\frac{\sigma_{ec}^{o}}{\sigma_{em}}\right)\left[X + \frac{b}{X} + \frac{c}{X^2} + a\right], \sigma_{ec}^{k}(\Delta T) = \sigma_{ec}^{o}(1 + y\Delta T + p\Delta T^{2} + q\Delta T^{3})}$		
$\boldsymbol{z}$	0.38[a]	0.50[b]
$\boldsymbol{a}$	8.6 ± 5.5	12.4 ± 6.1
$\boldsymbol{C_2}$ **(Å)**	73.3 ± 46.4	111.0 ± 54.7
$\boldsymbol{y}$ **(K^{-1})**	0.017 ± 0.015	0.027 ± 0.016
$\boldsymbol{b}$	−69.8 ± 69.4	−101.4 ± 71.5
$\boldsymbol{p}$ **(K^{-2})**	$-4.9\times10^{-4} \pm 4.9\times10^{-4}$	$-6.9\times10^{-4} \pm 4.9\times10^{-4}$
$\boldsymbol{c}$	159.5 ± 219.8	225.8 ± 208.0
$\boldsymbol{q}$ **(K^{-3})**	$3.0\times10^{-6} \pm 4.1\times10^{-6}$	$4.0\times10^{-6} \pm 3.7\times10^{-6}$

[a] $T_m^{GT}(z = 0.38)$ = 103.4°C was used to calculate M and X. [b] $T_m^{GT}(z = 0.50)$ = 109.6°C was used to calculate M and X.

If we assume that the Gibbs-Thomson equation (Eqn. (3.15)) accurately describes the relationship between melting temperature and lamellar thickness and that Eqns. (3.26) and (3A.18) accurately describe the relationship between lamellar thickness and undercooling for the low crystallization data, then we can apply the modified non-linear Hoffman-Weeks equations to model the melting temperature as a function of crystallization temperature over the entire range of data. These assumptions are not verified because there is no lamellar thickness data corresponding to these crystallization temperatures. As a result, all of the subsequent analyses will consider the results obtained using data from only the high temperatures in addition to the full temperature range. Figure 3.27 show the results for the modified non-linear Hoffman-Weeks analysis applied to the entire range of zero-heating-rate melting temperatures corresponding to z = 0.38 and 0.50 with second- and third-order kinetic fold surface free energies upon crystallization. Inspection of the data in the high crystallization temperature range reveals that the fit is

slightly poorer in this region when the low temperature data points are included in the analysis. However, it is apparent that the melting temperature data across the entire range of crystallization temperatures can be adequately modeled by the modified non-linear Hoffman-Weeks equation (Fig. 3.27). The melting temperature as a function of crystallization temperature for the z = 0.38 data only crosses the line $T_{\mathrm{m}}' = T_{\mathrm{x}}$ at the equilibrium melting temperature, but the modeled function for the z = 0.50 data actually intersects the line $T_{\mathrm{m}}' = T_{\mathrm{x}}$ at $T_{\mathrm{x,root}}$ = −55.9 and −41.8°C in addition to the equilibrium melting temperature. These two additional points of intersection are not physically significant, but they do support the conclusion that z = 0.38 data is the more appropriate choice of melting kinetics exponent. It is worth noting that we have included the data points below the glass transition temperature, mostly to illustrate the effectiveness of the modified model to model the melting behavior over the entire range of data. Nominal differences in the fits arise when considering only temperatures above the glass transition.

a)

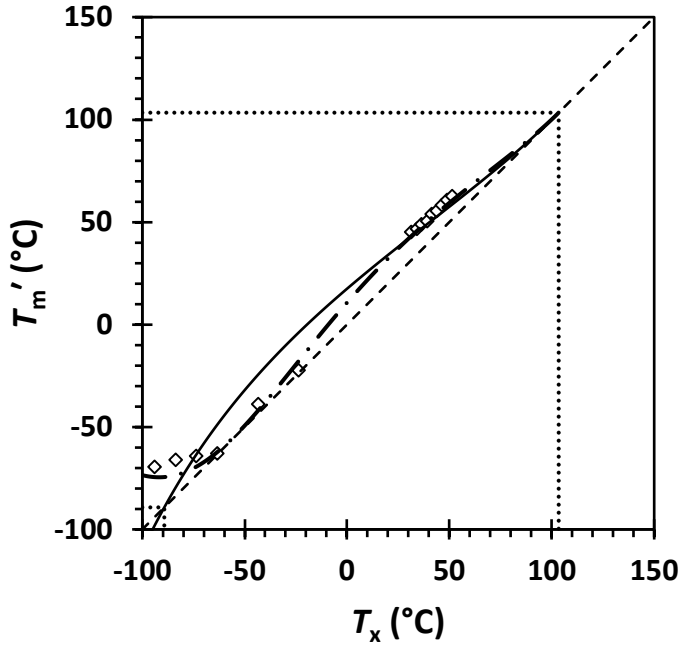

b)

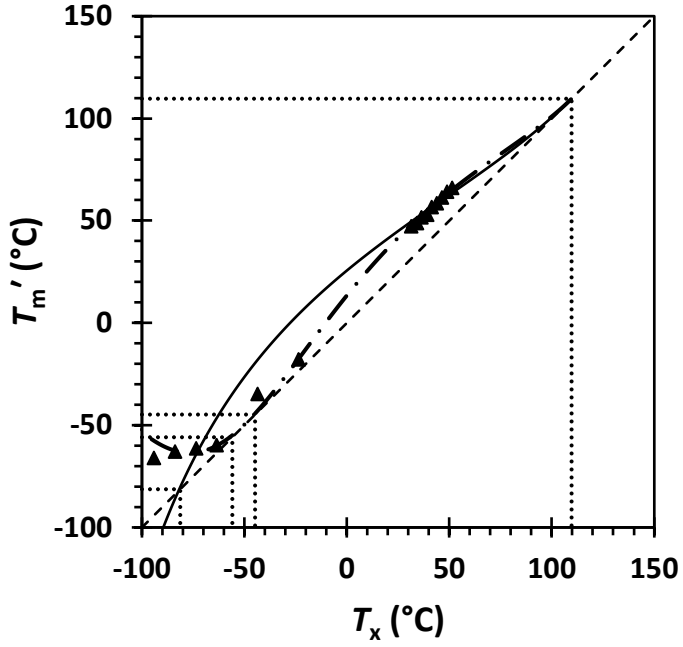

Figure 3.27: Relationship between the zero-heating-rate initial melting temperature, T_m', and crystallization temperature, T_x, for a) z = 0.38 and b) z = 0.50. The lines in both plots represent $T_m' = T_x$ (_ _ _ _ .), $T_m'(T_x)$ (———) with a quadratic $\sigma_{ec}^{k}(\Delta T)$ (Eqn. (3.27)), and $T_m'(T_x)$ (— . — .) with a cubic $\sigma_{ec}^{k}(\Delta T)$ (Eqn. (3A.19)). All crystallization temperatures (T_x = −94.1 to 51.4°C) were used to model $T_m'(T_x)$.

The fitted coefficients for the kinetic fold surface free energy upon crystallization are shown in Table 3.10. Both the coefficients and their fitted errors are smaller than when only the high crystallization temperatures are utilized for the analysis. The errors are most likely smaller simply because there are more data points in the non-linear least squares regression on Eqns. (3.28b) and (3A.20b). Extending the temperature range does not affect the signs of the parameters (Table 3.9). The magnitudes of the coefficients increase by about a factor of two when changing from a second-order to a third-order kinetic fold surface free energy upon crystallization, but the parameter errors decrease, contrary to when only the high crystallization temperatures are utilized for the analysis.

Table 3.10: Results for the modified non-linear Hoffman-Weeks analysis on all of the investigated isothermal crystallization temperatures incorporating quadratic and cubic undercooling dependences for the kinetic fold surface free energy of crystallization.

$\boldsymbol{M = \gamma\left(\frac{\sigma_{ec}^{o}}{\sigma_{em}}\right)\left[X + \frac{b}{X} + a\right],\ \sigma_{ec}^{k}(\Delta T) = \sigma_{ec}^{o}(1 + y\Delta T + p\Delta T^{2})}$		
z	0.38[a]	0.50[b]
a	2.21 ± 0.18	2.44 ± 0.20
C_2 (Å)	18.8 ± 1.5	21.9 ± 1.8
y (K^{-1})	$8.9\times10^{-5} \pm 6.1\times10^{-4}$	$8.9\times10^{-4} \pm 6.5\times10^{-4}$
b	−4.6 ± 0.6	−4.9 ± 0.6
p (K^{-2})	$-3.2\times10^{-5} \pm 4.0\times10^{-6}$	$-3.3\times10^{-5} \pm 4.2\times10^{-6}$
$\boldsymbol{M = \gamma\left(\frac{\sigma_{ec}^{o}}{\sigma_{em}}\right)\left[X + \frac{b}{X} + \frac{c}{X^{2}} + a\right],\ \sigma_{ec}^{k}(\Delta T) = \sigma_{ec}^{o}(1 + y\Delta T + p\Delta T^{2} + q\Delta T^{3})}$		
z	0.38[a]	0.50[b]
a	4.35 ± 0.20	5.01 ± 2.21
C_2 (Å)	37.0 ± 1.7	44.8 ± 2.7
y (K^{-1})	$5.8\times10^{-3} \pm 8.1\times10^{-4}$	$7.6\times10^{-3} \pm 1.0\times10^{-3}$
b	−21.7 ± 1.6	−24.2 ± 2.2
p (K^{-2})	$-1.5\times10^{-4} \pm 1.1\times10^{-5}$	$-1.7\times10^{-4} \pm 1.5\times10^{-5}$
c	26.9 ± 2.4	29.3 ± 3.3
q (K^{-3})	$5.0\times10^{-7} \pm 4.5\times10^{-8}$	$5.2\times10^{-7} \pm 5.9\times10^{-8}$

[a] $T_m^{GT}(z = 0.38)$ = 103.4°C was used to calculate M and X. [b] $T_m^{GT}(z = 0.50)$ = 109.6°C was used to calculate M and X.

Furushima et al.[13] observed melting temperatures that were greater than the crystallization temperatures by a constant value when studying the melting kinetics of PEEK. In other words, the melting

temperature as a function of crystallization temperature was parallel to the line $T_{\mathrm{m}}'(T_{\mathrm{x}})$. The authors attempted to reconcile these observations by relating the constant shift in melting temperature to the minimum number of crystalline stems that must deposit on the substrate during crystallization via secondary nucleation. However, there are several issues with their analysis and conclusions. First, the authors considered that the chemical potential between the bulk crystal and bulk melt is a linear function of undercooling. In other words, they assumed that the difference between the heat capacity of the crystal and the melt is equal to zero, which leads to constant values for the enthalpy and entropy of crystallization. While this assumption is standard for thermodynamic and kinetic considerations of polymer crystal growth at low undercoolings, it will not be valid for their data because they report crystallization across a ca. 100°C temperature range with a minimum undercooling of at least ΔT = 150°C ($T_{\mathrm{m}}^{\mathrm{LHW}}$ = 398°C).[21] The undercooling is most likely considerably larger because melting-recrystallization-remelting is prevalent in PEEK and the equilibrium melting temperature was determined via the linear Hoffman-Weeks method.[13, 21] Second, they neglected the contributions from $\frac{\sigma}{x}$ and $\frac{\sigma}{y}$ to the melting point depression of the lamellar crystals. This is a necessary approximation in deriving the Gibbs-Thomson equation (Eqn. (3.15)) in order to obtain a closed-form expression that can be used to obtain physically meaningful quantities when analyzing experimental data. However, the basal dimensions become small at large undercoolings, so these terms are no longer negligible for PEEK.[116, 117] Third, they neglected the undercooling dependence of the kinetic fold surface free energy upon crystallization in their analysis. As we have shown here, this assumption is most likely invalid given the large undercoolings they investigated. Fourth, the authors made no attempt to account for the variation of melting temperature with crystallization time, which means that the minimum number of stems necessary to form stable crystallites would be lower for lower degrees of crystallinity (i.e. short crystallization times). This doesn't seem logical, as longer crystallization times lead to larger crystallite dimensions, so more stems should not be required to deposit at once in order for the crystals to be stable. The authors applied their ideas to experimental

data for PCL measured with FDSC, and they determined that bundles of secondary nuclei should be at least six stems wide for crystallization between T_x = 30 and 40°C.[13]

Although we have taken into account the undercooling dependence of the kinetic fold surface free energy upon crystallization and the crystallization time dependence of the melting temperature, we have still assumed that the difference in heat capacities between the crystal and amorphous phases is zero and that the lateral surface free energy does not affect the melting temperature of the lamellae. This pervasive assumption in thermodynamic and kinetic theories of polymer crystallization is often necessary to obtain useful, analytical expressions.

3.4.7 Temperature dependence of the kinetic fold surface free energy

The kinetic fold surface free energy upon crystallization was modeled as quadratic and cubic functions of undercooling using Eqns. (3.25) and (3A.17) with the coefficients from Tables 3.9 and 3.10. Experimental values of the kinetic fold surface free energy upon crystallization were determined by rearranging Eqn. (3.13a), using the interpolated lamellar thicknesses for l_g^*, and calculating δl with Eqn. (3.10). Figures 3.28 and 3.29 show the values of the kinetic fold surface free energy upon crystallization determined using only the high temperature data ($T_x \geq 36.4$°C) and all temperatures (T_x = −91.4 to 51.4°C), respectively. Both figures include data corresponding to the Gibbs-Thomson melting temperatures for z = 0.38 and 0.50. The experimental values of the kinetic fold surface free energies upon crystallization decrease until the glass transition temperature, where they remain relatively constant. However, the highest temperature data point (ΔT = 52°C) is larger than the equilibrium value (σ_{ec}^o, ΔT = 0) for both cases of the melting kinetics exponent, which implies that a maximum value is reached before between ΔT = 0 and 52°C. Thus, a linear approximation to the kinetic fold surface free energy upon crystallization cannot describe the experimental results if $\sigma_{ec}^o = \sigma_{em}$. Assuming that $\sigma_{ec}^o \neq \sigma_{em}$ necessitates a negative y, which we have concluded is physically unmeaningful.

The second- and third-order approximations model the high crystallization temperature data well when using the parameters that were obtained by fitting only this temperature range (Fig. 3.28). However, there are unrealistic deviations when extrapolating beyond the limits of the crystallization temperatures that were used to obtain the coefficients of the kinetic fold surface free energy upon crystallization. Fig. 3.29 shows the kinetic fold surface free energy upon crystallization for the entire range of the z = 0.38 and 0.50 data. Only the cubic kinetic fold surface free energy upon crystallization models the data accurately over the full crystallization temperature range, and some quality of the fit is sacrificed in the high temperature range in order to model the data at low temperatures. This parallels the observations for modeling the melting temperatures as a function of crystallization temperatures (Figs. 3.26 and 3.27). Polynomial expansions of the kinetic fold surface free energy are necessary to model the data under the assumption that $\sigma_{\mathrm{em}} = \sigma_{\mathrm{ec}}^{\mathrm{o}}$ because they allow the function to have a maximum value.

a)

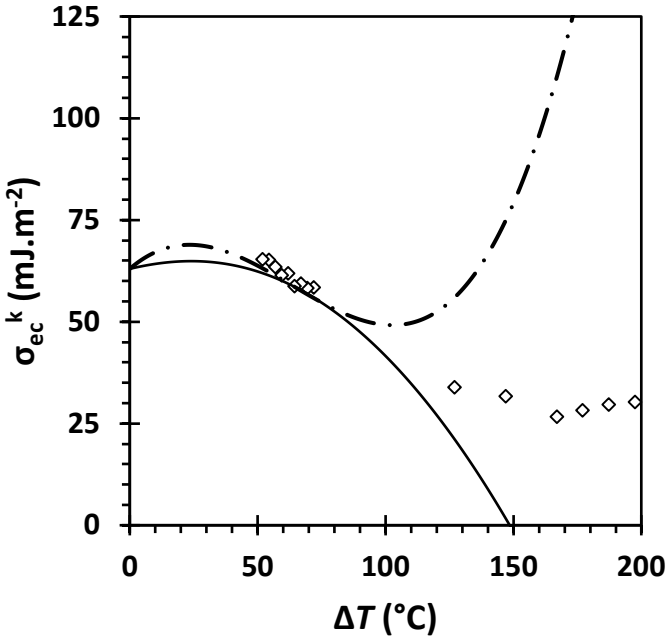

b)

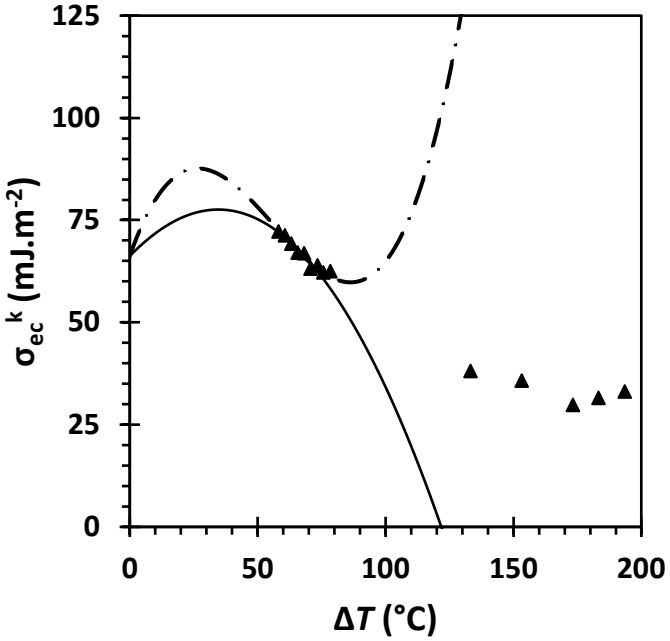

Figure 3.28: Relationship between the kinetic fold surface free energy upon crystallization, σ_{ec}^{k}, and the undercooling, ΔT corresponding to zero-heating-rate initial melting temperature data with a) z = 0.38 ($T_m^{GT}(z = 0.38)$ = 103.4°C and $\sigma_e^o(z = 0.38)$ = 63.0 mJ.m^{-2}) and b) z = 0.50 ($T_m^{GT}(z = 0.50)$ = 109.6°C and $\sigma_e^o(z = 0.50)$ = 66.2 mJ.m^{-2}). The points in both plots were calculated by rearranging Eqn. (3.13a), and the lines were calculated using a quadratic $\sigma_{ec}^{k}(\Delta T)$ (———) and a cubic $\sigma_{ec}^{k}(\Delta T)$ (— . — .). Only data for $T_x \geq$ 36.4°C were used to determine the coefficients for $\sigma_{ec}^{k}(\Delta T)$ (Table 3.9, Eqns. (3.25) and (3A.17)).

a)

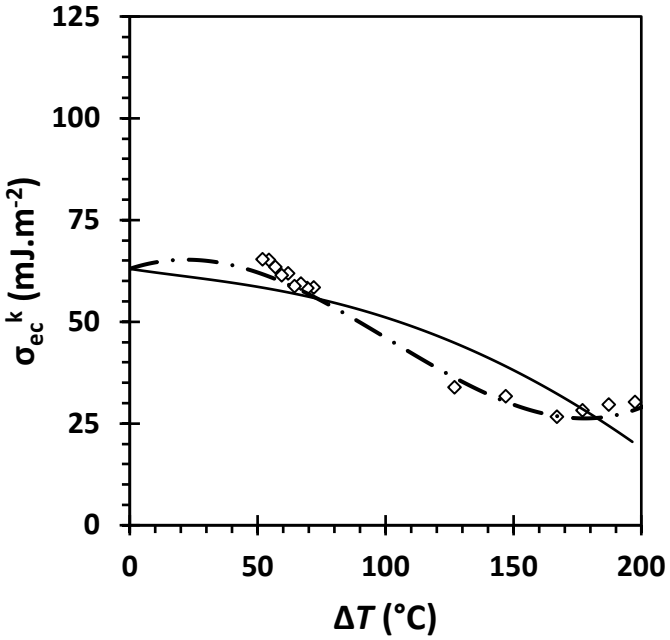

b)

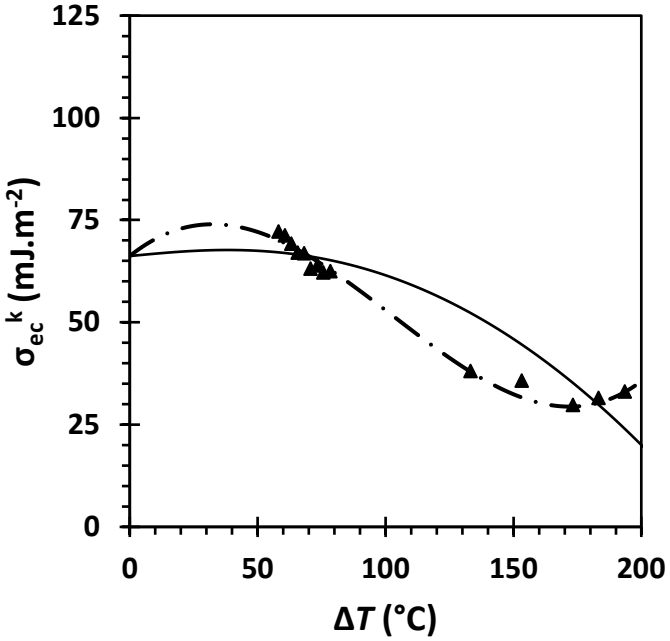

Figure 3.29: Relationship between the kinetic fold surface free energy upon crystallization, σ_{ec}^{k}, and the undercooling, ΔT corresponding to zero-heating-rate initial melting temperature data with a) z = 0.38 ($T_m^{GT}(z = 0.38)$ = 103.4°C and $\sigma_e^o(z = 0.38)$ = 63.0 mJ.m^{-2}) and b) z = 0.50 ($T_m^{GT}(z = 0.50)$ = 109.6°C and $\sigma_e^o(z = 0.50)$ = 66.2 mJ.m^{-2}). The points in both plots were calculated by rearranging Eqn. (3.13a), and the lines were calculated using a quadratic $\sigma_{ec}^{k}(\Delta T)$ (———) and a cubic $\sigma_{ec}^{k}(\Delta T)$ (— . — .). All crystallization temperatures from the FDSC study (T_x = −94.1 to 51.4°C) were used to determine the coefficients for $\sigma_{ec}^{k}(\Delta T)$ (Table 3.10, Eqns. (3.25) and (3A.17)).

The Lauritzen-Passaglia theory of kinetic roughening predicts that the kinetic fold surface free energy upon crystallization is a monotonically increasing, non-linear function of undercooling.[69] Although our results do not align with this prediction, there are a number of assumptions that limit the applicability of the LP theory to small undercoolings. Some of these assumptions are adjacent reentry folding, substrate completion as the dominant process of crystallization, and lack of interactions between layers of the crystals. Furthermore, the LP theory predicts a divergence of the lamellar thickness at $\Delta T = \sigma T_{\mathrm{m}}/a_0 \Delta H_{\mathrm{f}}^{0}$, implying it is not rigorously applicable to crystallization at high undercooling. Despite these shortcomings, the LP theory provides motivation for our approach to analyzing the experimental data.

3.4.8 Effects of the non-linear kinetic fold surface free energy on the lamellar thickness

The observation that the lamellar thickness varies linearly with the inverse undercooling (Eqn. (3.13b)) is universal to polymer crystallization,[49, 66, 69] making it a salient feature that any kinetic model must satisfy. Note that Strobl's multiphase model[49] actually uses a different reference temperature in place of the equilibrium melting temperature, but the idea is the same. As such, the effect of polynomial kinetic fold surface free energies upon crystallization on the average lamellar thickness needs to be assessed as a final measure of validity.

Figure 3.30 shows the lamellar thickness as a function of inverse undercooling calculated using kinetic fold surface free energies upon crystallization with fitting parameters obtained for $T_{\mathrm{x}} \geq 36.4$°C, and Figure 3.31 shows the same using fitting parameters obtained for all crystallization temperatures. The results are only shown for data with melting kinetics exponents of $z = 0.38$ and 0.50. The lamellar thickness as a function of inverse undercooling still appears to be linear in the range of experimental data for all cases considered, despite the fact that additional undercooling terms appear (Eqns. (3.26a) and (3A.18a)). The quadratic and cubic kinetic fold surface free energies upon crystallization yield fits that are essentially indistinguishable for both data sets when only the high crystallization temperatures are used to determine the coefficients in the kinetic fold surface free energy upon crystallization (Fig. 3.30).

However, the second- and third-order approximations deviate below the high temperature range, as expected. Note that the sudden increase in lamellar thickness at large undercoolings predicted by the cubic kinetic fold surface free energy (Figs. 3.30 and 3.31) is not related in any way to the δl-catastrophe from the Lauritzen-Hoffman secondary nucleation theory. Rather, the upward swing in the predicted lamellar thicknesses is simply an artifact from fitting the experimental data to Eqns. (3.28b) and (3A.20b). The Gibbs-Thomson equation (Eqn. (3.15)) and the zero-heating-rate initial melting temperatures were used to calculate the lamellar thicknesses of the low temperature data points. The lamellar thickness data is modeled very well by the third-order approximation when all of the crystallization temperatures are used to fit the kinetic fold surface free energy upon crystallization (Fig. 3.31). The second-order approximation sacrifices goodness of fit in the high crystallization temperature range in order to predict the lamellar thicknesses at low crystallization temperatures. All of these results mirror those for the kinetic fold surface free energy upon crystallization as a function of undercooling (Fig. 3.29) and the melting temperature as a function of crystallization temperature (Fig. 3.27). Our proposed incorporation of a power series expansion into the kinetic fold surface free energy upon crystallization is supported by the predictions of the lamellar thickness as a function of inverse undercooling, which still appears to be linear despite additional undercooling terms.

a)

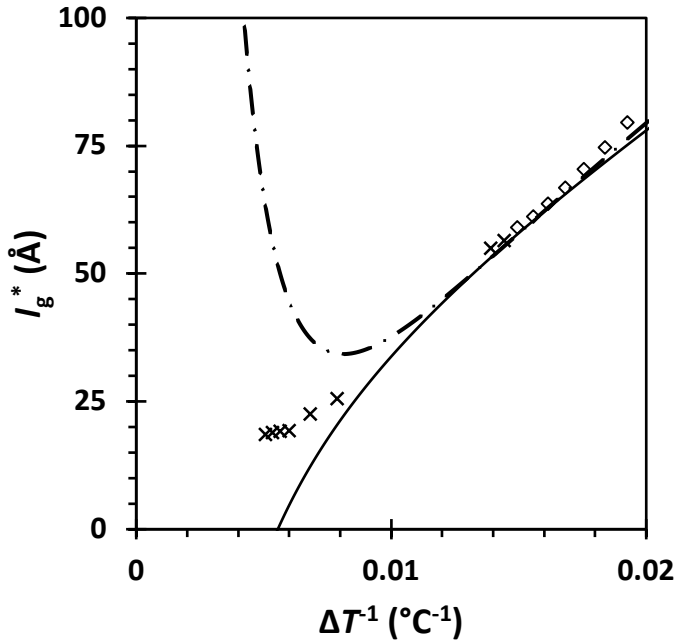

b)

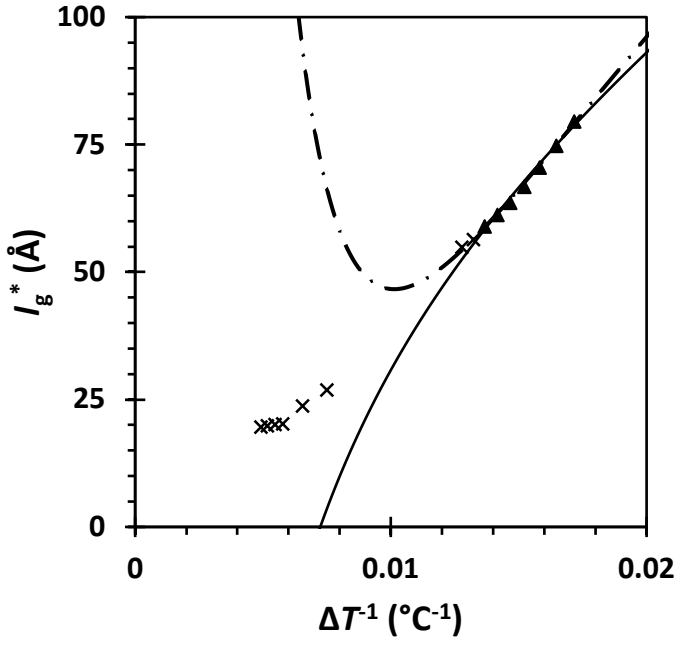

Figure 3.30: Relationship between the average initial lamellar thickness, l_g^*, and the inverse undercooling, ΔT, corresponding to zero-heating-rate initial melting temperature data with a) z = 0.38 ($T_m^{GT}(z = 0.38)$ = 103.4°C and $\sigma_e^o(z = 0.38)$ = 63.0 mJ.m^{-2}, Eqn. (3.26a)) and b) z = 0.50 ($T_m^{GT}(z = 0.50)$ = 109.6°C and $\sigma_e^o(z = 0.50)$ = 66.2 mJ.m^{-2}, Eqn. (3A.18a)). The markers (◇, ▲) in a) and b), respectively, are the lamellar thicknesses interpolated from Sheth,[44] and the (✕) were calculated by rearranging the Gibbs-Thomson equation (Eqn. (3.15)). The lines in both plots were calculated using a quadratic $\sigma_{ec}^k(\Delta T)$ (———) and a cubic $\sigma_{ec}^k(\Delta T)$ (— . — .). Only data for $T_x \geq$ 36.4°C were used to determine the coefficients for $\sigma_{ec}^k(\Delta T)$ (Table 3.9, Eqns. (3.25) and (3A.17)).

a)

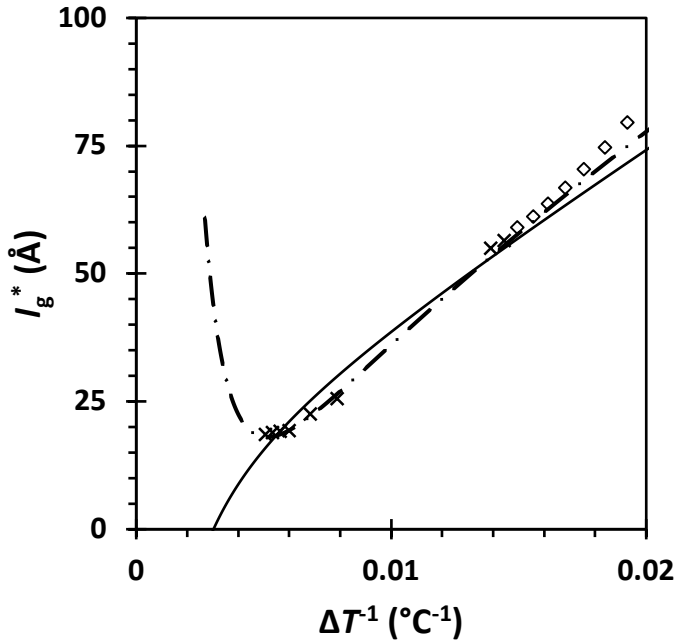

b)

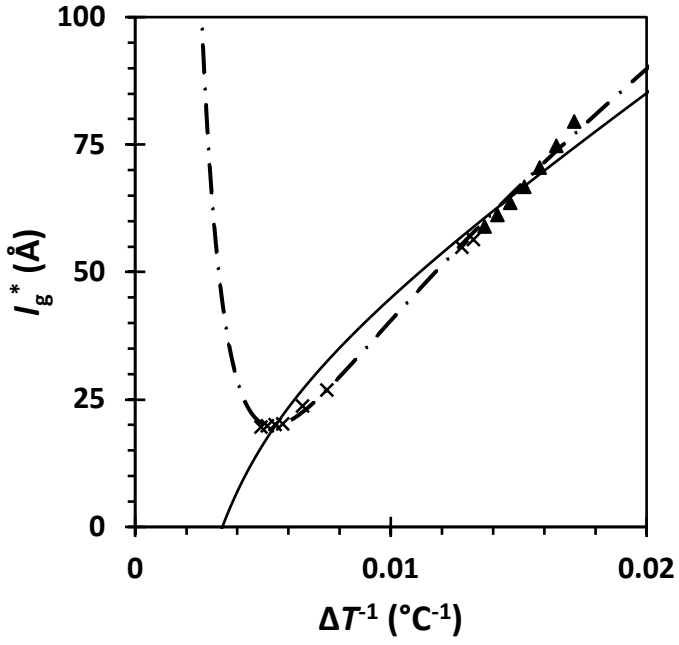

Figure 3.31: Relationship between the average initial lamellar thickness, l_g^*, and the inverse undercooling, ΔT, corresponding to zero-heating-rate initial melting temperature data with a) z = 0.38 ($T_m^{GT}(z = 0.38)$ = 103.4°C and $\sigma_e^o(z = 0.38)$ = 63.0 mJ.m^{-2}, Eqn. (3.26a)) and b) z = 0.50 ($T_m^{GT}(z = 0.50)$ = 109.6°C and $\sigma_e^o(z = 0.50)$ = 66.2 mJ.m^{-2} Eqn. (3A.18a)). The markers (◇,▲) in a) and b), respectively, are the lamellar thicknesses interpolated from Sheth,[44] and the (✕) were calculated by rearranging the Gibbs-Thomson equation (Eqn. (3.15)). The lines in both plots were calculated using a quadratic $\sigma_{ec}^k(\Delta T)$ (———) and a cubic $\sigma_{ec}^k(\Delta T)$ (— . — .). All temperatures (T_x = −94.1 to 51.4°C) were used to determine the coefficients for $\sigma_{ec}^k(\Delta T)$ (Table 3.10, Eqns. (3.25) and (3A.17)).

As a final consideration, we want to examine the implications polynomial kinetic fold surface free energy upon crystallization on Strobl's multistage crystallization model.[48-50, 118] This thermodynamic and kinetic model assumes that crystallization follows Ostwald's rule of stages by forming an intermediate mesophase prior to crystallization. In the multistage crystallization model, there are three different equilibrium transition temperatures, the amorphous-to-crystal transition temperature (T_{ac}^{∞} or T_{f}^{∞}), the mesophase-to-crystal transition temperature (T_{mc}^{∞} or T_{c}^{∞}), and the zero-growth temperature (T_{zg}). The amorphous-to-crystal transition temperature corresponds to the equilibrium melting temperature, and it is determined from the Gibbs-Thomson analysis (Eqn. (3.15)) (i.e. melting line). The mesophase-to-crystal equilibrium transition temperature is a virtual transition temperature that is always greater than the equilibrium melting temperature, and it is determined by linear extrapolation of the crystallization temperature as a function of the inverse lamellar thickness (i.e. crystallization line). This value controls the formation of the mesophase, and therefore the lamellar thickness. The crystallization line must intersect the melting line since the mesophase-to-crystal equilibrium transition temperature is greater than the equilibrium amorphous-to-crystal transition temperature. The zero-growth temperature controls the spherulite growth rate, and it is determined by extrapolation of the spherulite growth rate to 0. The zero-growth temperature is less than the amorphous-to-crystal equilibrium transition temperature.

The melting and crystallization temperatures are shown as a function of inverse lamellar thickness in Figure 3.32 for the data sets analyzed with melting kinetics exponents of z = 0.38 and 0.50. The crystallization and melting lines do not intersect for either data set because the melting temperatures are greater than the crystallization temperatures by a constant value. The equilibrium mesophase-to-crystal transition temperature is the same for the two data sets, but the equilibrium melting temperature increases ($T_{\mathrm{m}}^{\mathrm{GT}}(z = 0.38)$ = 103.4 ± 2.3°C and $T_{\mathrm{m}}^{\mathrm{GT}}(z = 0.50)$ = 109.6 ± 2.4°C, Table 3.3). The crystallization temperature as a function of inverse lamellar thickness becomes non-linear and extrapolates to the equilibrium melting temperature when the undercooling dependence of the kinetic

fold surface free energy upon crystallization is taken into account (Figs. 3.32a,b). Sheth[44] also found that the crystallization line extrapolated to a lower temperature than our Gibbs-Thomson results in a study on the same PCL sample. If the equilibrium mesophase-to-crystal transition temperature is lower than the equilibrium amorphous-to-crystal transition temperature, then the multistage thermodynamic scheme as proposed by Strobl no longer works. Polymer crystallization could still proceed through Ostwald's rule of stages, but mesophase formation would not be the rate-determining step in the phase change.

a)

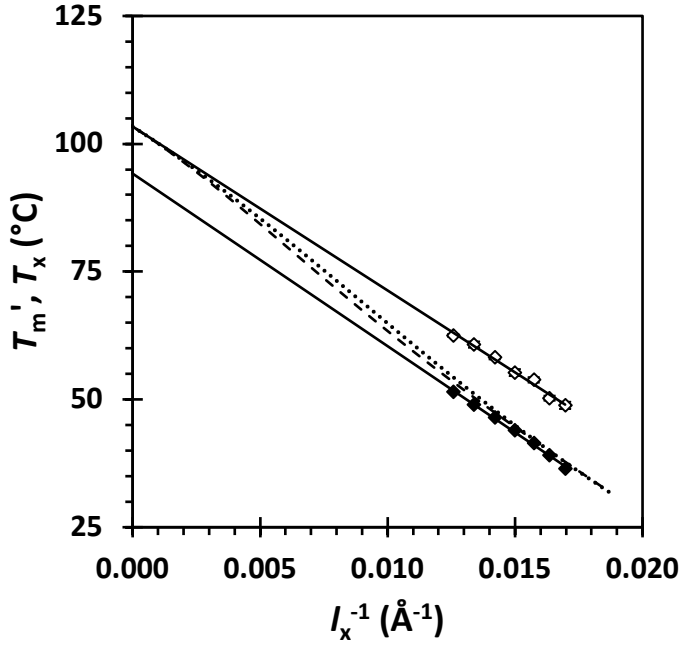

b)

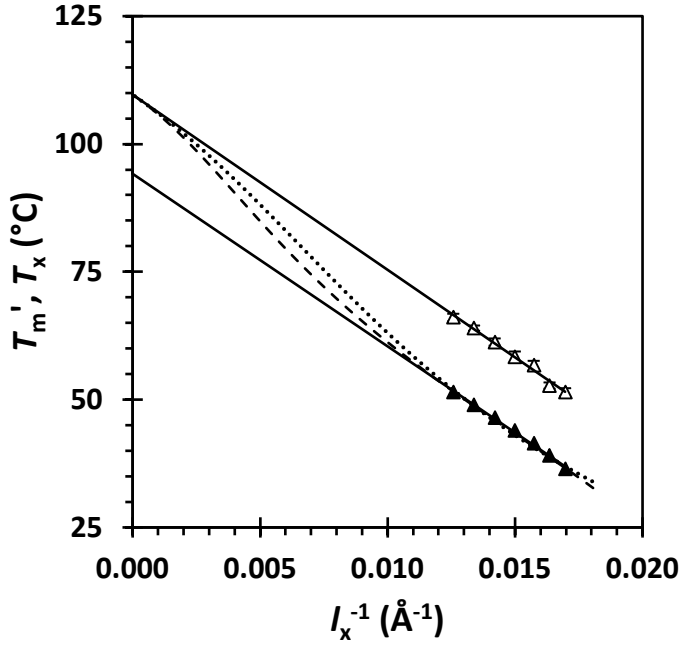

Figure 3.32: Relationship between both the zero-heating-rate initial melting temperatures (□, ◇, △), T_m', and the crystallization temperature (■, ◆, ▲), T_x, and the inverse lamellar thickness, l_x^{-1} for a) z = 0.38 and b) z = 0.50. The lines (_____) in both plots represent the Gibbs-Thomson melting line (Eqn. (3.15)) (empty markers) and Strobl's crystallization line (filled markers). The remaining lines in both plots represent lamellar thicknesses that were calculated with Eqn. (3.26a) using a quadratic $\sigma_{ec}^{k}(\Delta T)$ (.....) and with Eqn. (3A.18a) using a cubic $\sigma_{ec}^{k}(\Delta T)$ (_ _ _ _ .). Only $T_x \geq 36.4$°C were used to determine the coefficients for $\sigma_{ec}^{k}(\Delta T)$ (Table 3.9, Eqns. (3.25) and (3A.17)).

3.5 CONCLUSIONS

Flash differential scanning calorimetry was used to measure the melting temperature of poly(ε-caprolactone) as function of isothermal crystallization temperature and time over a 140°C temperature range. Two different experimental approaches to measuring melting temperatures were compared. It was found that the direct heating method yielded melting temperatures that are systematically larger than those obtained with the quench method. Analysis of the melting temperatures as a function of heating rate showed that the direct heating method tended toward a melting kinetics exponent of z = 0.49 ± 0.12 and the quench method tended toward z = 0.38 ± 0.06. The melting kinetics exponent did not depend on crystallization temperature or time. Despite the systematic difference between melting temperatures measured with the different methods, fixing the melting kinetics exponent for the heating rate analysis yielded zero-heating-rate melting temperatures that were indistinguishable within experimental error. The quench data had less error, and is the recommended method for measuring the melting temperature of PCL. As a result, we consider z = 0.38 as the most likely value of the melting kinetics exponent. The initial melting temperatures at each crystallization temperature were determined as the average of the melting temperatures measured over the short time interval where the first endothermic signals were detectable and the melting temperatures remained constant. The zero-heating-rate initial melting temperatures were determined for data collected with the quench method using z = 0.25, 0.38, and 0.50. The zero-heating-rate initial melting temperatures determined with z = 0.38 and 0.50 were shifted above the crystallization temperatures by a constant values, i.e. the melting temperatures as a function of crystallization temperature are parallel to the line $T_{\mathrm{m}}' = T_{\mathrm{x}}$.

The Gibbs-Thomson method was used to determine the equilibrium melting temperatures corresponding to zero-heating-rate initial melting temperatures with z = 0.25, 0.38, and 0.50 to yield $T_{\mathrm{m}}^{\mathrm{GT}}(z = 0.25)$ = 89.9 ± 2.2°C, $T_{\mathrm{m}}^{\mathrm{GT}}(z = 0.38)$ = 103.4 ± 2.3°C and $T_{\mathrm{m}}^{\mathrm{GT}}(z = 0.50)$ = 109.6 ± 2.4°C. These values are generally larger than previous reports in the literature. The conventional non-linear Hoffman-

Weeks analysis was conducted on the zero-heating-rate initial melting temperature data with z = 0.25 to obtain $T_{\mathrm{m}}^{\mathrm{NLHW}}(z = 0.25)$ = 94.6 ± 6.4°C. A linear extrapolation of this data yielded an equilibrium melting temperature that was 23°C lower. A modification was proposed to the non-linear Hoffman-Weeks model that incorporates a power series expansion of the undercooling into the kinetic fold surface free energy upon crystallization. It was demonstrated that accounting for non-linear dependence of the kinetic fold surface free energy upon crystallization allows the non-linear Hoffman-Weeks analysis to model the melting temperature as a function of crystallization temperature when the function is parallel to the line $T_{\mathrm{m}}' = T_{\mathrm{x}}$. Quadratic and cubic functions of undercooling were considered for the kinetic fold surface free energy upon crystallization for the data with z = 0.38 and 0.50. Incorporating either a quadratic or a cubic function of undercooling into the kinetic fold surface free energy upon crystallization permits accurate modeling of the zero-heating-rate initial melting temperature data with z = 0.38 and 0.50 across the entire range of crystallization temperatures, despite the fact that the data is parallel to the line $T_{\mathrm{m}}' = T_{\mathrm{x}}$.

The undercooling dependence of the kinetic fold surface free energy upon crystallization was analyzed, and it was found to be a non-linear function of undercooling which exhibited a maximum value at intermediate undercoolings and leveled off at large undercoolings. The behavior is fully captured using a cubic function of undercooling. The effect of the non-linear kinetic fold surface free energy upon crystallization on the lamellar thickness as a function of undercooling was considered, and linearity was observed in the range of crystallization temperatures where lamellar thicknesses are typically measured. Analysis of the crystallization and melting temperatures as functions of inverse lamellar thickness revealed that Strobl's multiphase thermodynamic scheme for polymer crystallization should not apply to PCL because the mesophase-to-crystal equilibrium transition temperature is lower than the amorphous-to-crystal equilibrium transition temperature. Accounting for the temperature dependence of the kinetic fold surface free energy upon crystallization led to non-linearity in the crystallization temperature as a

function of inverse lamellar thickness. As a result, the crystallization and melting lines both extrapolated to the equilibrium melting temperature.

Several groups have observed that the melting temperature as a function of crystallization temperature lies parallel to the line $T_{\mathrm{m}}' = T_{\mathrm{x}}$ for other crystal-fixed polymers.[9, 11-13, 15, 20-25] Future work should focus on correlating the initial melting and crystallization temperatures of crystal-fixed polymers using fast differential scanning calorimetry. Additionally, reliable lamellar thickness data should be obtained to conduct the Gibbs-Thomson analysis with melting temperatures measured with FDSC. These results can then be used to validate our proposed modification to the non-linear Hoffman-Weeks model that incorporates a power series expansion about the undercooling in the kinetic fold surface free energy upon crystallization.

3.6 ACKNOWLEDGEMENTS

The study of the original lamellar thickness data by Swapnil Sheth was funded by the National Science Foundation (NSF DMR 0923107). The original small-angle X-ray scattering experiments were conducted at Argonne National Lab on its DND-CAT operated beamline at the APS using a portion of Dr. Robert Moore's APS beam time. We would like to thank Hadi Mohammadi for helpful discussions and input throughout the course of data collection and analysis. We would also like to thank TA Instruments for the temporary loan of a TA Q2000 conventional differential scanning calorimeter.

3.7 APPENDIX A: DERIVATIONS AND ANALYSES OF THE GENERALIZED NON-LINEAR HOFFMAN-WEEKS EQUATION WITH POLYNOMIAL $\boldsymbol{\sigma_{\mathrm{ec}}^{\mathrm{k}}(\Delta T)}$

In the following we will solve for the points of intersection (i.e. roots) between the non-linear Hoffman-Weeks equation ($T_{\mathrm{m}}'(T_{\mathrm{x}})$) and the line $T_{\mathrm{m}}' = T_{\mathrm{x}}$. We will also analyze the consequences of the sign of a and whether $\frac{\sigma_{\mathrm{em}}}{\sigma_{\mathrm{ec}}^{\mathrm{o}}}$ is less than, equal to, or greater than unity for the case of a kinetic fold surface

free energy upon crystallization that is a linear function of undercooling. Note that the ratio of fold surface free energies is inverted relative to the MX equation (Eqn. (3.20)). The points of intersection between the non-linear Hoffman-Weeks equation and the line $T_{\mathrm{m}}' = T_{\mathrm{x}}$ will also be determined for the case of a kinetic fold surface free energy upon crystallization that is a quadratic function of undercooling. We will derive the relevant non-linear Hoffman-Weeks equations for a kinetic fold surface free energy upon crystallization that is a cubic function of undercooling and give consideration to solving for the points of intersection with the line $T_{\mathrm{m}}' = T_{\mathrm{x}}$.

3.7.1 Linear $\boldsymbol{\sigma_{ec}^{k}(\Delta T)}$: $\boldsymbol{\sigma_{ec}^{k} = \sigma_{ec}^{o}(1 + y\Delta T)}$

Recall Eqn. (3.19)

$$T_{\mathrm{m}}' = T_{\mathrm{m}}\left\{1 - \left(\frac{1}{\gamma}\right)\left(\frac{T_{\mathrm{m}} - T_{\mathrm{x}}}{T_{\mathrm{m}}}\right)\left(\frac{\sigma_{\mathrm{em}}}{\sigma_{\mathrm{ec}}^{\mathrm{o}}}\right)\left[\frac{1}{1 + \frac{C_2\Delta H_{\mathrm{f}}^{\mathrm{o}}}{2\sigma_{\mathrm{ec}}^{\mathrm{o}}}\left(\frac{T_{\mathrm{m}} - T_{\mathrm{x}}}{T_{\mathrm{m}}}\right)}\right]\right\} \tag{3A.1}$$

The Hoffman-Weeks equation will have roots when $(T_{\mathrm{m}}' - T_{\mathrm{x}})$ = 0, so the goal is to obtain a function $(T_{\mathrm{m}}' - T_{\mathrm{x}})$ and analytically solve for the roots. We begin by distributing all of the terms on the RHS of Eqn. (3A.1) to obtain

$$T_{\mathrm{m}}' = T_{\mathrm{m}} - T_{\mathrm{m}}\left(\frac{1}{\gamma}\right)\left(\frac{\sigma_{\mathrm{em}}}{\sigma_{\mathrm{ec}}^{\mathrm{o}}}\right)\left[\frac{1}{1 + \frac{C_2\Delta H_{\mathrm{f}}^{\mathrm{o}}}{2\sigma_{\mathrm{ec}}^{\mathrm{o}}}\left(\frac{T_{\mathrm{m}} - T_{\mathrm{x}}}{T_{\mathrm{m}}}\right)}\right] + T_{\mathrm{x}}\left(\frac{1}{\gamma}\right)\left(\frac{\sigma_{\mathrm{em}}}{\sigma_{\mathrm{ec}}^{\mathrm{o}}}\right)\left[\frac{1}{1 + \frac{C_2\Delta H_{\mathrm{f}}^{\mathrm{o}}}{2\sigma_{\mathrm{ec}}^{\mathrm{o}}}\left(\frac{T_{\mathrm{m}} - T_{\mathrm{x}}}{T_{\mathrm{m}}}\right)}\right] \tag{3A.2}$$

Grouping the second and third terms on the RHS of Eqn. (3A.2) and rearranging yields

$$T_{\mathrm{m}}' = T_{\mathrm{m}} - T_{\mathrm{m}}\left(\frac{1}{\gamma}\right)\left(\frac{\sigma_{\mathrm{em}}}{\sigma_{\mathrm{ec}}^{\mathrm{o}}}\right)\left[\frac{(T_{\mathrm{m}} - T_{\mathrm{x}})}{1 + \frac{C_2\Delta H_{\mathrm{f}}^{\mathrm{o}}}{2\sigma_{\mathrm{ec}}^{\mathrm{o}}}\left(\frac{T_{\mathrm{m}} - T_{\mathrm{x}}}{T_{\mathrm{m}}}\right)}\right] \tag{3A.3}$$

Subtracting T_{x} from both sides yields the equation of interest

$$(T_{\mathrm{m}}' - T_{\mathrm{x}}) = (T_{\mathrm{m}} - T_{\mathrm{x}}) - T_{\mathrm{m}}\left(\frac{1}{\gamma}\right)\left(\frac{\sigma_{\mathrm{em}}}{\sigma_{\mathrm{ec}}^{\mathrm{o}}}\right)\left[\frac{(T_{\mathrm{m}} - T_{\mathrm{x}})}{1 + \frac{C_2\Delta H_{\mathrm{f}}^{\mathrm{o}}}{2\sigma_{\mathrm{ec}}^{\mathrm{o}}}\left(\frac{T_{\mathrm{m}} - T_{\mathrm{x}}}{T_{\mathrm{m}}}\right)}\right] \tag{3A.4}$$

Equating Eqn. (3A.4) to 0 and rearranging to obtain a common denominator yields

$$(T_\mathrm{m}-T_\mathrm{x})\left[\frac{T_\mathrm{m}+\frac{C_2\Delta H_\mathrm{f}^\mathrm{o}}{2\sigma_\mathrm{ec}^\mathrm{o}}(T_\mathrm{m}-T_\mathrm{x})}{T_\mathrm{m}+\frac{C_2\Delta H_\mathrm{f}^\mathrm{o}}{2\sigma_\mathrm{ec}^\mathrm{o}}(T_\mathrm{m}-T_\mathrm{x})}\right]-T_\mathrm{m}\left(\frac{1}{\gamma}\right)\left(\frac{\sigma_\mathrm{em}}{\sigma_\mathrm{ec}^\mathrm{o}}\right)\left[\frac{(T_\mathrm{m}-T_\mathrm{x})}{T_\mathrm{m}+\frac{C_2\Delta H_\mathrm{f}^\mathrm{o}}{2\sigma_\mathrm{ec}^\mathrm{o}}\left(\frac{T_\mathrm{m}-T_\mathrm{x}}{T_\mathrm{m}}\right)}\right]=0 \tag{3A.5}$$

Considering the numerator of Eqn. (3A.5) gives

$$\left[T_\mathrm{m}-T_\mathrm{m}\left(\frac{1}{\gamma}\right)\left(\frac{\sigma_\mathrm{em}}{\sigma_\mathrm{ec}^\mathrm{o}}\right)\right](T_\mathrm{m}-T_\mathrm{x})+\frac{C_2\Delta H_\mathrm{f}^\mathrm{o}}{2\sigma_\mathrm{ec}^\mathrm{o}}(T_\mathrm{m}-T_\mathrm{x})^2=0 \tag{3A.6}$$

The first root is trivial and occurs when $T_\mathrm{x}=T_\mathrm{m}$. This should be obvious simply from the definition of T_m. The second root can be found by dividing the LHS of Eqn. (3A.6) by $(T_\mathrm{m}-T_\mathrm{x})$ and solving for T_x.

$$\left[T_\mathrm{m}-T_\mathrm{m}\left(\frac{1}{\gamma}\right)\left(\frac{\sigma_\mathrm{em}}{\sigma_\mathrm{ec}^\mathrm{o}}\right)\right]+\frac{C_2\Delta H_\mathrm{f}^\mathrm{o}}{2\sigma_\mathrm{ec}^\mathrm{o}}(T_\mathrm{m}-T_\mathrm{x})=0 \tag{3A.7a}$$

$$T_\mathrm{x}=\frac{2\sigma_\mathrm{ec}^\mathrm{o}T_\mathrm{m}}{C_2\Delta H_\mathrm{f}^\mathrm{o}}\left[1-\frac{1}{\gamma}\left(\frac{\sigma_\mathrm{em}}{\sigma_\mathrm{ec}^\mathrm{o}}\right)+\frac{C_2\Delta H_\mathrm{f}^\mathrm{o}}{2\sigma_\mathrm{ec}^\mathrm{o}}\right] \tag{3A.7b}$$

$$T_\mathrm{x}=T_\mathrm{m}\left[1+\frac{1}{a}\left(1-\frac{1}{\gamma}\left(\frac{\sigma_\mathrm{em}}{\sigma_\mathrm{ec}^\mathrm{o}}\right)\right)\right] \tag{3A.7c}$$

Recall that $a=\frac{C_2\Delta H_\mathrm{f}^\mathrm{o}}{2\sigma_\mathrm{ec}^\mathrm{o}}$ (Eqn. (3.23)) from the MX equation (Eqn. (3.20)).

There are now six possible cases to consider for the second root of the Hoffman-Weeks equation corresponding to the different combinations of the following conditions: $a > 0$, $a < 0$, $\left(\frac{\sigma_\mathrm{em}}{\sigma_\mathrm{ec}^\mathrm{o}}\right) = 1$, $\left(\frac{\sigma_\mathrm{em}}{\sigma_\mathrm{ec}^\mathrm{o}}\right) > 1$, and $\left(\frac{\sigma_\mathrm{em}}{\sigma_\mathrm{ec}^\mathrm{o}}\right) < 1$. The three cases when $a = 0$ yield $T_{\mathrm{x,root}} = \infty$ as the second root to the Hoffman-Weeks equation. For simplicity, we are assuming that $\gamma = 1$ in the following discussion, but it could be further generalized for $\gamma \neq 1$ and applied to thickened lamellae. All six cases will start from Eqn. (3A.7c).

3.7.1.1 Case 1: $a > 0$, $\left(\frac{\sigma_\mathrm{em}}{\sigma_\mathrm{ec}^\mathrm{o}}\right) = 1$

This case corresponds to the conventional NLHW treatment originally proposed by Marand et al.[58] Since $\left(\frac{\sigma_\mathrm{em}}{\sigma_\mathrm{ec}^\mathrm{o}}\right) = 1$ then the product inside the square brackets of Eqn. (3A.7c) will be equal to 0. Thus,

$T_{x,root}$ = T_m. The melting temperature as a function of crystallization temperature exhibits positive curvature due to the positive value of a, and it is tangent to the line $T_m' = T_x$ at T_x = T_m. This description loses its physical meaning above the equilibrium melting temperature because crystallization, and therefore melting, cannot occur above the equilibrium melting temperature.

3.7.1.2 Case 2: $a < 0$, $\left(\frac{\sigma_{em}}{\sigma_{ec}^o}\right) = 1$

Since $\left(\frac{\sigma_{em}}{\sigma_{ec}^o}\right)$ = 1 then product inside the square brackets of Eqn. (3A.7c) will be equal to 0. Therefore, $T_{x,root}$ = T_m, just like Case 1. However, the melting temperature as a function of crystallization temperature displays negative curvature due to the negative value of a, and it is tangent to the line $T_m' = T_x$ at T_x = T_m. This case predicts that crystalline lamellae would melt at temperatures below the crystallization temperature, so crystalline lamellae would never form under these conditions. This description has no physical meaning at any crystallization temperature.

3.7.1.3 Case 3: $a > 0$, $\left(\frac{\sigma_{em}}{\sigma_{ec}^o}\right) > 1$

Since $\left(\frac{\sigma_{em}}{\sigma_{ec}^o}\right) > 1$ and $a > 0$ then the product inside the square brackets of Eqn. (3A.7c) will be negative. Hence, $T_{x,root} < T_m$. The melting temperature as a function of crystallization temperature exhibits positive curvature due to the positive value of a. The melting temperature would be greater than the crystallization temperature when $T_x < T_{x,root}$ and when $T_x > T_m$, and the melting temperature would be less than the crystallization temperature when $T_{x,root} < T_x < T_m$. It seems obvious that this description has no physical meaning.

3.7.1.4 Case 4: $a < 0$, $\left(\frac{\sigma_{em}}{\sigma_{ec}^o}\right) > 1$

Since $\left(\frac{\sigma_{em}}{\sigma_{ec}^o}\right) > 1$ and $a < 0$ then the product inside the square brackets of Eqn. (3A.7c) will be positive. As a result, $T_{x,root} > T_m$. The melting temperature as a function of crystallization temperature displays negative curvature resulting from the negative value of a. The melting temperature would be less

than the crystallization temperature when $T_x < T_m$ and when $T_x > T_{x,root}$, and the melting temperature would be greater than the crystallization temperature when $T_m < T_x < T_{x,root}$. This case is not physically meaningful.

3.7.1.5 Case 5: $a > 0$, $\left(\frac{\sigma_{em}}{\sigma_{ec}^{o}}\right) < 1$

Since $\left(\frac{\sigma_{em}}{\sigma_{ec}^{o}}\right) < 1$ and $a > 0$ then the product inside the square brackets of Eqn. (3A.7c) will be positive. Consequently, $T_{x,root} > T_m$. The melting temperature as a function of crystallization temperature exhibits positive curvature because a is positive. The melting temperature would be greater than the crystallization temperature when $T_x < T_m$ and when $T_x > T_{x,root}$, and the melting temperature would be less than the crystallization temperature when $T_m < T_x < T_{x,root}$.This description loses physical meaning above the equilibrium melting temperature.

3.7.1.6 Case 6: $a < 0$, $\left(\frac{\sigma_{em}}{\sigma_{ec}^{o}}\right) < 1$

This case corresponds to the experimental data presented in the present work. Since $\left(\frac{\sigma_{em}}{\sigma_{ec}^{o}}\right) < 1$ and $a < 0$ then the product inside the square brackets of Eqn. (3A.7c). Thus, $T_x < T_m$. The melting temperature as a function of crystallization temperature shows negative curvature. The melting temperature would be less than the crystallization temperature when $T_x < T_{x,root}$ and when $T_x > T_m$, and the melting temperature would be greater than the crystallization temperature when $T_{x,root} < T_x < T_m$. The description above T_m seems reasonable because no lamellae can form above T_m. The description below $T_{x,root}$ also seems reasonable in light of the fact that we presented experimental data showing that within ~70°C of T_g the $T_m'(\beta = 0) \approx T_x$ with $z = 0.38$, meaning that the lamellae being formed are not stable above the crystallization temperature at which they were formed.

3.7.2 Quadratic $\sigma_{ec}^{k}(\Delta T)$: $\sigma_{ec}^{k} = \sigma_{ec}^{o}\left(1 + y\Delta T + p\Delta T^2\right)$

The relevant non-linear Hoffman-Weeks equations were derived for the case of a second-order kinetic fold surface free energy upon crystallization in subsection 3.4.6 (Eqns. (3.25) through (3.31)). Only

the points of intersection between the melting temperature as a function of crystallization temperature and the line $T_m' = T_x$ will be considered herein. Let us start from an equation of the same form as Eqn. (3A.4) except with C_2 replaced by $C_2(\Delta T)$

$$(T_m' - T_x) = (T_m - T_x) - T_m\left(\frac{1}{\gamma}\right)\left(\frac{\sigma_{em}}{\sigma_{ec}^o}\right)\left[\frac{(T_m - T_x)}{1 + \frac{C_2(\Delta T)\Delta H_f^o}{2\sigma_{ec}^o}\left(\frac{T_m - T_x}{T_m}\right)}\right] \tag{3A.8}$$

Substituting for $C_2(\Delta T)$ from Eqn. (3.26b) and rearranging to obtain a common denominator yields

$$\begin{aligned}(T_m - T_x)&\left[\frac{T_m + pT_m(T_m - T_x)^2 + \frac{C_2\Delta H_f^o}{2\sigma_{ec}^o}(T_m - T_x)}{T_m + pT_m(T_m - T_x)^2 + \frac{C_2\Delta H_f^o}{2\sigma_{ec}^o}(T_m - T_x)}\right] \\ &- T_m\left(\frac{1}{\gamma}\right)\left(\frac{\sigma_{em}}{\sigma_{ec}^o}\right)\left[\frac{(T_m - T_x)}{T_m + pT_m(T_m - T_x)^2 + \frac{C_2\Delta H_f^o}{2\sigma_{ec}^o}\left(\frac{T_m - T_x}{T_m}\right)}\right] = 0\end{aligned} \tag{3A.9}$$

Considering the numerator of Eqn. (3A.9) gives

$$\left[T_m - T_m\left(\frac{1}{\gamma}\right)\left(\frac{\sigma_{em}}{\sigma_{ec}^o}\right)\right](T_m - T_x) + \frac{C_2\Delta H_f^o}{2\sigma_{ec}^o}(T_m - T_x)^2 + pT_m(T_m - T_x)^3 = 0 \tag{3A.10}$$

The first root is trivial and occurs when $T_x = T_m$. The second and third roots can be found by dividing the LHS of Eqn. (3A.10) by $(T_m - T_x)$ and solving for T_x

$$pT_mT_x^2 - \left(2pT_m^2 + \frac{C_2\Delta H_f^o}{2\sigma_{ec}^o}\right)T_x + \left\{T_m\left[1 - \left(\frac{1}{\gamma}\right)\left(\frac{\sigma_{em}}{\sigma_{ec}^o}\right) + \frac{C_2\Delta H_f^o}{2\sigma_{ec}^o} + pT_m^2\right]\right\} = 0 \tag{3A.11}$$

Eqn. (3A.11) is simply a quadratic equation of the form

$$c_1x^2 + c_2x + c_3 \tag{3A.12}$$

where $x = T_x$ and

$$c_1 = pT_m \tag{3A.13a}$$

$$c_2 = -\left(2pT_m^2 + \frac{C_2\Delta H_f^o}{2\sigma_{ec}^o}\right) \tag{3A.13b}$$

$$c_3 = \left\{ T_\mathrm{m} \left[1 - \left(\frac{1}{\gamma}\right)\left(\frac{\sigma_\mathrm{em}}{\sigma_\mathrm{ec}^\mathrm{o}}\right) + \frac{C_2 \Delta H_\mathrm{f}^\mathrm{o}}{2\sigma_\mathrm{ec}^\mathrm{o}} + pT_\mathrm{m}^2 \right] \right\} \tag{3A.13c}$$

The roots to Eqn. (3A.11) are determined using the quadratic formula such that

$$T_\mathrm{x} = \frac{-c_2 \pm \sqrt{c_2^2 - 4c_1 c_3}}{2c_1} \tag{3A.14}$$

Substituting the definitions of c_1, c_2, and c_3 in Eqn. (3A.14) and rearranging yields the second and third roots as

$$T_\mathrm{x} = T_\mathrm{m} \left\{ \frac{2b + a \pm \sqrt{a^2 - 4b\left[1 - \left(\frac{1}{\gamma}\right)\left(\frac{\sigma_\mathrm{em}}{\sigma_\mathrm{ec}^\mathrm{o}}\right)\right]}}{2b} \right\} \tag{3A.15}$$

where $b = pT_\mathrm{m}^2$ and $a = \frac{C_2 \Delta H_\mathrm{f}^\mathrm{o}}{2\sigma_\mathrm{ec}^\mathrm{o}}$. Considering the case of $\gamma = 1$ and $\left(\frac{\sigma_\mathrm{em}}{\sigma_\mathrm{ec}^\mathrm{o}}\right) = 1$ results in

$$T_\mathrm{x} = T_\mathrm{m} \tag{3A.16a}$$

$$T_\mathrm{x} = T_\mathrm{m}\left(1 + \frac{a}{b}\right) \tag{3A.16b}$$

3.7.3 Cubic $\boldsymbol{\sigma_{ec}^{k}(\Delta T)}$: $\boldsymbol{\sigma_{ec}^{k} = \sigma_{ec}^{o}\left(1 + y\Delta T + p\Delta T^2 + q\Delta T^3\right)}$

We shall assume that the kinetic fold surface free energy upon crystallization has the following functional form

$$\sigma_\mathrm{ec}^\mathrm{k} = \sigma_\mathrm{ec}^\mathrm{o}(1 + y\Delta T + p\Delta T^2 + q\Delta T^3) \tag{3A.17}$$

where y, p, and q are constants. Substituting Eqn. (3A.17) into the expression for initial lamellar thickness, Eqn. (3.9), yields

$$l_\mathrm{g}^* = \frac{2\sigma_\mathrm{ec}^\mathrm{o} T_\mathrm{m}}{\Delta H_\mathrm{f}^\mathrm{o} \Delta T} + \left(\frac{2\sigma_\mathrm{ec}^\mathrm{o} y T_\mathrm{m}}{\Delta H_\mathrm{f}^\mathrm{o}} + \frac{2\sigma_\mathrm{ec}^\mathrm{o} p \Delta T T_\mathrm{m}}{\Delta H_\mathrm{f}^\mathrm{o}} + \frac{2\sigma_\mathrm{ec}^\mathrm{o} q \Delta T^2 T_\mathrm{m}}{\Delta H_\mathrm{f}^\mathrm{o}} + \delta l \right) \tag{3A.18a}$$

$$l_\mathrm{g}^* = \frac{C_1}{\Delta T} + C_2(\Delta T) \tag{3A.18b}$$

Where C_1 has the same definition from section 3.2 (theoretical background) and $C_2(\Delta T)$ is equal to the four terms in parentheses on the right-hand-side of Eqn. (3A.18a). Combining the expressions for the initial lamellar thickness, Eqn. (3A.18b), with the Gibbs-Thomson equation, Eqn. (3.15), and rearranging yields the modified non-linear Hoffman-Weeks equation

$$T_{\mathrm{m}}' = T_{\mathrm{m}}\left\{1 - \left(\frac{1}{\gamma}\right)\left(\frac{T_{\mathrm{m}} - T_{\mathrm{x}}}{T_{\mathrm{m}}}\right)\left(\frac{\sigma_{\mathrm{em}}}{\sigma_{\mathrm{ec}}^{\mathrm{o}}}\right)\left[\frac{1}{1 + \frac{C_2(\Delta T)\Delta H_{\mathrm{f}}^{\mathrm{o}}}{2\sigma_{\mathrm{ec}}^{\mathrm{o}}}\left(\frac{T_{\mathrm{m}} - T_{\mathrm{x}}}{T_{\mathrm{m}}}\right)}\right]\right\} \tag{3A.19}$$

The modified MX equation can now be obtained by rearranging Eqn. (3A.19)

$$\frac{T_{\mathrm{m}}}{T_{\mathrm{m}} - T_{\mathrm{m}}'} = \gamma\left(\frac{\sigma_{\mathrm{ec}}^{\mathrm{o}}}{\sigma_{\mathrm{em}}}\right)\left[\frac{T_{\mathrm{m}}}{T_{\mathrm{m}} - T_{\mathrm{x}}} + pT_{\mathrm{m}}^2\left(\frac{T_{\mathrm{m}} - T_{\mathrm{x}}}{T_{\mathrm{m}}}\right) + pT_{\mathrm{m}}^3\left(\frac{T_{\mathrm{m}} - T_{\mathrm{x}}}{T_{\mathrm{m}}}\right)^2 + \frac{\Delta H_{\mathrm{f}}^{\mathrm{o}}}{2\sigma_{\mathrm{e}}^{\mathrm{o}}}\left(\frac{2\sigma_{\mathrm{ec}}^{\mathrm{o}} y T_{\mathrm{m}}}{\Delta H_{\mathrm{f}}^{\mathrm{o}}} + \delta l\right)\right] \tag{3A.20a}$$

$$M = \gamma\left(\frac{\sigma_{\mathrm{ec}}^{\mathrm{o}}}{\sigma_{\mathrm{em}}}\right)\left[X + \frac{b}{X} + \frac{c}{X^2} + a\right] \tag{3A.20b}$$

where $b = pT_{\mathrm{m}}^2$, $c = qT_{\mathrm{m}}^3$, and $a = \frac{C_2\Delta H_{\mathrm{f}}^{\mathrm{o}}}{2\sigma_{\mathrm{ec}}^{\mathrm{o}}}$.

Now, we will start from Eqn. (3A.8) to solve for the points of intersection between the melting temperature as a function of crystallization temperature and the line $T_{\mathrm{m}}' = T_{\mathrm{x}}$. Substituting for $C_2(\Delta T)$ using Eqn. (3A.18a) and rearranging to obtain a common denominator yields

$$\begin{aligned}(T_{\mathrm{m}} - T_{\mathrm{x}})&\left[\frac{T_{\mathrm{m}} + pT_{\mathrm{m}}(T_{\mathrm{m}} - T_{\mathrm{x}})^2 + qT_{\mathrm{m}}(T_{\mathrm{m}} - T_{\mathrm{x}})^3 + \frac{C_2\Delta H_{\mathrm{f}}^{\mathrm{o}}}{2\sigma_{\mathrm{ec}}^{\mathrm{o}}}(T_{\mathrm{m}} - T_{\mathrm{x}})}{T_{\mathrm{m}} + pT_{\mathrm{m}}(T_{\mathrm{m}} - T_{\mathrm{x}})^2 + qT_{\mathrm{m}}(T_{\mathrm{m}} - T_{\mathrm{x}})^3 + \frac{C_2\Delta H_{\mathrm{f}}^{\mathrm{o}}}{2\sigma_{\mathrm{ec}}^{\mathrm{o}}}(T_{\mathrm{m}} - T_{\mathrm{x}})}\right] \\ &- T_{\mathrm{m}}\left(\frac{1}{\gamma}\right)\left(\frac{\sigma_{\mathrm{em}}}{\sigma_{\mathrm{ec}}^{\mathrm{o}}}\right)\left[\frac{(T_{\mathrm{m}} - T_{\mathrm{x}})}{T_{\mathrm{m}} + pT_{\mathrm{m}}(T_{\mathrm{m}} - T_{\mathrm{x}})^2 + qT_{\mathrm{m}}(T_{\mathrm{m}} - T_{\mathrm{x}})^3 + \frac{C_2\Delta H_{\mathrm{f}}^{\mathrm{o}}}{2\sigma_{\mathrm{ec}}^{\mathrm{o}}}\left(\frac{T_{\mathrm{m}} - T_{\mathrm{x}}}{T_{\mathrm{m}}}\right)}\right] = 0\end{aligned} \tag{3A.21}$$

Considering the numerator of Eqn. (3A.21) results in

$$\left[T_{\mathrm{m}} - T_{\mathrm{m}}\left(\frac{1}{\gamma}\right)\left(\frac{\sigma_{\mathrm{em}}}{\sigma_{\mathrm{ec}}^{\mathrm{o}}}\right)\right](T_{\mathrm{m}} - T_{\mathrm{x}}) + \frac{C_2\Delta H_{\mathrm{f}}^{\mathrm{o}}}{2\sigma_{\mathrm{ec}}^{\mathrm{o}}}(T_{\mathrm{m}} - T_{\mathrm{x}})^2 + pT_{\mathrm{m}}(T_{\mathrm{m}} - T_{\mathrm{x}})^3 + qT_{\mathrm{m}}(T_{\mathrm{m}} - T_{\mathrm{x}})^4 = 0 \tag{3A.22}$$

The first root is trivial and occurs when $T_x = T_m$. The second, third, and fourth roots can be found by dividing the LHS of Eqn. (3A.22) by $(T_m - T_x)$ and solving for T_x.

$$-qT_mT_x^3 + (3qT_m^2 + pT_m)T_x^2 - \left(3qT_m^3 + 2pT_m^2 + \frac{C_2\Delta H_f^o}{2\sigma_{ec}^o}\right)T_x + \left\{T_m\left[1 - \left(\frac{1}{\gamma}\right)\left(\frac{\sigma_{em}}{\sigma_{ec}^o}\right) + \frac{C_2\Delta H_f^o}{2\sigma_{ec}^o} + qT_m^3 + pT_m^2\right]\right\} = 0 \quad \text{(3A.23)}$$

which is a cubic equation of the form

$$c_1x^3 + c_2x^2 + c_3x + c_4 \quad \text{(3A.24)}$$

where $x = T_x$ and

$$c_1 = -qT_m \quad \text{(3A.25a)}$$

$$c_2 = 3qT_m^2 + pT_m \quad \text{(3A.25b)}$$

$$c_3 = -\left(3qT_m^3 + 2pT_m^2 + \frac{C_2\Delta H_f^o}{2\sigma_{ec}^o}\right) \quad \text{(3A.25c)}$$

$$c_4 = \left\{T_m\left[1 - \left(\frac{1}{\gamma}\right)\left(\frac{\sigma_{em}}{\sigma_{ec}^o}\right) + \frac{C_2\Delta H_f^o}{2\sigma_{ec}^o} + qT_m^3 + pT_m^2\right]\right\} \quad \text{(3A.25d)}$$

The number of real and complex roots to Eqn. (3A.23) can be determined by the discriminant, Δ, of the cubic equation

$$\Delta = 18c_1c_2c_3c_4 - 4c_2^3c_4 + c_2^2c_3^2 - 4c_1c_3^3 - 27c_1^2c_4^2 \quad \text{(3A.26)}$$

If Δ > 0, then Eqn. (3A.23) has three real, distinct roots. If Δ = 0, then Eqn. (3A.23) has three real roots, with either a double root or a triple root. If Δ < 0, then Eqn. (3A.23) has one real root and two non-real, complex conjugate roots. The process of determining the roots in terms of the coefficients is tedious given the complicated definitions of the coefficients (Eqns. (3A.25a), (3A.25b), (3A.25c), and (3A.25d)). As such, we will end the discussion by noting that there is always at least one additional point of intersection between the melting temperature as a function of crystallization temperature and the line $T_m' = T_x$, which

could be the equilibrium melting temperature. In the case of our results over the entire range of crystallization temperatures, we found $\Delta < 0$ for the z = 0.38 data such that the only additional real root was T_{x} = $T_{\mathrm{m}}^{GT}(z = 0.38)$ = 103.4°C. However, we found $\Delta > 0$ for the z = 0.50 data, and the three additional roots were T_{x} = −55.9, −44.8, and $T_{\mathrm{m}}^{GT}(z = 0.50)$ = 109.6°C.

3.8 REFERENCES

1. Watson, E. S.; O'Neill, M. J.; Justin, J.; Brenner, N., A Differential Scanning Calorimeter for Quantitative Differential Thermal Analysis. *Analytical Chemistry* **1964,** *36* (7), 1233-1238.

2. Watson, E. S. O. N., M. J. Differential Microcalorimeter. U.S. Patent 3,263,484, Augst 2, 1966.

3. Toda, A.; Androsch, R.; Schick, C., Insights into polymer crystallization and melting from fast scanning chip calorimetry. *Polymer* **2016,** *91*, 239-263.

4. Toda, A.; Konishi, M., An evaluation of thermal lags of fast-scan microchip DSC with polymer film samples. *Thermochim. Acta* **2014,** *589*, 262-269.

5. Vanden Poel, G.; Istrate, D.; Magon, A.; Mathot, V., Performance and calibration of the Flash DSC 1, a new, MEMS-based fast scanning calorimeter. *J. Therm. Anal. Calorim.* **2012,** *110* (3), 1533-1546.

6. Li, Z.; Wang, J.; Pérez‐Camargo, R. A.; Müller, A. J.; Zhang, B.; Grayson, S. M.; Hu, W., Non‐monotonic molecular weight dependence of crystallization rates of linear and cyclic poly (epsilon‐caprolactone) s in a wide temperature range. *Polymer International* **2016,** *65* (9), 1074-1079.

7. Wang, J.; Li, Z.; Pérez, R. A.; Müller, A. J.; Zhang, B.; Grayson, S. M.; Hu, W., Comparing crystallization rates between linear and cyclic poly (epsilon-caprolactones) via fast-scan chip-calorimeter measurements. *Polymer* **2015,** *63*, 34-40.

8. Wurm, A.; Zhuravlev, E.; Eckstein, K.; Jehnichen, D.; Pospiech, D.; Androsch, R.; Wunderlich, B.; Schick, C., Crystallization and Homogeneous Nucleation Kinetics of Poly(ε-caprolactone) (PCL) with Different Molar Masses. *Macromolecules (Washington, DC, U. S.)* **2012,** *45* (9), 3816-3828.

9. Zhuravlev, E.; Schmelzer, J. W. P.; Wunderlich, B.; Schick, C., Kinetics of nucleation and crystallization in poly(ϵ-caprolactone) (PCL). *Polymer* **2011,** *52* (9), 1983-1997.

10. Zhuravlev, E.; Wurm, A.; Pötschke, P.; Androsch, R.; Schmelzer, J. W. P.; Schick, C., Kinetics of nucleation and crystallization of poly(ε-caprolactone) – Multiwalled carbon nanotube composites. *European Polymer Journal* **2014,** *52*, 1-11.

11. Furushima, Y.; Kumazawa, S.; Umetsu, H.; Toda, A.; Zhuravlev, E.; Schick, C., Melting and recrystallization kinetics of poly (butylene terephthalate). *Polymer* **2017,** *109*, 307-314.

12. Furushima, Y.; Nakada, M.; Ishikiriyama, K.; Toda, A.; Androsch, R.; Zhuravlev, E.; Schick, C., Two crystal populations with different melting/reorganization kinetics of isothermally crystallized polyamide 6. *Journal of Polymer Science Part B: Polymer Physics* **2016,** *54* (20), 2126-2138.

13. Furushima, Y.; Toda, A.; Rousseaux, V.; Bailly, C.; Zhuravlev, E.; Schick, C., Quantitative understanding of two distinct melting kinetics of an isothermally crystallized poly (ether ether ketone). *Polymer* **2016,** *99*, 97-104.

14. Jariyavidyanont, K.; Androsch, R.; Schick, C., Crystal reorganization of poly (butylene terephthalate). *Polymer* **2017,** *124*, 274-283.

15. Toda, A.; Taguchi, K.; Sato, K.; Nozaki, K.; Maruyama, M.; Tagashira, K.; Konishi, M., Melting kinetics of it-polypropylene crystals over wide heating rates. *Journal of Thermal Analysis and Calorimetry* **2013,** *113* (3), 1231-1237.

16. Mileva, D.; Androsch, R.; Zhuravlev, E.; Schick, C.; Wunderlich, B., Isotropization, perfection and reorganization of the mesophase of isotactic polypropylene. *Thermochimica acta* **2011,** *522* (1-2), 100-109.

17. Toda, A.; Taguchi, K.; Nozaki, K.; Konishi, M., Melting behaviors of polyethylene crystals: an application of fast-scan DSC. *Polymer* **2014,** *55* (14), 3186-3194.

18. Minakov, A. A.; Mordvintsev, D. A.; Tol, R.; Schick, C., Melting and reorganization of the crystalline fraction and relaxation of the rigid amorphous fraction of isotactic polystyrene on fast heating (30,000 K/min). *Thermochimica acta* **2006,** *442* (1-2), 25-30.

19. Adamovsky, S.; Schick, C., Ultra-fast isothermal calorimetry using thin film sensors. *Thermochimica Acta* **2004,** *415* (1), 1-7.

20. Chen, H.-L.; Porter, R. S., Melting behavior of poly(ether ether ketone) in its blends with poly(ether imide). *Journal of Polymer Science Part B: Polymer Physics* **1993,** *31* (12), 1845-1850.

21. Lee, Y.; Porter, R. S., Double-melting behavior of poly(ether ether ketone). *Macromolecules* **1987,** *20* (6), 1336-1341.

22. Konishi, T.; Sakatsuji, W.; Fukao, K.; Miyamoto, Y., Temperature Dependence of Lamellar Thickness in Isothermally Crystallized Poly(butylene terephthalate). *Macromolecules* **2016,** *49* (6), 2272-2280.

23. Xu, J.; Heck, B.; Ye, H.-M.; Jiang, J.; Tang, Y.-R.; Liu, J.; Guo, B.-H.; Reiter, R.; Zhou, D.-S.; Reiter, G. n., Stabilization of Nuclei of Lamellar Polymer Crystals: Insights from a Comparison of the Hoffman–Weeks Line with the Crystallization Line. *Macromolecules* **2016,** *49* (6), 2206-2215.

24. Gradys, A.; Sajkiewicz, P.; Adamovsky, S.; Minakov, A.; Schick, C., Crystallization of poly(vinylidene fluoride) during ultra-fast cooling. *Thermochimica Acta* **2007,** *461* (1), 153-157.

25. Arnold, L. Crystallization and Melting Behavior of (ε-caprolactone)-based Homopolymer and Triblock Copolymer. Ph.D Thesis, Virginia Polytechnic Institute & State University, Blacksburg, VA, 1995.

26. Chen, H.-L.; Li, L.-J.; Ou-Yang, W.-C.; Hwang, J. C.; Wong, W.-Y., Spherulitic Crystallization Behavior of Poly(ε-caprolactone) with a Wide Range of Molecular Weight. *Macromolecules* **1997,** *30* (6), 1718-1722.

27. Chen, Y.-F.; Woo, E. M., Growth regimes and spherulites in thin-film poly(ϵ-caprolactone) with amorphous polymers. *Colloid Polym. Sci.* **2008,** *286* (8-9), 917-926.

28. Cho, T. Y.; Stille, W.; Strobl, G., Zero growth temperature and growth kinetics of crystallizing poly(ε-caprolactone). *Colloid Polym. Sci.* **2007,** *285* (8), 931-934.

29. Ciardelli, G.; Chiono, V.; Vozzi, G.; Pracella, M.; Ahluwalia, A.; Barbani, N.; Cristallini, C.; Giusti, P., Blends of Poly(ε-caprolactone) and Polysaccharides in Tissue Engineering Applications. *Biomacromolecules* **2005,** *6* (4), 1961-1976.

30. Cordova, M. E.; Lorenzo, A. T.; Muller, A. J.; Hoskins, J. N.; Grayson, S. M., A Comparative Study on the Crystallization Behavior of Analogous Linear and Cyclic Poly(ε-caprolactones). *Macromolecules (Washington, DC, U. S.)* **2011,** *44* (7), 1742-1746.

31. Du, Z.-X.; Yang, Y.; Xu, J.-T.; Fan, Z.-Q., Effect of molecular weight on spherulitic growth rate of poly(ε-caprolactone) and poly(ε-caprolactone)-b-poly(ethylene glycol). *J. Appl. Polym. Sci.* **2007,** *104* (5), 2986-2991.

32. Goulet, L.; Prud'Homme, R. E., Crystallization kinetics and melting of caprolactone random copolymers. *J. Polym. Sci., Part B: Polym. Phys.* **1990,** *28* (12), 2329-52.

33. Heck, B.; Hugel, T.; Iijima, M.; Sadiku, E.; Strobl, G., Steps in the transition of an entangled polymer melt to the partially crystalline state. *New J. Phys.* **1999,** *1*, No pp. Given, Article 17.

34. Jonza, J. M.; Porter, R. S., Bisphenol A polycarbonate/poly(ε-caprolactone) blends: melting point depression and reactivity. *Macromolecules* **1986,** *19* (7), 1946-51.

35. Nie, K.; Zheng, S.; Lu, F.; Zhu, Q., Inorganic-organic hybrids involving poly(ε-caprolactone) and silica network: Hydrogen-bonding interactions and isothermal crystallization kinetics. *J. Polym. Sci., Part B: Polym. Phys.* **2005,** *43* (18), 2594-2603.

36. Nunez, E.; Ferrando, C.; Malmstrom, E.; Claesson, H.; Werner, P. E.; Gedde, U. W., Crystal structure, melting behavior and equilibrium melting point of star polyesters with crystallizable poly(ε-caprolactone) arms. *Polymer* **2004,** *45* (15), 5251-5263.

37. Ong, C. J.; Price, F. P., Blends of poly(ε-caprolactone) with poly(vinyl chloride). II. Crystallization kinetics. *J. Polym. Sci., Polym. Symp.* **1978,** *63*, 59-75.

38. Ong, C. J.; Price, F. P., Blends of poly(ε-caprolactone) with poly(vinyl chloride). I. Morphology. *J. Polym. Sci., Polym. Symp.* **1978,** *63*, 45-58.

39. Phillips, P. J.; Rensch, G. J., Crystallization studies of poly(ε-caprolactone). II. Lamellar thickening and melting. *J. Polym. Sci., Part B: Polym. Phys.* **1989,** *27* (1), 155-73.

40. Phillips, P. J.; Rensch, G. J.; Taylor, K. D., Crystallization studies of poly(ε-caprolactone). I. Morphology and kinetics. *J. Polym. Sci., Part B: Polym. Phys.* **1987,** *25* (8), 1725-40.

41. Pucciariello, R.; Villani, V.; Guadagno, L.; Vittoria, V., Equilibrium thermal behavior and morphology of organophilic montmorillonite/poly(ε-caprolactone) nanocomposites. *J. Polym. Sci., Part B: Polym. Phys.* **2005,** *44* (1), 22-32.

42. Rohindra, D., Miscibility determination in poly(ε-caprolactone)/poly(vinyl formal) blend by equilibrium melting temperature and spherulite morphology. *J. Macromol. Sci., Part B: Phys.* **2009,** *48* (6), 1103-1113.

43. Sanandaji, N.; Neway, B.; Hedenqvist, M. S.; Li, Y.; Hawker, C. J.; Takizawa, K.; Gedde, U. W., Crystallization and Melting Behavior of Monodisperse Oligomers of ϵ-Caprolactone. *J. Macromol. Sci., Part B: Phys.* **2012,** *51* (10), 2075-2092.

44. Sheth, S. Self-Consistency of the Lauritzen-Hoffman and Strobl Models of Polymer Crystallization Evaluated for Poly(Epsilon-Caprolactone) Fractions and Effect of Composition on the Phenomenon of Concurrent Crystallization in Polyethylene Blends. Ph.D Thesis, Virginia Polytechnic Institute and State University, Blacksburg, VA, 2013.

45. Shin, E. J.; Jeong, W.; Brown, H. A.; Koo, B. J.; Hedrick, J. L.; Waymouth, R. M., Crystallization of Cyclic Polymers: Synthesis and Crystallization Behavior of High Molecular Weight Cyclic Poly(ε-caprolactone)s. *Macromolecules (Washington, DC, U. S.)* **2011,** *44* (8), 2773-2779.

46. Siqueira, G.; Fraschini, C.; Bras, J.; Dufresne, A.; Prud'homme, R.; Laborie, M.-P., Impact of the nature and shape of cellulosic nanoparticles on the isothermal crystallization kinetics of poly(ε-caprolactone). *Eur. Polym. J.* **2011,** *47* (12), 2216-2227.

47. Strobl, G., From the melt via mesomorphic and granular crystalline layers to lamellar crystallites: a major route followed in polymer crystallization? *Eur. Phys. J. E* **2000,** *3* (2), 165-183.

48. Strobl, G., A thermodynamic multiphase scheme treating polymer crystallization and melting. *Eur. Phys. J. E* **2005,** *18* (3), 295-309.

49. Strobl, G., Crystallization and melting of bulk polymers: New observations, conclusions and a thermodynamic scheme. *Prog. Polym. Sci.* **2006,** *31* (4), 398-442.

50. Strobl, G.; Cho, T. Y., Growth kinetics of polymer crystals in bulk. *Eur. Phys. J. E* **2007,** *23* (1), 55-65.

51. Su, H.-H.; Chen, H.-L.; Diaz, A.; Casas, M. T.; Puiggali, J.; Hoskins, J. N.; Grayson, S. M.; Perez, R. A.; Muller, A. J., New insights on the crystallization and melting of cyclic PCL chains on the basis of a modified Thomson-Gibbs equation. *Polymer* **2013,** *54* (2), 846-859.

52. Vion, J. M.; Jerome, R.; Teyssie, P.; Aubin, M.; Prudhomme, R. E., Synthesis, characterization, and miscibility of caprolactone random copolymers. *Macromolecules* **1986,** *19* (7), 1828-38.

53. Xing, Z.; Yang, G., Crystallization, melting behavior, and wettability of poly(ϵ-caprolactone) and poly(ϵ-caprolactone)/ poly(N-vinylpyrrolidone) blends. *J. Appl. Polym. Sci.* **2010,** *115* (5), 2747-2755.

54. Labet, M.; Thielemans, W., Synthesis of polycaprolactone: a review. *Chem. Soc. Rev.* **2009,** *38* (12), 3484-3504.

55. Garozzo, D.; Giuffrida, M.; Montaudo, G., Primary thermal decomposition processes in aliphatic polyesters investigated by chemical ionization mass spectrometry. *Macromolecules* **1986,** *19* (6), 1643-9.

56. Persenaire, O.; Alexandre, M.; Degee, P.; Dubois, P., Mechanisms and Kinetics of Thermal Degradation of Poly(ε-caprolactone). *Biomacromolecules* **2001,** *2* (1), 288-294.

57. Sivalingam, G.; Karthik, R.; Madras, G., Kinetics of thermal degradation of poly(ε-caprolactone). *Journal of Analytical and Applied Pyrolysis* **2003,** *70* (2), 631-647.

58. Marand, H.; Xu, J.; Srinivas, S., Determination of the Equilibrium Melting Temperature of Polymer Crystals: Linear and Nonlinear Hoffman-Weeks Extrapolations. *Macromolecules* **1998,** *31* (23), 8219-8229.

59. Hay, J. N., Use of model compounds to determine equilibrium melting points of polymers. *J. Polym. Sci., Polym. Chem. Ed.* **1976,** *14* (12), 2845-52.

60. Broadhurst, M. G., Extrapolation of the orthorhombic normal paraffin melting properties to very long chain lengths. *J. Chem. Phys.* **1962,** *36*, 2578-82.

61. Broadhurst, M. G., *J. Res. Natl. Bur. Std.-Phys. Chem.* **1966,** *70A*.

62. Toda, A., Heating rate dependence of melting peak temperature examined by DSC of heat flux type. *J. Therm. Anal. Calorim.* **2016,** *123* (3), 1795-1808.

63. Toda, A.; Hikosaka, M.; Yamada, K., Superheating of the melting kinetics in polymer crystals: a possible nucleation mechanism. *Polymer* **2002,** *43* (5), 1667-1679.

64. Toda, A.; Taguchi, K.; Nozaki, K.; Fukushima, T.; Kaji, H., Superheated melting kinetics of metastable chain-folded polymer crystals. *Crystal Growth & Design* **2018**.

65. Hoffman, J. D.; Davis, G. T.; Lauritzen, J. I., Jr., The Rate of Crystallization of Linear Polymers with Chain Folding. In *Treatise on Solid State Chemistry, Vol. 3: Crystalline and Noncrystalline Solids*, Hannay, N. B., Ed. Plenum Press: New York, 1976.

66. Hoffman, J. D.; Miller, R. L., Kinetic of crystallization from the melt and chain folding in polyethylene fractions revisited: theory and experiment. *Polymer* **1997,** *38* (13), 3151-3212.

67. Lauritzen, J. I.; Hoffman, J. D., Extension of theory of growth of chain‐folded polymer crystals to large undercoolings. *Journal of Applied Physics* **1973,** *44* (10), 4340-4352.

68. Hoffman, J. D.; Miller, R. L.; Marand, H.; Roitman, D. B., Relationship between the lateral surface free energy. sigma. and the chain structure of melt-crystallized polymers. *Macromolecules* **1992,** *25* (8), 2221-2229.

69. Lauritzen, J. I.; Passaglia, E., Kinetics of crystallization in multicomponent systems: II. Chain-folded polymer crystals. *J. Res. Natl. Bur. Stand* **1967,** *71*, 261-275.

70. Hoffman, J. D.; Lauritzen, J. I.; Passaglia, E.; Ross, G. S.; Frolen, s. L. J.; Weeks, J. J., Kinetics of polymer crystallization from solution and the melt. *Kolloid-Zeitschrift und Zeitschrift für Polymere* **1969,** *231* (1-2), 564-592.

71. Mohammadi, H. On the Melting and Crystallization of Linear Polyethylene, Poly(ethylene oxide), and Metallocene Linear Low-Density Polyethylene. Ph.D. Thesis, Virginia Polytechnic Institute and State University, Blacksburg, VA, 2018.

72. Tammann, G., A method for determining the relationship between the melting point of a crystal lamella and its thickness. *Z. Anorg. Allg. Chem.* **1920,** *110*, 166-8.

73. Dlugosz, J.; Fraser, G. V.; Grubb, D.; Keller, A.; Odell, J. A.; Goggin, P. L., Study of crystallization and isothermal thickening in polyethylene using SAXD, low frequency Raman spectroscopy and electron microscopy. *Polymer* **1976,** *17* (6), 471-480.

74. Stack, G. M.; Mandelkern, L.; Voigt-Martin, I. G., Changes in crystallite size distribution during the isothermal crystallization of linear polyethylene. *Polymer Bulletin* **1982,** *8* (9), 421-428.

75. Peterlin, A., Thickening of polymer single crystals during annealing. *Journal of Polymer Science Part B: Polymer Letters* **1963,** *1* (6), 279-284.

76. Marand, H.; Huang, Z., Isothermal lamellar thickening in linear polyethylene: Correlation between the evolution of the degree of crystallinity and the melting temperature. *Macromolecules* **2004,** *37* (17), 6492-6497.

77. Hoffman, J. D.; Weeks, J. J., X‐ray study of isothermal thickening of lamellae in bulk polyethylene at the crystallization temperature. *The Journal of chemical physics* **1965,** *42* (12), 4301-4302.

78. Maiti, P.; Hikosaka, M.; Yamada, K.; Toda, A.; Gu, F., Lamellar Thickening in Isotactic Polypropylene with High Tacticity Crystallized at High Temperature. *Macromolecules* **2000,** *33* (24), 9069-9075.

79. Kovacs, A. J.; Straupe, C.; Gonthier, A., Isothermal growth, thickening, and melting of poly(ethylene oxide) single crystals in the bulk. II. *J. Polym. Sci., Polym. Symp.* **1977,** *59* (Recent Adv. Field Cryst. Fusion Polym.), 31-54.

80. Cheng, S. Z. D.; Zhang, A.; Chen, J.; Heberer, D. P., Nonintegral and integral folding crystal growth in low-molecular mass poly(ethylene oxide) fractions. I. Isothermal lamellar thickening and thinning. *J. Polym. Sci., Part B: Polym. Phys.* **1991,** *29* (3), 287-97.

81. Schulz, M.; Seidlitz, A.; Kurz, R.; Bärenwald, R.; Petzold, A.; Saalwächter, K.; Thurn-Albrecht, T., The Underestimated Effect of Intracrystalline Chain Dynamics on the Morphology and Stability of Semicrystalline Polymers. *Macromolecules* **2018,** *51* (21), 8377-8385.

82. Lee, B.; Shin, T. J.; Lee, S. W.; Yoon, J.; Kim, J.; Youn, H. S.; Ree, M., Time-resolved X-ray scattering and calorimetric studies on the crystallization behaviors of poly (ethylene terephthalate)(PET) and its copolymers containing isophthalate units. *Polymer* **2003,** *44* (8), 2509-2518.

83. Hsiao, B.; Wang, Z.-g.; Yeh, F.; Gao, Y.; Sheth, K., Time-resolved X-ray studies of structure development in poly(butylene terephthalate) during isothermal crystallization. *Polymer* **1999,** *40* (12), 3515-3523.

84. Verma, R. K.; Velikov, V.; Kander, R. G.; Marand, H.; Chu, B.; Hsiao, B. S., SAXS studies of lamellar level morphological changes during crystallization and melting in PEEK. *Polymer* **1996,** *37* (24), 5357-5365.

85. Kohn, P.; Strobl, G., Continuous Changes in the Inner Order of the Crystalline Lamellae during Isothermal Crystallization of Poly(ε-caprolactone). *Macromolecules* **2004,** *37* (18), 6823-6826.

86. Kurz, R.; Schulz, M.; Scheliga, F.; Men, Y.; Seidlitz, A.; Thurn-Albrecht, T.; Saalwächter, K., Interplay between Crystallization and Entanglements in the Amorphous Phase of the Crystal-fixed Polymer Poly (ϵ-caprolactone). *Macromolecules* **2018,** *51* (15), 5831-5841.

87. Bark, M.; Zachmann, H. G.; Alamo, R.; Mandelkern, L., Investigations of the crystallization of polyethylene by means of simultaneous small‐angle and wide‐angle X‐ray scattering. *Die Makromolekulare Chemie* **1992,** *193* (9), 2363-2377.

88. Fischer, E. W., Effect Of Annealing And Temperature On The Morphological Structure Of Polymers. *Pure and Applied Chemistry* **1972,** *31* (1-2), 113-132.

89. McCready, M. J.; Schultz, J. M.; Lin, J. S.; Hendricks, R. W., Effect of crystallization time on the properties of melt‐crystallized linear polyethylene. *Journal of Polymer Science: Polymer Physics Edition* **1979,** *17* (5), 725-740.

90. Bartczak, Z.; Argon, A. S.; Cohen, R. E.; Kowalewski, T., The morphology and orientation of polyethylene in films of sub-micron thickness crystallized in contact with calcite and rubber substrates. *Polymer* **1999,** *40* (9), 2367-2380.

91. Jeon, K.; Krishnamoorti, R., Morphological behavior of thin linear low-density polyethylene films. *Macromolecules* **2008,** *41* (19), 7131-7140.

92. Mellbring, O.; Kihlman Øiseth, S.; Krozer, A.; Lausmaa, J.; Hjertberg, T., Spin coating and characterization of thin high-density polyethylene films. *Macromolecules* **2001,** *34* (21), 7496-7503.

93. Mohammadi, H.; Vincent, M.; Marand, H., Investigating the equilibrium melting temperature of linear polyethylene using the non-linear Hoffman-Weeks approach. *Polymer* **2018,** *146*, 344-360.

94. Sarge, S. M.; Gmelin, E.; Hoehne, G. W. H.; Cammenga, H. K.; Hemminger, W.; Eysel, W., The caloric calibration of scanning calorimeters. *Thermochim. Acta* **1994,** *247* (2), 129-68.

95. Zhuravlev, E.; Schick, C., Fast scanning power compensated differential scanning nano-calorimeter: 1. The device. *Thermochim. Acta* **2010,** *505* (1-2), 1-13.

96. Vanden Poel, G.; Mathot, V. B. F., High-speed/high performance differential scanning calorimetry (HPer DSC): Temperature calibration in the heating and cooling mode and minimization of thermal lag. *Thermochim. Acta* **2006,** *446* (1-2), 41-54.

97. Androsch, R.; Rhoades, A. M.; Stolte, I.; Schick, C., Density of heterogeneous and homogeneous crystal nuclei in poly (butylene terephthalate). *European Polymer Journal* **2015,** *66*, 180-189.

98. Schawe, J. E. K., Influence of processing conditions on polymer crystallization measured by fast scanning DSC. *J. Therm. Anal. Calorim.* **2014,** *116* (3), 1165-1173.

99. Rhoades, A. M.; Wonderling, N.; Gohn, A.; Williams, J.; Mileva, D.; Gahleitner, M.; Androsch, R., Effect of cooling rate on crystal polymorphism in beta-nucleated isotactic polypropylene as revealed by a combined WAXS/FSC analysis. *Polymer* **2016,** *90*, 67-75.

100. Schawe, J. E. K., Analysis of non-isothermal crystallization during cooling and reorganization during heating of isotactic polypropylene by fast scanning DSC. *Thermochimica Acta* **2015,** *603*, 85-93.

101. Jariyavidyanont, K.; Focke, W.; Androsch, R., Crystallization kinetics of polyamide 11 in the presence of sepiolite and montmorillonite nanofillers. *Colloid Polym. Sci.* **2016,** *294* (7), 1143-1151.

102. Fischer, C.; Seefried, A.; Drummer, D., Crystallization and Component Properties of Polyamide 12 at Processing‐Relevant Cooling Conditions. *Polymer Engineering & Science* **2017,** *57* (4), 450-457.

103. Androsch, R.; Monami, A.; Kucera, J., Effect of an alpha-phase nucleating agent on the crystallization kinetics of a propylene/ethylene random copolymer at largely different supercooling. *Journal of Crystal Growth* **2014,** *408*, 91-96.

104. Androsch, R.; Di Lorenzo, M. L.; Schick, C.; Wunderlich, B., Mesophases in polyethylene, polypropylene, and poly(1-butene). *Polymer* **2010,** *51* (21), 4639-4662.

105. Furushima, Y.; Nakada, M.; Yoshida, Y.; Okada, K., Crystallization/Melting Kinetics and Morphological Analysis of Polyphenylene Sulfide. *Macromolecular Chemistry and Physics* **2018,** *219* (2).

106. Marand, H.; Hoffman, J. D., Determination of the fold surface free energy and the equilibrium melting temperature for α-phase poly(pivalolactone) crystals. *Macromolecules* **1990,** *23* (15), 3682-7.

107. Hu, W. G.; Schmidt‐Rohr, K., Polymer ultradrawability: the crucial role of α‐relaxation chain mobility in the crystallites. *Acta Polymerica* **1999,** *50* (8), 271-285.

108. Mandelkern, L.; Peacock, A. J., The structure of linear polyethylene crystals formed in dilute solution. *Polymer Bulletin* **1986,** *16* (6), 529-536.

109. Voigt‐Martin, I. G.; Mandelkern, L., A quantitative electron microscopic study of the crystallite structure of molecular weight fractions of linear polyethylene. *Journal of Polymer Science: Polymer Physics Edition* **1984,** *22* (11), 1901-1917.

110. Crescenzi, V.; Manzini, G.; Calzolari, G.; Borri, C., Thermodynamics of fusion of poly-β-propiolactone and poly-E-caprolactone. Comparative analysis of the melting of aliphatic polylactone and polyester chains. *Eur. Polym. J.* **1972,** *8* (3), 449-63.

111. Flory, P. J.; Vrij, A., Melting points of linear-chain homologs. The normal paraffin hydrocarbons. *J. Am. Chem. Soc.* **1963,** *85* (22), 3548-53.

112. Miller, R. L., Polymer crystal formation: On an analysis of the dilute solution lamellar thickness-crystallization temperature data for poly(ethylene). *Kolloid-Zeitschrift und Zeitschrift für Polymere* **1968,** *225* (1), 62-69.

113. Huseby, T. W.; Bair, H. E., Dissolution of Polyethylene Single Crystals in Xylene and Octadecane. *Journal of Applied Physics* **1968,** *39* (11), 4969-4973.

114. Xu, J.; Srinivas, S.; Marand, H.; Agarwal, P., Equilibrium Melting Temperature and Undercooling Dependence of the Spherulitic Growth Rate of Isotactic Polypropylene. *Macromolecules* **1998,** *31* (23), 8230-8242.

115. Juhász, P.; Varga, J.; Belina, K.; Marand, H., Determination of the equilibrium melting point of the β-form of polypropylene. *Journal of thermal analysis and calorimetry* **2002,** *69* (2), 561-574.

116. Hudson, S. D.; Davis, D. D.; Lovinger, A. J., Semicrystalline morphology of poly (aryl ether ether ketone)/poly (ether imide) blends. *Macromolecules* **1992,** *25* (6), 1759-1765.

117. Lovinger, A. J.; Hudson, S. D.; Davis, D. D., High-temperature crystallization and morphology of poly (aryl ether ether ketone). *Macromolecules* **1992,** *25* (6), 1752-1758.

118. Strobl, G., From the melt via mesomorphic and granular crystalline layers to lamellar crystallites: A major route followed in polymer crystallization? *Eur. Phys. J. E* **2000,** *3* (2), 165-183.

CHAPTER 4

Crystallization Kinetic Study of Poly(ethylene oxide) (PEO) with Different Molar Masses Using Fast Differential Scanning Calorimetry

4.1 INTRODUCTION

Poly(ethylene oxide) (PEO) is a semi-crystalline polyether that has been extensively studied as a model compound for investigation of the kinetics of polymer crystallization.[1-16] PEO's low nucleation density makes it well-suited for spherulite growth rate analyses using polarized optical microscopy[3-6, 9-11, 13, 14] in addition to bulk kinetics analyses using thermal analysis techniques.[1, 2, 7-9, 12, 15-17] The crystallization kinetics of PEO for crystallization from dilute solution[2, 15] and the melt[1, 7-9, 12, 16] has been analyzed using the Avrami model. Avrami exponents as high as n = 4 were obtained for the case of dilute solution crystallization, and Avrami exponents ranging from n = 2 – 3 were obtained for melt crystallization. For the melt crystallization of PEO studied by dilatometry or calorimetry, the lowest isothermal crystallization temperatures that could be investigated were ca. T_x = 35°C due to slow cooling available with conventional instrumentation.[1, 7-9, 12, 16]

The recent advances in fast differential scanning calorimetry (FDSC) have given access to a much larger range of crystallization temperatures due to the much higher cooling rates that can be achieved using chip calorimeter designs.[18, 19] The Mettler-Toledo Flash™ DSC 1, one of two commercially available FDSCs currently on the market, can achieve linear cooling rates of 2×10^3 K.s^{-1} and linear heating rates of 10^4 K.s^{-1} with properly prepared samples (i.e. thicknesses of 1–2 μm and masses of 10–100 ng).[19, 20] A number of other FDSCs are capable of faster heating and cooling rates, but these instruments are not commercially available.[19] The only three reports of an Avrami analysis for isothermal crystallization data acquired using FDSC focused on poly(ether ether ketone) (PEEK)[21], blends of isotactic polypropylene with ethylene-*co*-propylene rubber (*i*-PP/EPR)[22], and high density polyethylene (HDPE).[23] In the case of PEEK,[21] the largest Avrami constant corresponded to the minimum peak time of crystallization. Additionally, the

authors reported that the Avrami exponent was independent of crystallization temperature over a 160°C temperature range. In the case of *i*-PP/EPR,[22] the authors did not report the rate constant, but showed a strong, non-monotonic temperature dependence for the exponent. Here, the authors relate the changing Avrami exponent to differences in crystallization rates of the propylene and ethylene sequences and to the heterogeneous nucleation at the blend interfaces. For HDPE,[23] no rate constants were measured, and the Avrami exponent was reported to range from n = 1.5 at low temperatures to n = 3 at high temperatures, which the authors attributed to changes in nucleation and growth mechanisms.

Studies at the lower crystallization temperatures reached by FDSC (as low as the polymer's glass transition temperature) have shown that the temperature dependence of crystallization times is bimodal for polymers such as isotactic polypropylene (*i*-PP)[24-33], poly(butylene terephthalate) (PBT)[24, 34-37], poly(butylene-2,6-naphthalate) (PBN)[38], nylon-6,6 (PA-6,6)[39-41], nylon-11 (PA-11)[42-44], poly(ε-caprolactone) (PCL)[45, 46] , isotactic poly(propylene-*co*-ethylene) (*i*-PP-*co*-PE)[47], and *i*-PP/EPR.[22] On the other hand, poly(ethylene terephthalate) (PET)[36], poly(phenylene sulfide) (PPS)[48], and PEEK[21] exhibit only unimodal behavior when investigated with FDSC. The bimodal crystallization curves observed with FDSC have been attributed to a change in primary nucleation mechanism from heterogeneous nucleation at high temperatures to homogeneous nucleation at low temperatures.[24-28, 30, 31, 33, 34, 36, 37, 40, 42-44, 46, 47, 49-51] The change in primary nucleation mechanism from low supercooling to high supercooling is supported by morphological studies using polarized optical and atomic force microscopies,[34, 40, 44] measurements of nucleation density using polarized optical microscopy,[34, 49-51] and FDSC investigations of crystallization kinetics for samples with nucleating agents.[24-28, 30, 31, 33, 36, 37, 42, 43, 46, 47] The low temperature region of crystallization has also been linked to the existence of a mesophase for *i*-PP,[52] PA-6,[53] PA-6,6,[40] PA-11,[42, 44, 54] PBT,[34] and PBN.[38] Despite calorimetric evidence of two different nucleation mechanisms in PCL,[45, 46] there is no data at this time to corroborate the existence of a low temperature mesophase for this material. Furthermore, there are neither reports of different primary nucleation mechanisms nor

evidence of thermally controlled mesophase formation in PET,[36] PPS,[48] and PEEK,[21] polymers that exhibit unimodal crystallization kinetics. These results indicate that the bimodality observed in a number of crystallization curves likely results from polymorphism[34, 38, 40, 42, 44, 52-54] and changing primary nucleation mechanism.[24-28, 30, 31, 33, 34, 36, 37, 40, 42-44, 46, 47, 49-51]

Despite the fact that PEO has been extensively studied using conventional thermal analysis techniques, in the only account of its thermal characterization using FDSC Mathot et al.[55] simply reported that a PEG 6000 underwent cold crystallization after following rapid cooling. In the present work, we will analyze the non-isothermal and isothermal crystallization behaviors of narrow molecular weight PEO fractions using a Mettler-Toledo Flash™ DSC 1. In particular, we will characterize the isothermal crystallization rate and degree of crystallinity over a 100°C temperature range and compare the results to those from conventional DSC. PEO has a sub-ambient glass transition temperature (T_g = −70°C) close to that of PCL, and both polymers are not known to exhibit polymorphism. As such, it will be interesting to see if PEO exhibits bimodal crystallization kinetics like PCL. We will utilize the isothermal crystallization data to carry out an Avrami analysis and relate these findings to the primary nucleation and crystal growth mechanisms. Finally, we will discuss the complications of applying classical primary and secondary nucleation theories to model the results of the Avrami analysis when conducted over the wide range of crystallization temperatures afforded by fast differential scanning calorimetry.

4.2 THEORETICAL BACKGROUND

The Avrami equation was originally formulated to describe the volume transformation kinetics for liquid-solid and solid-solid phase transitions in metals.[56-58] A version that is commonly employed in the polymer field describes the kinetics of crystallization in terms of the degree of crystallinity, where

$$X_c(t) = X_c^{\infty}[1 - \exp(-kt^n)] \tag{4.1}$$

Here, $X_c(t)$ is the time-dependent crystallinity, X_c^∞ is the maximum crystallinity developed in the long time limit, k is the Avrami crystallization rate constant, and n is the Avrami exponent.[57, 59] The Avrami exponent reflects the type of primary nucleation mechanism, thermal or athermal, and the growth geometry.[57, 59] Here, thermal nucleation means that the crystals were nucleated sporadically and started growing at different times, while athermal nucleation means that all the crystals were nucleated instantaneously and started growing at the same time. Homogeneous primary nucleation is almost always thermal nucleation, while heterogeneous nucleation is typically athermal. Four key assumptions were made in deriving the original Avrami model:[56-58] (1) The growing phase is modeled by a hard object (i.e. spherulites are not modeled as a system of growing lamellae that splay and fill space in three dimensions but rather as a homogeneous hard spheres of constant crystallinity (X_c^∞), (2) nuclei are consumed by either initiating new phase growth or being swallowed by a growing phase front, (3) only one nucleation mechanism and one growth mechanism are present throughout the entire crystallization process at a given temperature, (4) the nucleation rate, growth rate, and the sample volume remain constant throughout the phase transformation. In all reality, polymer crystallization is a complex process that often leads to the violation of at least one of these assumptions. Many authors have developed variations on the original Avrami model in an attempt to generalize the theory by foregoing at least one of the assumptions given above.[59-68]

The following will provide a detailed overview of the Avrami model as applied to polymer crystallization. For the case of athermal, or instantaneous, nucleation, the crystallization rate constant is defined as

$$k = CNG^s \tag{4.2a}$$

where C is a constant that describes the geometry of crystal growth, N is the number of nuclei per unit volume (nucleation density), G is the crystal growth rate, and s is the dimensionality of crystal growth.[59] For the case of thermal, or sporadic, nucleation, the crystallization rate constant is defined as

$$k = CIG^s \tag{4.2b}$$

where I is the primary nucleation rate.[59] According to classical nucleation theory,[69-71] the primary nucleation rate is given by

$$I = I_0 \exp\left(-\frac{U^*}{R(T_x - T_\infty)}\right) \exp\left(-\frac{K_n}{T_x \Delta T^2}\right) \tag{4.3}$$

such that I_o is the exponential prefactor for the nucleation rate, U^* is the activation energy for chain transport across the melt-crystal interface according to the Vogel-Fulcher-Tamman-Hesse equation, R is the ideal gas constant, T_∞ is the temperature below which cooperative large scale molecular relaxation processes become infinitely slow ($T_\infty = T_g - 30$ K), K_n is the primary nucleation rate constant, and ΔT is the undercooling, defined as the difference between the equilibrium melting temperature and the crystallization temperature ($T_m - T_x$). For the case of homogeneous nucleation, the primary nucleation rate constant takes the following form

$$K_n^{homo} = \frac{2c^2\sigma^2\sigma_e T_m^2}{\Delta H_f^{o\,2} k} \tag{4.4}$$

where c is a constant that is determined by the nucleus shape, σ is the lateral surface free energy, σ_e is the fold surface free energy, ΔH_f^o is the theoretical heat of fusion, and k is Boltzmann's constant.[70-74] The preceding expression is specific to the bundle-like nucleus that is commonly assumed to form for polymers. The constant c is defined as

$$c = 2\sqrt{\pi} \tag{4.5a}$$

for a cylindrical nucleus,[73, 75] or as

$$c = \frac{2}{\sqrt{\sin\psi}}\left(\frac{x+y}{\sqrt{xy}}\right) \tag{4.5b}$$

for a parallelepiped with cross-sectional sides of length x and y and an apex angle of ψ.[73] For the case of heterogeneous nucleation on a flat surface, the primary nucleation rate constant becomes

$$K_{\mathrm{n}}^{\mathrm{hetero}} = \frac{c'\Delta\sigma\sigma\sigma_{\mathrm{e}}T_{\mathrm{m}}^{2}}{\Delta H_{\mathrm{f}}^{\mathrm{o}\,2}k} \tag{4.6}$$

where c' is a constant that is determined by the nucleus shape and location (i.e. on a flat substrate, in a niche, etc.) and $\Delta\sigma$ is the surface free energy difference parameter accounting for crystal-melt contact at one interface and the crystal-heterogeneity contact on the opposite interface.[72, 76, 77] Classical Lauritzen-Hoffman secondary nucleation theory[73, 78-80] defines the radial growth rate of three-dimensional spherulites, as

$$G = G_0 \exp\left(-\frac{U^*}{R(T_{\mathrm{x}} - T_{\infty})}\right)\exp\left(-\frac{K_{\mathrm{g,j}}}{T_{\mathrm{x}}\Delta T}\right) \tag{4.7}$$

where G_{o} is the exponential prefactor for the crystal growth rate and $K_{\mathrm{g,j}}$ is the secondary nucleation rate constant, which is expressed by

$$K_{\mathrm{g,j}} = \frac{jb_0\sigma\sigma_{\mathrm{e}}T_{\mathrm{m}}}{\Delta H_{\mathrm{f}}^{\mathrm{o}}k} \tag{4.8}$$

Here, j is either 4 for crystallization in regimes I or III or 2 for crystallization in regime II and b_0 is the width of crystalline stem. The kinetic regime of crystallization is governed by the undercooling. Classical primary and secondary nucleation theories assume that the lateral surface free energy, the fold surface free energy, and the heat of fusion are all independent of temperature.

The original formulation of the Avrami model gave expressions for both athermal and thermal nucleation of rods, discs, and spheres.[57] Keeping in mind the definition of the Avrami rate constant from Eqns. (4.2a) and (4.2b), the different forms of the Avrami equation adapted to athermally and thermally nucleated rods, discs, spheres, and solid sheaves can be expressed in terms of the degree of crystallinity by substituting the n and k values found in Table 4.1 into Eqn. (4.1).[57, 59, 81, 82]

Table 4.1: Summary of the relationships between the primary nucleation mechanism, the crystalline geometry, the Avrami exponent, and the rate constant.[57, 59, 81, 82]

Crystalline geometry	Primary nucleation mechanism	n	k
circular rod	athermal	1	$d^2NG/2^*$
circular rod	thermal	2	$\pi Id^2G/4^*$
circular disc	athermal	2	πlNG^2
circular disc	thermal	3	πlIG^2
sphere	athermal	3	$4\pi NG^3/3^\dagger$
sphere	thermal	4	$\pi IG^3/3^\dagger$
solid sheaf	athermal	≥5‡	approximation
solid sheaf	thermal	≥6‡	approximation

The reader is referred to Ref. 59 for an exhaustive list of Avrami exponents under different nucleation and growth conditions (such as those observed under diffusion control). *d is the diameter of the growing rod. †l is the thickness of the disc. The diameter and thickness of rods and discs, respectively, are assumed constant throughout the growth process, and both are assumed to grow in all directions. ‡Booth and Hay[82] showed that the Avrami exponent can reach values as high as n = 14 under high branching conditions (10^6 branches/cm, i.e. a distance of 100 Å between branch points).

Two different approaches have been developed to describe the effect of branching on rod-like crystal growth, both of which show Avrami exponents greater than n = 4. The first was developed by Morgan[81] and assumes a solid sheaf structure of uniform density is formed by branching of a rod around minor auxiliary circles of radius a. The volume of the sheaf is then given by[59, 81]

$$V = 2\pi a^3\left[\left(\frac{Gt}{a}\right)^3 - 6\left(\frac{Gt}{a} - \sin\frac{Gt}{a}\right)\right] = \frac{\pi G^5 t^5}{10a^2}\left[1 - \frac{1}{42}\left(\frac{Gt}{a}\right)^2 + \frac{1}{3024}\left(\frac{Gt}{a}\right)^4 - \cdots\right] \tag{4.9}$$

Here, $\frac{Gt}{a}$ is the angle that the rod turns around the auxiliary circles, or the branching angle. By assuming the branching angle is much less than one radian, the series expansion for the volume in Eqn. (4.9) can be truncated after the first term to yield

$$V = \frac{\pi G^5 t^5}{10a^2} \tag{4.10}$$

The problem is further simplified by assuming that the average linear growth in all directions surrounding the point of nucleation in the center of the auxiliary circle is proportional to the cube root of the volume. This leads to the approximate expression for the growth of athermally nucleated solid sheaves

$$X_c(t) = X_c^{\infty}[1 - \exp(-k't^5)] \tag{4.11a}$$

and a similar approximate expression for the growth of thermally nucleated solid sheaves

$$X_c(t) = X_c^{\infty}[1 - \exp(-k''t^6)] \tag{4.11b}$$

where k' and k'' are not given exact forms because Eqns. (4.9a) and (4.9b) are approximations to a power series expansion describing the volume of the solid sheaf. The second approach to describing the branching of crystallizing rods was developed by Booth and Hay.[82] Here, a fibrillar crystal of cross-sectional area $\frac{d^2\pi}{4}$ grows from both ends and branches into two fibers at each growth site after growing b cm. The cross-sectional area and the distance between branches are both assumed to be constant. The total cross-sectional area of the branching rods is

$$A = d^2\pi 2^{\left(\frac{r}{b}-1\right)} \tag{4.12}$$

where r is the fibrillar radius. A series expansion is used to describe the time-dependence of the crystallizing volume to arrive at the Avrami expression in terms of crystallinity[59, 83]

$$X_c(t) = X_c^{\infty}\left\{1 - \exp\left[-\frac{\pi d^2 NG}{2}t\left(1 + \frac{\ln 2}{2b}Gt + \frac{(\ln 2)^2}{6b^2}(Gt)^2 + \cdots\right)\right]\right\} \tag{4.13a}$$

The expression above is well approximated by the Avrami equation such that

$$X_c(t) = X_c^{\infty}[1 - \exp(-k'''t^n)] \tag{4.13b}$$

where k''' does not have an exact form because Eqn. (4.13b) is an approximation of the power series expansion in Eqn. (4.13a). Increasing exponents are used in order to account for increased branching, i.e. smaller b values, and increased growth, i.e. the product Gt. For equivalent branching frequency or growth, the exponent value for athermal nucleation will simply be equal to the value for thermal nucleation plus 1. The authors showed that Avrami exponents from Eqn. (4.11b) as large as n = 14 can be obtained for sufficiently high branching (10^6 branches/cm, or b = 100 Å).[82]

4.3 EXPERIMENTAL

4.3.1 Materials and sample preparation

Narrow molecular weight distribution poly(ethylene oxide) samples were purchased in powder form from Scientific Polymer Products, Inc. (Ontario, NY, USA) and used without further purification. Samples will be referred to as PEO-# throughout the body of this publication, where # denotes the approximate number average molecular mass in kg.mol^{-1}. A small particle of polymer was placed onto the Flash DSC chip sensor using an eyelash. When melted, PEO wets the surface of the aluminum-coated heater and spreads out to form a circular, thin film. The key step in the film preparation process lies in using enough material to form a film ca. 1 μm thick for the crystallization to proceed without confinement effect. If the film thickness is less than 1 μm, then other morphologies will form upon crystallization.[84-87] To ensure the samples had spread to their fullest extent before studying the crystallization behavior, they were heated from 0°C to 100°C at a rate β = 1 K.s^{-1}, held at 100°C for 1 s, then cooled back to 0°C at a rate $-\beta$ = 1 K.s^{-1}. This process was repeated about 15 times for each sample until the films dimensions and the melting endotherms remained constant. The mass, m, of each sample was estimated by comparing the heat capacity of the melt measured by FDSC with that determined from CDSC (TA Instruments Q2000). Polarized optical micrographs were recorded to measure the sample area, which in conjunction with the sample mass and density allowed the determination of $L_{85°C}$, the sample thickness at 85°C. The melt density at 85°C was taken as ρ_{melt} = 1.071 g.cm^{-3}.[88] Sample information is listed in Table 4.2.

Table 4.2: Sample information used in the present study.

Sample	M_n (kg.mol^{-1})	PDI	m (ng)	$L_{85°C}$ (μm)	ΔT_{cal} (°C)
PEO-33	33.0	1.02	18	2.0	+5.1
PEO-66	66.1	1.06	281	4.9	−0.1
PEO-98	97.6	1.04	150	3.0	+0.1
PEO-223	223.2	1.04	155	3.8	+5.4

4.3.2 Fast differential scanning calorimetry

A power-compensated Mettler-Toledo Flash DSC 1 equipped with the UFS1 sensors (XENA15 36058, XENA15 36059, XENC17 40678, and XENC17 40679) was used to investigate both the non-isothermal and isothermal crystallization kinetics of PEO. The samples were heated at a rate β = 10^3 K.s^{-1}, and a maximum temperature of 110°C with a 0.5 s isothermal hold was used to erase any previous thermal history. The non-isothermal crystallization behavior was studied in duplicate over the range of cooling rates $-\beta$ = 2 – 2×10^3 K.s^{-1} with a minimum temperature of −90°C. The isothermal crystallization kinetics was studied in the range of crystallization temperatures from −55 to 35°C. Each isothermal experiment was repeated ten times, except at the highest isothermal crystallization temperatures, where a minimum of fifteen exotherms were collected because the onset of nucleation became inconsistent.

For the purpose of temperature calibration, a small piece of indium was cut with a scalpel under an optical microscope and placed on top of each PEO film using an eyelash after the completion of all crystallization experiments. The melting onset, $T_{\mathrm{m}}^{\mathrm{onset}}$, was recorded in triplicate with β = 10 – 10^3 K.s^{-1} and linearly extrapolated to β = 0 K.s^{-1} according to standard DSC calibration procedure[89-91] using the equation:

$$T_{\mathrm{m}}^{\mathrm{onset}}(\beta) = T_{\mathrm{m}}^{\mathrm{onset}}(\beta = 0) + A\beta \tag{4.14}$$

Although a non-linear extrapolation procedure has been employed recently to calibrate the Mettler-Toledo Flash™ DSC 1,[92] a linear extrapolation is sufficient here due to the relatively low heating rates used for calibration in addition to the relatively large polymer sample masses and thicknesses in the present study.[90] The difference between extrapolated and literature values of the melting onset was used to calculate ΔT_{cal}, the single-point calibration constant, to correct crystallization and melting temperatures and compare data collected on different chips. The values of ΔT_{cal} for the different samples are listed in Table 4.2.

Figure 4.1 shows the results of $T_{\mathrm{m}}^{\mathrm{onset}}$ vs. β for the indium samples used to calibrate the individual FDSC chips. Linear fits according to Eqn. (4.14) are shown for each chip. The relatively large sample mass and film thickness prohibited the collection of reliable data for heating at rates above 5×10^3 K.s^{-1} as a result of significant thermal gradients evidenced by oscillations in the heat flow signal. Temperature calibration was therefore only performed for heating rates up to 10^3 K.s^{-1}.

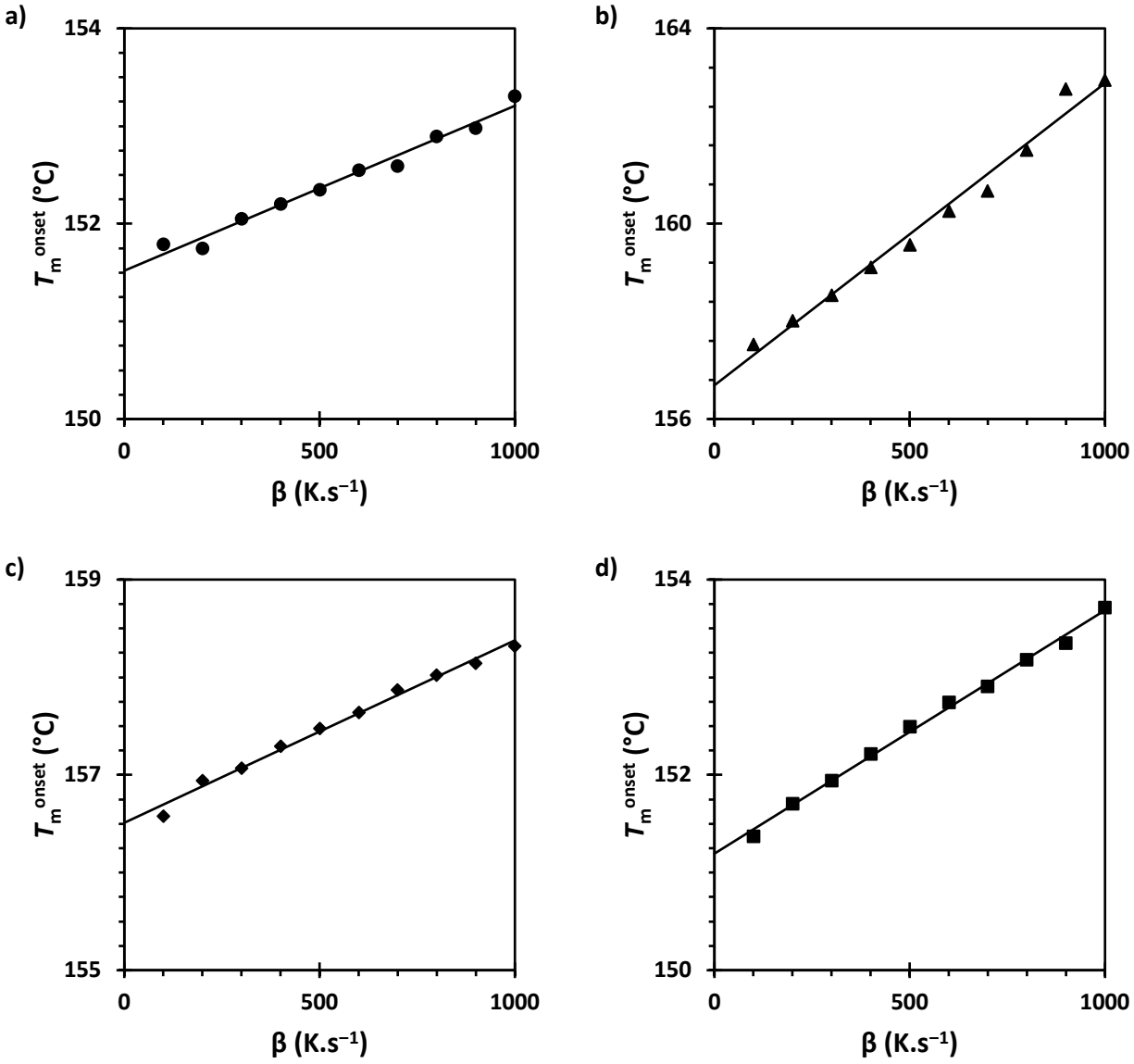

Figure 4.1: Plots of melting onset, $T_{\mathrm{m}}^{\mathrm{onset}}$, as a function of heating rate, β, for indium particles on top of a) PEO-33, b) PEO-66, c) PEO-98, and d) PEO-223.

Take note of the differences in the vertical scales between the four graphs. PEO-33 and PEO-223 (Fig. 4.1a,d) were studied using one batch of chips, while PEO-66 and PEO-98 (Fig. 4.1b,c) were studied using a different batch of chips. It is apparent from Fig. 4.1 that there was a significant disparity in the apparent indium melting temperature between the two different lots of sensors, which led to a significant difference in the single-point calibration constants. The chips used to study PEO-33 and PEO-223 had ΔT_{cal} = +5.1 and +5.4°C, respectively, and the chips used to study PEO-66 and PEO-98 had ΔT_{cal} = −0.1 and +0.1°C, respectively. The single-point calibration constants for the former set of samples are within the reported error limit for sensors following pre-calibration during manufacturing.[18]

4.4 RESULTS

4.4.1 Non-isothermal crystallization

The peak crystallization temperatures are shown in Figure 4.2 for different cooling rates for both CDSC and FDSC. While there is no clear trend with respect to molecular weight for the CDSC data up to the maximum cooling rate of $-\beta$ = 30 K.min^{-1}, the PEO-98 data consistently lies 9–10°C higher than the other three. This sample appears to nucleate the most efficiently, as we were able to acquire isothermal crystallization data using FDSC at crystallization temperatures up to T_{x} = 35°C, before random nucleation became an issue.

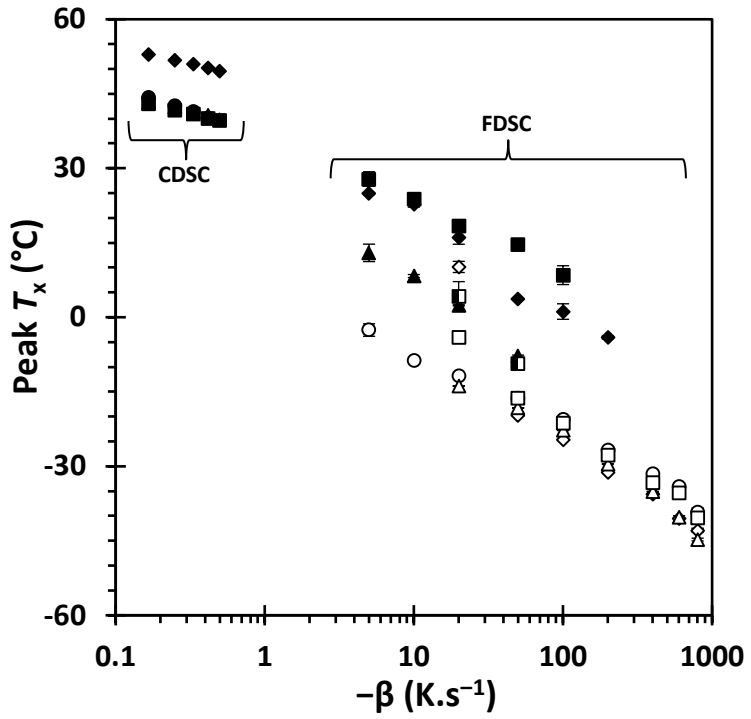

Figure 4.2: Peak crystallization temperature, T_x, as a function of cooling rate, $-\beta$, for PEO-33 (●, ○), PEO-66 (▲, △), PEO-98 (◆, ◇), PEO-223 (■, ◧, □). The filled symbols correspond to the highest temperature exotherm, the half-filled symbols correspond to the intermediate temperature exotherm, and the empty symbols correspond to the lowest temperature exotherm.

First, we note that crystallization is suppressed for cooling rates in excess of 10^3 K.s^{-1}. Second, there is no apparent molecular weight dependence for the FDSC data in Fig. 4.2. Third, the FDSC cooling traces exhibit one or more exothermic peaks depending on the cooling rate and the molecular weight. Multiple exotherms are only present when the cooling rate is neither too low nor too large. A single exotherm is observed for PEO-33, the lowest molecular weight sample in our study, at all cooling rates that were studied. In contrast, PEO-223 exhibits three crystallization peaks for $-\beta$ = 20 and 50 K.s^{-1}.

4.4.2 Isothermal crystallization

The majority of the isothermal crystallization exotherms exhibit similar shapes to data already published in the literature. That is, the exotherms are highly symmetric for low crystallization temperatures ($T_x \approx -40 - 0$°C), where the phase change occurs rapidly. These endotherms develop

asymmetric tails as crystallization proceeds more slowly outside this temperature range. Unusual isotherms were collected in the crystallization temperature range T_x = 10 – 25°C for PEO-98 and PEO-223 and at the highest crystallization temperatures for each sample. Figure 4.3 show exotherms for PEO-98 at T_x = 10, 15, 20, and 25°C. Note the jagged peaks for T_x = 10 and 15°C (Fig. 4.3a,b) and the double peaks for T_x = 20 and 25°C (Fig. 4.3c,d). Isothermal crystallization data was only collected up to T_x = 5°C for PEO-33, so this erratic behavior was not observed in this sample. Figure 4.4 shows nineteen replicate experiments for PEO-66 isothermally crystallized at T_x = 19.9°C, the highest isothermal crystallization temperature investigated for this particular sample. Eleven of these exotherms are develop in less than 5 s, and nucleation was observed in only eighteen of these nineteen replicate experiments.

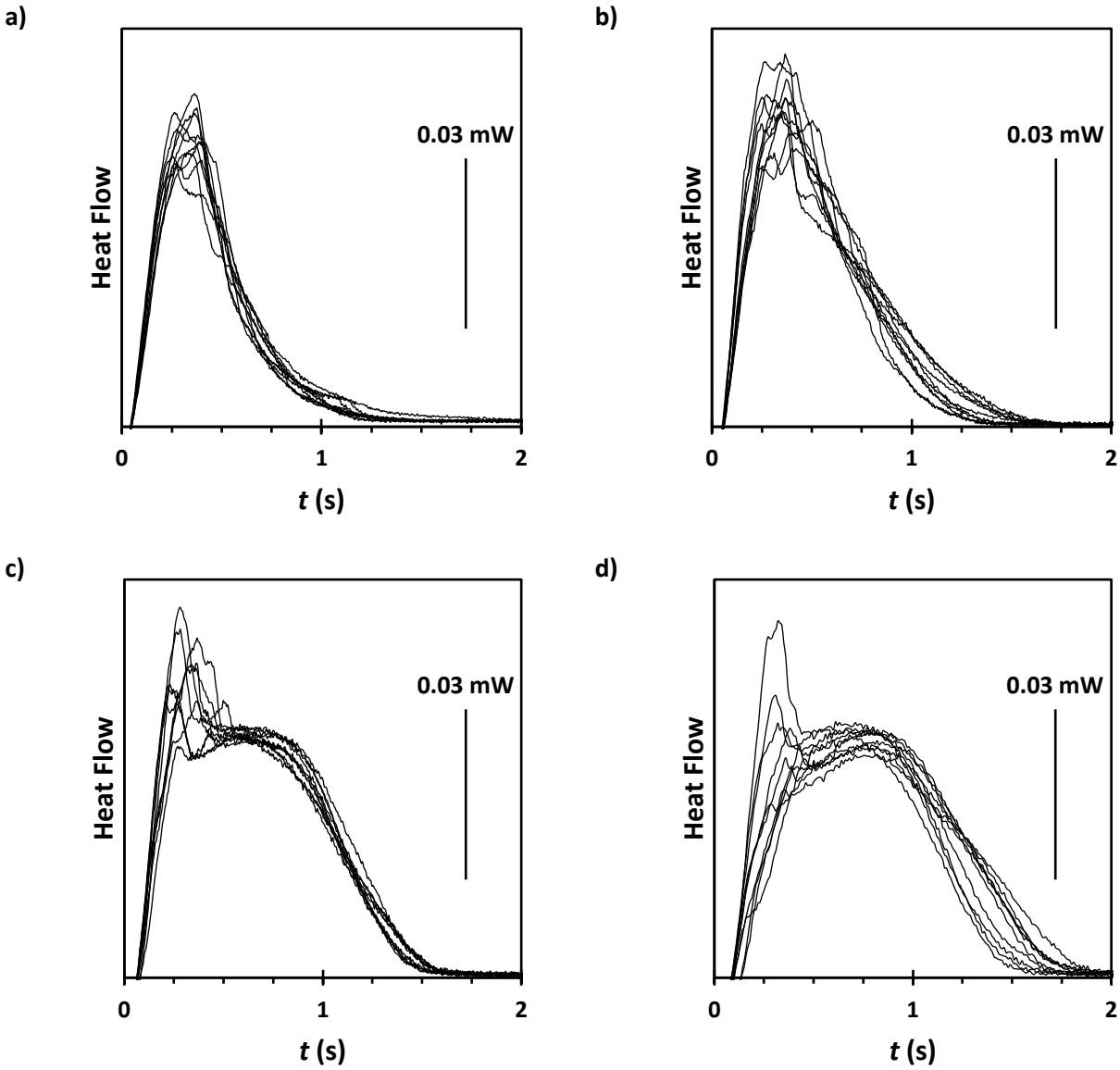

Figure 4.3: Overlays of exotherms for isothermal crystallization of PEO-98 at a) T_x = 10°C, b) T_x = 15°C, c) T_x = 20°C, and d) T_x = 25°C. Note that exo is up.

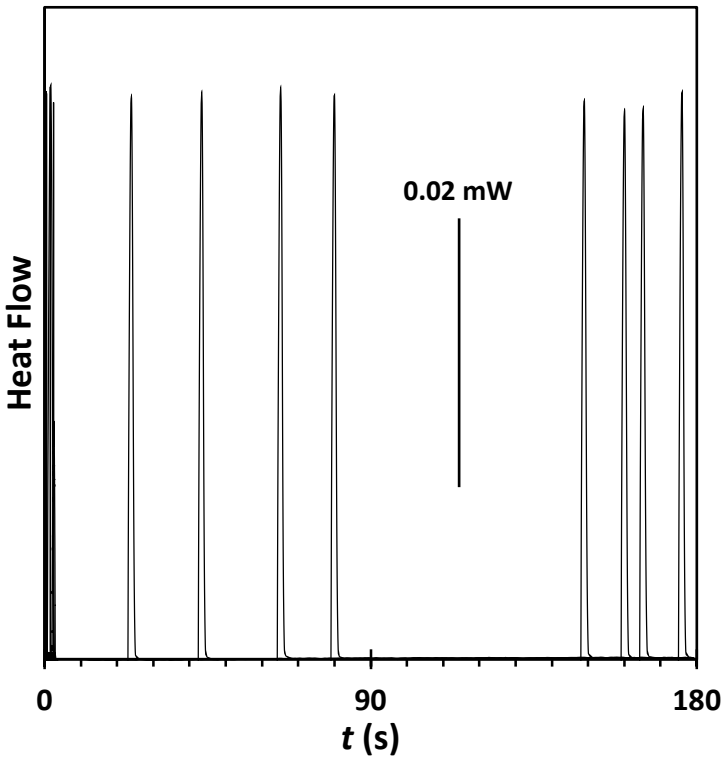

Figure 4.4: Exotherms of isothermal crystallization for PEO-66 at T_x = 19.9°C. Note that exo is up.

The peak crystallization time, τ_{peak}, was evaluated directly from each isotherm by taking the time associated with the maximum heat flow during crystallization. The peak crystallization time was found to be indiscernible within experimental error from the time required to release 50% of the enthalpy of crystallization, $\tau_{0.5}$, except for the extremes of the investigated temperatures. This finding is consistent with data from Rhoades et al. on PA-11.[42] Figure 4.5 shows that the peak crystallization time as function of the crystallization temperature is bimodal, and there is a global minimum at T_x = −25°C and a local minimum at T_x = 10°C with a cusp around T_x = −5°C. PEO-33 does not show a clear cusp, and the sample did not nucleate above T_x = 5°C on a reasonable time scale for data to be collected. It is clear from Fig. 4.5 that the peak crystallization time has no molecular weight dependence over the entire range of crystallization temperatures that were studied.

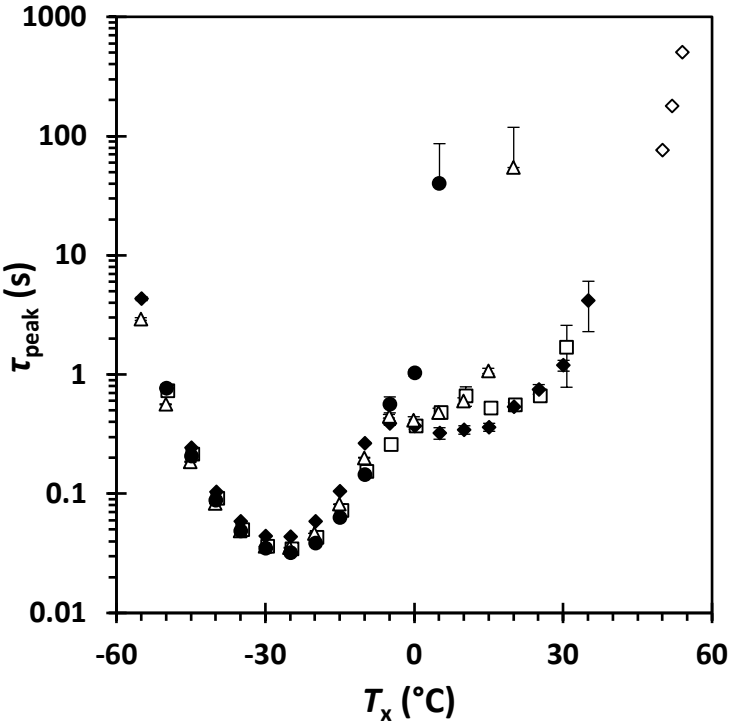

Figure 4.5: Relationship between peak crystallization time, τ_{peak}, and the isothermal crystallization temperature, T_{x}, for PEO-33 (●), PEO-66 (△), PEO-98 (◆), PEO-98 (CDSC) (◇), and PEO-223 (□). All data shown here was obtained using FDSC unless otherwise noted.

The maximum measured degree of crystallinity was calculated according to

$$X_{\mathrm{c}}^{\infty} = \frac{\Delta H_{\mathrm{c}}(T_{\mathrm{x}})}{\Delta H_{\mathrm{f}}^{\mathrm{o}}} \tag{4.15}$$

where X_{c}^{∞} is the largest measured degree of crystallinity, which ranges from 0 to unity, $\Delta H_{\mathrm{c}}(T_{\mathrm{x}})$ is the maximum measured enthalpy of crystallization, and $\Delta H_{\mathrm{f}}^{\mathrm{o}}$ = 197 J.g^{-1}.[6] The results for the degree of crystallinity as a function of isothermal crystallization temperature for the molecular weights studied are shown in Figure 4.6. There is a monotonic increase in the degree of crystallinity with increasing isothermal crystallization temperature for the four molecular weights, which begins to plateau at 20°C. Just like the peak crystallization time data, there is no clear dependence on molecular weight for the degree of crystallinity at the temperatures investigated. Unlike the crystallization time data, there is no cusp in the

degree of crystallinity data shown in Fig. 4.6. However, there are systematic differences in the degrees of crystallinity calculated from data collected on chips from two different batches.

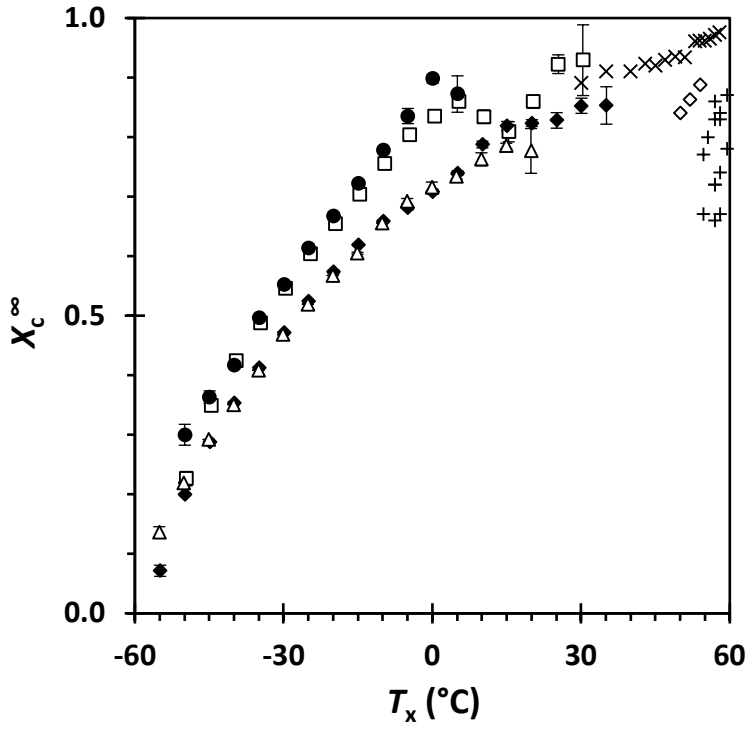

Figure 4.6: Relationship between degree of crystallinity and crystallization temperature for PEO-33 (●), PEO-66 (△), PEO-98 (◆), PEO-98 (CDSC) (◇), PEO-223 (□), Calleja et al.[93] (×),and Maclaine et al.[12] (+). For calculation of the degree of crystallinity, we assumed the theoretical heat of fusion to be independent of temperature. Our experimental data was recorded using FDSC unless otherwise noted.

A classical Avrami analysis was conducted by rearranging Eqn. (4.1) to obtain

$$\ln\left[-\ln\left(1-\frac{X_c(t)}{X_c^{\infty}}\right)\right] = \ln k + n\ln t \tag{4.16}$$

where a linear regression yields the natural logarithm of the Avrami crystallization rate constant as the y-intercept and the Avrami exponent as the slope of the line of best fit. Figure 4.7a shows conversion curves for PEO-98 at T_x = −50, −25, 0, and 25°C, and Fig. 4.7b shows the same data fit according to Eqn. (4.16). As expected from previous studies, systematic deviations are observed for the longest crystallization times in the best fit lines in Fig. 4.7b.[1, 2, 7-9, 12, 15, 16, 59] The Avrami rate constants and exponents are plotted as a

function of the crystallization temperature in Fig. 4.7c and Fig. 4.7d, respectively. Neither the Avrami crystallization rate constants nor the exponents show a discernible trend with respect to molecular weight. Both the Avrami rate constants and exponents show global maxima for all of the molecular weights around T_x = −25°C, corresponding the global minimum in the peak crystallization time (Fig. 4.5). The rate constants appear to level off at T_x = −5°C, corresponding to the cusp in the peak crystallization time data, before decreasing again at higher temperatures, while the exponents appear to level off at the same temperature and remain approximately constant at higher temperatures. Note that possible errors in the degree of crystallinity caused by heat flow losses (Fig. 4.6) are cancelled out in the Avrami analysis by taking the ratio of the degree of crystallinity to the maximum degree of crystallinity.

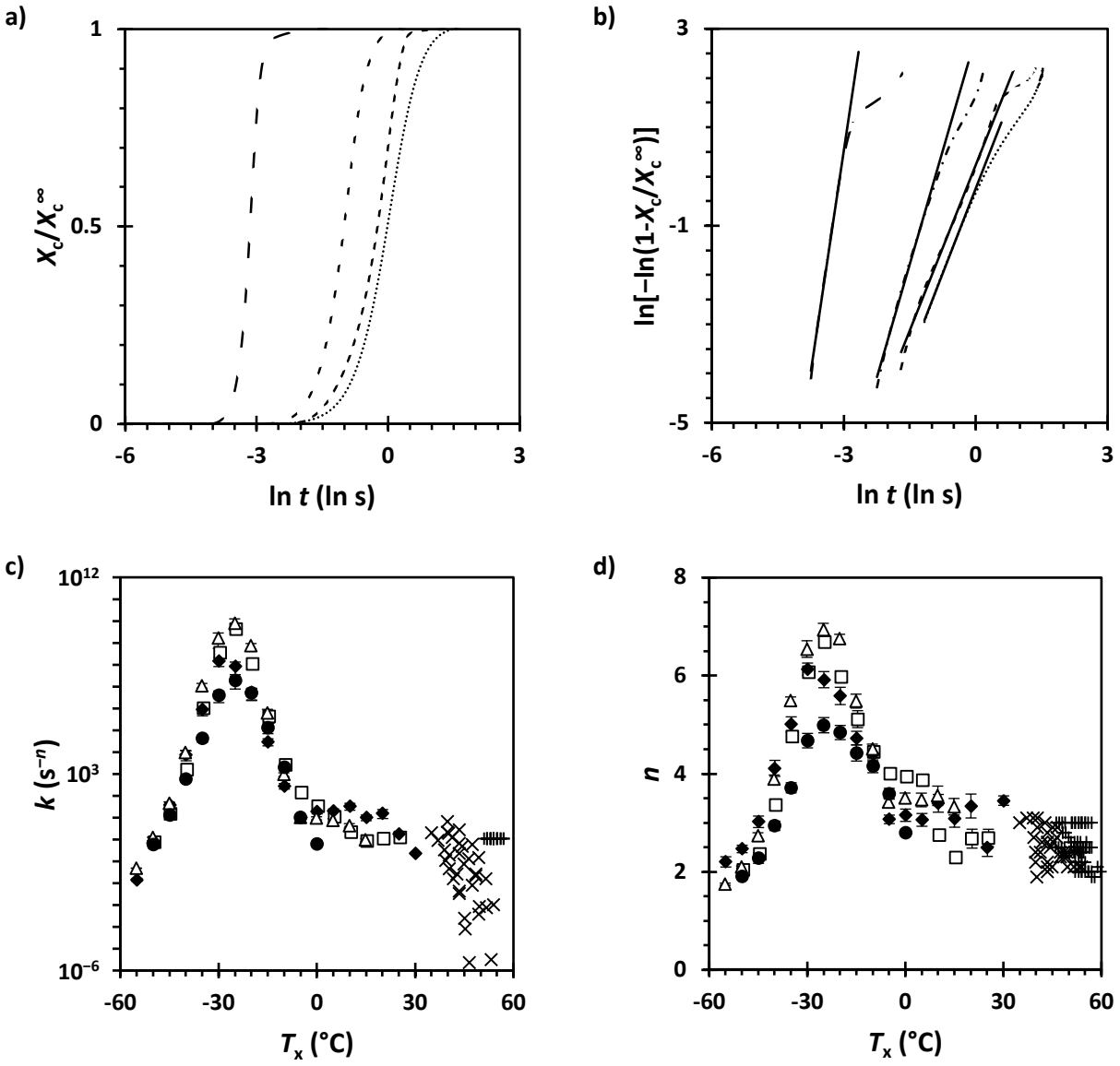

Figure 4.7: Data for PEO-98 showing a) the relationship between the normalized degree of crystallinity, X_c/X_c^∞, and the natural logarithm of crystallization time $\ln\ t$ and b) the Avrami plot for T_x = −50°C (.....), −25°C (⎯ . . ⎯), 0°C (⎯ . ⎯ . ⎯), and 25°C (⎯ ⎯ ⎯ ⎯ .) with best fit lines (⎯⎯⎯) according to Eqn. (4.16). The relationship between c) the Avrami constant, k, and the isothermal crystallization temperature, T_x, and d) the Avrami exponent, n, and the isothermal crystallization temperature, T_x, for PEO-33 (●), PEO-66 (△), PEO-98 (◆), PEO-223 (□), Cheng et al.[7] (×), and Hay et al.[8, 9] (+). Our experimental data was recorded using FDSC unless otherwise noted.

4.5 DISCUSSION

4.5.1 Non-isothermal crystallization

The data for PEO-66 and PEO-98 in Fig. 4.2 suggests that two different processes occur during cooling at high rates and low rates, and both processes can occur for intermediate cooling rates. This

conclusion is supported by the isothermal crystallization data. Low cooling rates, $-\beta \leq 10$ K.s^{-1}, yield high peak crystallization temperatures corresponding to the region above the cusp in the peak crystallization time data (Fig. 4.5), while high cooling rates, $-\beta \geq 200$ K.s^{-1}, yield low peak crystallization temperatures corresponding to the region below the cusp in the peak crystallization time data. Intermediate cooling rates, $-\beta = 20 - 100$ K.s^{-1}, showed at least two exotherms. These cooling rates are too fast for the first process to complete before reaching the temperature region of the second process. Similar double exothermic behavior has been observed when cooling at high rates with FDSC for *i*-PP[24-28, 94, 95], PBT[24, 34], PA-11[43], PA-12[96], and *i*-PP-co-PE[47]. In these cases, the higher temperature exotherm is associated with the formation of a stable crystalline phase, and the lower temperature exotherm is associated with the formation of a metastable mesophase. However, none of these cases exhibited a single exotherm, like PEO-33 for all cooling rates, or three exotherms, like PEO-223 for intermediate cooling rates. PEO-33 only exhibited non-isothermal crystallization at temperatures corresponding to the region below the cusp in the peak crystallization time data (Fig. 4.5). This is not surprising since PEO-33 did not nucleate on a time scale that was reasonable for isothermal crystallization experiments at temperatures greater than 5°C when analyzed with FDSC. The three exothermic peaks that are observed for PEO-223 may result from epitaxial nucleation and growth on the crystals that are formed during crystallization process that occurs at temperatures above $T_x = -5$°C. There is currently no crystallographic data at this time for PEO to confirm the origin of the multiple exothermic events during cooling, so it is unclear if the lowest temperature endotherm observed at high cooling rates arises from mesophase formation. Note that the higher molecular weights utilized in this study allow complete vitrification for $-\beta > 800$ K.s^{-1} as opposed to the report from Mathot et al.[55] on a PEG 6000 sample.

Studies on nucleation density of monodisperse PEO microdroplets on a polystyrene surface analyzed by polarized optical microscopy revealed that the probability of primary nucleation depends on the sample volume.[47, 48] Thus, the discontinuity between the CDSC and the FDSC data could be attributed

to the large difference in volume between the two types of samples, approximately five to six orders of magnitude. Sample volume effects could also explain why PEO-33 only exhibited one exotherm for all of the cooling rates investigated with FDSC since it was the smallest sample in the study (Table 4.2).

4.5.2 Isothermal crystallization

The two minima in the peak time of crystallization data (Fig. 4.5) have been observed for *i*-PP[24-33], PBT[24, 34-37], PBN[38], PA-6,6[39-41], PA-11[42-44], PCL[45, 46], *i*-PP-*co*-PE[47], and *i*-PP/EPR[22]. These reports attribute the bimodality to a change from heterogeneous primary nucleation at high temperatures to homogenous primary nucleation at low temperatures. Our results are qualitatively similar to all of these studies, with the exception of PA-6,6, in that the global minimum occurs below the cusp, or crossover temperature, in the peak time of crystallization data. There does not appear to be a distinct correlation between chemical structure, intermolecular interactions, or chain stiffness in determining whether a polymer will exhibit unimodal or bimodal crystallization behavior.

The appearance of two different nucleation mechanisms in the low and high crystallization temperature ranges, homogeneous and heterogeneous, respectively, is supported by nucleation density data of monodisperse PEO microdroplets on a polystyrene surface studied by polarized optical microscopy.[50, 51] Massa and Dalnoki-Veress[51] reported a change in nucleation mechanism at the same crossover temperature found here (T_x = −5°C). In later experiments with varied molecular mass, Massa et al.[50] showed that the nucleation mechanism crossover temperature was independent of molar mass. The change in nucleation mechanism is further supported by FDSC data for PBT[24, 36, 37], *i*-PP[25-28, 30, 31, 33], PA-11[42, 43], PCL[46], and *i*-PP-*co*-PE[47] containing nucleating agents. In these cases, the addition of nucleating agents not only decreased the peak time of crystallization by at least a factor of two in the high crystallization temperature region but also lowered the crossover temperature by at least 10°C. Moreover, the addition of nucleating agents had no effect on the peak time of crystallization in the low crystallization temperature region, which is to be expected if homogeneous primary nucleation occurs in this temperature range. The

highest crystallization temperature for each sample analyzed by FDSC was limited by statistical primary heterogenous nucleation, which prohibited collecting data over a reasonable time scale. PEO-33 had the lowest upper limit of crystallization temperatures at T_x = 5°C and PEO-98 had the highest upper limit at T_x = 35°C highest FDSC crystallization temperature, but the lowest CDSC data point for PEO-98 is at T_x = 50°C. It seems plausible that the FDSC sample dimensions may reduce the number and type of heterogeneities that would otherwise be present in CDSC samples of much larger dimensions considering that typical FDSC and CDSC sample volumes differ by five to six orders of magnitude. This statistical heterogeneous nucleation process exaggerated by the small FDSC sample size provides a plausible explanation for the unusually shaped exotherms shown in Fig. 4.3 and the random onset of crystallization in Fig. 4.4. Possible nucleation issues due to the small dimensions of FDSC samples may also be more apparent with PEO compared to the other polymers discussed herein since PEO is known to have low nucleation density and is sometimes studied using self-seeding techniques as a result.[6, 10, 16, 97]

It has been shown previously that the peak time of crystallization displays no molecular weight dependence below the crossover temperature for the cases of *i*-PP[24, 25, 28] and PA-6,6[41] and a relatively weak inverse molecular weight dependence above the crossover temperature. The lack of molecular weight dependence in the low temperature region has been attributed to the rapid morphological developments. At low crystallization temperatures, the crystallite dimensions become tiny and crystallization occurs at much faster time scales than disentanglement. As a result, the chain's length and number of entanglements no longer affect the kinetics of crystallization. This hypothesis has found support from atomic force microscopy and polarized optical microscopy observations for PBT[34], PA-6,6[40], and PA-11,[44] which show the disappearance of lamellar and spherulitic morphology at low crystallization temperatures, giving way to disordered, nodular crystallites that lack an organized superstructure. The inverse molecular weight dependence in the high temperature region becomes stronger as the crystallization temperature increases for the case of *i*-PP.[25, 28] However, studies on *i*-PP by Schawe et al.[28]

and Luijsterburg et al.[25] showed that the crystallization rate in high temperature region was more strongly influenced by the presence of heterogeneities (i.e. nucleating agents) and the origin of the samples (i.e. virgin vs. recycled) than it was by the molecular weight.

On a note of what may be regarded at this time as interesting coincidence, PEO exhibits a thermally activated relaxation of the crystalline phase, an α_c-relaxation, between −10 and 0°C measured by DMA, and a minimum in nuclear spin-lattice relaxation time, T_1, in the same temperature range.[98] It is generally accepted that the α_c-relaxation provides a mechanism for segmental motion of polymer chains within crystalline lamellae.[99, 100] Of the polymers discussed throughout this work that display bimodal or unimodal crystallization kinetics, only *i*-PP exhibits an α_c-relaxation.[101, 102] In this case, the α_c-relaxation temperature also coincides with the crossover temperature in peak crystallization time around 70°C. However, exactly how the primary nucleation mechanism, primary nucleation rate, and crystal growth rate via secondary nucleation are related to changes in crystalline mobility remains unclear at this time.

The degree of crystallinity calculated from CDSC data at high isothermal crystallization temperatures matches the values calculated from FDSC data well. Additionally, the CDSC and FDSC results lie below data from Calleja and Santa Cruz[93] for a sample with M_n = 13 kg.mol^{-1} and above data from Maclaine and Booth[12] for samples with M_v = 23 – 244 kg.mol^{-1}, both measured using CDSC (Fig. 4.6). Maclaine and Booth[12] did show an inverse relationship between the degree of crystallinity and molecular weight that we did not observe in our FDSC results, but this may be a result of the relatively higher temperatures, T_x > 54°C, from their study. There is a systematic deviation in values calculated from FDSC data that arises from differences in chips manufactured in two different batches. The chips for PEO-33 and PEO-223 came from the same batch while the chips for PEO-66 and PEO-98 came from a different batch. The degree of crystallinity values calculated for chips from the same batch are nearly equivalent, and the degree of crystallinity values calculated for chips from different batches differ by about 0.1. The sample geometry is similar for the chips (Table 4.2), nearly cylindrical and differing only in thickness, so it

should not give rise to significant differences in heat flow from one sample to another. There are differences in the masses of the samples, but PEO-98 and PEO-223 have nearly identical masses and yet they show a distinct systematic difference in the degree of crystallinity. Since the sample geometries are similar and there does not appear to be a systematic correlation between the deviation and sample mass then it seems reasonable to attribute the deviation to different batches of chips. There are currently no widely used methods of calibrating the heat flow for FDSC chips since this requires a sapphire standard with precisely measured mass. A focused ion beam could be used to mill a piece of sapphire with precisely controlled dimensions, and therefore precisely controlled mass, then placed on the chip and used to calibrate the heat flow.

Recall that the Avrami exponent is correlated to the primary nucleation mechanism and the crystal growth geometry (see Table 4.1). Please take note that this is an abridged compilation meant to facilitate the discussion to follow, and the reader is referred to Ref. 59 for a more comprehensive list. Since there does not appear to be a clear effect of molecular weight on the Avrami exponents, the following discussion will consider the average values for all four samples rather than considering each molecular weight individually. Starting at the lowest crystallization temperature, T_x = −55°C, the Avrami exponent of $n \approx 2$ corresponds to homogeneously nucleated rods. Formation of rod-like structures at temperatures approaching the glass transition seems reasonable due to limited long-range mobility in the polymer melt. As we previously mentioned, other studies on PBT[34], PA-6,6[40], and PA-11[44] have indicated that spherulitic morphology gives way to disorganized, nodular crystallites in the low crystallization temperature region. As the crystallization temperature increases, the Avrami exponent increases to a maximum value of $n \approx 6$ at T_x = −25°C, which corresponds to the minimum observed τ_{peak}, then decreases to $n \approx 3$ at $T_x \approx$ −5°C. This indicates homogeneous primary nucleation and growth of branching rods according to the model of Booth and Hay.[82] Within the framework of their model, the scaling exponent could be attributed to some combination of changes in the branching frequency, growth rate, and/or

cross-sectional area of the rods with changing crystallization temperature. There is another fibrillar branching mechanism that was proposed by Morgan,[81] but this model proposes fixed values of n = 5 or 6 for athermal and thermal nucleation, respectively. The maximum value of n reported here corresponds to the thermal nucleation of highly branched rods as proposed by Morgan. The values of n remain approximately constant at $n \approx 3$ for crystallization at temperatures greater than −5°C, indicating constant primary nucleation and crystal growth mechanisms above this temperature. Spherulite growth rate studies[3-6, 9-11, 13, 14] and nucleation studies[50, 51] on PEO suggest that the high temperature limit of $n \approx 3$ results from heterogeneously nucleated spherulite growth.

There is good agreement between the exponents from the present Avrami analysis in the high temperature limit and those from past studies of melt crystallized PEO using CDSC or dilatometry.[1, 7-9, 12, 17] Beech et al.[17] studied fractions with molecular weights ranging from 1 to 600 kg.mol^{-1} and reported Avrami exponents as low as 1.3 and as high as 3.0 for crystallization temperatures between 34.7 and 59.4°C. They did not report any trend with respect to molecular weight or crystallization temperature. Maclaine and Booth[12] found that fractions with molecular weights of 23 and 42 kg.mol^{-1} showed n = 3.5 for T_x between 54.7 and 59.4°C. Cheng and Wunderlich[7] published exponent values from 2.1 to 3.1 for samples with molecular weights between 3.5 and 5,000 kg.mol^{-1} for crystallization temperatures ranging from 35 to 54°C. Barnes et al.[1] concluded that early times of crystallization all yielded n = 4 for three different PEO samples crystallized from 46.2 to 55.5°C, but that the values decreased to a limiting value of 3 or 2 at long times, depending on the sample. Hay et al.[8, 9] reported Avrami exponents ranging from 1.8 to 3.7 for samples with molecular weights ranging from 4 to 6,000 kg.mol^{-1} over a range of crystallization temperatures from 48.2 to 57.4°C. There was no discernible trend with respect to molecular weight or crystallization temperature.

Cheng et al.[7] tested the validity of Eqn. (4.2a) for several PEO fractions by combining the results of an Avrami analysis conducted on CDSC data with nucleation density and spherulite growth rate data

collected using polarized optical microscopy. Based on their results, mentioned in the previous paragraph, they assumed growth of athermally nucleated spheres and calculated growth rates that were comparable to their experimental values. It would be an interesting test of primary nucleation theory, the Lauritzen-Hoffman secondary nucleation theory of polymer crystal growth, and the Avrami kinetic model to predict the rate constants according to Eqns. (4.2a) and (4.2b). Doing so would also potentially give physical insight into the origin of the crossover in crystallization kinetics observed in Fig. 4.6. The analysis would require four key pieces of information: 1) the crystalline morphology (i.e. mechanism of primary nucleation and crystal growth), 2) homogeneous primary nucleation rate, 3) heterogeneous nucleation density, and 4) spherulite growth rate.

The crystalline morphology determines the exponent s and the geometric factor C in Eqns. (4.2a) and (4.2b). Our results suggest that low temperature crystallization corresponds to growth of thermally nucleated rods with varying degrees of branching, indicating s = 1 in Eqn. (4.2b), and that high temperature crystallization corresponds to growth of athermally nucleated spheres, indicating s = 3 in Eqn. (4.2a). The Avrami theory predicts geometric factors $C = \frac{\pi d^2}{4}$ for the growth of thermally nucleated rods, corresponding to crystallization at T_x = −55°C, and $C = \frac{4\pi}{3}$ for the growth of athermally nucleated spheres, corresponding to crystallization at $T_x \geq -5$°C. It should be apparent that a reliable estimate of the rod diameter is necessary to calculate the geometric factor for crystallization at T_x = −55°C. Explicit geometric factors are not expected for the remainder of the low crystallization temperatures, where Avrami exponents ranging from 2 to 6 are observed, because Eqn. (4.13b) is an approximation to the power series expansion given in Eqn. (4.13a). Experimental data for the rod diameter and branching frequency could be useful here in determining a reasonable estimate of the geometric factor for the low crystallization temperature range.

The homogeneous primary nucleation rate data for use in Eqn. (4.2b) could potentially be measured in some systems using droplet methods, but this may present considerable experimental

difficulties for some polymers. Droplet methods have been used to measure the homogeneous primary nucleation kinetics in polyethylene[103] and poly(ethylene oxide).[50, 51] Experimental data could be extrapolated beyond the limits of the experimental data range according to classical nucleation theory[70-72] (Eqn. 4.3), or theoretical nucleation rate data could even be calculated given a reliable estimate of the primary nucleation rate constant, $K_{\mathrm{n}}^{\mathrm{homo}}$ (Eqn. 4.4). However, caution must be exercised when applying classical primary nucleation rate theory as known discrepancies exist between theory and experiment. The origin of the inconsistencies is commonly attributed to the assumption that the surface free energies are independent of temperature and that the free energy of crystallization varies linearly with undercooling (i.e. $\Delta C_{\mathrm{p}} = 0$).[70, 74, 103, 104]

Heterogeneous nucleation density for use in Eqn. (4.2a) can be obtained experimentally with polarized optical microscopy measurements. Conventional hot stages used for microscopy can cool samples at rates similar to CDSC, approximately 30 to 50 K.min^{-1}, which will limit data collection to temperatures that are well above the crossover temperature. For example, the lower limit for nucleation density measurements in PEO with this approach is about T_{x} = 35°C,[7] some 40°C above the crossover temperature.

The isothermal spherulite growth rate can be measured with polarized optical microscopy, but the lower temperature limit will be well above the crossover temperature, just like heterogeneous nucleation density measurements. Experimental spherulite growth rate data could be extrapolated to lower temperatures using the Lauritzen-Hoffman secondary nucleation theory (Eqns. 4.7 and 4.8),[73, 78-80] but there are two potential problems with this. First, a kinetic regime must be assumed in order to extrapolate the growth rate data to lower crystallization temperatures, but the crystal growth rates of many polymers, particularly PEO, are not characterized at the large undercoolings of interest. Second, just like classical primary nucleation theory, there are known inconsistencies in the Lauritzen-Hoffman secondary nucleation theory that may be partially explained by allowing the surface free energies to

depend on temperature[92, 105-109] and by accounting for the non-linear dependence of the free energy of fusion on temperature.[110, 111]

The modeling problem described herein is complex, and any inaccuracies in one component will compensate for those in another component, rendering the deconvolution of contributing errors nearly impossible. Unfortunately, more information than currently available is required to conduct a reliable analysis that would yield physically meaningful insight into the consistency between the Avrami theory, primary nucleation theory, and secondary nucleation theory in addition to the origin of the change in primary nucleation mechanism at low temperature.

4.6 CONCLUSIONS

The non-isothermal crystallization peak temperatures and the isothermal crystallization rates of four narrow molecular weight poly(ethylene oxide) fraction were measured using fast differential scanning calorimetry. The isothermal crystallization kinetics revealed a bimodal function of τ_{peak} vs. T_{x} that was independent of molecular weight for crystallization temperatures ranging from −55°C to 35°C. A common cusp was observed in the peak crystallization time data for all of the molecular weights around T_{x} = −5°C, which coincides with the α_{c}-relaxation in PEO. Crystallization at temperatures below the cusp is initiated by homogeneous primary nucleation while temperatures above the cusp leads to heterogeneous primary nucleation. An Avrami analysis of the isothermal crystallization data revealed significant temperature dependences in both the Avrami constant and exponent, with $n \approx 2$ approaching the glass transition temperature (T_{x} = −55), $n \approx 6$ at the maximum peak time of crystallization (T_{x}≈ −25°), and $n \approx 3$ approaching the highest crystallization temperature investigated (T_{x} = 35°C). The variable Avrami exponent in the low crystallization temperature region has been linked to the existence of a branching mechanism, and the limiting value of n = 3 has been attributed to the athermal nucleation of spherulites. Issues surrounding modeling the Avrami rate constant as a function of crystallization

temperature have been discussed, and the problem has been deemed intractable at the current time. This problem could potentially be addressed given sufficient morphological characterization and data for the homogeneous nucleation rate, the heterogeneous nucleation density, and the spherulite growth rate at low crystallization temperatures.

Unfortunately, the sub-ambient glass transition temperature of PEO (T_g = −70°C) precludes the analysis of the morphology and crystalline structure of the samples at this time. Isothermal crystallization below the crossover temperature yields metastable crystalline structures that reorganize immediately upon reheating to ambient conditions for morphological or structural analysis outside of the instrument. In the future, *in situ* measurements using X-ray diffraction, atomic force microscopy, or polarized optical microscopy could be utilized to determine if there is a correlation between the crossover temperature of PEO and mesophase formation. Future studies should also focus on testing multiple samples of the same molecular weight and with consistent sample volume to ascertain if there is a statistically significant difference in crystallization behavior arising from the exclusion of heterogeneities in the small specimen volume used in FDSC experiments. Such behavior could potentially obscure any molecular weight dependence in the high crystallization temperature range due to differences in heterogeneities and sample volume between specimens with different molecular weights.

4.7 ACKNOWLEDGEMENTS

We would like to thank Hadi Mohammadi for helpful discussions and input throughout the course of data collection and analysis. We would also like to thank TA Instruments for the temporary loan of a TA Q2000 conventional differential scanning calorimeter.

4.8 REFERENCES

1. Barnes, W. J.; Luetzel, W. G.; Price, F. P., Crystallization of poly-(ethylene oxide) in bulk. *The Journal of Physical Chemistry* **1961,** *65* (10), 1742-1748.

2. Beech, D. R.; Booth, C., Crystallization of high-molecular-weight fractions of poly(ethylene oxide) from dilute solution in ethanol. *Polymer* **1972,** *13* (7), 355-9.

3. Beech, D. R.; Booth, C.; Hillier, I. H.; Pickles, C. J., Crystallization of poly(ethylene oxide) fractions. Temperature dependence of growth rate. *Eur. Polym. J.* **1972,** *8* (6), 799-807.

4. Buckley, C. P., Kinetic theory of polymer crystal growth applied to melt crystallization of low molecular weight poly(ethylene oxide). *Polymer* **1980,** *21* (4), 444-57.

5. Cheng, S. Z. D.; Chen, J.; Heberer, D. P., Extended-chain crystal growth of low-molecular-mass poly(ethylene oxide) and α,ω-methoxy poly(ethylene oxide) fractions near their melting temperatures. *Polymer* **1992,** *33* (7), 1429-36.

6. Cheng, S. Z. D.; Chen, J.; Janimak, J. J., Crystal growth of intermediate-molecular-weight poly(ethylene oxide) fractions from the melt. *Polymer* **1990,** *31* (6), 1018-24.

7. Cheng, S. Z. D.; Wunderlich, B., Molecular segregation and nucleation of poly(ethylene oxide) crystallized from the melt. II. Kinetic study. *J. Polym. Sci., Part B: Polym. Phys.* **1986,** *24* (3), 595-617.

8. Hay, J. N.; Sabir, M., Crystallization kinetics of high polymers. Poly(ethylene oxide). II. *Polymer* **1969,** *10* (3), 203-11.

9. Hay, J. N.; Sabir, M.; Steven, R. L. T., Crystallization kinetics of high polymers. Poly(ethylene oxide). I. *Polymer* **1969,** *10* (3), 187-202.

10. Kovacs, A. J.; Gonthier, A., Crystallization and fusion of self-seeded polymers. II. Growth rate, morphology, and isothermal thickening of single crystals of low-molecular-weight poly(ethylene oxide) fractions. *Kolloid-Z. Z. Polym.* **1972,** *250* (5), 530-51.

11. Maclaine, J. Q. G.; Booth, C., Effect of molecular weight on spherulite growth rates of high molecular weight poly(ethylene oxide) fractions. *Polymer* **1975,** *16* (3), 191-5.

12. Maclaine, J. Q. G.; Booth, C., Effect of molecular weight on crystallization isotherms of high molecular weight poly(ethylene oxide) fractions. *Polymer* **1975,** *16* (9), 680-4.

13. Marentette, J. M.; Brown, G. R., The (010)–(120) crystal growth face transformation in poly (ethylene oxide) spherulites. *Polymer* **1998,** *39* (6-7), 1405-1414.

14. Point, J. J.; Kovacs, A. J., A critical look at some conceptual aspects of kinetic theories of polymer crystal growth. *Macromolecules* **1980,** *13* (2), 399-409.

15. Riande, E.; Fatou, J. G.; Alcazar, J. C., Crystallization kinetics of poly (ethylene oxide) diluted with xylene. *Polymer* **1977,** *18* (11), 1095-1099.

16. Vidotto, G.; Levy, D.; Kovacs, A. J., Crystallization and melting of self-seeding polymers. I. High-molecular-weight poly(1-butene), polyethylene and polyoxyethylene. *Kolloid-Z. Z. Polym.* **1969,** *230* (2), 289-305.

17. Beech, D. R.; Booth, C.; Dodgson, D. V.; Hillier, I. H., Crystallization of poly(ethylene oxide) fractions. Crystallization isotherms. *J. Polym. Sci., Part A-2* **1972,** *10* (8), 1555-64.

18. Vanden Poel, G.; Istrate, D.; Magon, A.; Mathot, V., Performance and calibration of the Flash DSC 1, a new, MEMS-based fast scanning calorimeter. *J. Therm. Anal. Calorim.* **2012,** *110* (3), 1533-1546.

19. Toda, A.; Androsch, R.; Schick, C., Insights into polymer crystallization and melting from fast scanning chip calorimetry. *Polymer* **2016,** *91*, 239-263.

20. Toda, A.; Konishi, M., An evaluation of thermal lags of fast-scan microchip DSC with polymer film samples. *Thermochim. Acta* **2014,** *589*, 262-269.

21. Tardif, X.; Pignon, B.; Boyard, N.; Schmelzer, J. W. P.; Sobotka, V.; Delaunay, D.; Schick, C., Experimental study of crystallization of PolyEtherEtherKetone (PEEK) over a large temperature range using a nano-calorimeter. *Polymer Testing* **2014,** *36*, 10-19.

22. Cai, J.; Luo, R.; Lv, R.; He, Y.; Zhou, D.; Hu, W., Crystallization kinetics of ethylene-co-propylene rubber/isotactic polypropylene blend investigated via chip-calorimeter measurement. *Eur. Polym. J.* **2017,** *96*, 79-86.

23. Treviño‐Quintanilla, C. D.; Krishnamoorti, R.; Bonilla‐Ríos, J., Flash DSC crystallization study for blown film grade bimodal HDPE resins. I. Isothermal kinetics and its application of the blown film modeling. *Journal of Polymer Science Part B: Polymer Physics* **2016,** *54* (23), 2425-2431.

24. Schawe, J. E. K., Influence of processing conditions on polymer crystallization measured by fast scanning DSC. *J. Therm. Anal. Calorim.* **2014,** *116* (3), 1165-1173.

25. Luijsterburg, B. J.; de Kort, G. W.; van Drongelen, M.; Govaert, L. E.; Goossens, J. G. P., Fast cooling of (non)-nucleated virgin and recycled poly(propylenes): effect of processing conditions on structural and mechanical properties. *Thermochim. Acta* **2015,** *603*, 94-102.

26. Schawe, J. E. K.; Potschke, P.; Alig, I., Nucleation efficiency of fillers in polymer crystallization studied by fast scanning calorimetry: Carbon nanotubes in polypropylene. *Polymer* **2017,** *116*, 160-172.

27. Schawe, J. E. K.; Vermeulen, P. A.; van Drongelen, M., New crystallization process in polypropylene highly filled with calcium carbonate. *Colloid Polym. Sci.* **2015,** *293* (6), 1607-1614.

28. Schawe, J. E. K.; Vermeulen, P. A.; van Drongelen, M., Two processes of α-phase formation in polypropylene at high supercooling. *Thermochim. Acta* **2015,** *616*, 87-91.

29. Silvestre, C.; Cimmino, S.; Duraccio, D.; Schick, C., Isothermal crystallization of isotactic poly(propylene) studied by superfast calorimetry. *Macromol. Rapid Commun.* **2007,** *28* (7), 875-881.

30. Ray, V. V.; Banthia, A. K.; Schick, C., Fast isothermal calorimetry of modified polypropylene clay nanocomposites. *Polymer* **2007,** *48* (8), 2404-2414.

31. De Santis, F.; Adamovsky, S.; Titomanlio, G.; Schick, C., Isothermal Nanocalorimetry of Isotactic Polypropylene. *Macromolecules* **2007,** *40* (25), 9026-9031.

32. Kalapat, D.; Tang, Q.; Zhang, X.; Hu, W., Comparing crystallization kinetics among two G-resin samples and iPP via Flash DSC measurement. *J. Therm. Anal. Calorim.* **2017,** *128* (3), 1859-1866.

33. Schawe, J. E. K.; Budde, F.; Alig, I., Nucleation activity at high supercooling: Sorbitol-type nucleating agents in polypropylene. *Polymer* **2018,** *153*, 587-596.

34. Androsch, R.; Rhoades, A. M.; Stolte, I.; Schick, C., Density of heterogeneous and homogeneous crystal nuclei in poly (butylene terephthalate). *European Polymer Journal* **2015,** *66*, 180-189.

35. Jariyavidyanont, K.; Androsch, R.; Schick, C., Crystal reorganization of poly (butylene terephthalate). *Polymer* **2017,** *124*, 274-283.

36. Wurm, A.; Herrmann, A.; Cornelius, M.; Zhuravlev, E.; Pospiech, D.; Nicula, R.; Schick, C., Temperature Dependency of Nucleation Efficiency of Carbon Nanotubes in PET and PBT. *Macromolecular Materials and Engineering* **2015,** *300* (6), 637-649.

37. Furushima, Y.; Kumazawa, S.; Umetsu, H.; Toda, A.; Zhuravlev, E.; Wurm, A.; Schick, C., Crystallization kinetics of poly(butylene terephthalate) and its talc composites. *Journal of Applied Polymer Science* **2017,** *134* (16), n/a-n/a.

38. Cavallo, D.; Mileva, D.; Portale, G.; Zhang, L.; Balzano, L.; Alfonso, G. C.; Androsch, R., Mesophase-Mediated Crystallization of Poly(butylene-2,6-naphthalate): An Example of Ostwald's Rule of Stages. *ACS Macro Letters* **2012,** *1* (8), 1051-1055.

39. Rhoades, A. M.; Williams, J. L.; Androsch, R., Crystallization kinetics of polyamide 66 at processing-relevant cooling conditions and high supercooling. *Thermochim. Acta* **2015,** *603*, 103-109.

40. Gohn, A. M.; Rhoades, A. M.; Wonderling, N.; Tighe, T.; Androsch, R., The effect of supercooling of the melt on the semicrystalline morphology of PA 66. *Thermochimica Acta* **2017,** *655*, 313-318.

41. Faraj, J.; Boyard, N.; Pignon, B.; Bailleul, J.-L.; Delaunay, D.; Orange, G., Crystallization kinetics of new low viscosity polyamides 66 for thermoplastic composites processing. *Thermochimica Acta* **2016,** *624*, 27-34.

42. Rhoades, A. M.; Wonderling, N.; Schick, C.; Androsch, R., Supercooling-controlled heterogeneous and homogenous crystal nucleation of polyamide 11 and its effect onto the crystal/mesophase polymorphism. *Polymer* **2016,** *106*, 29-34.

43. Jariyavidyanont, K.; Focke, W.; Androsch, R., Crystallization kinetics of polyamide 11 in the presence of sepiolite and montmorillonite nanofillers. *Colloid Polym. Sci.* **2016,** *294* (7), 1143-1151.

44. Mollova, A.; Androsch, R.; Mileva, D.; Schick, C.; Benhamida, A., Effect of supercooling on crystallization of polyamide 11. *Macromolecules* **2013,** *46* (3), 828-835.

45. Zhuravlev, E.; Schmelzer, J. W. P.; Wunderlich, B.; Schick, C., Kinetics of nucleation and crystallization in poly(ϵ-caprolactone) (PCL). *Polymer* **2011,** *52* (9), 1983-1997.

46. Zhuravlev, E.; Wurm, A.; Pötschke, P.; Androsch, R.; Schmelzer, J. W. P.; Schick, C., Kinetics of nucleation and crystallization of poly(ε-caprolactone) – Multiwalled carbon nanotube composites. *European Polymer Journal* **2014,** *52*, 1-11.

47. Androsch, R.; Monami, A.; Kucera, J., Effect of an alpha-phase nucleating agent on the crystallization kinetics of a propylene/ethylene random copolymer at largely different supercooling. *Journal of Crystal Growth* **2014,** *408*, 91-96.

48. Furushima, Y.; Nakada, M.; Yoshida, Y.; Okada, K., Crystallization/Melting Kinetics and Morphological Analysis of Polyphenylene Sulfide. *Macromolecular Chemistry and Physics* **2018,** *219* (2).

49. Androsch, R.; Di Lorenzo, M. L.; Schick, C., Optical Microscopy to Study Crystal Nucleation in Polymers Using a Fast Scanning Chip Calorimeter for Precise Control of the Nucleation Pathway. *Macromolecular Chemistry and Physics* **2018,** *219* (3), 1700479-n/a.

50. Massa, M. V.; Carvalho, J. L.; Dalnoki-Veress, K., Confinement Effects in Polymer Crystal Nucleation from the Bulk to Few-Chain Systems. *Phys. Rev. Lett.* **2006,** *97* (24), 247802/1-247802/4.

51. Massa, M. V.; Dalnoki-Veress, K., Homogeneous Crystallization of Poly(Ethylene Oxide) Confined to Droplets: The Dependence of the Crystal Nucleation Rate on Length Scale and Temperature. *Phys. Rev. Lett.* **2004,** *92* (25, Pt. 1), 255509/1-255509/4.

52. Androsch, R.; Di Lorenzo, M. L.; Schick, C.; Wunderlich, B., Mesophases in polyethylene, polypropylene, and poly(1-butene). *Polymer* **2010,** *51* (21), 4639-4662.

53. Mileva, D.; Androsch, R.; Zhuravlev, E.; Schick, C., Morphology of mesophase and crystals of polyamide 6 prepared in a fast scanning chip calorimeter. *Polymer* **2012,** *53* (18), 3994-4001.

54. Baeten, D.; Mathot, V. B. F.; Pijpers, T. F. J.; Verkinderen, O.; Portale, G.; Van Puyvelde, P.; Goderis, B., Simultaneous Synchrotron WAXD and Fast Scanning (Chip) Calorimetry: On the (Isothermal) Crystallization of HDPE and PA11 at High Supercoolings and Cooling Rates up to 200 °C s−1. *Macromolecular Rapid Communications* **2015,** *36* (12), 1184-1191.

55. Mathot, V.; Pyda, M.; Pijpers, T.; Poel, G. V.; Van de Kerkhof, E.; Van Herwaarden, S.; Van Herwaarden, F.; Leenaers, A., The Flash DSC 1, a power compensation twin-type, chip-based fast scanning calorimeter (FSC): first findings on polymers. *Thermochimica Acta* **2011,** *522* (1-2), 36-45.

56. Avrami, M., Kinetics of phase change. I. General theory. *J. Chem. Phys.* **1939,** *7*, 1103-12.

57. Avrami, M., Kinetics of phase change. II. Transformation-time relations for random distribution of nuclei. *J. Chem. Phys.* **1940,** *8*, 212-24.

58. Avrami, M., Granulation, phase change and microstructure. Kinetics of phase change. III. *J. Chem. Phys.* **1941,** *9*, 177-84.

59. Wunderlich, B., CHAPTER VI - The Growth of Crystals. In *Macromolecular Physics*, Wunderlich, B., Ed. Academic Press: 1976; pp 115-347.

60. Hay, J. N.; Booth, A., Effect of a secondary process on the course of polymer crystallization. *Brit. Polym. J.* **1972,** *4* (1), 19-26.

61. Price, F. P., Phenomenological theory of spherulitic crystallization: primary and secondary crystallization processes. *J. Polym. Sci., Part A: Gen. Pap.* **1965,** *3* (9), 3079-86.

62. Price, F. P., Some Comments on the``Avrami''Equation. *Journal of Applied Physics* **1965,** *36* (10), 3014-3016.

63. Hillier, I. H., Modified Avrami equation for the bulk crystallization kinetics of spherulitic polymers. *J. Polym. Sci., Part A: Gen. Pap.* **1965,** *3* (9), 3067-78.

64. Hoshino, S.; Meinecke, E.; Powers, J.; Stein, R. S.; Newman, S., Crystallization kinetics of polypropylene fractions. *J. Polym. Sci., Part A: Gen. Pap.* **1965,** *3* (9), 3041-66.

65. Hay, J. N., Application of the modified avrami equations to polymer crystallisation kinetics. *British Polymer Journal* **1971,** *3* (2), 74-82.

66. Hay, J. N.; Przekop, Z. J., Extensions of the Avrami equation to various polymer crystallization models. *Journal of Polymer Science: Polymer Physics Edition* **1979,** *17* (6), 951-959.

67. Banks, W.; Sharples, A.; Hay, J. N., The effect of simultaneously occurring processes on the course of polymer crystallization. *Journal of Polymer Science Part A: General Papers* **1964,** *2* (9), 4059-4067.

68. Price, F. P.; Thornton, J. M., Effect of impingement of rods on the Avrami equation. *Journal of Applied Physics* **1973,** *44* (10), 4312-4313.

69. Turnbull, D., Kinetics of heterogeneous nucleation. *The Journal of Chemical Physics* **1950,** *18* (2), 198-203.

70. Turnbull, D., Kinetics of solidification of supercooled liquid mercury droplets. *The Journal of chemical physics* **1952,** *20* (3), 411-424.

71. Turnbull, D.; Fisher, J. C., Rate of nucleation in condensed systems. *The Journal of chemical physics* **1949,** *17* (1), 71-73.

72. Wunderlich, B., CHAPTER V - The Nucleation Step. In *Macromolecular Physics*, Wunderlich, B., Ed. Academic Press: 1976; pp 1-114.

73. Lauritzen, J. I., Jr.; Hoffman, J. D., Theory of formation of polymer crystals with folded chains in dilute solution. *J. Res. Natl. Bur. Stand., Sect. A* **1960,** *64A* (No. 1), 73-102.

74. Spaepen, F., Homogeneous nucleation and the temperature dependence of the crystal-melt interfacial tension. In *Solid State Physics*, Elsevier: 1994; Vol. 47, pp 1-32.

75. Mandelkern, L.; Quinn, F. A., Jr.; Flory, P. J., Crystallization kinetics in high polymers. I. Bulk polymers. *J. Appl. Phys.* **1954,** *25*, 830-9.

76. Binsbergen, F. L., Heterogeneous nucleation in the crystallization of polyolefins. III. Theory and mechansim. *Journal of Polymer Science: Polymer Physics Edition* **1973,** *11* (1), 117-135.

77. Binsbergen, F. L., Heterogeneous nucleation of crystallization. *Progress in solid state chemistry* **1973,** *8*, 189-238.

78. Hoffman, J. D.; Lauritzen, J. I., Jr., Crystallization of bulk polymers with chain folding: theory of growth of lamellar spherulites. *J. Res. Natl. Bur. Stand., Sect. A* **1961,** *65A*, 297-336.

79. Hoffman, J. D.; Miller, R. L., Test of the reptation concept: crystal growth rate as a function of molecular weight in polyethylene crystallized from the melt. *Macromolecules* **1988,** *21* (10), 3038-51.

80. Hoffman, J. D.; Miller, R. L., Kinetic of crystallization from the melt and chain folding in polyethylene fractions revisited: theory and experiment. *Polymer* **1997,** *38* (13), 3151-3212.

81. Morgan, L. B., Crystallization phenomena in polymers-The course of the crystallization. *Phil. Trans. R. Soc. Lond. A* **1954,** *247* (921), 13-22.

82. Booth, A.; Hay, J. N., An extension of polymer crystallisation kinetics to a branching mechanism for spherulitic growth. *British Polymer Journal* **1972,** *4* (1), 9-17.

83. Hay, J. N., Use of model compounds to determine equilibrium melting points of polymers. *J. Polym. Sci., Polym. Chem. Ed.* **1976,** *14* (12), 2845-52.

84. Bartczak, Z.; Argon, A. S.; Cohen, R. E.; Kowalewski, T., The morphology and orientation of polyethylene in films of sub-micron thickness crystallized in contact with calcite and rubber substrates. *Polymer* **1999,** *40* (9), 2367-2380.

85. Jeon, K.; Krishnamoorti, R., Morphological behavior of thin linear low-density polyethylene films. *Macromolecules* **2008,** *41* (19), 7131-7140.

86. Mellbring, O.; Kihlman Øiseth, S.; Krozer, A.; Lausmaa, J.; Hjertberg, T., Spin coating and characterization of thin high-density polyethylene films. *Macromolecules* **2001,** *34* (21), 7496-7503.

87. Zhang, G.; Zhai, X.; Ma, Z.; Jin, L.; Zheng, P.; Wang, W.; Cheng, S. Z. D.; Lotz, B., Morphology diagram of single-layer crystal patterns in supercooled poly (ethylene oxide) ultrathin films: Understanding macromolecular effect of crystal pattern formation and selection. *ACS Macro Letters* **2011,** *1* (1), 217-221.

88. Ruzette, A.-V. G.; Mayes, A. M., A Simple Free Energy Model for Weakly Interacting Polymer Blends. *Macromolecules* **2001,** *34* (6), 1894-1907.

89. Sarge, S. M.; Gmelin, E.; Hoehne, G. W. H.; Cammenga, H. K.; Hemminger, W.; Eysel, W., The caloric calibration of scanning calorimeters. *Thermochim. Acta* **1994,** *247* (2), 129-68.

90. Toda, A., Heating rate dependence of melting peak temperature examined by DSC of heat flux type. *J. Therm. Anal. Calorim.* **2016,** *123* (3), 1795-1808.

91. Vanden Poel, G.; Mathot, V. B. F., High-speed/high performance differential scanning calorimetry (HPer DSC): Temperature calibration in the heating and cooling mode and minimization of thermal lag. *Thermochim. Acta* **2006,** *446* (1-2), 41-54.

92. Mohammadi, H.; Vincent, M.; Marand, H., Investigating the equilibrium melting temperature of linear polyethylene using the non-linear Hoffman-Weeks approach. *Polymer* **2018,** *146*, 344-360.

93. Calleja, F. J.; Cruz, C. S., Novel aspects of the microstructure of poly (ethylene oxide) as revealed by microhardness: Influence of chain ends. *Acta polymerica* **1996,** *47* (6‐7), 303-309.

94. Schawe, J. E. K., Analysis of non-isothermal crystallization during cooling and reorganization during heating of isotactic polypropylene by fast scanning DSC. *Thermochimica Acta* **2015,** *603*, 85-93.

95. Rhoades, A. M.; Wonderling, N.; Gohn, A.; Williams, J.; Mileva, D.; Gahleitner, M.; Androsch, R., Effect of cooling rate on crystal polymorphism in beta-nucleated isotactic polypropylene as revealed by a combined WAXS/FSC analysis. *Polymer* **2016,** *90*, 67-75.

96. Fischer, C.; Seefried, A.; Drummer, D., Crystallization and Component Properties of Polyamide 12 at Processing‐Relevant Cooling Conditions. *Polymer Engineering & Science* **2017,** *57* (4), 450-457.

97. Kovacs, A. J.; Gonthier, A.; Straupe, C., Isothermal growth, thickening, and melting of poly(ethylene oxide) single crystals in the bulk. *J. Polym. Sci., Polym. Symp.* **1975,** *50* (Int. Symp. Macromol., Invited Lect., 1974), 283-325.

98. Connor, T. M.; Read, B. E.; Williams, G., The dielectric, dynamic mechanical, and nuclear resonance properties of poly(ethylene oxide) as a function of molecular weight. *J. Appl. Chem.* **1964,** *14*, 74-80.

99. Boyd, R. H., Relaxation processes in crystalline polymers: experimental behavior. *Polymer* **1985,** *26* (3), 323-47.

100. Boyd, R. H., Relaxation processes in crystalline polymers: molecular interpretation - a review. *Polymer* **1985,** *26* (8), 1123-33.

101. Hu, W. G.; Schmidt‐Rohr, K., Polymer ultradrawability: the crucial role of α‐relaxation chain mobility in the crystallites. *Acta Polymerica* **1999,** *50* (8), 271-285.

102. Wu, H.-y.; Li, X.-x.; Xiang, F.-m.; Huang, T.; Shi, Y.-y.; Wang, Y., Microstructure evolution of isotactic polypropylene during annealing: Effect of poly (ethylene oxide). *Chinese Journal of Polymer Science* **2012,** *30* (2), 199-208.

103. Cormia, R. L.; Price, F. P.; Turnbull, D., Kinetics of crystal nucleation in polyethylene. *The Journal of Chemical Physics* **1962,** *37* (6), 1333-1340.

104. Turnbull, D.; Cormia, R. L., Kinetics of crystal nucleation in some normal alkane liquids. *The Journal of Chemical Physics* **1961,** *34* (3), 820-831.

105. Hoffman, J. D.; Lauritzen, J. I.; Passaglia, E.; Ross, G. S.; Frolen, s. L. J.; Weeks, J. J., Kinetics of polymer crystallization from solution and the melt. *Kolloid-Zeitschrift und Zeitschrift für Polymere* **1969,** *231* (1-2), 564-592.

106. Huseby, T. W.; Bair, H. E., Dissolution of Polyethylene Single Crystals in Xylene and Octadecane. *Journal of Applied Physics* **1968,** *39* (11), 4969-4973.

107. Lauritzen, J. I.; Passaglia, E., Kinetics of crystallization in multicomponent systems: II. Chain-folded polymer crystals. *J. Res. Natl. Bur. Stand* **1967,** *71*, 261-275.

108. Marand, H.; Xu, J.; Srinivas, S., Determination of the Equilibrium Melting Temperature of Polymer Crystals: Linear and Nonlinear Hoffman-Weeks Extrapolations. *Macromolecules* **1998,** *31* (23), 8219-8229.

109. Mohammadi, H. On the Melting and Crystallization of Linear Polyethylene, Poly(ethylene oxide), and Metallocene Linear Low-Density Polyethylene. Ph.D. Thesis, Virginia Polytechnic Institute and State University, Blacksburg, VA, 2018.

110. Hoffman, J. D., Thermodynamic Driving Force in Nucleation and Growth Processes. *The Journal of Chemical Physics* **1958,** *29* (5), 1192-1193.

111. Hoffman, J. D.; Weeks, J. J., Rate of spherulitic crystallization with chain folds in polychlorotrifluoroethylene. *The Journal of Chemical Physics* **1962,** *37* (8), 1723-1741.

CHAPTER 5

Preparation, Fractionation, and Thermal Characterization of Poly(δ-valerolactone)

5.1 INTRODUCTION

Poly(δ-valerolactone) (PVL) is a linear, aliphatic polylactone that is semi-crystalline and bioresorbable with mechanical and physical properties similar to poly(ε-caprolactone) (PCL). These attributes make PVL well-suited for various biomedical applications such as drug delivery,[1] biological implants,[2] and tissue scaffolds.[3] PVL is synthesized via ring opening polymerization of δ-valerolactone proceeding through coordination-insertion, cationic, or anionic mechanisms.[4, 5] Synthetic procedures similar to these for PCL are often employed, but the lower ring strain in the 6-membered δ-valerolactone can make the synthesis of high molecular weight samples more difficult and may necessitate experimental modifications.[4]

Linear, aliphatic polyesters, such as PVL and other polylactones, are interesting polymers for studies of the thermodynamics and kinetics of polymer crystallization because they introduce a basic chemical functionality into the linear polyethylene backbone. Additionally, there are facile synthetic routes that yield controlled molecular weight polymers with narrow polydispersity indices.[4, 5] Polylactones with relatively low to moderate methylene content, like PVL, can be soluble in common solvents (i.e. dichloromethane, toluene, etc.) from room temperature up to moderately elevated temperatures.[6] This makes solvent-based batch fractionation methods to obtain monodisperse samples much simpler and cheaper compared to many polyolefins. Polylactones typically exhibit good thermal stability,[7-9] which makes them well-suited for repeated crystallization and melting measurements. Furthermore, they are free from defects, such as branching, and the end groups can be controlled through the polymerization conditions or by post-polymerization modification.

PVL is also particularly attractive for studies of the physics of polymer crystallization because it is structurally and chemically similar to poly(ε-caprolactone), which has been extensively studied, but it has a distinctive difference regarding its crystal structure. The unit cell of PVL is orthorhombic with a and b dimensions similar to those of polyethylene and PCL, but the c dimension and the orientation of its ester carbonyls differ considerably from PCL. All ester dipoles are oriented in the same direction within the unit cell for polymers derived from odd-carbon-atom monolactones, like δ-valerolactone, while the ester dipoles orient in alternating (opposing) directions for even-carbon-atom monolactones, like ε-caprolactone. Ultimately, this means that the c dimension of any odd-carbon-atom monolactone unit cell is equal to the length of one monomer, and the c dimension of any even-carbon-atom monolactone unit cell is equal to the length of two monomers. Thus, the orientation of chemical functional groups in the crystal unit cell can be controlled simply by the parity of the carbon atoms in monolactone precursors. This control over the crystal structure of polylactones offers a straightforward approach to developing structure-property relationships that quantify the effects of chemical functionality on the thermodynamics and kinetics of polymer crystallization.

The molecular weight, molecular weight distribution, chemical composition (i.e. comonomer content), chain topology (i.e. extent of branching), and microstructure (i.e. tacticity) of polymers are known to affect the thermal,[10-12] mechanical,[11, 12] rheological,[11, 12] and charge transport[13] properties of polymeric materials. The aforementioned physical and chemical characteristics also affect the primary nucleation and spherulite growth rates.[14] As such, the molecular weight, chemical composition, etc. play a crucial role in determining the overall performance and applications for different materials. Polymer samples with narrow molecular weight distributions and tailored chemical compositions, chain topologies, and microstructures are necessary to ascertain the effects of physical and chemical characteristics on material properties. However, polymerization leads to a distribution of molecular weights and chemical compositions which necessitate fractionation methods to obtain model

compounds. Polymers can be separated by molecular weight, chemical composition, chain topology, and microstructure using fractionation methods, which fall into three different categories: crystallization,[15-19] chromatographic,[15, 18] and liquid-liquid phase separation.[20-31]

There are three common types of crystallization-based fractionation methods that can be performed on analytical or preparative scales to separate polymer mixtures with varying chemical compositions, topologies, or tacticities.[15-19] Temperature rising elution fractionation (TREF)[15-17, 19] involves dissolving the sample at a high temperature, then allowing the polymer to crystallize onto a solid support, typically packed inside a column, by slowly decreasing the temperature. The temperature is then slowly raised while the column is eluted. The least crystallizable chains are eluted first, and the most crystallizable chains are eluted last. A major drawback of TREF is the long analysis time, up to 100 hr depending on the experimental set up.[19] Crystallization elution fractionation (CEF)[16, 18, 19] is similar to TREF in that the hot polymer solution is loaded into a column packed with a solid support, except solvent is pumped through the column during the cooling step. This enhances the physical separation of the components that crystallize to different extents. The final step involves heating and elution, similar to TREF. A CEF experiment only takes about 30 min, making it a considerable improvement over both TREF and CRYSTAF.[19]

Two different chromatographic separation techniques are employed for the separation of polymer samples according to molar mass. Preparative size exclusion chromatography (prep-SEC)[16, 19] is a column-based fractionation technique that utilizes the hydrodynamic volume of polymer chains to separate them by molar mass. Prep-SEC utilizes existing SEC instrumentation, used to analyze the molar mass distribution of polymer samples, with the addition of a fraction collector, similar to automated chromatography equipment used in the purification of small molecules. Field flow fractionation (FFF)[16, 19] is a chromatographic technique in that it utilizes a constantly flowing mobile phase, but there is no stationary phase and the separation occurs within a channel as opposed to a column. Here, the solution

is pumped through a very thin, hollow channel, with a force field applied perpendicular to the direction of laminar flow. Similar to prep-SEC, a fraction collector is used to collect different molecular weight samples as they exit the channel.

The two predominant batch liquid-liquid phase separation fractionation methods exploit the dependence of polymer solubility on chain length. The composition of a quasi-ternary system consisting of polydisperse polymer, solvent, and nonsolvent is adjusted by the addition of nonsolvent to induce liquid-liquid phase separation between a polymer-rich (gel) phase and a polymer-lean (sol) phase.[20, 23] Note that a true ternary system would consist of monodisperse polymer, solvent, and nonsolvent. In successive solution fractionation (SSF),[23-27] an excess of nonsolvent is added to precipitate the majority of the high molecular weight polymer, and the polymer-lean phase is isolated to obtain fractions with increasing molecular weights. Inversely, in successive precipitation fractionation (SPF),[21-23, 28-31] a minimum amount of nonsolvent is added to precipitate a small amount of the high molecular weight polymer, and the polymer-rich phase is isolated to yield decreasing molecular weight fractions. Both methods proceed through multiple iterations, where the polydispersity index, PDI, of each successive fraction decreases.

Extensive studies by Kamide et al.[21-31] determined that the initial molecular weight, initial molecular weight distribution, initial solution concentration, choice of solvent and nonsolvent, and the volumes of individual fractions all impact solution fractionation. Furthermore, the two methods exhibit distinct differences:[21-31]

1) Each iteration of SSF requires considerably more volume of nonsolvent compared to SPF.
2) The PDI of fractions collected by SSF are lower than those collected by SPF.
3) SSF is less sensitive to the initial PDI and molecular weight compared to SPF.
4) SPF is highly sensitive to the polymer concentration at the start of fractionation. Additionally, lower initial concentrations must be used with SPF in order to obtain fractions with low PDIs.

5) Precise temperature control is required in SPF, which can be a severe disadvantage if the fractionation is conducted at temperatures far from ambient conditions.
6) The total volume of solution at each step is precisely controlled in SSF, whereas the total volume of solution increases at each step in SPF.
7) Reverse fractionation early in the process is possible with SPF.
8) When compared to the initial sample, the first fraction always has a larger PDI for SPF and a smaller PDI for SSF.

In general, SSF is recommended as the superior fractionation protocol, but SPF has found more widespread use partially because it requires considerably less total volume of nonsolvent. SSF also requires more extensive knowledge of the system's phase and precipitation behavior when compared to SPF, which makes the former method harder to implement.[20, 23]

There are currently no reports on the fractionation of PVL in the literature. However, narrow molecular weight fractions of PCL have been obtained via SPF by several groups using different solvent/nonsolvent pairs, shown in Table 5.1.[32-35] The solubility of PCL has been studied, but no work has been dedicated to the solubility of PVL.[6] The strengths of solvents and nonsolvents should be similar for the two polymers considering the similarities in their chemical structures, intermolecular interactions, and thermal properties.

Table 5.1: Solvent/nonsolvent combinations that have been used for the successive precipitation fractionation of PCL.

Reference	Solvent	Nonsolvent
Chen et al.[32]	THF	methanol
Crescenzi et al.[36]	benzene	petroleum ether
Koleske et al.[33]	benzene	*n*-heptane
Perret et al.[35]	benzene	isooctane
Sheth[34]	toluene	*n*-heptane

The primary objective of the present study was to obtain narrow molecular weight fractions of PVL with known origin for use as model compounds in kinetics and thermodynamics studies of polymer crystallization. To that end, we will demonstrate the synthesis of PVL using microwave irradiation to obtain samples with high molecular weight and low polydispersity indices. The applicability of successive precipitation fractionation using toluene/*n*-heptane as the solvent/nonsolvent pair will be considered to prepare materials of even lower polydispersity. Lastly, we will present the basic thermal characterization of five narrow molecular weight fractions spanning ca. 50 $kg.mol^{-1}$.

5.2 EXPERIMENTAL

5.2.1 Materials

HPLC grade dichloromethane, *n*-heptane, methanol, 1,1,2,2-tetrachloroethane, tetrahydrofuran, toluene, and deionized water were purchased from Fisher Scientific. Dichloromethane and toluene were purified, dried over calcium hydride, and distilled prior to use in polymerization. Solvents used for purification, fractionation, or characterization were used as received. Concentrated nitric acid, deuterated chloroform, deuterated chloroform with tetramethylsilane, and sodium chloride were purchased from Sigma Aldrich and used without further purification. δ-valerolactone was purchased from Sigma-Aldrich, vacuum distilled, and stored under nitrogen atmosphere. Tin(II) trifluoromethanesulfonate was purchased from Strem Chemicals Inc., stored inside of a glove box under nitrogen atmosphere, and used as received. Tin(II) octoate was purchased from Sigma Aldrich, stored over activated molecular sieves, and used without further purification.

5.2.2 Synthesis

5.2.2.1 Conventional thermal synthesis (CTS)

The following outlines a characteristic procedure for the conventional thermal synthesis of PVL that was adapted from Stevens et al.[1] A 50 mL Schlenk flask, stir bar, and syringes for reagent transfer

were dried overnight at 110°C and cooled to room temperature under nitrogen purge. The Schlenk flask was flame dried and cooled to room temperature under vacuum, then it was back-filled with nitrogen three times. $Sn(OTf)_2$ (195 mg, 4.68 mmol) was added to the Schlenk flask inside of a glovebox under nitrogen atmosphere. 10.0 mL of 0.0933 M isoamyl alcohol (82.2 mg, 9.33 mmol) in anhydrous dichloromethane was added by syringe to the Schlenk flask containing the $Sn(OTf)_2$ and stirred for 30 min. 15 mL of neat δ-valerolactone (16.2 g, 0.162 mol) was added to the reaction flask via syringe, and the mixture was stirred under nitrogen atmosphere at room temperature for 72 hr. The product was obtained by precipitating the reaction mixture into cold methanol (250 mL) by dropwise addition from a separatory funnel to yield the product as a fine white powder. The product was further purified by dissolving in dichloromethane (ca. 30 mL) and precipitation by dropwise addition into cold methanol (250 mL) two more times. Residual solvents were removed by drying under vacuum at 40°C for 48 hr.

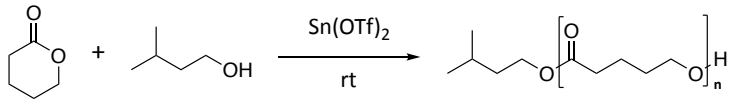

Scheme 5.1: Reaction scheme for the conventional thermal synthesis of PVL.

5.2.2.2 Microwave-assisted synthesis (MAS)

The following outlines a characteristic experimental procedure for the microwave-assisted synthesis of PVL. A 2.45 GHz CEM Discover SP microwave synthesizer with a maximum power of 250 W was used to conduct the polymerizations under microwave irradiation. A clean 10 mL microwave reaction tube, stir bar, and syringes for reagent transfer were dried overnight at 110°C and cooled to room temperature under nitrogen purge. While maintaining a nitrogen purge, 0.5 mL (0.540 g, 0.162 mol) of neat δ-valerolactone and 0.12 mL of 0.02 $g.mL^{-1}$ $Sn(Oct)_2$ (2.4 g, 5.92 µmol) in dry toluene were added to the microwave reaction tube via syringes. The nitrogen inlet was removed, and the reaction was irradiated with microwaves and reacted at a predetermined temperature (ranging from

110 to 165°C) for a predetermined amount of time (ranging from 30 to 180 min) with stirring. The reaction temperature was monitored with infrared temperature sensors and maintained by varying the magnetron power. After cooling to room temperature, the product was dissolved in ca. 2 mL aliquots of dichloromethane with vortex mixing (total volume ca. 30 mL). The polymer was precipitated into cold methanol (250 mL) by dropwise addition from a separatory funnel to yield the product as a fibrous, white mat. The product was further purified by dissolving in dichloromethane (ca. 15 mL) and precipitation by dropwise addition into cold methanol (125 mL) two more times. Residual solvents were removed by drying under vacuum at 40°C for 48 hr.

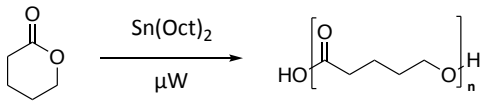

Scheme 5.2: Reaction scheme for the microwave-assisted synthesis of PVL.

5.2.3 Nuclear magnetic resonance (NMR) spectroscopy

^{1}H NMR spectra were recorded using an Agilent U4-DD2 400 MHz FT-NMR spectrometer using either $CDCl_3$ or $CDCl_3$/TMS as the solvent. The data was processed using the Mnova software from Mestrelab Research.

5.2.4 Inductively coupled plasma atomic emission spectroscopy

Four different PVL samples were prepared by digesting 25 mg of PVL in 5 mL of concentrated nitric acid overnight. The solutions were diluted to 25 mL with HPLC grade deionized water to obtain samples with a final concentration of 1 mg.mL^{-1} PVL in 14% HNO_3(*aq*). A Spectro Analytical Instruments, Inc. SPECTROBLUE TI ICP Model FHM22 equipped with a Teledyne CETAC Technologies ASX-560 autosampler was used to analyze the residual tin content in the PVL samples. The atomic emission of tin was monitored with axial plasma viewing at λ = 189.991 nm, and the applied power was 1.4 kW. The argon gas pressure at the inlet was 120 psi. The plasma, auxiliary, and sample gas flow rates were 14.00,

1.15, and 0.90 L.min^{-1}, respectively. The samples were introduced using a Texas Scientific Products Cyclonic spray chamber and an Optimist nebulizer.

The average concentration of tin was determined to be 8.09 ± 0.47 ppm. This is similar to the limits required for medical devices and implants made from similar polymers like poly(*l*-lactic acid) or polyglycolide.[37] According to Kim et al.,[7] adding 400 ppm $SnCl_2$ decreased the activation energy of thermal degradation from 183 ± 12 kJ.mol^{-1} to 92 ± 11 kJ.mol^{-1}. Thermal degradation experiments have demonstrated that metal complexes coordinate with the ester carbonyl in the chain backbone and catalyze three different degradation mechanisms: 1) an unzipping reaction from the ω-hydroxyl chain-end, 2) a random *cis*-elimination reaction at ester bonds, and 3) intramolecular transesterification that eliminates cyclized monomers.[7, 9, 38]

5.2.5 Differential refractometry

The differential refractive index increment, $\frac{dn}{dc}$, of PVL was determined using a Wyatt Opti-Lab T-rEX refractometer. This value is required for absolute molar mass characterization by size exclusion chromatography using a light scattering detector. The differential refractive index data was processed using the ASTRA software provided by Wyatt Technology. The instrument was calibrated according to the manufacturer's procedure using sodium chloride in HPLC grade deionized water. The sodium chloride was dried under vacuum at 75°C overnight prior to use. Four different PVL samples were used to prepare solutions in THF at five concentrations ranging from 0.25 to 3.0 g.mL^{-1}. The differential refractive index, $n_{\text{solution}} - n_{\text{solvent}}$, was plotted against the concentration to yield the differential refractive index increment from the slope. The average differential refractive index increment at T = 30°C and λ = 690.0 nm was $\frac{dn}{dc}$ = 0.0761 ± 0.0032 mL.g^{-1}.

5.2.6 Size exclusion chromatography

Size exclusion chromatography (SEC) was conducted using two Agilent PLgel 10 µm MIXED-B columns connected in series with a Wyatt Dawn Heleos 2 light scattering detector and a Wyatt Optilab

T-rEX refractive index detector. The initial sample concentration was 1.0 g.mL^{-1}, and the experiments were carried out in THF with a flow rate of 1 mL.min^{-1} and at a temperature of 30°C. No calibration standards were used, and the differential refractive index increment at T = 30°C and λ = 690.0 nm was $\frac{dn}{dc}$ = 0.0761 ± 0.0032 mL.g^{-1}. The data was processed using the ASTRA software provided by Wyatt Technology.

5.2.7 Successive precipitation fractionation

The procedure was adapted from Sheth[34] for the successive precipitation fractionation of PCL using toluene as the solvent and *n*-heptane as the nonsolvent. The initial solution was prepared according to the following. A ca. 1% (w/v) solution of PVL in toluene (solvent) was made by dissolving 0.8388 g of PVL (M_n = 65 kg.mol^{-1}, PDI = 1.52) in 84 mL toluene in a 250 mL round bottom flask. The flask was fitted with a reflux condenser and a stir bar, and the mixture was heated in a jacketed water bath to a temperature of 65°C for 15 min to ensure that all crystalline material had dissolved. The solution was then cooled to room temperature over the course of several hours with stirring. The temperature was controlled to within ±0.01°C at all times during the fractionation procedure with a PolyScience Digital Temperature Controller, a recirculating pump, and a jacketed water bath.

The following details the general procedure used at each step of the successive precipitation fractionation method. *n*-heptane (nonsolvent) was added dropwise from a burette to the stirred solution at 25°C until the solution developed a slight, persistent turbidity. The solution was allowed to stir for 30 min, then it was fitted with a reflux condenser and heated until homogeneous. The solution was then cooled slowly and with stirring to 25°C over the course of several hours. The stir bar and reflux condenser were removed, and the solution was allowed to set overnight (ca. 18 hr). The supernatant was removed with a transfer pipet, a small amount of the interphase between the two layers was discarded, and the remaining gel was dissolved in ca. 10 mL of dichloromethane. The polymer solution

was then precipitated dropwise into ca. 100 mL of cold methanol. The fraction was then dried under vacuum at 40°C for 48 hr.

5.2.8 Polarized optical microscopy

Thin films with thicknesses ca. 2 μm were prepared by spin casting from a 0.1 g.mL^{-1} (w/v) solution in 1,1,2,2-tetrachloroethane onto glass cover slips at 3,000 RPM and room temperature. The films were dried under vacuum at 40°C for 48 hr prior to analysis. A Linkam THM 600 heating-cooling stage was used in conjunction with a Linkam TMS 93 temperature controller to regulate the temperature within ±0.1°C. Thermo-oxidative degradation was minimized by running experiments under a dry nitrogen purge with a flow rate of 50 mL.min^{-1}. The temperature scale was calibrated in the range of 50 to 150°C using benzophenone (T_m = 50°C), benzotriazole (T_m = 98–99°C), and *l*-xylose (T_m = 150–152°C). The thermal history was erased before each experiment by heating to 100°C followed by an isothermal hold for 1 min. The films were cooled to the desired crystallization temperature with a cooling rate ca. $-\beta$ = 50 K.min^{-1} using compressed air. The isothermal spherulite growth was monitored at temperatures ranging from T_x = 32.8 to 52.2°C with an Olympus BX-50 polarized light optical microscope interfaced to a video camera. The FIJI image analysis software[39] was employed to measure spherulite radii as a function of time for 5 to 11 spherulites. The increase in the spherulite radii with time was linear for all samples at all investigated crystallization temperatures, and the radial spherulite growth rates were determined as the slope of the linear regression of radius vs. time. The relative standard deviations of the spherulite growth rates ranged from 0.8 to 7.9% with an average value of 3.5%.

5.2.9 Conventional differential scanning calorimetry

A TA Instruments Q2000 conventional differential scanning calorimeter (CDSC) with an RCS-90 intracooler was operated under a nitrogen purge of 50 mL.min^{-1}. The heat flow was calibrated using a sapphire standard and the temperature scale was calibrated using an indium standard according to the

recommended calibration protocols from TA Instruments. The effects of instrumental thermal lag were accounted for through the indium temperature calibration. Aluminum Tzero hermetic sample pans were used. Films with a thickness of 340 μm were prepared using a Carver laboratory press operated at 110°C under a nitrogen atmosphere. The thermal history was erased before all crystallization experiments by heating to 100°C followed by an isothermal hold for 1 min. The non-isothermal crystallization behavior was examined by cooling with rates ranging from $-\beta$ = 1 to 30 K.min^{-1}. The corresponding melting endotherms were recorded by heating with rates β = 10 to 100 K.min^{-1}. The isothermal crystallization behavior at T_x = 40 and 45°C was investigated by crystallizing for t_x = 60 and 180 min, respectively, and the resulting melting endotherms were recorded by heating with rates β = 10 to 100 K.min^{-1}. The enthalpies of fusion were determined by integrating the melting endotherms for experiments conducted with β = 10 K.min^{-1}.

5.3 RESULTS AND DISCUSSION

5.3.1 Synthesis and characterization

Stevens et al.[1] demonstrated the conventional thermal synthesis of PVL homopolymers and copolymers with polydispersity indices less than 1.28 using $Sn(OTf)_2$ as a catalyst and isoamyl alcohol as an initiator. We attempted to use their procedure and several others, which employed $Sn(Oct)_2$,[40] $FeCl_3 \bullet 6H_2O$,[41] and anhydrous $FeCl_3$[41] with isoamyl alcohol as an initiator, but molecular weights greater than 10 kg.mol^{-1} were not obtained using any of these routes. One successful reaction did yield the sample with M_n = 12.3 kg.mol^{-1} and PDI = 1.07 (Scheme 1, Fig. 5.1a) that was used in the CDSC study without further fractionation. Characteristic ^{1}H NMR spectra are shown in Figure 5.1 for samples prepared via CTS and MAS. The spectra agree with previous reports.[1, 42] The CTS sample contains additional signals from aliphatic protons in the isoamyl alcohol initiator (Fig. 5.1a), which offers an

additional method of molar mass determination. The number average molar mass by NMR was found to be M_n = 10 kg.mol^{-1}, which is within error of the determination by SEC (Table 5.5).

Due to the lack of success with conventional thermal synthetic methods, our attention turned towards implementing a robust MAS method, which has been shown to reduce reaction times and temperatures for polymer synthesis.[43] Although MAS procedures have been published for the synthesis of poly(ε-caprolactone)[44, 45] and poly(*l*-lactide)[46, 47] there are no reports for the microwave-assisted synthesis of poly(δ-valerolactone). Attempts to use $Sn(OTf)_2$ as the catalyst for the MAS method resulted in product solutions that were red or yellow in color. Although they had slightly higher viscosities than the starting solutions, they did not yield useful polymeric product. The results were similar with and without isoamyl alcohol as an initiator. As a result, $Sn(OTf)_2$ was substituted with $Sn(Oct)_2$, a widely used catalyst in lactone polymerizations.[4, 5, 48] Interestingly, there was no need to include an initiator (isoamyl alcohol) in the reaction mixture for the MAS method after changing the catalyst to $Sn(Oct)_2$ (Scheme 2, Fig. 1b). This is unusual because $Sn(Oct)_2$ typically requires a nucleophilic initiator (i.e. alcohol) and high reaction temperatures for the polymerization of ε-caprolactone,[4, 5, 48] which is more readily polymerized than δ-valerolactone due to higher ring strain in the 7-membered lactone. When isoamyl alcohol was included, there was an increase in the solution's viscosity, but the product was not high enough molecular weight to precipitate as a solid.

a)

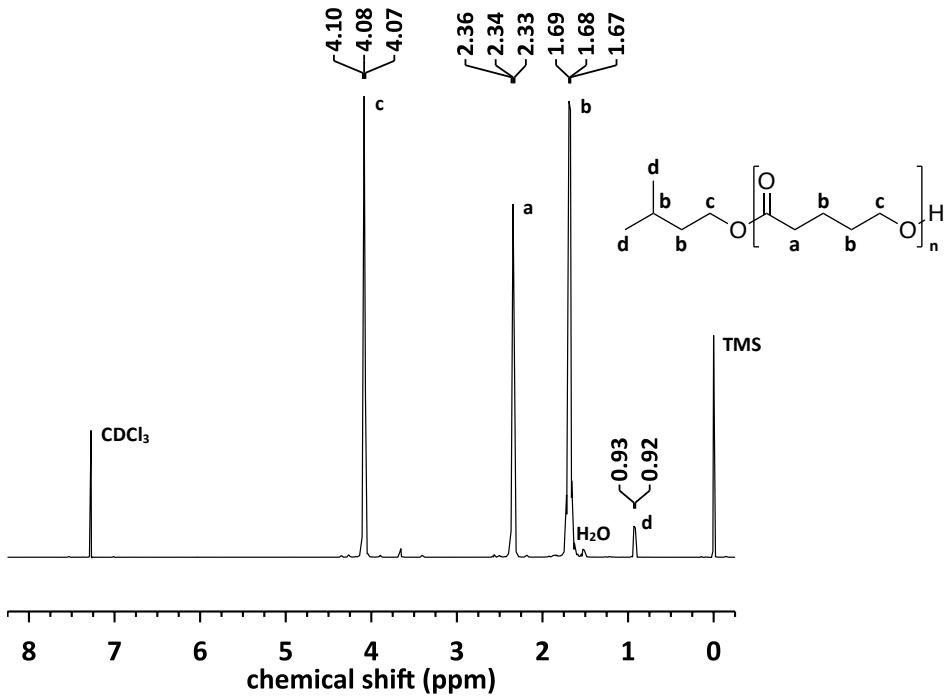

b)

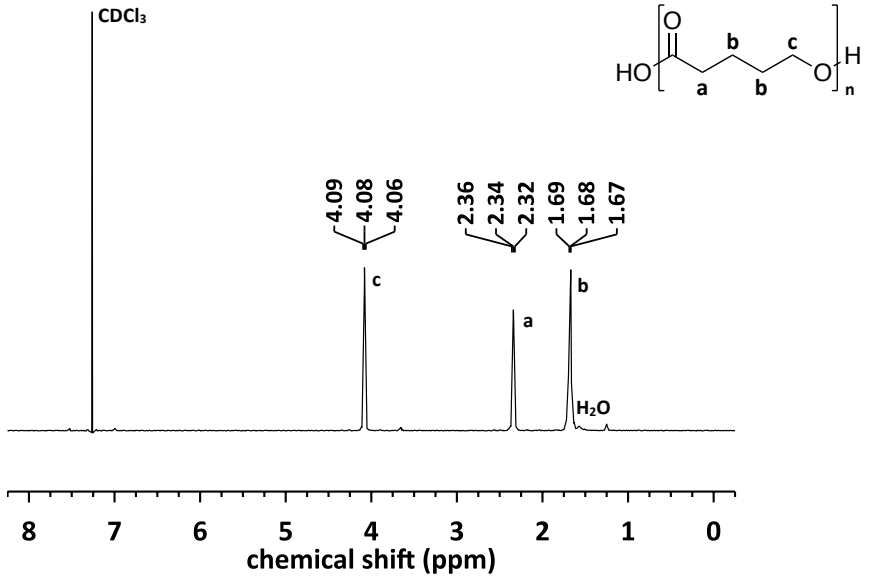

Figure 5.1: ^{1}H NMR spectrum of PVL synthesized using a) the conventional thermal method and b) the microwave assisted method.

The results for different reaction temperatures and times using the MAS method are tabulated in Table 5.2. The molecular weight was controlled by varying the reaction time at T = 110 and 135°C, but

this control was lost at $T \geq 150$°C. This is most likely the result of increased intra- and intermolecular reactions that are catalyzed by $Sn(Oct)_2$ at higher temperatures.[4, 5, 48] The yields fluctuated between ca. 70 and 90% with no signs of correlation to the reaction temperature or time. Similarly, the PDIs fluctuated between 1.5 and 1.9 with no apparent correlation to the reaction conditions. Most reports of PVL synthesis are for low molecular weights less than 20 kg.mol^{-1},[1, 49, 50] but molecular weights as high as 195 kg.mol^{-1} and with PDI = 1.30 have been reported for the polymerization of δ-valerolactone catalyzed using yttrium complexes.[51]

Table 5.2: Summary of reaction temperatures, T, and reaction times, t, that were investigated using the MAS method along with the resulting number average molecular weight, M_n, polydispersity index, PDI, and yield.

T (°C)	t (min)	M_n (kg.mol^{-1})	PDI	Yield (%)
110	60	36	1.5	32
110	120	69	1.5	80
110	180	81	1.7	87
135	30	45	1.6	72
135	60	56	1.6	79
135	120	65	1.5	79
135	180	84	1.5	92
150	60	40	1.6	84
150	120	50	1.8	85
150	180	43	1.6	81
165	60	32	1.9	82
165	120	30	1.6	79
165	180	24	1.8	75

5.3.2 Quantitative analysis of successive precipitation fractionation

Table 5.3 shows the quantitative results at each step of the successive precipitation fractionation of poly(δ-valerolactone) using toluene/*n*-heptane (solvent/nonsolvent). Higher fractionation steps required larger nonsolvent volumes to induce phase separation and higher temperatures to homogenize the solution prior to collecting the fractions. The cumulative mass fraction

only reaches 0.87 at the final step because a small amount of interphase between the two layers was discarded at each step and the remaining supernatant from the final step was discarded.

Table 5.3: Tabulated quantitative data for the successive precipitation fractionation of poly(δ-valerolactone) in toluene/*n*-heptane (solvent/nonsolvent). Quantities include the volume of *n*-heptane required to induce persistent turbidity, $V_{n\text{-heptane}}$, the temperature at which the turbid solution became homogeneous, T_{homo}, the mass of each fraction, m, the cumulative mass fraction at each step, w, the number average molecular weight, M_{n}, the weight average molecular weight, M_{w}, and the polydispersity index, PDI. The errors on the number average molecular weight, M_{n}, and the weight average molecular weight, M_{w}, are ± 2.1 kg.mol^{-1}, and the errors on the polydispersity indices, PDI, are ± 0.02.

Fraction	$V_{n\text{-heptane}}$ (mL)	T_{homo} (°C)	m (mg)	w	M_{n} (kg.mol^{-1})	M_{w} (kg.mol^{-1})	PDI
Bulk	–	–	838.8	–	65.1	99.0	1.52
1	14.7	36	41.1	0.05	54.4	95.7	1.76
2	0.7	40	101.8	0.17	70.6	109.4	1.55
3	0.4	37	98.0	0.29	73.0	94.9	1.30
4	0.3	37	53.8	0.35	67.8	86.1	1.27
5	0.5	37	44.1	0.40	66.7	78.1	1.17
6	0.6	38	83.3	0.50	53.3	65.0	1.22
7	0.9	39	77.2	0.60	49.3	55.2	1.12
8	1.2	48	73.7	0.68	39.2	44.7	1.14
9	2.0	45	61.9	0.76	32.5	36.4	1.12
10	3.0	45	97.4	0.87	12.9	17.5	1.36

The molecular weight characteristics of the fractions are tabulated in Table 5.3. The molecular weights of successive fractions increased for fractions 1, 2, and 3, then decreased for the remaining successive fractions. This behavior is known as reverse order fractionation, and it is known to occur with SPF.[28] The initial polymer concentration, molecular weight, and molecular weight distribution all contribute to the occurrence of reverse order fractionation.[28] Note that reverse order fractionation does not occur with SSF. The molecular weight distribution of successive fractions decreased, including the first three steps where reverse order fractionation was observed. These observations agree with theoretical predictions of SPF[23, 28-31] and with the experimental results of Sheth[34] for the fractionation of PCL using the same solvent/nonsolvent system. However, Sheth[34] did not observe reverse order

fractionation. The successful fractionation of PVL using toluene/*n*-heptane suggests that this is a good solvent/nonsolvent pair for the preparation of narrow molecular weight PVL samples.

5.3.3 Spherulite growth rate

Table 5.4 gives the molecular weight characteristics of the two samples that were analyzed using polarized light optical microscopy. Spherulitic morphology was observed at all of the investigated crystallization temperatures (T_x = 32.8 to 50.2°C), and the lower inset in Figure 5.2 shows a characteristic polarized optical micrograph of the observed spherulites. No ring bands were observed at any temperature. The spherulite growth rates were measured for a bulk sample and a fraction, both prepared via MAS. We expect the growth rate to decrease with increasing molecular weight,[52] but the fraction displayed a lower spherulite growth rate than the higher molar mass bulk sample. This unexpected behavior most likely results from fractionation effects of the more polydisperse sample during crystallization.[53] The spherulite growth rates for two PCL fractions (M_n = 25 and 40 kg.mol^{-1}) analyzed by Sheth[34] are also included in Fig. 5.2 for comparison to the PVL data. The spherulite growth rates were expected to be comparable for the two polymers considering their similar chemical and thermal properties. However, the growth rates of the PVL samples are one to two orders of magnitude slower than PCL at all studied crystallization temperatures. While this observation cannot be explained by differences in molecular weights or chain length, it may be the consequence of a lower equilibrium melting temperature for PVL than for PCL. Indeed, at a given crystallization temperature, PVL would exhibit a smaller undercooling, hence a lower thermodynamic driving force of crystallization and thus lower crystallization rate. The magnitudes of the lateral surface free energy, fold surface free energy, and enthalpy of fusion could also contribute to the disparity. Additionally, the dihydroxyl-terminated chain ends of the samples prepared and MAS could associate in the melt, which would lead to a larger apparent molar mass and a lower growth rate.

Table 5.4: Molecular weight characteristics of the PVL fractions used in the CDSC study. For PVL-33, the errors on the number average molecular weight, M_n, and the weight average molecular weight, M_w, are ± 2.1 kg.mol^{-1}, and the errors on the polydispersity indices, PDI, are ± 0.02.

Sample	M_n (kg.mol^{-1})	M_w (kg.mol^{-1})	PDI
PVL-33	32.5	36.4	1.12
PVL-45B	45	72	1.6

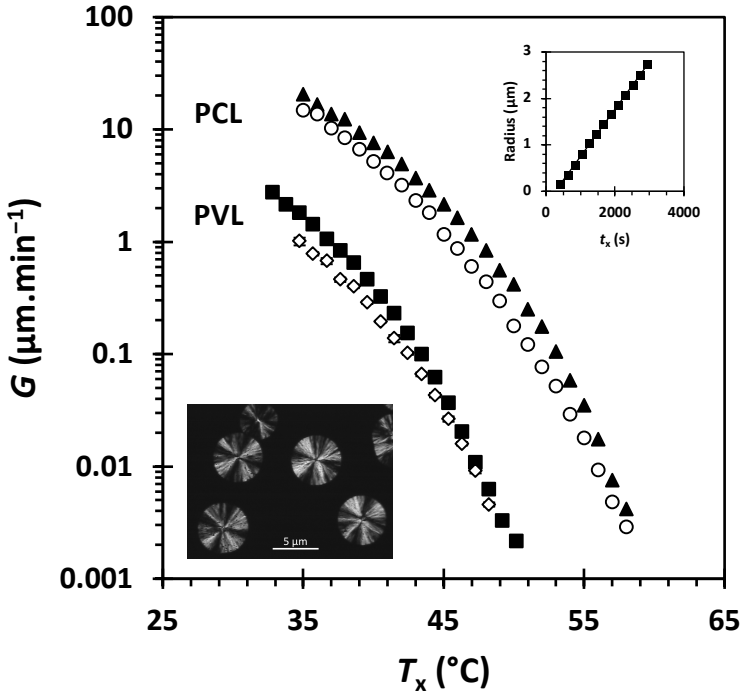

Figure 5.2: Relationship between the spherulite growth rate, G, and the isothermal crystallization temperature, T_x, for PVL-45B (■), PVL-33 (◇), PCL-25 (▲), and PCL-40 (○). The bottom inset shows the spherulitic morphology of PVL-45B at T_x = 47.3°C, and the top inset shows the linear increase in spherulite radius with time for PVL-45B at T_x = 44.0°C.

Polymer crystallization kinetics are commonly analyzed in the context of the classical Lauritzen-Hoffman (LH) secondary nucleation theory of polymer crystal growth, which relates the spherulite growth rate, G, to the undercooling, $\Delta T = T_m - T_x$, according to

$$G = G_0 \exp\left(-\frac{Q_D^*}{RT_x}\right) \exp\left(-\frac{K_g}{T_x \Delta T}\right) \tag{5.1}$$

Here, T_{m} is the equilibrium melting temperature, G_0 is a constant, R is the gas constant, Q_{D}^{*} is the activation energy for center of mass diffusion, and K_{g} is the regime-dependent secondary nucleation rate constant. Growth rate data is typically analyzed by linearizing Eqn. (3.1) to obtain a Lauritzen-Hoffman plot such that

$$\ln G + \frac{Q_{\mathrm{D}}^{*}}{RT_{\mathrm{x}}} = \ln G_0 - \frac{K_{\mathrm{g}}}{T_{\mathrm{x}}\Delta T} \tag{5.2}$$

The equilibrium melting temperature can be estimated by minimizing the variance of the linear fit according to Eqn. (5.2) (see Chapter 2).[34, 54-58] An LH plot for PVL-45B corresponding to the minimum variance equilibrium melting temperature of T_{m} = 69.7°C is shown in Figure 5.3a. Strobl proposed using the following equation to determine the zero-growth temperature, T_{zg},

$$\left(-\frac{d\ln(G/G_0)}{d\,T_{\mathrm{x}}} + \frac{Q_{\mathrm{D}}^{*}}{RT_{\mathrm{x}}^{2}}\right)^{-\frac{1}{2}} = K_{\mathrm{g}}'^{-\frac{1}{2}}\left(T_{\mathrm{zg}} - T_{\mathrm{x}}\right) \tag{5.3}$$

Fitting the experimental data for PVL-45B according to Eqn. (5.3) yielded T_{zg} = 73.5°C from the y-intercept (Fig. 5.3b) (see chapter 2). Note that we assumed the equilibrium melting and zero-growth temperatures have the same physical meaning. Using similar approaches, Sheth[34] found the equilibrium melting temperature of PCL-40 (Fig. 5.2) to be T_{m} = 91.9°C and the zero-growth temperature to be T_{zg} = 86.2°C. Thus, PCL crystallizes at larger undercoolings than PVL for fixed crystallization temperatures. The methods presented herein strongly depend on the choice of the spherulite growth rate model, so no errors were provided on the estimated quantities because they are simply meant to be first approximations and give context to the spherulite growth rate data (Fig. 5.2). There are known inconsistencies in the LH and multiphase models that are still being assessed,[59] so we chose to forego extensive spherulite growth rate measurements on additional fractions pending more thorough analysis and refinement of the LH model.

a)

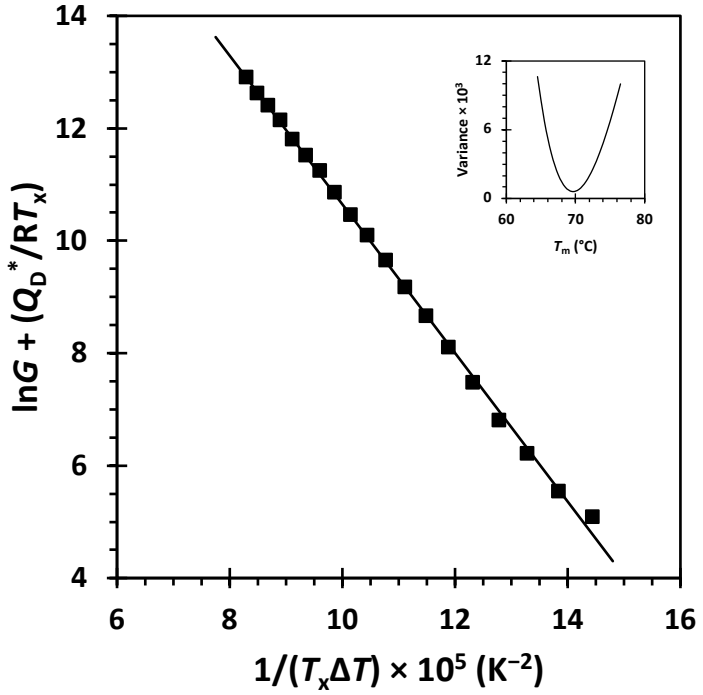

b)

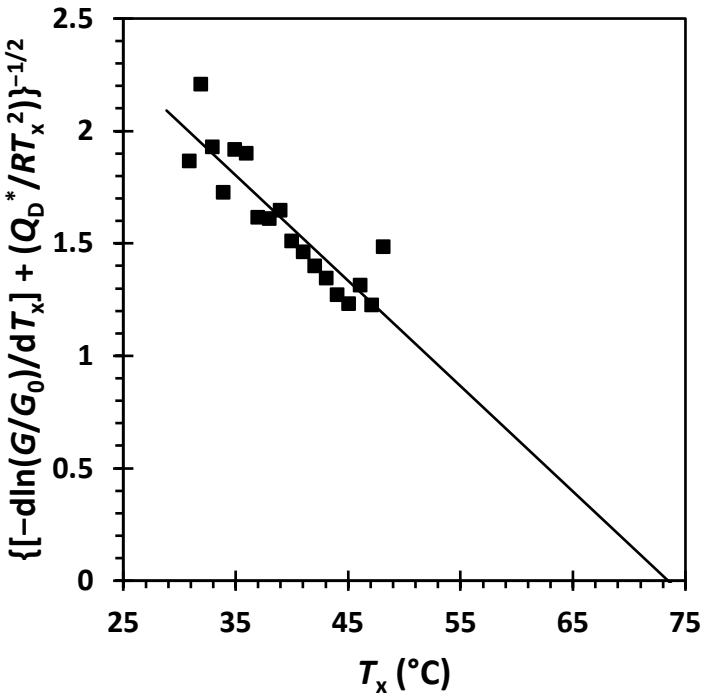

Figure 5.3: a) Lauritzen-Hoffman plot for PVL-45B with T_m = 69.7°C, the value which minimized the variance of Eqn. (3.2). The inset shows the relationship between the variance and choice of the equilibrium melting temperature, T_m. b) Strobl plot for PVL-45B according to Eqn. (3.3) which yields T_{zg} = 73.5°C.

5.3.4 Calorimetric studies

Table 5.5 gives the molecular weight characteristics of the samples that were chosen for thermal analysis with CDSC. Note that PVL-12 was synthesized via the conventional thermal method and used without fractionation.

Table 5.5: Molecular weight characteristics of the PVL fractions used in the CDSC study. The errors on the number average molecular weight, M_n, and the weight average molecular weight, M_w, are ± 2.1 kg.mol^{-1}, and the errors on the polydispersity indices, PDI, are ± 0.02.

Sample	M_n (kg.mol^{-1})	M_w (kg.mol^{-1})	PDI
PVL-12	12.3	13.2	1.07
PVL-33	32.5	36.4	1.12
PVL-39	39.2	44.7	1.14
PVL-49	49.3	55.2	1.12
PVL-67	66.7	78.1	1.17

5.3.4.1 Non-isothermal crystallization

The peak temperatures for non-isothermal crystallization exotherms recorded at different cooling rates are shown in Figure 5.4. As expected, the peak crystallization temperatures decrease with increasing cooling rate. Fig. 5.2 clearly shows that the crystal growth rate increases as the temperature decreases, where 1°C can alter the growth rate by as much as a factor of two. The bulk crystallization rate is proportional to G^3 for athermal spherulitic growth,[52, 60] so a 2-fold increase in growth rate would result in an 8-fold increase in the bulk crystallization rate. The temperatures of maximum crystallization (Fig. 5.4) rate are scattered within a 1°C range and do not appear to depend on molar mass. Within experimental uncertainty, a slightly parabolic shape could be argued for the present data where PVL-67 may be shifted to artificially higher temperatures as the result of increased heterogeneities relative to the other samples. Primary nucleation in this temperature range almost certainly proceeds via a heterogeneous mechanism. Each fractionation step essentially acts as a purification step, and this sample was collected earlier than the others in the course of SPF. For low to moderate undercoolings, Mandelkern and coworkers[61-63] demonstrated that the bulk crystallization rate of linear polyethylene

increased with decreasing crystallization temperature. Furthermore, the crystallization rate exhibited a maximum when plotted as a function of molecular weight at fixed crystallization temperatures. A slight decrease in the peak crystallization temperature over a ca. 2°C range with increasing molecular weight was observed by Sheth[34] for PCL.

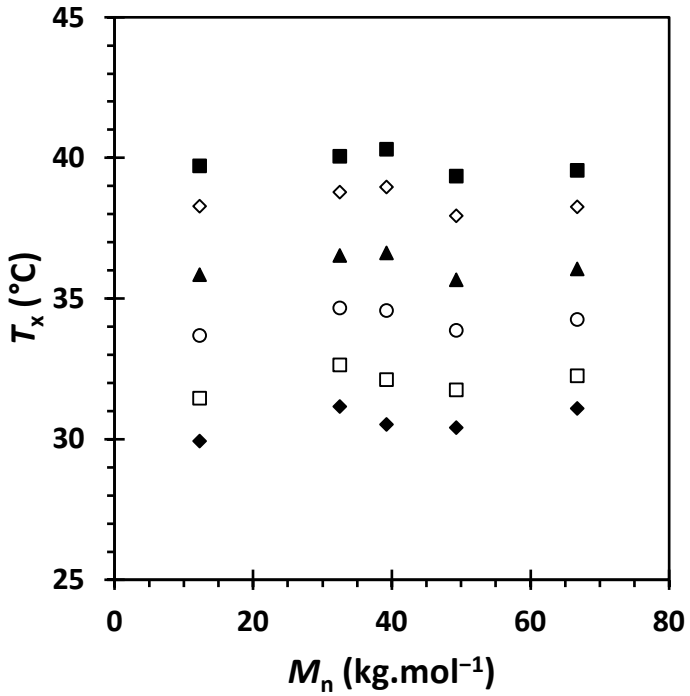

Figure 5.4: Relationship between the peak crystallization temperature, T_x, and the number average molecular weight, M_n, measured during cooling with $-\beta$ = 1 (■), 2 (◇), 5 (▲), 10 (○), 20 (□), and 30 K.min^{-1} (◆).

Figure 5.5 shows thermograms for PVL-39 and PVL-67 recorded with different heating rates following cooling with $-\beta$ = 30 K.min^{-1}. A single endothermic peak is observed which appears to broaden with increasing heating rate. PVL-12 melts at the lowest temperatures, but there is no clear trend with respect to molecular weight. The melting temperature initially decreases with increasing heating rate for all of the samples, regardless of the previous cooling rate. High enough heating rates eventually lead to an increase in melting temperature for all of the samples except PVL-67, and the critical threshold to observe superheating depended on the sample. Superheating from both thermal lag

and melting kinetics leads us to expect that the melting temperature should increase with increasing heating rate.[64] Hence, high enough heating rates suppress a stabilization mechanism that occurs during heating. These results suggest that CDSC is not useful for analyzing the thermal stability of non-isothermally crystallized PVL because the crystals are significantly affected by the heating conditions prior to melting. Hence, the measured thermograms may not completely reflect the prior thermal history.

a)

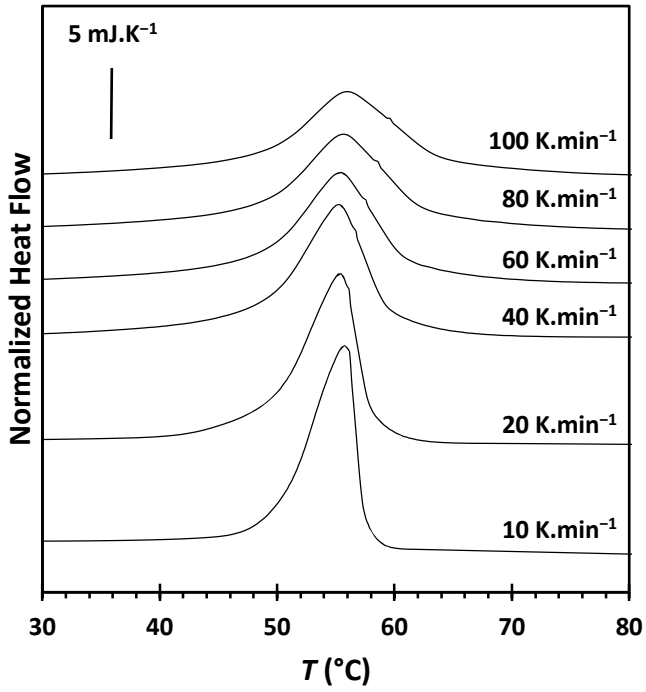

b)

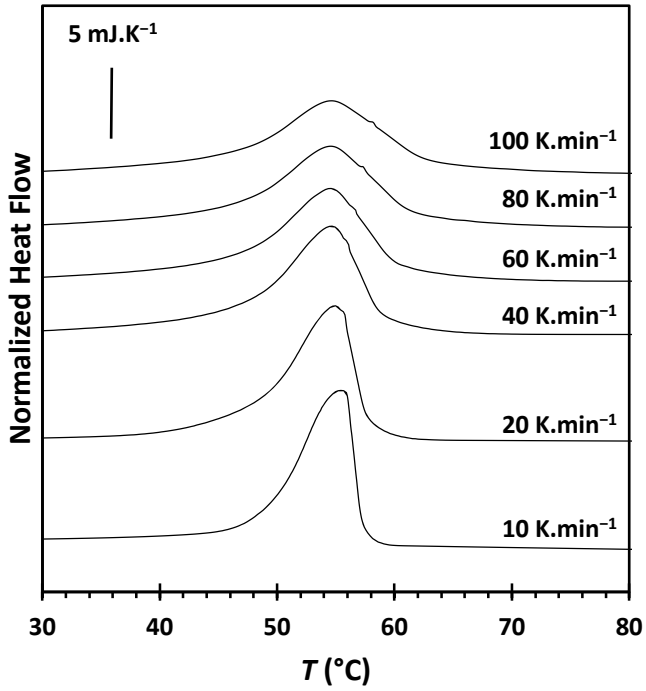

Figure 5.5: Thermograms following cooling at $-\beta$ = 20 K.min^{-1} for a) PVL-39 and b) PVL-67. The melting temperatures were measured with β = 10, 20, 40, 60, 80, and 100 K.min^{-1}.

5.3.4.2 Melting subsequent to isothermal crystallization

In this section, we will show that melting experiments cannot be carried out in a conventional DSC at sufficiently high heating rates to yield useful information. Examples of typical melting endotherms are shown in Figure 5.6 for PVL-67. All fractions exhibit a small, endothermic shoulder (arrows in Fig. 5.6) prior to the main melting peak following isothermal crystallization at T_x = 40 and 45°C. The main endothermic peak decreases in magnitude relative to the low-temperature shoulder as the heating rate is increased, strongly suggesting that melting-recrystallization-remelting may occur during heating. In this case, the observed endotherms result from the superposition of the melting of isothermally crystallized material, recrystallization, and remelting of recrystallized material. Furthermore, the magnitude of the main peak relative to the shoulder is smaller for crystallization at T_x = 45°C compared to T_x = 40°C. Crystallization at higher temperatures leads to thicker, more stable lamellae, which should undergo less melting-recrystallization-remelting upon heating. It should be noted that PVL cannot undergo lamellar thickening because it lacks an α_c-relaxation, which provides the molecular mechanism for intracrystalline chain dynamics.[65, 66] Multiple melting behavior was recently observed following isothermal crystallization of PCL, but melting-recrystallization-remelting during heating was suppressed with β = 80 K.min^{-1}.[67]

a)

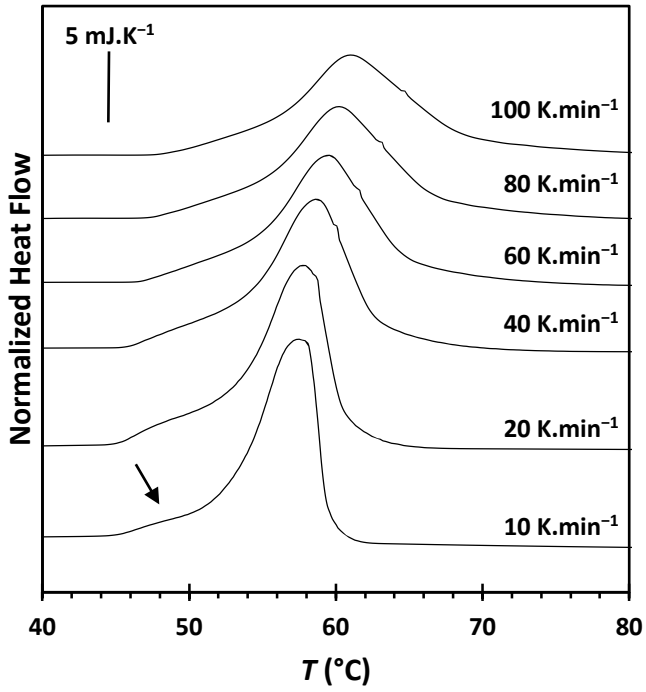

b)

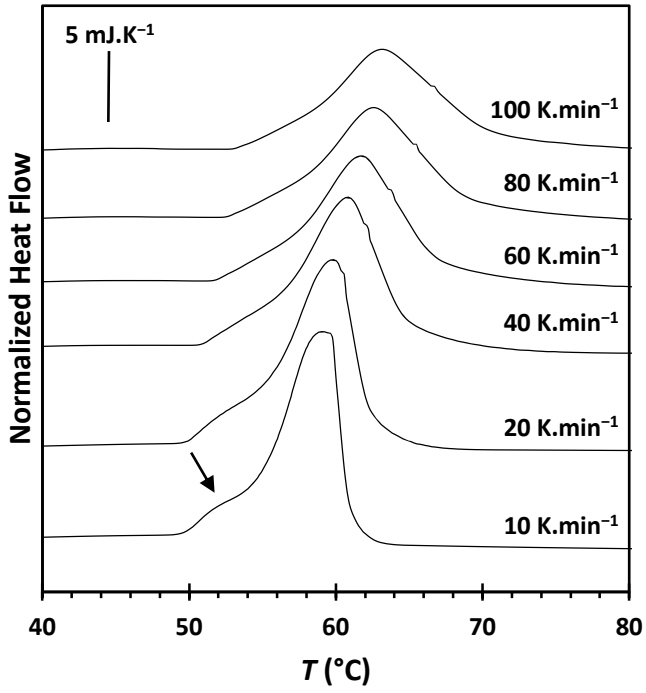

Figure 5.6: Thermograms for PVL-67 corresponding to the melting of crystals formed after isothermal crystallization at a) T_x = 40°C and b) T_x = 45°C. The melting temperatures were measured with β = 10, 20, 40, 60, 80, and 100 K.min^{-1}.

The larger endothermic peak melting temperatures, which correspond to the remelting of recrystallized material, are shown as a function of heating rate in Figure 5.7. Following crystallization at T_x = 40°C, the three lowest molecular weight samples show nearly constant melting temperatures with increasing heating rate until β = 40 K.min^{-1}, above which the melting temperatures increase. The highest molecular weight fractions that were studied, PVL-49 and PVL-67, display melting temperatures that constantly increase with increasing heating rate. Isothermal crystallization at T_x = 45°C results in melting temperatures that monotonically increase with increasing heating rate for all fractions. As expected, the thicker lamellae formed at higher temperatures undergo stabilization and melting-recrystallization-remelting during heating. The melting kinetics were not analyzed due to the complex interplay between the three superposed processes, so the results would most likely lack physical meaning. The appearance of the low temperature shoulders following isothermal crystallization imply that β = 100 K.min^{-1} is not fast enough to measure melting temperatures that accurately reflect the original thermal history.

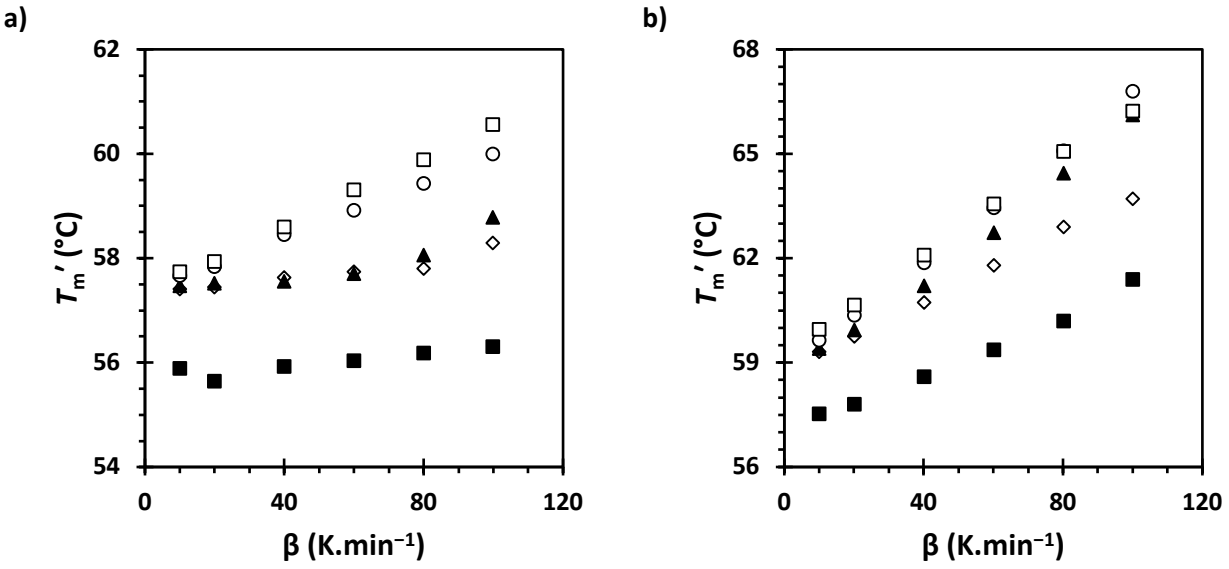

Figure 5.7: Relationship between the main peak melting temperature, T_m', and the heating rate, β, following isothermal crystallization at a) T_x = 40°C and b) T_x = 45°C. The symbols in both plots correspond to PVL-12 (■), PVL-33 (◇), PVL-39 (▲), PVL-49 (○), and PVL-67 (□).

Further investigation into the effects of crystallization temperature, crystallization time, and heating rate on the relative peak positions and enthalpies would help confirm the cause of the multiple melting behavior. The use of fast differential scanning calorimetry is suggested to measure the melting temperatures of PVL fractions at high heating rates and potentially suppress secondary processes that appear to occur during heating with conventional DSC.

The enthalpy of fusion was observed to decrease with increasing molecular weight, as shown in Figure 5.8. Slightly lower values were obtained at 45°C compared to 40°C, but a trend cannot be confirmed at this time without more data at different temperatures for comparison. The theoretical heat of fusion is not known for PVL, so the degree of crystallinity was not determined. However, if we assume the theoretical heat of fusion is identical to PCL ($\Delta H_{\mathrm{f}}^{o}$ = 129 J.g^{-1}), then the degrees of crystallinity would range from X_{c} = 0.47 to 0.64. Mandelkern et al.[68] and Glotin and Mandelkern[69] demonstrated that the degree of crystallinity decreases with increasing crystallization temperature in linear polyethylene and branched polyethylene, respectively. Decreasing crystallinity with increasing molecular weight has been reported for fractions of PCL,[34] poly(aryl ether ether ketone),[70] linear polyethylene,[68] branched polyethylene,[69] and syndiotactic polypropylene.[71] This observation is explained by increasing numbers of entanglements with increasing molecular weight, which inhibit crystallization. In a study on PCL fractions, Ou-Yang et al.[72] observed a maximum in the crystallinity as a function of molecular weight, where the degree of crystallinity ranged from X_{c} = 0.35 to 0.65. The authors also reported that the crystallinity as a function of crystallization temperature displayed a maximum for samples with M_{n} < 10 kg.mol^{-1} but increased monotonically for M_{n} > 40 kg.mol^{-1}. In contrast, Strobl[73] reported that the crystallinity of PCL with M_{n} = 42.5 (PDI = 1.5) was constant at X_{c} = 0.42 over a range of crystallization temperatures between T_{x} = 26°C and 56°C.

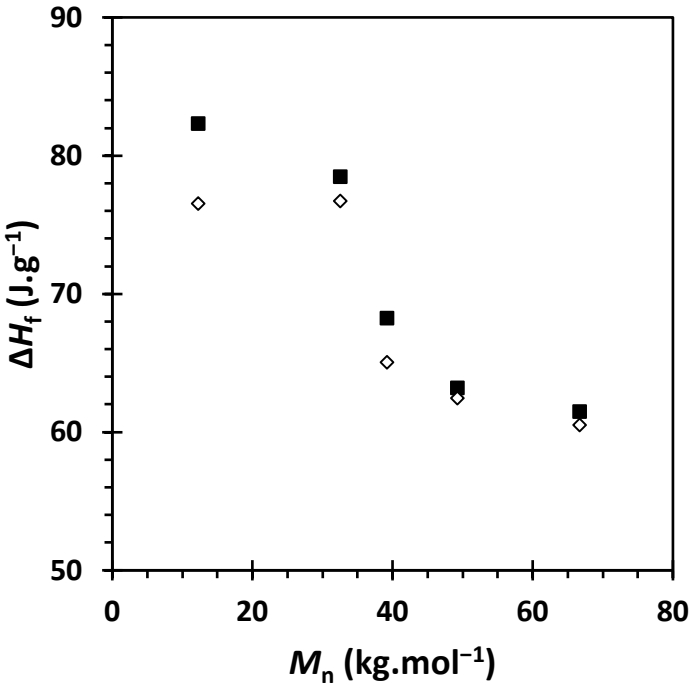

Figure 5.8: Relationship between the heat of fusion ΔH_f, and the number average molecular weight, M_n, following isothermal crystallization at T_x = 40 (■) and 45°C (◇).

5.4 CONCLUSIONS

Microwave-assisted synthesis was utilized to yield moderate to high molecular weight samples of poly(δ-valerolactone) with polydispersity indices ranging from 1.5 to 1.9. No alcoholic initiator was required for the polymerization of δ-valerolactone in the presence of $Sn(Oct)_2$ and microwave radiation. The reaction time was used to control the molecular weight for reaction temperatures at or below 135°C. Molecular weight control was lost for reaction temperatures exceeding this limit. Successive precipitation fractionation with toluene/*n*-heptane as the solvent/nonsolvent pair was employed to obtain narrow molecular weight samples with polydispersity indices ranging from 1.07 to 1.17.

The spherulite growth rates were one to two orders of magnitude smaller than those of poly(ε-caprolactone) of similar molecular weight at the same temperature. Possible explanations for this behavior are a lower equilibrium melting temperature for PVL compared to PCL and effect of chain end

association in the case of PVL. The equilibrium melting and zero-growth temperatures of a polydisperse sample with M_n = 45 kg.mol^{-1} were estimated to be T_m = 69.7°C and T_{zg} = 73.5°C, respectively, which are lower than the values estimated for PCL of similar molar mass. Analysis of the non-isothermal crystallization behavior using conventional differential scanning calorimetry revealed that peak crystallization temperatures are approximately independent of molar mass in the range of molar mass investigated. The enthalpies of fusion following isothermal crystallization at T_x = 40 and 45°C decreased with increasing molecular weight and increasing crystallization temperature. Melting endotherms recorded subsequent to isothermal crystallization display a multiple melting behavior that is likely to result from melting-recrystallization-remelting effects. Heating rates up to β = 100 K.min^{-1} were not sufficient to prevent recrystallization subsequent to melting, indicating that CDSC is not well suited to provide valuable information on the melting of isothermally crystallized PVL. Future studies on PVL fractions should focus on analyzing the effects of the crystallization temperature, crystallization time, and heating rate on the evolution of the melting temperature and the melting enthalpy using fast differential scanning calorimetry to suppress secondary processes during heating and confirm the origin of the multiple melting behavior following isothermal crystallization.

5.5 ACKNOWLEDGEMENTS

The authors would like to thank TA Instruments for the temporary loan of a TA Q2000 conventional differential scanning calorimeter. We would like to Dr. John Matson and Scott Radzinski for assisting with the size exclusion chromatography measurements. We would also like to thank Dr. Alan Esker for access to his group's differential refractometer. Additionally, we would like to thank Dr. Paul Deck and Dr. Jatinder Josan for the use of synthetic equipment and granting access to the microwave synthesizer used to synthesize poly(δ-valerolactone). Lastly, we would like to thank Athena Tilley at Virginia Tech for measuring the Sn content of the poly(δ-valerolactone) samples using ICP-AES.

5.6 REFERENCES

1. Stevens, D. M.; Watson, H. A.; LeBlanc, M.-A.; Wang, R. Y.; Chou, J.; Bauer, W. S.; Harth, E., Practical polymerization of functionalized lactones and carbonates with Sn(OTf)2 in metal catalyzed ring-opening polymerization methods. *Polym. Chem.* **2013,** *4* (8), 2470-2474.

2. Imasaka, K.; Yoshida, M.; Fukuzaki, H.; Asano, M.; Kumakura, M.; Mashimo, T.; Yamanaka, H.; Nagai, T., Evaluation of new pasty-type implantable devices consisting of poly(ε-caprolactone/δ-valerolactone) and estracyt or estramustine. *Chem. Pharm. Bull.* **1991,** *39* (8), 2096-9.

3. Peng, S.; Yang, S.-R.; Ko, C.-Y.; Peng, Y.-S.; Chu, I. M., Evaluation of a mPEG-polyester-based hydrogel as cell carrier for chondrocytes. *J. Biomed. Mater. Res., Part A* **2013,** *101A* (11), 3311-3319.

4. Lecomte, P.; Jérôme, C., Recent developments in ring-opening polymerization of lactones. In *Synthetic biodegradable polymers*, Springer: 2011; pp 173-217.

5. Löfgren, A.; Albertsson, A.-C.; Dubois, P.; Jérôme, R., Recent Advances in Ring-Opening Polymerization of Lactones and Related Compounds. *Journal of Macromolecular Science, Part C* **1995,** *35* (3), 379-418.

6. Brandrup, J., *Polymer handbook*. 1999; Vol. 89.

7. Abe, H., Thermal degradation of environmentally degradable poly(hydroxyalkanoic acid)s. *Macromol. Biosci.* **2006,** *6* (7), 469-486.

8. Garozzo, D.; Giuffrida, M.; Montaudo, G., Primary thermal decomposition processes in aliphatic polyesters investigated by chemical ionization mass spectrometry. *Macromolecules* **1986,** *19* (6), 1643-9.

9. Kim, K. J.; Doi, Y.; Abe, H., Effect of metal compounds on thermal degradation behavior of aliphatic poly(hydroxyalkanoic acid)s. *Polym. Degrad. Stab.* **2008,** *93* (4), 776-785.

10. Alamo, R. G.; Chan, E. K.; Mandelkern, L., The molecular weight dependence of the thermodynamic and structural properties of ethylene copolymers. *Polym. Prepr. (Am. Chem. Soc., Div. Polym. Chem.)* **1989,** *30* (2), 312.

11. Jordens, K.; Wilkes, G. L.; Janzen, J.; Rohlfing, D. C.; Welch, M. B., The influence of molecular weight and thermal history on the thermal, rheological, and mechanical properties of metallocene-catalyzed linear polyethylenes. *Polymer* **2000,** *41* (19), 7175-7192.

12. Nunes, R. W.; Martin, J. R.; Johnson, J. F., Influence of molecular weight and molecular weight distribution on mechanical properties of polymers. *Polymer Engineering & Science* **1982,** *22* (4), 205-228.

13. Kline, R. J.; McGehee, M. D., Morphology and charge transport in conjugated polymers. *Journal of Macromolecular Science Part C: Polymer Reviews* **2006,** *46* (1), 27-45.

14. Reiter, G.; Strobl, G. R., *Progress in understanding of polymer crystallization*. Springer: 2007; Vol. 714.

15. Monrabal, B., Temperature rising elution fractionation and crystallization analysis fractionation. *Encyclopedia of Analytical Chemistry: Applications, Theory and Instrumentation* **2006**.

16. Monrabal, B., Polyolefin Characterization: Recent Advances in Separation Techniques. In *Polyolefins: 50 years after Ziegler and Natta I: Polyethylene and Polypropylene*, Kaminsky, W., Ed. Springer Berlin Heidelberg: Berlin, Heidelberg, 2013; pp 203-251.

17. Monrabal, B.; del Hierro, P., Characterization of polypropylene–polyethylene blends by temperature rising elution and crystallization analysis fractionation. *Analytical and bioanalytical chemistry* **2011,** *399* (4), 1557-1561.

18. Monrabal, B.; Sancho‐Tello, J.; Mayo, N.; Romero, L. In *Crystallization elution fractionation. A new separation process for polyolefin resins*, 2007; Wiley Online Library: pp 71-79.

19. Pasch, H.; Malik, M. I., Crystallization-Based Fractionation Techniques. In *Advanced Separation Techniques for Polyolefins*, Pasch, H.; Malik, M. I., Eds. Springer International Publishing: Cham, 2014; pp 11-73.

20. Francuskiewicz, F., *Polymer fractionation*. Springer Science & Business Media: 2013.

21. Kamide, K.; Miyazaki, Y., Operating conditions for preparative successive solutional fractionation. 2. Miscellaneous factors including experimental performance, a modified procedure, and repetition of fractionation. *Makromol. Chem.* **1975,** *176* (5), 1447-70.

22. Kamide, K.; Miyazaki, Y., Operating conditions for preparative successive solutional fractionation. 1. Effect of initial concentration and fraction size. *Makromol. Chem.* **1975,** *176* (5), 1427-46.

23. Kamide, K.; Miyazaki, Y., Comparison of successive solutional fractionation with successive precipitational fractionation. *Die Makromolekulare Chemie* **1975,** *176* (11), 3453-3469.

24. Kamide, K.; Miyazaki, Y., Effect of average molecular weight of the original polymer on the separation characteristics in successive solutional fractionation. *Die Makromolekulare Chemie* **1975,** *176* (4), 1029-1050.

25. Kamide, K.; Miyazaki, Y., Effect of molecular weight distribution of the original polymer on separation characteristics in successive solutional fractionation. *Die Makromolekulare Chemie* **1975,** *176* (4), 1051-1069.

26. Kamide, K.; Miyazaki, Y., Operating conditions for preparative successive solutional fractionation, 1. Effect of initial concentration and fraction size. *Die Makromolekulare Chemie* **1975,** *176* (5), 1427-1446.

27. Kamide, K.; Miyazaki, Y., Operating conditions for preparative successive solutional fractionation, 2. Miscellaneous factors including experimental performance, a modified procedure, and repetition of fractionation. *Die Makromolekulare Chemie* **1975,** *176* (5), 1447-1470.

28. Kamide, K.; Miyazaki, Y., Study on the possibility of reverse‐order fractionation in successive precipitational fractionation. *Die Makromolekulare Chemie* **1975,** *176* (8), 2393-2412.

29. Kamide, K.; Miyazaki, Y.; Yamaguchi, K., Operating conditions for successive precipitational fractionation of macromolecules. 2. Analytical fractionation. *Makromol. Chem.* **1973,** *173*, 175-93.

30. Kamide, K.; Miyazaki, Y.; Yamaguchi, K., Operation conditions for successive precipitational fractionation of macromolecules. 1. Preparative fractionation. *Makromol. Chem.* **1973,** *173*, 157-74.

31. Kamide, K.; Yamaguchi, K.; Miyazaki, Y., Effect of molecular weight distribution of the original polymer on separation characteristics in successive precipitational fractionation. *Die Makromolekulare Chemie* **1973,** *173* (1), 133-155.

32. Chen, H.-L.; Li, L.-J.; Ou-Yang, W.-C.; Hwang, J. C.; Wong, W.-Y., Spherulitic Crystallization Behavior of Poly(ε-caprolactone) with a Wide Range of Molecular Weight. *Macromolecules* **1997,** *30* (6), 1718-1722.

33. Koleske, J. V.; Lundberg, R. D., Lactone polymers. II. Hydrodynamic properties and unperturbed dimensions of poly-ε-caprolactone. *J. Polym. Sci., Part A-2* **1969,** *7* (5), 897-907.

34. Sheth, S. Self-Consistency of the Lauritzen-Hoffman and Strobl Models of Polymer Crystallization Evaluated for Poly(Epsilon-Caprolactone) Fractions and Effect of Composition on the Phenomenon of Concurrent Crystallization in Polyethylene Blends. Ph.D Thesis, Virginia Polytechnic Institute and State University, Blacksburg, VA, 2013.

35. Perret, R.; Skoulios, A., Synthèse et caractérisation de copolymères séquencés polyoxyéthylène/poly ‐ ε ‐ caprolactone. *Die Makromolekulare Chemie* **1972,** *156* (1), 143-156.

36. Crescenzi, V.; Manzini, G.; Calzolari, G.; Borri, C., Thermodynamics of fusion of poly-β-propiolactone and poly-E-caprolactone. Comparative analysis of the melting of aliphatic polylactone and polyester chains. *Eur. Polym. J.* **1972,** *8* (3), 449-63.

37. Bendix, D. E., G.; Catalsty-Free Resorbable Homopolymers and Copolymers. 4,960,866, 1990.

38. Nishida, H.; Mori, T.; Hoshihara, S.; Fan, Y.; Shirai, Y.; Endo, T., Effect of tin on poly(l-lactic acid) pyrolysis. *Polym. Degrad. Stab.* **2003,** *81* (3), 515-523.

39. Schindelin, J.; Arganda-Carreras, I.; Frise, E.; Kaynig, V.; Longair, M.; Pietzsch, T.; Preibisch, S.; Rueden, C.; Saalfeld, S.; Schmid, B., Fiji: an open-source platform for biological-image analysis. *Nature methods* **2012,** *9* (7), 676.

40. Möller, M.; Kånge, R.; Hedrick, J. L., Sn (OTf) 2 and Sc (OTf) 3: efficient and versatile catalysts for the controlled polymerization of lactones. *Journal of Polymer Science Part A: Polymer Chemistry* **2000,** *38* (11), 2067-2074.

41. Gowda, R. R.; Chakraborty, D., Environmentally benign process for bulk ring opening polymerization of lactones using iron and ruthenium chloride catalysts. *J. Mol. Catal. A: Chem.* **2009,** *301* (1-2), 84-92.

42. Lou, X.; Detrembleur, C.; Jérôme, R., Living cationic polymerization of δ-valerolactone and synthesis of high molecular weight homopolymer and asymmetric telechelic and block copolymer. *Macromolecules* **2002,** *35* (4), 1190-1195.

43. Bogdal, D.; Pisarek, U. In *Polymer chemistry under microwave irradiation*, Wiley-VCH Verlag GmbH & Co. KGaA: 2012; pp 1013-1057.

44. Fang, X.; Simone, C. D.; Vaccaro, E.; Huang, S. J.; Scola, D. A., Ring‐opening polymerization of ϵ‐caprolactam and ϵ‐caprolactone via microwave irradiation. *Journal of Polymer Science Part A: Polymer Chemistry* **2002,** *40* (14), 2264-2275.

45. Liao, L. Q.; Liu, L. J.; Zhang, C.; He, F.; Zhuo, R. X.; Wan, K., Microwave‐assisted ring‐opening polymerization of ϵ‐caprolactone. *Journal of Polymer Science Part A: Polymer Chemistry* **2002,** *40* (11), 1749-1755.

46. Singla, P.; Mehta, R.; Berek, D.; Upadhyay, S. N., Microwave assisted synthesis of poly(lactic acid) and its characterization using size exclusion chromatography. *J. Macromol. Sci., Part A: Pure Appl. Chem.* **2012,** *49* (11), 963-970.

47. Ristic, I. S.; Radusin, T.; Pilic, B.; Cakic, S.; Budinski-Simendic, J., The influence of isosorbide on thermal properties of poly(L-lactide) synthesized by different methods. *Polym. Eng. Sci.* **2013,** *53* (7), 1374-1382.

48. Labet, M.; Thielemans, W., Synthesis of polycaprolactone: a review. *Chem. Soc. Rev.* **2009,** *38* (12), 3484-3504.

49. Zhu, N.; Feng, W.; Hu, X.; Zhang, Z.; Fang, Z.; Zhang, K.; Li, Z.; Guo, K., Organocatalyzed continuous flow ring-opening polymerizations to homo- and block-polylactones. *Polymer* **2016,** *84*, 391-397.

50. Yang, J.; Li, Q.; Li, Y.; Jia, L.; Fang, Q.; Cao, A., Chemical preparation and characterization of new biodegradable aliphatic polyesters end-capped with diverse steroidal moieties. *J. Polym. Sci., Part A: Polym. Chem.* **2006,** *44* (6), 2045-2058.

51. Wang, X.; Brosmer, J. L.; Thevenon, A.; Diaconescu, P. L., Highly Active Yttrium Catalysts for the Ring-Opening Polymerization of ε-Caprolactone and δ-Valerolactone. *Organometallics* **2015,** *34* (19), 4700-4706.

52. Wunderlich, B., CHAPTER VI - The Growth of Crystals. In *Macromolecular Physics*, Wunderlich, B., Ed. Academic Press: 1976; pp 115-347.

53. Wunderlich, B., CHAPTER V - The Nucleation Step. In *Macromolecular Physics*, Wunderlich, B., Ed. Academic Press: 1976; pp 1-114.

54. Arnold, L. Crystallization and Melting Behavior of (ε-caprolactone)-based Homopolymer and Triblock Copolymer. Ph.D Thesis, Virginia Polytechnic Institute & State University, Blacksburg, VA, 1995.

55. Huang, J.; Marand, H., Kinetics of Spherulitic Growth of Poly(pivalolactone) in Blends with Poly(vinylidene fluoride-co-tetrafluoroethylene): Effect of Specific Interactions on the Thermodynamic and Kinetic Secondary Nucleation Parameters. *Macromolecules* **1997,** *30* (4), 1069-1073.

56. Huang, J.; Prasad, A.; Marand, H., Study of the temperature dependence of isothermal spherulitic growth rate data for poly(pivalolactone) in blends with poly(vinylidene fluoride): a link between coherent secondary nucleation theory and mixing thermodynamics. *Polymer* **1994,** *35* (9), 1896-908.

57. Iler, H. D. A Study of the Crystallization Kinetics of Isotactic Polystyrene. Doctor of Philosophy, Vriginia Polytechnic Institute and State University, Blacksburg, VA, 1995.

58. Xu, J. Virginia Polytechnic Institute and State University, 1999.

59. Mohammadi, H. On the Melting and Crystallization of Linear Polyethylene, Poly(ethylene oxide), and Metallocene Linear Low-Density Polyethylene. Ph.D. Thesis, Virginia Polytechnic Institute and State University, Blacksburg, VA, 2018.

60. Avrami, M., Kinetics of phase change. II. Transformation-time relations for random distribution of nuclei. *J. Chem. Phys.* **1940,** *8*, 212-24.

61. Ergoz, E.; Fatou, J. G.; Mandelkern, L., Molecular weight dependence of the crystallization kinetics of linear polyethylene. I. Experimental results. *Macromolecules* **1972,** *5* (2), 147-157.

62. Fatou, J. G.; Marco, C.; Mandelkern, L., The influence of molecular weight on the regime crystallization of linear polyethylene. *Polymer* **1990,** *31* (9), 1685-1693.

63. Fatou, J. G.; Marco, C.; Mandelkern, L., The crystallization kinetics of low-molecular-weight polyethylene fractions. *Polymer* **1990,** *31* (5), 890-898.

64. Toda, A., Heating rate dependence of melting peak temperature examined by DSC of heat flux type. *J. Therm. Anal. Calorim.* **2016,** *123* (3), 1795-1808.

65. Schulz, M.; Seidlitz, A.; Kurz, R.; Bärenwald, R.; Petzold, A.; Saalwächter, K.; Thurn-Albrecht, T., The Underestimated Effect of Intracrystalline Chain Dynamics on the Morphology and Stability of Semicrystalline Polymers. *Macromolecules* **2018,** *51* (21), 8377-8385.

66. Hu, W. G.; Schmidt‐Rohr, K., Polymer ultradrawability: the crucial role of α‐relaxation chain mobility in the crystallites. *Acta Polymerica* **1999,** *50* (8), 271-285.

67. Vincent, M. Crystallization and Melting Studies of Poly(ε-caprolactone) and Poly(ethylene oxide) using Flash™ Differential Scanning Calorimetry and Characterization of Poly(δ-valerolactone) Fractions. Virginia Polytechnic Institute and State University, Blacksburg, VA, 2019.

68. Mandelkern, L.; Allou Jr, A. L.; Gopalan, M. R., Enthalpy of fusion of linear polyethylene. *The Journal of Physical Chemistry* **1968,** *72* (1), 309-318.

69. Glotin, M.; Mandelkern, L., Crystalline morphology of isothermally crystallized branched polyethylene. *Macromolecules* **1981,** *14* (5), 1394-1404.

70. Day, M.; Deslandes, Y.; Roovers, J.; Suprunchuk, T., Effect of molecular weight on the crystallization behaviour of poly(aryl ether ether ketone): a differential scanning calorimetry study. *Polymer* **1991,** *32* (7), 1258-1266.

71. Rodriguez-Arnold, J.; Zhang, A.; Cheng, S. Z. D.; Lovinger, A. J.; Hsieh, E. T.; Chu, P.; Johnson, T. W.; Honnell, K. G.; Geerts, R. G.; Palackal, S. J., Crystallization, melting and morphology of syndiotactic polypropylene fractions: 1. Thermodynamic properties, overall crystallization and melting. *Polymer* **1994,** *35* (9), 1884-1895.

72. Ou-Yang, W.-C.; Li, L.-J.; Chen, H.-L.; Hwang, J. C., Bulk crystallization behavior of poly (ε-caprolactone) with a wide range of molecular weight. *Polymer journal* **1997,** *29* (11), 889.

73. Strobl, G., From the melt via mesomorphic and granular crystalline layers to lamellar crystallites: a major route followed in polymer crystallization? *Eur. Phys. J. E* **2000,** *3* (2), 165-183.

CHAPTER 6

General Conclusions and Suggested Future Work

6.1 GENERAL CONCLUSIONS

Chapter 3 reported the melting behavior of poly(ε-caprolactone) (PCL) as a function of isothermal crystallization temperature and time using fast differential scanning calorimetry (FDSC). The melting kinetics exponent was shown to be independent of isothermal crystallization temperature and time. The zero-heating-rate initial melting temperatures were parallel to the line $T_m' = T_x$ for isothermal crystallization above 31.4°C, equal to the crystallization temperature following isothermal crystallization below −23.6°C, and approximately −63°C for crystallization at or below the glass transition temperature (T_g = −63°C). This behavior prohibits determining the equilibrium melting temperature with the conventional Hoffman-Weeks method. To circumvent this problem, the Gibbs-Thomson method was used to determine the equilibrium melting temperature as T_m = 103.4 ± 2.3°C. This value is higher than any previously reported equilibrium melting temperature, but previous melting temperature analyses are unreliable due to stabilization or annealing during heating with conventional differential scanning calorimetry. A modification was proposed to the conventional Hoffman-Weeks equation that incorporated a power series expansion into the kinetic fold surface free energy upon crystallization, and the observed melting behavior was accurately modeled by the new modified non-linear Hoffman-Weeks equation. Additionally, our results indicated that PCL does not follow a three-stage mechanism, as Strobl[1] proposed, because the crystallization and melting lines never intersect.

The isothermal crystallization kinetics of poly(ethylene oxide) (PEO) were analyzed in Chapter 4. The peak time of crystallization was a bimodal function of the crystallization temperature, which was attributed to a change from homogeneous to heterogeneous primary nucleation at low and high crystallization temperatures, respectively. There was no apparent molecular weight dependence across

the ca. 100°C temperature range that was investigated. We hypothesized the molecular weight dependence is obscured by varying levels of heterogeneities and differences in sample volume that alter the primary nucleation kinetics. The Avrami exponents displayed a strong temperature dependence where $n \approx 2$ approaching the glass transition temperature (T_x = −55°C), n scaled from 2 to 6 in the temperature range of homogeneous primary nucleation (T_x = −5°C), and $n \approx 3$ in the temperature range of heterogeneous primary nucleation. Changing primary nucleation mechanisms and crystal growth geometries give rise to the changing Avrami exponents. The low temperature and high temperature limits correspond to homogeneously nucleated rods and heterogeneously nucleated spheres, respectively. At intermediate temperatures, the scaling exponents from 2 to 6 correspond to homogeneously nucleated solid sheaves, where larger exponents indicate higher extent of branching.[2, 3]

In Chapter 5, we demonstrated the synthesis of poly(δ-valerolactone) (PVL) using a microwave-assisted approach. Narrow molecular weight fractions were obtained via successive precipitation fractionation using toluene and *n*-heptane as the solvent/nonsolvent pair. The spherulite growth rates at the same isothermal crystallization temperature appeared to be at least one order of magnitude slower than poly(ε-caprolactone) of comparable molecular weight. The equilibrium melting temperature of PVL was estimated to be ca. 15°C lower than that of PCL. Basic thermal characterization of the fractions showed that the crystallinity decreased with increasing molecular weight and crystallization temperature. Stabilization effects occurred during heating with conventional differential scanning calorimetry, which prevented determination of meaningful melting temperatures following isothermal crystallization.

6.2 SUGGESTED FUTURE WORK

6.2.1 Elucidating the origin of increasing melting temperature in crystal-fixed polymers

Crystal-fixed polymers do not possess an α_c-relaxation,[4] which is generally accepted as the mechanism for intracrystalline dynamics that leads to isothermal lamellar thickening. Hoffman and Weeks[5, 6] originally proposed that isothermal lamellar thickening was the cause for increasing melting temperature with increasing crystallization time, but this cannot be the case for crystal-fixed polymers. Melting temperatures that are parallel to the line $T_m' = T_x$ have been reported for PCL[7] and other polymers[8-14] crystallized to completion, but the behavior persisted over the entire measurable range of isothermal crystallization temperatures. These results differ considerably from our observations of the zero-heating-rate initial melting temperatures. A better understanding of the interplay between morphology development and thermal stability will help develop a universal theory describing polymer crystallization. Fast differential scanning calorimetry should be combined with time-resolved morphological characterization, such as small-angle X-ray scattering, wide angle x-ray diffraction, or atomic force microscopy, to elucidate the mechanism of increasing melting temperature with crystallization time. Ideally, the thermal and morphological characterization would be conducted simultaneously, but atomic force microscopy cannot be conducted *in situ* on a FDSC sample because the chip membrane must be removed from the ceramic chip frame.

6.2.2 Investigating the effects of isothermal crystallization temperature and time on polymer melting kinetics

There is contention in the literature regarding the effects of isothermal crystallization temperature on polymer melting kinetics.[9, 10, 13, 15] Our study on PCL is the first to study the effects of isothermal crystallization time on polymer melting kinetics. As such, this is an open area that requires investigation. Understanding the effects of isothermal crystallization temperature and time on the melting behavior of polymers is crucial for determining the equilibrium melting temperature of

polymers using the non-linear Hoffman-Weeks method. Future studies should also focus on determining possible effects from chain length, chemical structure, and chain stiffness on the melting kinetics, although not until the simpler cases of isothermal crystallization temperature and time are resolved.

6.2.3 Validating the proposed modifications to the non-linear Hoffman-Weeks equation

Chapter 3 proposed modifications to the non-linear Hoffman-Weeks equation that incorporated a power series expansion into the kinetic fold surface free energy upon crystallization. The proposed modification should undergo further validation by incorporating the non-linear kinetic fold surface free energy upon crystallization into the spherulite growth rate equation and analyzing experimental spherulite growth rate data. Additionally, the modification should be applied to other polymers that exhibit similar melting behavior to PCL. Doing so will require reliable lamellar thickness data in addition to melting data measured with FDSC. Ideally the data would be acquired in tandem using time-resolved small-angle X-ray scattering.

6.2.4 Sampling statistics on the isothermal crystallization of poly(ethylene oxide)

In Chapter 4, we hypothesized that the effect of molecular weight on the crystallization kinetics of PEO was obscured by some combination of differences in sample volume or varying amounts of heterogeneities. Unfortunately, testing this hypothesis requires experiments on enough samples to develop reliable statistics. A proposed experimental approach to answering this question would be running a series of experiments on five to ten samples with similar volumes. Heterogeneities could be removed from the bulk sample by passing a dilute solution through a micron-dimension filter, then the same series of experiments rerun on five to ten sample with similar volumes.

6.2.5 Conducting the Avrami analysis at large undercoolings for additional polymers

There are only a handful of publications on the Avrami analysis using data measured with FDSC,[16-18] and the literature does not contain any other results for the Avrami analysis similar to our findings on PEO. More polymers should be analyzed, but special focus should be given to polymers with

glass transition temperatures above room temperature. These materials can be crystallized at large undercoolings in a fast differential scanning calorimeter, then the morphology or crystalline structure can be analyzed conveniently at room temperature. Prime candidates include polyamide-6,6[19, 20] and poly(butylene terephthalate)[21, 22] because they have glass transition temperatures above room temperature and they exhibit similar trends to PEO in peak time of crystallization as a function of crystallization temperature. These experiments would help confirm the morphology at large undercoolings where primary homogeneous nucleation occurs.

6.2.6 Investigating the melting and crystallization of poly(δ-valerolactone) using fast differential scanning calorimetry

The melting of poly(δ-valerolactone) (PVL) fractions following isothermal crystallization with conventional differential scanning calorimetry (CDSC) appeared to be affected by a secondary process during heating, i.e. stabilization, reorganization, or annealing (Chapter 5). As a result, we proposed that CDSC is not adequate to measure true melting behavior of PVL, and FDSC should be used to study the isothermal crystallization behavior of PVL fractions. This data could be combined with lamellar thickness data to determine the equilibrium melting temperature of PVL more accurately, and help determine why the spherulite growth rate of this material is considerably slower than PCL.

6.3 REFERENCES

1. Strobl, G., A thermodynamic multiphase scheme treating polymer crystallization and melting. *Eur. Phys. J. E* **2005,** *18* (3), 295-309.

2. Booth, A.; Hay, J. N., An extension of polymer crystallisation kinetics to a branching mechanism for spherulitic growth. *British Polymer Journal* **1972,** *4* (1), 9-17.

3. Morgan, L. B., Crystallization phenomena in polymers-The course of the crystallization. *Phil. Trans. R. Soc. Lond. A* **1954,** *247* (921), 13-22.

4. Hu, W. G.; Schmidt‐Rohr, K., Polymer ultradrawability: the crucial role of α‐relaxation chain mobility in the crystallites. *Acta Polymerica* **1999,** *50* (8), 271-285.

5. Hoffman, J. D.; Weeks, J. J., Melting process and equilibrium melting temperature of poly(chlorotrifluoroethylene). *J. Res. Natl. Bur. Stand., Sect. A* **1962,** *66A* (1), 13-28.

6. Weeks, J. J., Melting temperature and change of lamellar thickness with time for bulk polyethylene. *J. Res. Natl Bur. Stand. A* **1963,** *67*, 441-451.

7. Zhuravlev, E.; Schmelzer, J. W. P.; Wunderlich, B.; Schick, C., Kinetics of nucleation and crystallization in poly(ϵ-caprolactone) (PCL). *Polymer* **2011,** *52* (9), 1983-1997.

8. Furushima, Y.; Kumazawa, S.; Umetsu, H.; Toda, A.; Zhuravlev, E.; Schick, C., Melting and recrystallization kinetics of poly (butylene terephthalate). *Polymer* **2017,** *109*, 307-314.

9. Furushima, Y.; Nakada, M.; Ishikiriyama, K.; Toda, A.; Androsch, R.; Zhuravlev, E.; Schick, C., Two crystal populations with different melting/reorganization kinetics of isothermally crystallized polyamide 6. *Journal of Polymer Science Part B: Polymer Physics* **2016,** *54* (20), 2126-2138.

10. Furushima, Y.; Toda, A.; Rousseaux, V.; Bailly, C.; Zhuravlev, E.; Schick, C., Quantitative understanding of two distinct melting kinetics of an isothermally crystallized poly (ether ether ketone). *Polymer* **2016,** *99*, 97-104.

11. Gradys, A.; Sajkiewicz, P.; Adamovsky, S.; Minakov, A.; Schick, C., Crystallization of poly(vinylidene fluoride) during ultra-fast cooling. *Thermochimica Acta* **2007,** *461* (1), 153-157.

12. Konishi, T.; Sakatsuji, W.; Fukao, K.; Miyamoto, Y., Temperature Dependence of Lamellar Thickness in Isothermally Crystallized Poly(butylene terephthalate). *Macromolecules* **2016,** *49* (6), 2272-2280.

13. Toda, A.; Taguchi, K.; Sato, K.; Nozaki, K.; Maruyama, M.; Tagashira, K.; Konishi, M., Melting kinetics of it-polypropylene crystals over wide heating rates. *Journal of Thermal Analysis and Calorimetry* **2013,** *113* (3), 1231-1237.

14. Xu, J.; Heck, B.; Ye, H.-M.; Jiang, J.; Tang, Y.-R.; Liu, J.; Guo, B.-H.; Reiter, R.; Zhou, D.-S.; Reiter, G. n., Stabilization of Nuclei of Lamellar Polymer Crystals: Insights from a Comparison of the Hoffman–Weeks Line with the Crystallization Line. *Macromolecules* **2016,** *49* (6), 2206-2215.

15. Toda, A.; Taguchi, K.; Nozaki, K.; Konishi, M., Melting behaviors of polyethylene crystals: an application of fast-scan DSC. *Polymer* **2014,** *55* (14), 3186-3194.

16. Cai, J.; Luo, R.; Lv, R.; He, Y.; Zhou, D.; Hu, W., Crystallization kinetics of ethylene-co-propylene rubber/isotactic polypropylene blend investigated via chip-calorimeter measurement. *Eur. Polym. J.* **2017,** *96*, 79-86.

17. Tardif, X.; Pignon, B.; Boyard, N.; Schmelzer, J. W. P.; Sobotka, V.; Delaunay, D.; Schick, C., Experimental study of crystallization of PolyEtherEtherKetone (PEEK) over a large temperature range using a nano-calorimeter. *Polymer Testing* **2014,** *36*, 10-19.

18. Treviño‐Quintanilla, C. D.; Krishnamoorti, R.; Bonilla‐Ríos, J., Flash DSC crystallization study for blown film grade bimodal HDPE resins. I. Isothermal kinetics and its application of the blown film modeling. *Journal of Polymer Science Part B: Polymer Physics* **2016,** *54* (23), 2425-2431.

19. Gohn, A. M.; Rhoades, A. M.; Wonderling, N.; Tighe, T.; Androsch, R., The effect of supercooling of the melt on the semicrystalline morphology of PA 66. *Thermochimica Acta* **2017,** *655*, 313-318.

20. Rhoades, A. M.; Williams, J. L.; Androsch, R., Crystallization kinetics of polyamide 66 at processing-relevant cooling conditions and high supercooling. *Thermochim. Acta* **2015,** *603*, 103-109.

21. Androsch, R.; Rhoades, A. M.; Stolte, I.; Schick, C., Density of heterogeneous and homogeneous crystal nuclei in poly (butylene terephthalate). *European Polymer Journal* **2015,** *66*, 180-189.

22. Schawe, J. E. K., Influence of processing conditions on polymer crystallization measured by fast scanning DSC. *J. Therm. Anal. Calorim.* **2014,** *116* (3), 1165-1173.